Modélisation de l'émission des noyaux actifs de galaxie à l'ère Fermi

Thomas Vuillaume

UNIVERSITÉ DE GRENOBLE

THÈSE

Pour obtenir le grade de

DOCTEUR DE L'UNIVERSITÉ DE GRENOBLE

Spécialité : **Astronomie & Astrophysique**

Arrêté ministériel : du 7 Août 2006

Présentée par

Thomas Vuillaume

Thèse dirigée par **Gilles Henri**
et codirigée par **Pierre-Olivier Petrucci**

préparée au sein **de l'équipe Sherpas à l'Institut de Planétologie et d'Astrophysique de Grenoble**
et de **l'École Doctorale de Physique de Grenoble**

Modeling the emission of active galactic nuclei at Fermi's era

Thèse soutenue publiquement le **16 Octobre 2015**,
devant le jury composé de :

Pr Laurent Derome
Professeur au Laboratoire de physique subatomique et de cosmologie de Grenoble, Président

Pr Gabriele Ghisellin
Professeur à Osservatorio Astronomico di Brera, Rapporteur

Dr Julien Malzac
Chargé de recherche à l'Institut de Recherche en Astrophysique et Planétologie de Toulouse, Rapporteur

Dr Catherine Boisson
Astronome à l'Observatoire de Paris, Examinateur

Pr Gilles Henri
Professeur à l'Institut de Planétologie et d'Astrophysique de Grenoble, Directeur de thèse

Dr Pierre-Olivier Petrucci
Chargé de recherche á l'Institut de Planétologie et d'Astrophysique de Grenoble, Co-Directeur de thèse

Remerciements

Quand j'ai commencé cette thèse, je ne savais pas trop dans quoi je m'engageais, je savais juste que c'était ce que je voulais faire. Mais quelle aventure ! Intellectuelle comme humaine... Quelle chance de pouvoir travailler dans un domaine qui m'attire et me passionne depuis l'enfance. Je n'oublie pas que c'est une chance inouïe, que malheureusement peu de personnes ont. Mais je n'oublie pas non plus que c'est une chance pour laquelle il faut se battre tous les jours, pour ne pas perde de vue que la découverte est non seulement vitale, mais plus encore l'accomplissement de toute société humaine. Si j'ai la chance de m'accomplir dans un domaine si enthousiasmant, c'est grâce à quelques personnes (et institutions) qui me sont chères et qu'il me faut remercier grandement.

En premier lieu, je dois remercier le jury, et en particulier les rapporteurs, Julien Malzac et Gabriele Ghisellini, sans qui vous n'auriez pas l'opportunité de parcourir de magnifique manuscrit. Merci pour leur travail et leur implication. Je remercie ensuite l'IPAG tout entier, fantastique laboratoire d'accueil où j'ai rencontré des collègues en or et où j'ai pu évoluer sereinement. Merci aux personnels administratifs et techniques qui font tourner la boutique dans l'ombre !

Merci aux Sherpas, une équipe bien singulière au sein de laquelle l'humain est au coeur des échanges. La plus belle façon de faire de la science... C'est avec regret que je vous quitterai bientôt. Je voudrais remercier en particulier Didier, qui a été très attentif et d'une grande aide pour la résolution des problèmes d'optimisation, ainsi que Morgan, étudiant excellent et intéressé qui a fortement contribué au développement et à l'amélioration de l'algorithme génétique. Et bien sur, il y a Gilles et Pop, le duo de choc, les *Starsky et Hutch* des hautes énergies ("ces scientifiques rieurs et un peu rêveurs"... je vous laisse deviner qui est qui). Je n'aurais pas pu imaginer meilleurs encadrants, autant scientifiques qu'humanistes. Merci pour tout.

Merci aussi à tous les thésards, compagnons de fortune(s). En particulier Solenn, bien plus qu'un co-bureau, un véritable ami. Ces trois années n'auraient vraiment pas eu la même saveur sans toi pour les faire résonner dans nos aventures sportives et fromagères. Bien sur ces aventures là ne s'arrêteront pas avec la thèse ! Rendez-vous dans les vignes bourguignonnes et sur les sommets savoyards !

Mes pensées vont ensuite à mes amis et ma famille. À Robin et Ju, Max et Rosa, chaudière (ce touriste), tous les autres dont la liste formerait une véritable bibliographie (je ne vous oublie pas !) et toute la fratrie (Loïc, Arnaud, Mathilde, Lucie, Théo et Paul), merci pour votre amitié qui me donne la liberté d'être moi même. Merci à tous ceux qui ont pris le temps (et eu le courage !) de venir me soutenir le jour de ma soutenance (tous mes grand parents, Daniel, Caroline, Charlotte et Julie, Myriam, Thierry, Mathieu, Fanny et Alice, Jeremy et Fanny, Julien, Cyril, Valérian - merci pour la relecture !, Romain et Julie, Katrin et Robert, Marie et Pat' - merci pour le pot !, Domi - hope you are fine,

Jo, Nikos, les roux, Onintza, Pierre et Pauline, Will et Kim, Mag et Marc, Manutéa, Fanny... j'espère n'oublier personne !) mais aussi à ceux qui m'ont encouragé à distance. Et surtout, surtout, merci à mes parents (les 4! - qui ensemble doivent rassembler toutes les qualités du monde). Si j'ai eu la chance d'arriver jusque là, c'est bien grâce à vous qui m'avez permis d'accéder à une vie et une éducation privilégiées. Pour votre amour et pour votre soutien, même quand ce que je fais vous semble terriblement obscur, merci.

Last but not least, merci à la plus belle des folies qu'il me soit arrivé. À ton oreille attentive, ton soutien inconditionnel, ton optimisme indéfectible, ta patience, ton sourire, ton amitié et ton amour, à toi, Marina, merci.

"As for me, I am tormented with an everlasting itch for things remote. I love to sail forbidden seas, and land on barbarous coasts."
– Herman Melville, Moby-Dick.

A tous ceux qui repoussent les frontières,

Summary

Active galactic nuclei (AGN) are the most energetic objects known in the universe. Their fantastic luminosity is due to efficient conversion of gravitational energy of mass accreted on super-massive black-holes at the center of galaxy. About 10% of AGN are even more incredible as they display relativistic jets on galaxy scales. Those jets are observed at all energies, from far radio to the highest $\gamma - rays$. Despite intense study since their discovery in the 50's and more and more observations, encouraged by rapid progress in instrumentation, AGN are still widely misunderstood. The questions of formation, composition, and acceleration of jets are central but still a matter of debates. Models aiming at reproducing observed emission have been developed throughout the years. The most common one, the one-zone model, often relies on ad-hoc hypothesis and does not provide a satisfactory answer.

The two-flow paradigm developed at IPAG and based on an original idea from Sol et al. (1989) aims at giving a more coherent and physical representation of AGN jets. The principal assumption is that jets are actually composed of two coaxial flows: an inner spine made of a pure pair plasma, moving at relativistic speed and responsible for the non-thermal observed emission surrounded by an external sheath, made of a baryonic MHD plasma, mildly relativistic but carrying most of the power. The two-flow paradigm finds roots in observations as well as theoretical arguments and has been able to explain many AGN features.

During my PhD, I studied this paradigm and contributed to the development of a numerical model based on its concepts. I have been particularly interested in the inverse Compton scattering of thermal photons, fundamental process in the modeling of AGN emission, as well as the Compton rocket effect, key to the acceleration of the spine in the two-flow paradigm.

However, taking completely into account the inverse Compton emission can be very time consuming. To accomplish fast and efficient computation of the external Compton emission, I have had to formulate new analytical approximations of the scattering of a thermal distribution of photons.

I have also studied the Compton rocket effect, responsible for the acceleration of the inner spine in the two-flow paradigm. I showed that the resulting bulk Lorentz factor of the flow in the complex photon field of an AGN is subject to variations along the jet as a function of the distance to the central engine. These variations can have drastic effects on the observed emission and could induce variability, both spatially and temporally. I also showed that the terminal bulk Lorentz factor obtained are compatible with physical conditions expected in jets and with observations.

The complete model produce spectral energy distribution (SED) comparable to observed ones. However, the model is by nature erratic and it is difficult to make a direct link between the model parameters (input) and the SED (output). Unfortunately, standard data fitting procedures (e.g. based on gradient methods) are not adapted to the model due to its important number of parameters, its important computing time and its non-linearity. In order to circumvent this issue, I have developed a fitting tool based on genetic algorithms. The application of this algorithm allowed me to successfully fit several SED. In particular, I have also showed that the model, because based on a structured jet model, can reproduce observations with low bulk Lorentz factor, thus giving hope to match observations and theoretical requirements in this matter.

Résumé

Les noyaux actifs de galaxie (NAG) sont les objets les plus énergétiques de l'univers. Cette incroyable puissance provient de l'énergie gravitationnelle de matière en rotation autour d'un trou noir super-massif siégeant au centre des galaxies. Environ 10% des NAG sont pourvus de jets relativistes émanant de l'objet central (trou noir et matière environnante) et s'étalant sur des échelles de l'ordre de la galaxie hôte. Ces jets sont observés à toutes les longueurs d'ondes, de la radio aux rayons gamma les plus énergétiques. En dépit de nombreuses études et d'instruments de plus en plus précis depuis leur découverte dans les années 1950, les NAG sont encore très mal compris et la formation, la composition et l'accélération des jets sont des questions pleinement ouvertes. Le modèle le plus répandu visant à reproduire l'émission des NAG, le modèle "une zone", repose souvent sur des hypothèses *ad hoc* et ne parvient pas à apporter une modélisation satisfaisante.

Le paradigme du "*two-flow*" (deux fluides) développé à l'IPAG, et fondé sur une idée originale de Sol et al. (1989), a pour but de fournir une vision unifiée et cohérente des jets de NAG. Cette théorie repose sur une l'hypothèse principale que les jets seraient en fait composés de deux fluides co-axiaux. La colonne centrale composée d'un plasma purement leptonique (électrons/positrons) se déplaçant à des vitesses relativistes est responsable de la grande partie de l'émission non thermique observée. Elle est entourée d'une enveloppe composée d'un plasma baryonique (électrons/protons), régie par la magnéto-hydrodynamique, se déplaçant à des vitesses sous-relativistes mais transportant la majorité de l'énergie. Cette hypothèse s'appuie sur des indices observationnels ainsi que sur des arguments théoriques et permet d'expliquer nombre des caractéristiques des NAG.

Afin d'étudier plus en profondeur le paradigme du two-flow, un modèle numérique établie sur ses concepts et produisant des observables comparables aux observations est nécessaire. Durant ma thèse, j'ai participé au développement de ce modèle, m'intéressant notamment à la diffusion Compton inverse de photons provenant de l'extérieur du jet. Ce processus, primordial dans la modélisation des NAG, est aussi central dans le paradigme du *two-flow* car il est à l'origine de l'accélération de la colonne via l'effet fusée Compton. Pour cela, j'ai du développer de nouvelles approximations analytiques de la diffusion Compton d'une distribution thermique de photons.

En m'intéressant à l'effet fusée Compton, j'ai pu montrer que dans le champ de photons thermiques d'un NAG, le facteur de Lorentz d'ensemble du plasma pouvait être sujet à des variations le long du jet en fonction de la distance à l'objet central. Ces variations peuvent avoir un effet important sur l'émission observée et peuvent induire de la variabilité spatiale et temporelle. J'ai également montré que les facteurs de Lorentz terminaux obtenus étaient compatibles avec les conditions physiques attendues dans les jets et avec les observations.

Le modèle complet produit des densités spectrales d'énergies (DES) directement comparables aux observations. Néanmoins, le modèle est par nature erratique et il est quasiment impossible de relier directement les paramètres du modèles avec les DES produites. Malheureusement, les procédures standards d'adaptation automatique aux données (*e.g.*

les méthodes de gradient) ne sont pas adaptées au modèle du fait de son grand nombre de paramètres, de sa non-linéarité et du temps de calcul important. Afin de pallier ce problème, j'ai développé une procédure d'adaptation automatique s'appuyant sur les algorithmes génétiques. L'utilisation de cet outil a permis la reproduction de plusieurs DES par le modèle. J'ai également montré que le modèle était capable de reproduire les DES observées avec des facteurs de Lorentz d'ensemble relativement bas, ce qui pourrait potentiellement apporter une harmonisation entre les observations et les nécessités théoriques.

Contents

Part I

Introduction

Chapter 1

Active galactic nuclei you said ?

Contents

1.1 *A bit of history*

The discovery of active galactic nuclei (AGN) is not very old. One may argue that the history begins in 1930 with Jansky who worked as an engineer for the Bell Telephone Company. He was studying interferences in radio communication between USA and UK and was able to divide them into three main sources: two of them were due to thunderstorms but the last one was a mysterious steady source in the sky. Paradoxically, it was the first galactic nuclei ever detected and a peculiar one, the center of the Milky Way. Even if Jansky thought about an astrophysical source[1], no one at the time thought about the galactic center. This discovery did not really catch the interest of astronomers and was forgotten for a while.

Then war came and the hot topic was not astronomy. But it pushed research to make important progresses in radio communication, for obvious purposes. It allowed radioastronomy to really developed at the end of WWII, based on these new technologies and numerous people able to use it. In 1949, Bolton, Stanley and Slee identify two bright radio sources as two galaxies, Virgo A (NGC 4486) and Centaurus A (NGC 5128). These were the two first radio-galaxies identified (and thus the two first extragalactic radio sources) and marked the beginning of a whole field.

[1] he attributed it to interstellar gas

A bit earlier, in 1943, Seyfert discovered[2] a dozen of peculiar galaxies with a very bright nucleus rich in emission lines whom large widths were attributed to Doppler shifts. Interestingly, two of these galaxies were also detected in radio (NGC1068 and NGC1275 in 1955) and it was thought than there was a link between radio-galaxies and Seyfert galaxies.

Other radio sources were detected but the identification was very difficult with the angular resolution of radio telescope at this time. Moreover, these sources did not always have an optical counterpart (observations in optical were done with photographic plates). It was therefore not clear whether they were galactic sources or extragalactic sources. In 1961, T. Matthews associated the radio source 3C48 with an object detected in optical and similar to star. Spectral analysis showed a very peculiar spectrum, very different from a stellar one and it was thought that one was dealing with a new type of star, a radio-star. But in 1963, Hazard, Mackey and Shimmins detected a similar object, 3C 273. A spectral analysis allowed Schmidt to show that all spectral emission lines were red-shifted of a factor $1 + z$ with $z = 0.158$. Then the redshift of 3C48 could be calculated to $z = 0.37$. As the nature of these quasi-stellar objects (later called quasars) was unknown, possible origins of such redshifts were discussed. From their spectral distribution and their emission lines, the idea of a massive ($10^9 M_\odot$) galactic nucleus has been advanced quite early (Greenstein and Schmidt (1964)).

In 1968, yet another type of radio source is discovered, VRO 42.22.01. It shows a complex spectrum, low angular dimensions and very fast and important flux variability. Even if it shows many similarities with quasars, it can not be assimilated to this class because of its rapid variability and lack of emission lines. On the contrary, the important variability suggested an association to the previously discovered variable star BL Lacertae[3] by Cuno Hoffmeister in 1929.

The 70's marked an interesting turn in AGNs discovery thanks to the development of long based interferometry in radio. The first milestone was the discovery of superluminal motion thanks to very long based interferometry (VLBI). By recording separately the signals from two different antennas on magnetic tapes and correlating them later, Knight et al. (1971) observed the presence of two emission points in 3C273 separated with $(1.55 \pm 0.05) \times 10^{-3}$ arc second. Only four months later, Whitney et al. (1971) observe the same two points with an angular separation of $(1.69 \pm 0.02) \times 10^{-3}$. With the known redshift of $z = 0.538$, the corresponding distance between the two observations could be calculated to almost 4 light-years, which meant that the source moved at a linear speed of 10 times the speed of light. Such a superluminal motion was then confirmed in 3C273 by Cohen et al. (1971).

The second great discovery of long based interferometry has been the presence of jets emanating from the nuclei of the radio-galaxies 3C 219 (Turland (1975)) and B0844+31 (van BREUGEL and MILEY (1974)). The connection was made with Cygnus A observed much earlier by Jennison and Das Gupta in 1953 as these jets could be able to power the radio structures extending outside of the Cygnus A galaxy.

The development of high-energy observations was the next step in AGNs surprising observations. It started with the installation of X-ray detectors aboard rockets in 1962 but the first active galaxies detected at high-energies were M87 and 3C273 by Friedman and Byram (1967) followed by Centaurus A by Bowyer et al. (1970). Then the space race

[2]The actual discovery of a Seyfert galaxy must be attributed to Edward A. Fath and Vesto Slipher who noticed that NGC 1068 showed six bright emission lines in 1908. But with the discovery of many more, Seyfert proved that one was dealing with an actual type of galaxy.

[3]which later gave its name to the AGN group BL Lacs

allowed the launch of scientific satellites which opened the path to γ-ray astronomy with the Orbiting Solar Observatory (OSO-7) in 1971. The Celestial Observation Satellite B (COS-B) was launched in 1975 and carried a detector sensitive to γ-rays (up to 1 GeV). Measurement from COS-B allowed SWANENBURG et al. (1978) to establish 3C 273 as a γ-ray source. Finally, the TeV range becomes accessible thanks to atmospheric Cherenkov telescopes (HEGRA - High Energy Gamma Ray Astronomy Array, CAT - Cherenkov Array at Themis and TAP - Telescope Array Prototype) in 1997 which detect several TeV flares from the blazar Markarian 501.

Another great field for AGN studies throughout history has been the study of emission lines, starting with the ones from Seyfert galaxies. In 1959 already, Woltjer (1959) derives a density $N_e \approx 10^{-4}\text{cm}^{-3}$ and a temperature $T \approx 20000K$ in Seyferts. Distincts narrow and broad lines were detected in some Seyferts (called Seyfert 1 or Sy 1) whereas some other showed only narrow lines (Seyfert 2). And a key question arising from this fact was wether or not the broad and narrow lines were emitted by the same region (as proposed by Woltjer (1959)). This hypothesis kept being discussed for many years but found great support when photoionization proved to be the source of heating and ionization and that the broad line region (BLR) responsible for the broad emission lines was a small region of dense, fast-moving clouds. The narrow line region (NLR), responsible for the narrow emission lines, is however a larger region of less dense, slower moving clouds. The story continued and made huge progress with the creation of the reverberation mapping techniques which allowed a study of the spatial repartition of the BLR relying on time delays between the ionizing continuum and the line variations (Blandford and McKee (1982)). It is still a major source of information about this region nowadays (e.g Wandel et al. (1999), Kaspi et al. (2000) or Kaspi et al. (2005)).

1.2 What we know and what we do not

> "The more you know, the more you know you don't know"
>
> — Socrates

1.2.1 Some certainties

Supermassive black-holes

AGNs show enormous bolometric luminosities, sometimes up to 10^{48-49} erg.s^{-1} which is 100 times the luminosity of all integrated stars of the host galaxy. Because the size of the emitting region was known to be small early on, such huge luminosities were very difficult to explain as stellar activity could hardly produce so much energy. Proposed models included violent activity from concentrated regions with possibly chain reaction of supernovae, star collisions or starbursts. In 1964, Salpeter (1964) and Zel'dovich (1964) studied the possibility of energy production through accretion of matter onto a supermassive black-hole.

In the Newtonian approximation, the potential power released by matter flowing at a rate $\dot{M}$ at a distance r of a mass M is given by:

$$P_{acc} = \frac{1}{2}\frac{GM}{r}\dot{M} \tag{1.1}$$

If we suppose that the accreting object is a supermassive black-hole of mass $M_\bullet$, the power available is tremendous:

$$P_{acc} \approx \left(\frac{\dot{M}}{\dot{M}_{edd}}\right)\left(\frac{M_\bullet}{10^8 M_\odot}\right)\left(\frac{\eta}{0.1}\right) 10^{46}\mathrm{erg.s}^{-1} \tag{1.2}$$

where $\dot{M}_{edd}$ is the Eddington limit for spherical accretion[4] and η is the efficiency of the system to extract potential energy (for a Schwarschild non-spinning black-hole $\eta = 1/12$ in the Newtonian approximation corrected to $\eta \approx 6\%$ by general relativity and $\sim 42\%$ for a Kerr maximum spinning black-hole). This process releases enough energy to power an AGN[5] and found progressively great support. The black-hole paradigm has been beautifully confirmed by Kormendy (1988) who measured rotation velocities and velocity dispersions in M31 and deduced the presence of a dark central mass of about $10^7 M_\odot$. Similar work has now been done in our own galaxy, observing the path of many stars around the central black-hole, Sagittarius A*. The next generation of instruments[6] should be able to push the angular resolution further enough to picture the event horizon, which will bring the final piece of evidence for supermassive black-holes existence.

Accretion discs and matter around black-holes

The spatial distribution of matter in AGNs and around the central black-hole is still a matter of discussion (despite improvements in reverberation mapping) but it is now certain that there are several emitting regions that we can group under different labels: the accretion disc, the dusty torus, the broad line region and the narrow line region.

The presence of a "Big Blue Bump" (optical/UV continuum) in many AGNs is interpreted as the thermal emission from hot matter plunging onto the black-hole under the form of an accretion disc. It is not present, or at least no visible, in all AGNs (see section 1.3 but when this continuum is detected, it is almost always accompanied with emission lines (Antonucci (2012)). These lines come into two distinct forms, broad and narrow, and are interpreted as the emission from ionized matter gravitationally bound to the black-hole. Finally, the presence of hot dust has been demonstrated by infrared observations. First observations, made for 3C 273 in the K filter by Johnson (1964) and Low and Johnson (1965), already showed a continuum emission. The same kind of emission, less variable than emission at other wavelengths has been found in more and more objects and is consistent with the presence of hot dust sublimating at a temperature between 1200 and 1500 K.

Relativistic motion

It has been suspected quite early by Rees (1966) that relativistic motion was possible in AGNs. The main motivation was to reconcile the size of the emitting region inferred by self-absorption argument and the one deduced by variability and light time travel arguments. Rees computed the apparent speed of an emitting plasma moving at relativistic speed and

[4] the Eddington accretion rate corresponds to the limit when accretion forces are balanced by radiative pression forces.

[5] Recent studies show that even the accretion power might not be enough to power AGNs (Ghisellini et al. (2014)). In this case, a possible additional source of energy would be the black-hole spin.

[6] In particular, the instrument GRAVITY, to be installed on the VLTI and developed in part at IPAG, should be able to probe the very hearth of our galaxy and to dynamically measure the mass of several AGN supermassive black-holes.

predicted the possibility of apparent superluminal motion. This was wonderfully confirmed a few years later as we saw in the section 1.1.

Apparent superluminal motion is actually very easy to understand. Consider an emitting source moving with a constant speed $\vec{v}$ making an angle θ with the line of sight of the observer (figure 1.1).

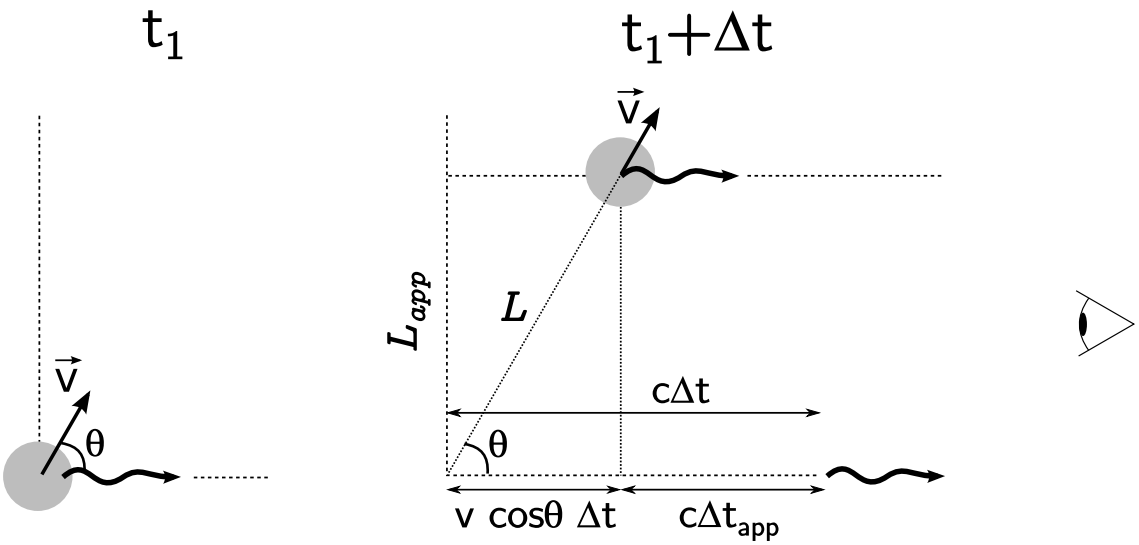

Figure 1.1: A source moving at a speed $\vec{v}$ emits at the times t_1 and $t_1 + \Delta t$ in the direction of an observer whom line of sight makes an angle θ with the source direction of motion.

Radiation is emitted at t_1 in the observer direction. Then the source moves and emits again at $t_1 + \Delta t$. During this time Δt, the light emitted a t_1 has travelled a distance $c\Delta t$ in the observer direction and the source has travelled a total distance L which corresponds to a distance $v \cos\theta \Delta t$ in the direction of the observer.

Therefore, the light emitted at $t_1 + \Delta t$ will reach the observer with a delay Δt_{app} (deduced from figure 1.1):

$$\Delta t_{app} = \Delta t \left(1 - \frac{v}{c} \cos\theta\right) \tag{1.3}$$

For the observer, the source traveled an apparent distance $L_{app} = L \sin\theta$ in a time Δt_{app} and thus the apparent velocity of the source is given by:

$$v_{app} = \frac{L_{app}}{t_{app}} = \frac{v \sin\theta}{\left(1 - \frac{v}{c}\cos\theta\right)} \tag{1.4}$$

It is easy to show that one might obtain $v_{app} > c$ given the condition on the viewing angle:

$$\frac{c}{v} < \sin\theta + \cos\theta < \sqrt{2} \tag{1.5}$$

which is possible for $\frac{v}{c} \gtrsim \frac{\sqrt{2}}{2}$

A representation of the apparent velocity in light speed units in function of the viewing angle and of the source Lorentz factor is given in figure 1.2. The Lorentz factor is a

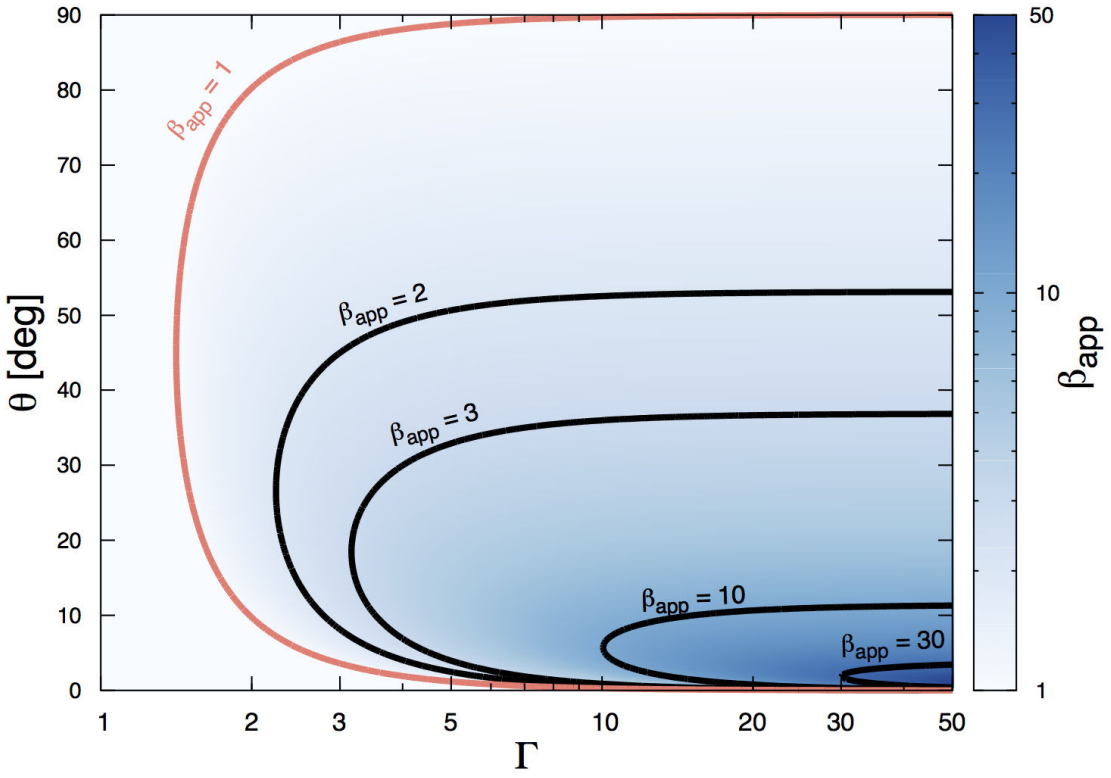

Figure 1.2: Evolution of the apparent velocity in function of the actual Lorentz factor of the source in motion and of the angle between the light of sight and the source motion direction

representation of the velocity adequate for relativistic motions that will be presented in further details in section 2.1.1.

Other evidences of relativistic motion include the brightness temperature and the apparent absence of counter jet. As shown by Kellermann and Pauliny-Toth (1969), a homogeneous and isotropic source emitting synchrotron and synchrotron self-Compton radiations has a maximum brightness temperature of $T_{max} \approx 10^{12} K$. At higher temperatures, the losses due to inverse Compton scattering become catastrophic and the temperature quickly goes down[7]. Therefore, the only way to explain observed brightness temperatures superior to this limit is to invoke relativistic motion as in this case, the brightness temperature is enhanced: $T_{obs} = \delta T$ (see 2.1.1 for more information on boosting). It is also frequent to see one jet coming out from one side of the nuclei but not from the other one whereas one can observe radio lobe structures on both sides. This is another effect of relativistic boosting which enhance emission from a source moving in the observer direction but reduce the emission of a source moving away (here again, see 2.1.1).

Non-thermal emission from particles at very high energy

As discussed previously, the spectral energy distribution (SED) of AGNs shows thermal emission in the UV/optical and in infrared coming from matter present (at very different

[7] at equipartition between particle energy and magnetic energy however, the maximum temperature is even lower: $T_{max} \approx 10^{10.5} K$ (Readhead (1994))

scales) around the central black-hole. The rest of a typical SED is also very interesting as it shows emission at all energies, from radio to γ-rays. This is definite proof of the presence of very-high energy particles emitting through non-thermal processes (an emission with a brightness temperature such as $k_b T > m_e c^2 \approx k_b \times 10^{10} K$ must definitely be non-thermal). Such processes differ depending on the nature of the particle but require particles at energies of at least several GeV in the most extreme sources.

1.2.2 Open questions & big issues

Knowledge and certainties come with their share of questions and non-fitting pieces. AGNs make no exception and it seems that the more we study them, the more enigmas arise. In this chapter, I will try to review some selected current big questions around AGNs. Of course this is not an exhaustive list but what I think are crucial questions to answer in order to understand better these wild beasts.

Jet composition

The biggest uncertainty might well be the jet composition, with two possible admitted answers: purely leptonic or lepto-baryonic. Purely leptonic jets present the problem to be light and strongly tight to radiation (see Ghisellini (2008) and sections 2.3.6, 4 and 7). Lepto-baryonic jets require huge power to accelerate a plasma loaded with baryons to relativistic speeds. For recent and precise calculations on this issue, see Celotti and Ghisellini (2008) and Ghisellini et al. (2014) - the later showing that jets might require power larger than the accretion power.

Emission processes

Two main branches of emission processes are generally considered in AGN jets: leptonic or hadronic. Leptonic processes involve the interaction of relativistic leptons with a magnetic field of a photon field[8] whereas hadronic processes are based on proton-proton or proton-photon interaction creating pion that can emit high energy photons when decaying and thus require relativistic baryons. Unfortunately, a photon emitted through leptonic processes cannot be discerned from one emitted by baryonic processes. However, theoretical arguments might be able to rule out one or the other. The main issue of hadronic processes is the requirement of huge power (Böttcher et al. (2013)), defying our knowledge on accretion (Zdziarski and Böttcher (2015)). They also have more difficulties to explain the very fast and correlated variability at high energies (though Barkov et al. (2012) proposed a work around scenario with stars crossing jets). For those reasons, leptonic processes are largely preferred. Note that lepto-baryonic jets do not necessarily imply hadronic processes (the baryons might not be relativistic).

Jet formation

The second tough question is the one of the jet formation, its creation, its collimation and its acceleration to relativistic speeds. The two known processes to launch a jet are the Blandford & Payne (BP) process (Blandford and Payne (1982)), prevailing in other objects showing jets (such as young stars) and the Blandford & Znajek (BZ) process (Blandford and Znajek (1977)) allowing energy extraction from a spinning black-hole. Unfortunately, MHD simulations still have trouble to link accretion and ejection and this problem remains

[8] leptonic processes will be presented in section 2

unsolved and the question of whether powerful AGN require a rapidly spinning BH is still open.

In these solutions, self-confinement of the jet can be done by the magnetic field exerting a magnetic pressure (from the Lorentz force) balancing internal pressure and centrifugal force. However, the confinement of a highly relativistic jet through this process seems impossible. This has been shown first in numerical simulation by Bogovalov (2001) and Bogovalov and Tsinganos (2001) and then demonstrated based on theoretical argument[9] by Pelletier (2004). If not self-collimated, relativistic flows must be collimated by external pressure of the ambient medium. It could be realized by interstellar medium or by a non-relativistic wind/jet coming from the disk (which could be self-collimated).

Jet speed

The question of the actual speed of jets is also crucial as it has a direct impact on relativistic effects. However, many observations point to discrepancies in jets bulk speeds in what can be called the bulk Lorentz factor crisis. On one side, several theoretical arguments require high Lorentz factor:

- *Variability:* Because information cannot travel faster than light, a zone of typical size R can only emit with a minimum timescale of R/c. For a black-hole of mass $10^9 M_\odot$, a typical size is $R_s \approx 2 \times 10^{12} m$, which implies a variability timescale of about $10^4 s$. This is in huge contradiction with the shortest variability down to a few minutes observed in many AGN (such as PKS 2155-304 - Aharonian et al. (2007) or Mrk 501 - Albert et al. (2007)). The observed variability can be explained through relativistic boosting (see section 2.1.1) but requires Lorentz factor as high as 100 for the shortest variability. One could suppose a smaller emitting region but that would enhance the second issue...

- *γ-ray opacity:* Photons can interact with each other given that they have the adequate energies (see section 5.2) which leads to self-absorption of these photons. Absorption of γ-ray photons by infrared/optical photons produced locally can be reduced thanks to relativistic effects. Based on a one-zone model, Begelman et al. (2008) deduced values of $\Gamma \geq 50$ to avoid this absorption.

- *SED fitting:* One-zone SSC models usually need high value of Γ to reproduce the observed high-energy emission from AGN. In particular, fits of TeV BL Lacs observed by Fermi are fitted by Tavecchio et al. (2010) with $20 < \Gamma < 40$ with a one-zone model.

On the other side, even though some objects show very high Lorentz factor (PKS 1510-089 shows typical $\Gamma > 30$ - Jorstad et al. (2005)), observations and theoretical arguments suggest much modest values on average:

- *VLBI measurements* display slow motions at parsec scales (Piner and Edwards (2004), Giroletti et al. (2004), Piner and Edwards (2014)).

- Apparent speeds observed in all types of AGNs are typically around 10c, corresponding to $\Gamma \approx 10$ (Lister et al. (2013))

[9] the bottom line is that electric field increases in relativistic outflows and become too strong to allow self-collimation by the magnetic field

- Apparent speeds in BL Lacs tend to be even slower but the statistics are still low. However, the generally admitted unification between BL Lacs and FRI galaxies that will be presented in section 1.3 requires BL Lacs to have $\Gamma \lesssim 5$.
- Statistics on the number of detected BL Lacs versus FR I galaxies are in strong disagreement with the possibility of high Lorentz factor (Henri and Saugé (2006) - hereafter HS06)
- The brightness temperature is enhanced by relativistic effects and has been a strong evidence that jets were indeed the hosts of relativistic motion. However Piner and Edwards (2014) argued that the modest measured values of T_B suggest low Doppler factor on average.

These contradictions led to the "bulk Lorentz factor crisis" (HS06), describing the disagreement between required Lorentz factor by one-zone models and observational facts. In addition to the unknown average speed in jets, the question of the dependence of the speed with the distance in the jet is also important. Accelerating or decelerating jets have been considered by theoretical literature (Marscher (1980), Ghisellini et al. (1985), Georganopoulos and Marscher (1998) or Boutelier et al. (2008)) but actual measurements of differential speeds in jets are very recent (Homan et al. (2015)) and will most certainly bring strong information on the dynamic of jets in the coming years.

Particle acceleration & emission processes

As stated in the previous section, high-energy particles must be present in AGN. However, the question of their acceleration to these energies is still open. There are three main processes able to produce relativistic particles: shocks (observed and studied in other astrophysical objects such as supernovae), magnetic reconnection and turbulence (second-order Fermi processes). Once accelerated to high-energies, particle can emit light through various processes. Knowing the nature of the processes at play is of course essential and is strongly related with the composition question. At low energies (from radio to UV), the synchrotron process (Alfvén and Herlofson (1950)) is now largely admitted but at higher energies, hadronic and leptonic processes are still discussed.

And more...

Other central questions that I will not talk about include:

- The topology of the magnetic field. Is it ordered on large scales? Disordered on small scales? Is it radial, longitudinal or toroidal, poloidal? What is its mean value? How does it vary along the jet?
- What are the mass, energy and momentum flux of jet? Is there a transfer to the environment? Observations suggest that the environment is affected by the presence of jets as they are only present in elliptical galaxies.

1.3 Taxonomy & Unification

As we saw in the historical introduction (section 1.1), there are several types of AGNs. Here I will recall and complete the characteristics of these types of AGNs and we will see that characteristics which seems so different can well be explained by characteristics of the viewer, more than by profound differences between objects.

1.3.1 Radio-quiet objects

The first discrepancy between AGN arise from their radio flux, some being very bright at long wavelengths (the so-called *radio-loud* sources) while other are not (*radio-quiet* sources). The radio-loudness parameter has been defined historically by Kellermann et al. (1989) as:

$$R = \frac{F_\nu^{rad}}{F_\nu^{opt}(4400\text{Å})} \tag{1.6}$$

Kellermann et al. (1989) showed that the quasars and AGN followed a bimodal distribution. With a radio-loudness limit between radio-quiet and radio-loud objects set at 30, one obtains a proportion of radio-loud objects of the order of 10%-15%.

Radio-quiet AGN show no signature of jets and are divided into two categories: Seyfert galaxies and quasi stellar objects (QSO or quasars).

Seyfert galaxies

Seyferts display an active center with strong ionization lines and are mostly spiral galaxies (Malkan et al. (1998)) with a relatively low bolometric luminosity compared to other AGN ($10^{43} - 10^{45}$ erg.s^{-1}). Several main components appear in the SED of these objects: 1. The big blue bump in the UV/optical, which is believe to come from the accretion disc around the central black-hole. 2. The emission in the X-rays, usually following a power-law between 2 and 20 keV with an exponential cut-off around 100 keV and though to come from a ionized corona. 3. The thermal emission in the infrared coming from hot dust.

The emission lines are due to the ionization of gas by the central emitter. These lines allow a division of Seyfert into two types (also called type 1 and type 2):

- Seyfert I galaxies show narrow emission lines and broad emission lines
- Seyfert II galaxies show only the narrow emission lines

QSO

As state their name, QSO look like stars. But this comparison is limited to their point-like appearance. Their continuum is much bluer than stars and they show strong redshifted emission lines, proving their extragalactic origin. In fact, QSO are the bright nucleus of their host galaxy. So bright that they outshine their host galaxy, which is thus almost undetectable. They also come in two kinds, type 1 and type 2, depending on wether they respectively show broad emission lines or not. Quasars were first distinguished from QSO by their radio-loudness[10]. This is no longer the case and we talk alike of quasars and QSO as AGN of small angular size in the optical.

1.3.2 Radio-loud galaxies

Radio-loud galaxies represent 10% of all AGN and are the hosts of a striking feature: the presence of jets on kilo-parsec scales (or more). Like radio-quiet sources, they are also divided into two main categories: radio-galaxies and blazars.

[10]Quasars correspond to the radio-stars discovered by Matthews (see section 1.1)

(a) Seyfert galaxy NGC 1566. Image Credit: ESA/Hubble & NASA

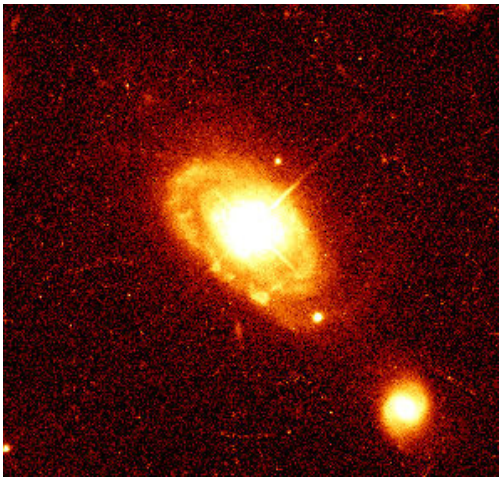

(b) Quasar PG 0052+251. Credit: John Bahcall (Institute for Advanced Study, Princeton) Mike Disney (University of Wales) & NASA/ESA

Figure 1.3: Two kinds of radio-quiet AGN: a Seyfert galaxy and a quasar

Radio-galaxies

Radio galaxies display very nicely their jets (see figure 1.4). This allowed Fanaroff and Riley (1974) to propose a classification of the radio-galaxies based on the morphology of their jets:

- FR-I galaxies are characterized by jets weakly collimated whose luminosity decreases with distance and end-up in a diffuse emission. Their bolometric luminosity is less that $L_{FR-I} < 10^{42}\text{erg.s}^{-1}$.
- FR-II galaxies however, are more luminous ($L_{FR-I} > 10^{42}\text{erg.s}^{-1}$) and presents highly collimated jets which look fainter. These jets end-up in tremendous terminal shocks called hot spots.

Two typical radio-galaxies are displayed figure 1.4: Centaurus A (FR-I galaxy) and Cygnus A (FR-II galaxy). FR-I are typically much less luminous in the radio band than FR-II and tend to lack broad emission lines. In this matter, FR-I are equivalent to type II quasars or Seyferts. FR-II come in both types however, which allow a further distinction between broad line radio galaxies (BLRG) and narrow line radio galaxies (NLRG).

Blazars

Blazars are not only the most luminous class of AGN, they are the most energetic objects in the universe. They belong to the radio-loud category and their characteristics are:

- A non thermal emission from the radio to the γ-rays
- A flat radio spectrum
- A polarized optical and radio emission ($> 3\%$)
- A very rapid variability at all wavelengths, especially at high-energies.

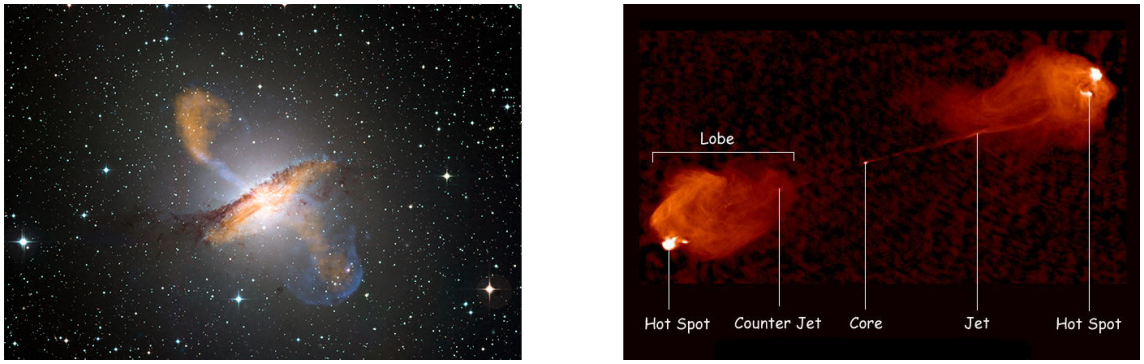

Figure 1.4: *Left:* Composite image of Centaurus A, a FR-I galaxy. Credit: ESO/WFI (Optical); MPIfR/ESO/APEX/A.Weiss et al. (Submillimetre); NASA/CXC/CfA/R.Kraft et al. (X-ray). *Right:* Cygnus A, a FR-II galaxy. Image courtesy of NRAO/AUI

Like radio-galaxies, they show powerful jets with superluminal motion, sign of relativistic speeds and they can also be divided into two main sub-categories:

- FSRQ (for Flat Spectrum Radio Quasars) correspond to the type 1 AGN. They show signs of bright optical emission, either directly seen in the SED, or through broad emission lines, ionized by the continuum.

- BL Lacs. Their name comes from the historical association with the variable stars BL Lacertae. They usually display no emission lines (except sometimes narrow emission lines) and therefore correspond to type 2 AGN.

1.3.3 Unification

In the classification that was described in the previous section, there are two main features: radio-loudness and emission lines. Table 1.1 summarizes these features and the main classes of AGN[11].

		Broad & narrow lines	No broad lines (or no lines at all)
Radio quiet	Seyfert	Seyfert I	Seyfert II
	QSO	Type 1	Type 2
Radio loud	Radio Galaxy	FR II	FR I
	Blazars	FSRQ	BL Lacs

Table 1.1: Main AGN categories organized by radio and emission lines properties

With this classification done, the natural question to ask is what causes these differences between objects.

[11] note that other subclasses exist and that the distinction between categories is often not as clear as what is presented here

The radio emission as a jet signature

It became clear very early than the loud radio emission from AGN was due to synchrotron processes occurring in the jets and was as such, the signature of the presence of jet. The presence or absence or jet can therefore be seen as a distinction between two types of AGN, radio-loud and radio-quiet[12]. Resolved images made a clear distinction in radio between the jet and the host galaxy, confirming without doubt the jet origin of the radio emission.

Emission lines, broad or narrow ?

Emission lines come from gas ionized by strong UV radiation - thought to come from the accretion disc. The narrow lines, with line-widths corresponding to gas velocities of a few 100 km.s^{-1} and moderate densities ($n \approx 10^3 - 10^6 \mathrm{cm}^{-3}$), are thought to come from gas far from the central BH (more than one parsec), in a region called the Narrow Line Region (NLR). Broad lines however, correspond to much faster (up to 10^4km.s^1) and much denser ($n \approx 10^9 \mathrm{cm}^{-3}$) gas. This gas evolves much closer from the BH (within 0.1 parsec) in the so-called Broad Line Region (BLR).

While one could think that Seyfert II simply do not have a BLR (as they show no broad lines), Antonucci and Miller (1985) discovered the presence of broad emission lines in polarized light coming from a typical Seyfert II - NGC 1068. Explaining the polarization of the light by scattering, the conclusion from these results (and others similar) was that the BLR is actually present in all Seyfert galaxies but their presence is hidden in type 2 by a torus of gas and dust (see section 6.2).

Therefore, the difference between Seyfert 1 and Seyfert 2 is only a question of orientation: when observed face on, the core of the galaxy is reachable and one can directly observe the BLR whereas when observed edge on, the core and the BLR are hidden and one can only observe the NLR directly, and sometimes the BLR indirectly, thanks to polarized light scattered by particles above the hidding torus.

Jet & orientation

Jets are highly asymmetric objects and it is clear that they must look different depending on the observation angle. This asymmetry is highly enhanced by relativistic motion that comes with relativistic effects such as Doppler boosting (see section 2.1). If there are objects including jets that we see edge on (FR galaxies), there must exist their equivalent seen face on, directly into the jet. It is admitted that these objects are the other subclass of radio-loud AGN, the extreme blazars, whose emission (in term of flux and variability) is enhanced by Doppler boosting.

Unification picture

These orientation considerations led to the orientation unification paradigm (Barthel (1989), Urry and Padovani (1995)) in which differences between many subclasses of AGN can actually be explained by the way we look at them. A sketch of this paradigm is presented in figure 1.5 where BL Lacs objects are associated with FR I and FSRQ with FR II. On the other side, Seyferts I and II are the counterparts without jets. However, some objects challenge the unification picture. In particular, "true Seyfert II" which do not show strong absorption but do not show either broad emission lines or Seyferts of changing type (Aretxaga et al. (1999), Tran et al. (1992)) show that the picture is more

[12] A few rare Seyfert galaxies show weak jets, making the distinction fuzzy

complex than one might want to think at first sight. More and more evidence or outflows (Blustin et al. (2005), Tombesi and Cappi (2014)) or gas passing along the light of sight indicate that the dynamics of these objects must be taken into account in order to clarify the picture.

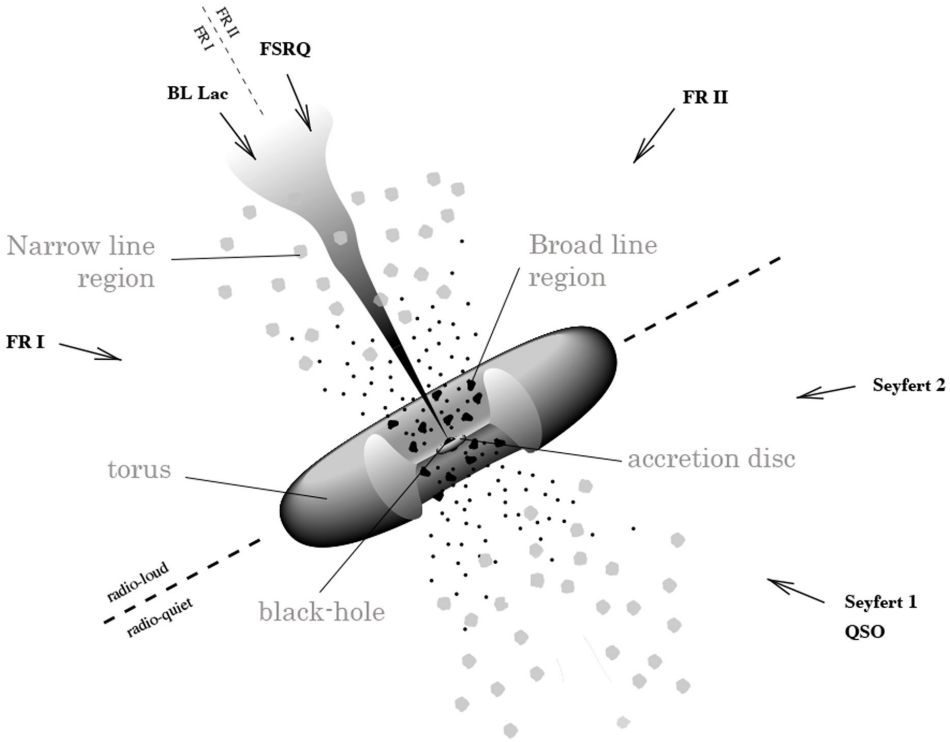

Figure 1.5: Sketch of the AGN orientation unification paradigm. Are represented and labeled in gray the different parts that compose an AGN. Seen from different angles, they give the main categories of AGN (labeled in black with arrows representing the viewing angle). Adapted from Collmar (2001).

1.4 Why this PhD?

As explained throughout this introduction, AGN are fascinating objects but their behavior is still poorly understood. Even if a global picture has emerged (figure 1.5), a lot of crucial questions remain (section 1.2). A way to unlock AGN mysteries is to reproduce their broadband spectral energy distribution (SED) with a coherent model. The most common emission model is the one-zone, homogeneous, leptonic model. It supposes an emitting region (most of the time, a sphere or radius R) where particles are injected (most of the time, at a constant rate) following a power-law of index s between two arbitrary energies γ_{min} and γ_{max}. The blob moves at a speed described by its Lorentz factor Γ in a magnetic field of strength B and is viewed from an angle i_{obs} by the observer. The success of the one-zone model comes from its simplicity, its capability to reproduce part of the SED and/or part of the observed objects and to explain some of the correlated variability. However, one can argue that it has now reached its limits to reproduce the

very complex object that are AGN. In particular, it is unable to reproduce completely the radio emission and often requires very large Doppler factor. For obvious reasons, it is also unable to explain the non-correlated variabilty. To overcome these problems, more complex models have emerged but are most of the time based on ad-hoc hypothesis (such as the two-zones model or the broken power-law distribution).

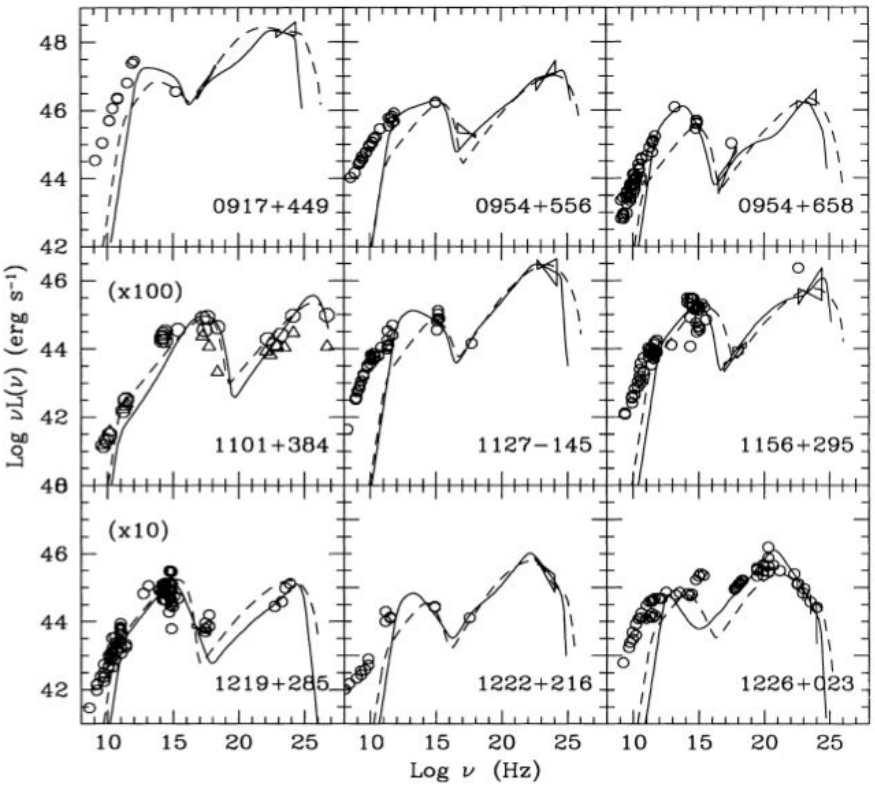

Figure 1.6: Example of broadband SED of blazars fitted by one-zone modeling emission. Figure extracted from Ghisellini et al. (1998). One can see the typical double bump SED. In the leptonic model, the first bump (in mm-IR) is explained by synchrotron radiation from relativistic leptons while the second bump is due to Compton scattering of soft photons on the same relativistic leptons.

In order to better understand AGN, a global coherent picture based on physical arguments and able to answer the main questions is necessary. The two-flow paradigm, based on the original work of Sol et al. (1989), and developed at IPAG (Institut de Planétologie et d'Astrophysique de Grenoble) is aiming at this AGN Graal. It is driven by physical arguments that I will present in section 4 but need to be compared to observations. This has been successfully done previously by Saugé (2004) and Boutelier et al. (2008) for BL Lacs with a pure synchrotron self-Compton[13] heterogeneous and time-dependent model. FSRQ, with the presence of strong external sources of soft photons, require a more complete modeling including the external Compton process. This process is important for two main reasons: it brings another source of emission that might be imperative to explain FSRQ high-energy emission and it is a strong source of cooling for the particle in the inner parts of the jet.

[13]I will present emission processes in section 2

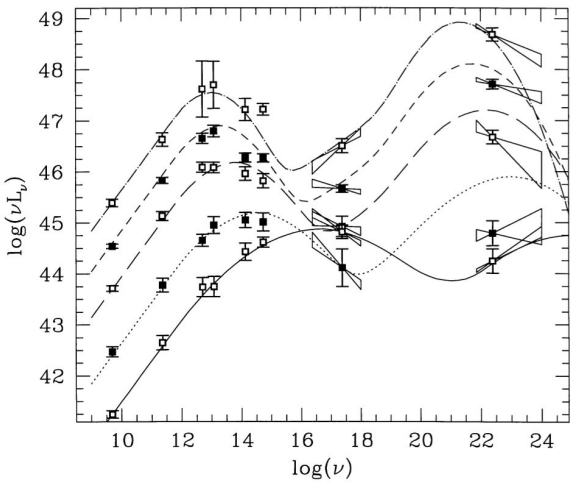

This second argument is validated by the "blazar sequence" discovered by Fossati et al. (1998) (from which the figure on the right has been extracted). It shows an anti-correlation between total luminosity and synchrotron peak emission which decreases from $10^{16} - 10^{17}$Hz from the less luminous sources to $10^{13} - 10^{14}$Hz for the most luminous ones. This sequence has been interpreted as an indication of more intense cooling in more powerful objects due to the presence of external sources of soft photons (Ghisellini et al. (1998)). Compton scattering on external soft photons coming from the accretion disc, the broad line region and the dusty torus present in powerful FSRQ must therefore being taken into account to understand these objects.

My project has been to develop the modeling of external sources (see section 6) and the associated external Compton emission and to include it in the heterogeneous numerical model of the two-flow (presented in section 5) taking into account subtle effects and implications such as anisotropy, pair creation and absorption. Modeling precisely the external Compton radiation allowed me to study in great details the Compton rocket effect and its implication in the complex photon field of an AGN (section 7) which explains the jet acceleration in the two-flow model. However, a complete computation of the external Compton emission is challenging in term of computing time. That is why an important part of my work has been to develop analytical and numerical approximations (section 3) in order to be able to run the model in an appropriate amount of time. Finally, comparison to observation and model fitting can be very complex in the case of an heterogeneous model and the exploration of physical parameters revealed to be much more demanding than for a one-zone model. Therefore, I had to develop numerical solutions to solve the model fitting problem (section 8) and reproduce objects emission (section 9).

1.5 *[En résumé]* Qu'est ce qu'un noyau actif de galaxie ?

Un peu d'histoire

La découverte des noyaux actifs de galaxie (NAG, ou AGN en anglais) est relativement récente et remonte probablement aux années 1930 alors que Jansky travaillait comme ingénieur à la "Bell Telephone Company". Alors qu'il étudiait les interérences dans les communications radios entre les Etats-Unis et le Royaume Uni, il découvrit une source d'intérférences inconnue et immobile dans le ciel. Sans le savoir, Jansky venait de détecter le tout premier noyau actif de galaxie. Et pas n'importe lequel ! Il s'agissait en fait de notre propre centre galactique. Bien que Jansky eut l'intuition d'avoir détecté une source astrophysique, personne ne fut en mesure de résoudre ce mystère à l'époque et cette découverte fut vite oubliée alors que survient la seconde Guerre Mondiale.

Cette dernière, malgré le lot d'horreur qu'elle engendra, permit le développement très important des communications radios. Ces avancées, une fois la guerre terminée, trouvèrent leur intérêt dans l'astrophysique. Ainsi débutat la radio astronomie. En 1949, Bolton Stanley et Lee identifieèrent les deux premières galaxies émettant d'importantes quantités de rayonnement radio : Virgo A (aussi nommée NGC 4486) et Centaurus A (NGC 5128). D'autres importantes sources radio furent détectées mais leur identification était ardue car ces sources n'apparaissaient pas toujours sur les plaques photographiques. Il n'était donc pas clair si ces sources résidaient dans notre propre galaxie ou étaient extragalactiques.

En 1963, Hazard, Mackey et Shimmins réussirent à faire l'analyse spectrale d'un objet très particulier, ressemblant à une étoile, mais avec une très forte émission radio (alors appelée une "étoile-radio"). Cette analyse montre que les raies démission du spectre sont décalées d'un facteur $1 + z$ avec $z = 0.158$. Ce décalage vers le rouge peut être expliqué par la loi de Hubble mais implique alors une origine extragalactique pour ces "étoiles-radio". De part ces résultats ainsi que la distribution spectrale en énergie de ces nouveaux objets, plus tard appelés quasars (pour "quasi-stellaire"), l'idée d'un trou noir supermassif ($10^9 M_\odot$[14]) est rapidement proposée (Greenstein and Schmidt (1964)).

En 1968, un autre type de source radio est découverte avec l'objet VRO 42.22.01. Il présente un spectre complexe, des dimensions angulaires très faibles et une variabilité importante. Malgré ses similarités avec les quasars, cette source est associée à une étoile variable, BL Lacertae, détectée par Cuno Hoffmeister en 1929.

Les années 70 marquèrent un tournant important pour les NAG grâce au développement de l'intérferométrie à très grande base (VLBI pour "Very Long Based Interferometry" en anglais). Knight et al. (1971) enregistre deux signaux de deux antennes différentes afin de les correlés plus tard et observe alors la présence de deux points dans 3C 273 séparés de $(1.55 \pm 0.05) \times 10^{-3}$ arc secondes. Quatre mois plus tard, Whitney et al. (1971) mesure une séparation entre ces deux points de $(1.69 \pm 0.02) \times 10^{-3}$ arc secondes. La distance de 3C 273 étant connue par son décalage vers le rouge ($z = 0.538$), la distance entre les deux observations est déterminée à presque quatre années lumières, signifiant que la source semblait se déplacer à dix fois la vitesse de la lumière, ce qui sera confirmé plus tard par Cohen et al. (1971). Cet effet, qui est en fait un simple problème de projection, avait déjà été prédi par Rees (1966) (voir équation 1.4). L'autre grande découverte de la VLBI fut celle des jets émanants du noyau des galaxies radio 3C 219 (Turland (1975)) et B0844+31 (van BREUGEL and MILEY (1974)).

Le développement des observations hautes-énergies apporta de nouvelles lumières sur les NAG. Les premiers détecteurs à rayons-X furent installés à bord de fusées en 1962

[14] masse solaire

mais la première détection d'un NAG dans cette gamme d'énergie ne survint pas avant l'observation de M87 et 3C 273 par Friedman and Byram (1967). La course à l'espace permit ensuite le lancement de satellites scientifiques, ouvrant la voie à l'astronomie gamma avec le "Orbiting Solar Observatory" (OSO-7) en 1971. Le "Celestial Observation Satellite B" (COS-B) fut lancé en 1975 permit la détection de 3C 273 dans la gamme des rayons gamma. Et enfin, les énergies extraèmes au delà de 1 TeV sont devenus accessibles gràce aux télescopes Tcherenkov (HEGRA - High Energy Gamma Ray Astronomy Array, CAT - Cherenkov Array at Themis and TAP - Telescope Array Prototype) en 1997. Ces techniques d'observations font toujours l'objet de nombreux développments et ont encore beaucoup à nous apprendre.

Ce que nous savons et ce que nous ignorons

L'immense luminosité bolométrique (atteignant parfois 10^{48-49}erg.s^{-1}, soit 100 fois la luminosité intégrée de toutes les étoiles de la galaxie hôte) des NAG provenant de régions de taille très faible ne peut être expliquée par l'activité stéllaire. En revanche, l'accrétion de matière sur un trou noir supermassif peut libérer des quantités d'énergies extrèmes, suffisantes pour expliquer les luminosités observées. Cette théorie fut confirmée par Kormendy (1988) qui mesura les vitesses de rotation et de dispersion des étoiles dans M31 et qui en déduisit la présence d'une masse centrale d'environ $10^7 M_\odot$.

La matière en rotation autour du trou noir supermassif forme un disque d'accrétion. Ce disque très chaud peut s'avérer extrêmement lumineux. Son émission visible dans l'optique forme alors le "Big Blue Bump" (la grande bosse bleue) dans son spectre. De nombreuses raies d'émission traduisant la présence de matière ionisée sont également détectées et nous renseignent sur la composition des disques d'áccrétion.

Comme expliqué précédement, les mouvements superluminiques observés prouvent l'existence de déplacement relativistes proches de la vitesse de la lumière (voir figures 1.1 et 1.2 et l'équation 1.4).

Les émission lumineuses à très hautes énergies sont une preuve de l'existence de particules très énergétiques rayonnant selon des processus démission non thermique.

Malgré tout, il y a encore de très nombreuses inconnues concernant les NAG et les jets. En particulier, il n'y a toujours pas de consensus sur la composition des jets ou sur les processus démission responsables du rayonnement émis. La formation et l'accélération des jets à des vitesses relativistes est également sujet à controverses. La vitesse exacte des jets n'est pas claire non plus. Ces grandes questions ouvertes sont fascinantes mais ne peuvent malheureusement pas être tranchées par les méthodes d'observation actuelles et doivent donc être évaluées par des modélisations complexes.

Taxonomie et unification

Les NAG apparaissent très différemment selon la position de l'observateur. Historiquement, de nombreux objets de nature à priori différente ont été découverts et classés dans des catégories distinctes. Deux grandes distinctions sont à faire selon le niveau démission radio ("radio quiet" contre "radio loud"[15]) et selon la présence ou non de raies d'émission intenses (voir le tableau 1.1). Un modèle d'unification a été proposé par Barthel (1989) et Urry and Padovani (1995) regroupant les différents objets en fonction de la présence ou non d'un jet et selon l'angle d'observation (voir schéma 1.5).

[15] respectivement silencieux et bruyant dans le domaine radio

But de cette thèse

Même si une image globale des NAG a émergé au fil des années, leur fonctionnement est encore très mal compris. Une façon de percer les mystères des NAG est de reproduire les observations grâce à des modèles d'émission cohérents. Le modèle le plus couramment utilisé est le modèle "une zone". Comme son nom l'indique, ce modèle tente de reproduire l'ensemble de l'émission des NAG grâce à une seule zone d'émission. Ce modèle doit sont succès à sa simplicité et sa relative bonne reproduction des observations. Malheureusement, avec la multiplication des observations, ce modèle est de plus en plus mis en défaut. De plus, sa physique reste rudimentaire et il peine à fournir une image globale cohérente du fonctionnement des NAG. Mon rôle a été de développé un modèle numérique complexe des jets de NAG s'inscrivant dans le paradigme du jet à deux fluides (voir chapitre 4) afin de vérifier si ce paradigme, qui fournit une explication plus séduisante à la méchanique globale des jets, pouvait reproduire les observations de façon satisfaisante.

Pour ce faire, j'ai déjà du développer des approximations analytiques et numériques au processus démission Compton afin de réduire suffisamment les temps de calcul (voir chapitre 3). L'étude du processus démission Compton m'a permis de développer en détails l'effet fusée Compton dans le cadre complexe des NAG (voir chapitre 7). Le modèle numérique est présenté en détail dans le chapitre 5 et la modélisation des sources de photons externes, tel que le disque d'áccrétion est décrite dans le chapitre 6. La comparaison du modèle aux observations (chapitre 9) étant compliquée, j'ai du au préalable développer une solution numérique d'adaptation basée sur les algorithmes génétiques (chapitre 8).

Chapter 2

Radiative processes

Contents

In this chapter I will present the leptonic processes at play to describe the emission from active galactic nuclei in our model. We will deal with non thermal radiation here, meaning radiation which is not produced by electrons changing orbit in atoms. As these non-thermal processes involve relativistic particles, relativistic effects need to be taken into account. I will therefore present them first.

2.1 Emission of relativistic sources

2.1.1 Lorentz transformation

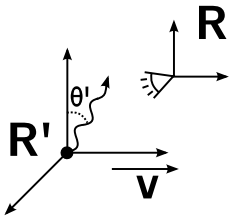

Let's consider a source moving at a speed $v = \beta c$ with respect to an observer at rest. The source rest frame is noted $\mathbf{R}'$, the observer rest frame $\mathbf{R}$ and they are both chosen so that their axis are parallel and $\boldsymbol{v}$ is parallel to (Ox). The source emits a photon of energy E' in a direction making an angle θ with the movement direction (Ox) in R frame. If we want to compute physical quantities such as the photon energy as seen by the observer and if the source is moving at relativistic speeds, Newtonian physics is no longer sufficient and Lorentz transformations need to be used.

In the case described above, to compute a 4-vector X' in $\mathbf{R}'$ as a function of the 4-vector X in $\mathbf{R}$, we must apply the transformation:

$$X' = \mathcal{L}X = \begin{pmatrix} \gamma & -\gamma\beta & 0 & 0 \\ -\gamma\beta & \gamma & 0 & 0 \\ 0 & 0 & 1 & 0 \\ 0 & 0 & 0 & 1 \end{pmatrix} X \tag{2.1}$$

with $\mathcal{L}$ the Lorentz matrix and

$$\gamma = \frac{1}{\sqrt{1-\beta^2}} \tag{2.2}$$

the Lorentz factor.

To compute the photon energy in the observer rest frame, the relevant 4-vector is the energy-momentum one: (E', p'_x, p'_y, p'_z). In the case of a photon, one has the relation $E = pc$ and one can always rotate the frames so that $p'_z = 0$ so we have the 4-vector energy-momentum $E'(\cos\theta', \sin\theta', 0)$. Applying equation (2.1) gives immediately:

$$\begin{cases} E' = \gamma(1 - \beta\cos\theta)E \\ E'\cos\theta' = E\gamma(-\beta + \cos\theta) \\ E'\sin\theta' = E\sin\theta \end{cases} \tag{2.3}$$

From it we can deduce the angle transformations[1]:

$$\begin{cases} \cos\theta' = \dfrac{\cos\theta - \beta}{1 - \beta\cos\theta} & (2.4) \\ \sin\theta' = \dfrac{\sin\theta}{\gamma(1 - \beta\cos\theta)} & (2.5) \end{cases}$$

By applying the same kind of transformation one can deduce frame transformations for other physical quantities. Here is a summary of relevant ones that will be of use:

$$\begin{cases} \text{The energy} & : & E' & = & \delta^{-1}\,E \\ \text{The time} & : & t' & = & \delta^{-1}\,t \\ \text{The volume} & : & V' & = & \delta^{-1}\,V \\ \text{The solid angle} & : & \mathrm{d}\Omega' & = & \delta^{2}\,\mathrm{d}\Omega \end{cases} \tag{2.6}$$

with δ the Doppler factor:

$$\delta = \frac{1}{\gamma\,(1 - \beta\cos\theta)} \tag{2.7}$$

Knowing these relations, one can compute the received power per unit of frequency and solid angle in the observer rest frame as a function of the power emitted in the source rest frame:

$$\frac{\mathrm{d}E}{\mathrm{d}t\mathrm{d}\Omega\mathrm{d}\nu} = \left(\frac{\mathrm{d}E}{\mathrm{d}E'}\right)\left(\frac{\mathrm{d}t'}{\mathrm{d}t}\right)\left(\frac{\mathrm{d}\Omega'}{\mathrm{d}\Omega}\right)\left(\frac{\mathrm{d}\nu'}{\mathrm{d}\nu}\right)\frac{\mathrm{d}E'}{\mathrm{d}t'\mathrm{d}\Omega'\mathrm{d}\nu'} \tag{2.8}$$

$$= \delta^3\frac{\mathrm{d}E'}{\mathrm{d}t'\mathrm{d}\Omega'\mathrm{d}\nu'} \tag{2.9}$$

[1]To obtain quantities in $\mathbf{R}$ as a function of quantities in $\mathbf{R}'$, one can consider the observer moving at a speed $-\beta$. Then, it is sufficient to replace β with $-\beta$ in any equation.

The specific intensity is the quantity defined as:

$$I_\nu = \frac{\mathrm{d}E}{\mathrm{d}t\mathrm{d}\Omega\mathrm{d}\nu\mathrm{d}S} \tag{2.10}$$

From equation 2.8, one can immediately deduce the relation:

$$I_\nu(\nu) = \delta^3 I'_\nu(\nu') \tag{2.11}$$

and show that $\frac{I_\nu}{\nu^3}$ is a relativistic invariant.

Because quantities such as received power are not invariant by frame transformation, there are some interesting relativistic effects to take into account when one deals with sources moving at relativistic speed. Relativistic aberration and beaming are two of them, as we will see now.

2.1.2 Aberration & beaming

As we just saw, the function $\delta(\gamma, \theta)$ governs the observed emission in the rest frame **R**. Figure 2.1 displays a representation of $\delta(\beta, \theta)$.

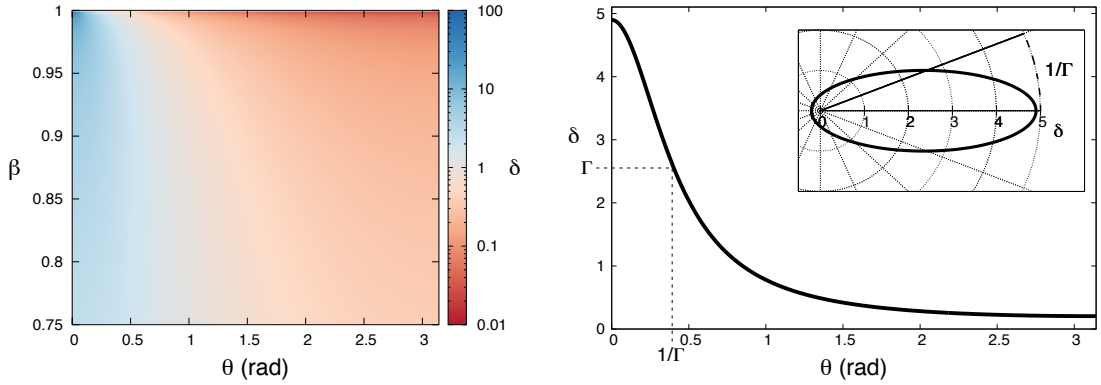

Figure 2.1: *Left:* Surface plot of $\delta(\beta, \theta)$. In blue, values of $\delta > 1$ and in red, values of $\delta < 1$.
Right: Plot of $\delta(\theta)$ for a fixed value of $\beta = 0.92$ ($\Gamma \approx 2.55$) and its polar representation in the frame. The function peaks at $\theta = 0$.

Relativistic aberration

Aberration is the change in a photon's apparent direction with frame transformation. This happens when the observer has a transverse motion relative to the object. A classical example is the biker under the rain. Even if water drops are falling straight to the ground (no wind), the face of our unlucky biker will get wet whereas his back might stay dry. This is due to apparent change in direction of water drops in the biker rest frame called aberration. A similar aberration will affect relativistic particle seeing photons coming right at them and corresponds to the relation given by (2.4) and (2.5).

Relativistic beaming

Not only the direction of the water drops will change but also the energy with which they will hit the biker's face. In the case of relativistic sources, this effect is called Doppler

beaming. An incoming photon sees its energy changed in the source rest frame. Equivalently, if a relativistic source radiates, its emission gets shifted in the observer frame (see equation 2.6). A shift at higher energy is called "blueshift" whereas a shift at lower energy is called a redshift (in the optical, blue light is at higher energy than red light). Astrophysics found use of this effect in discovery of exoplanets or determination of galaxies distances.

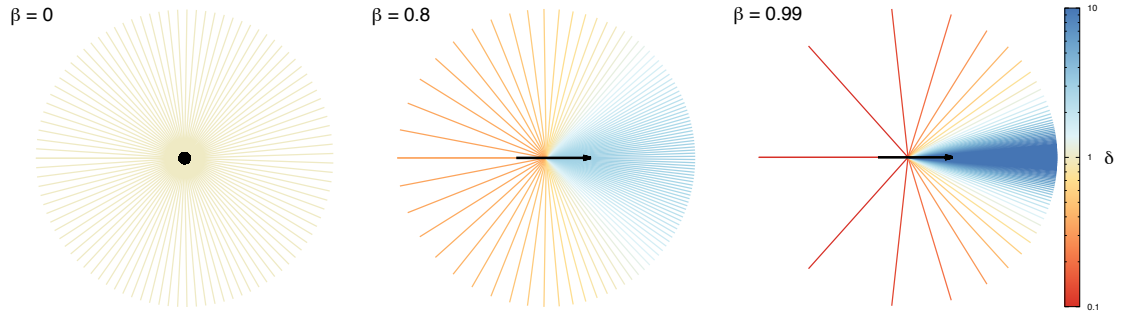

Figure 2.2: Illustration of the relativistic aberration and beaming. On the left, a particle at rest ($\beta = 0$) in an isotropic radiation field. When the particle moves with a relativistic speed ($\beta = 0.8$ or $\beta = 0.99$), the radiation field changes in the particle rest frame. Most of the radiation seems to come from the direction in which the particle is moving. Doppler boosting also change the energy of the incoming photons by a factor δ. Equivalently, a source emitting isotropically and moving at relativistic speed is seen beamed by an external observer.

Relativistic aberration and beaming can explain why quasars are so luminous. In the case of a source moving at relativistic speed ($\Gamma \gg 1$) and emitting isotropically a power P_0 in its rest frame, the bolometric emitted power per solid angle in the observer rest frame is:

$$\frac{\mathrm{d}E}{\mathrm{d}t\mathrm{d}\Omega} = \delta^4 \frac{P_0}{4\pi} \tag{2.12}$$

An external observer sees an emission highly beamed in the direction of motion in a cone of semi-aperture $1/\Gamma$ (see figures 2.1 and 2.2). If the observer happens to be in this precise direction (for blazars, the jet is pointing at the observer), the luminosity can reach tremendous values. On the contrary, if the source is moving away from the observer, its emission is deboosted. This contrast leads to the observed disparity between the jet and the counter jet of radio-galaxies.

2.2 Synchrotron emission

Classical electrodynamics teaches us that any charged particle accelerating emits radiation.[2]

If we consider a charged particle placed in a magnetic field, then it undergoes the Lorentz force. In the relativistic case, this force follows the equation (in CGS system):

$$\frac{\mathrm{d}}{\mathrm{d}t}\left(\gamma m \mathbf{v}\right) = \frac{q}{c}\mathbf{v} \times \mathbf{B} \tag{2.13}$$

[2]Question about whether an uniformly accelerated charge actually radiates has been extensively debated over the years. Interesting reviews and recent point of views might be found in Shariati and Khorrami (1999) and de Almeida and Saa (2006).

The outcoming velocity of the particle is given by its parallel and perpendicular components relative to the magnetic field:

$$a_{\parallel} = 0 \tag{2.14}$$

$$a_{\perp} = \frac{q}{\gamma mc} v_{\perp} B \tag{2.15}$$

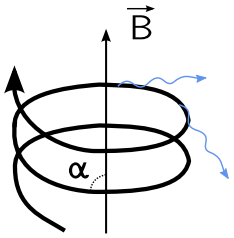

The resulting motion is helical with a pitch angle α, combination of a circular motion around the field lines and a uniform motion along the field lines. The particle is under a perpendicular acceleration and therefore it must radiates. In the classical case, this radiation is called cyclotron emission whereas in the relativistic case, it is called synchrotron emission. As we are interested in relativistic sources, we will consider only synchrotron emission here. Because we are interested in relativistic particles, the effects seen in section 2.1.2 apply and the emission is beamed in the direction of the particle motion in the observer frame.

The Larmor formulae gives us the radiated power:

$$P_{Larmor} = \frac{2q^2}{3c^3} \gamma^4 \left(a_{\perp}^2 + \gamma^2 a_{\parallel}^2 \right) \tag{2.16}$$

With the calculated acceleration in (2.15), one can deduce the synchrotron emitted power per particle:

$$P_{syn} = \frac{2}{3} r_e^2 c \, \beta_{\perp}^2 \, \gamma^2 B^2 \tag{2.17}$$

with $r_e = \dfrac{e^2}{m_e c^2}$ the classical electron radius.

For an isotropic distribution of particles, one has:

$$< \beta_{\perp}^2 >= \frac{1}{4\pi} \int \beta^2 \sin^2 \alpha \, \mathrm{d}\Omega = \frac{2\beta^2}{3} \tag{2.18}$$

and one gets the average synchrotron emitted power:

$$P_{syn} = \frac{4}{3} c \sigma_{Th} U_B \beta^2 \gamma^2 \tag{2.19}$$

with $\sigma_{Th} = 8\pi r_e^2/3$ is the Thomson cross section and $U_B = B^2/8\pi$ is the magnetic energy density.

By noting $P = \mathrm{d}E/\mathrm{d}t = m_e c^2 (\mathrm{d}\gamma/\mathrm{d}t)$, on can deduce the characteristic synchrotron cooling time of a particle:

$$t_{syn} = \frac{\gamma}{\mathrm{d}\gamma/\mathrm{d}t} = \frac{3 m_e c}{4 \sigma_{Th} U_B} \frac{1}{\beta^2 \gamma} \tag{2.20}$$

2.3 Inverse Compton scattering

2.3.1 Compton scattering

The Compton effect is the scattering of a photon by a charged particle. With a particle initially at rest, it results in a decrease of the photon energy: there is a transfer of energy from the photon to the particle.

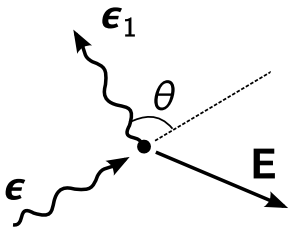

Figure 2.3: Compton scattering of a photon of energy ϵ by an electron at rest. After the scattering, the electron and the photon have respectively an energy E and ϵ_1

This process has been originally described by Compton (1923) who studied the elastic collision of X-ray photons with electrons. He showed that X-rays were scattered through an angle θ (see figure 2.3) and were subject to a change in wavelength called Compton shift given by the relation:

$$\Delta\lambda = \frac{h}{m_e c}(1 - \cos\theta) \tag{2.21}$$

Using the dimensionless energy $\epsilon = \dfrac{h\nu}{m_e c^2} = \dfrac{h}{m_e c}\dfrac{1}{\lambda}$, it comes immediately that the energy of the photon after scattering is:

$$\epsilon_1 = \frac{\epsilon}{1 + \epsilon(1 - \cos\theta)} \tag{2.22}$$

The case of elastic scattering ($\Delta\epsilon = 0$) has been first studied by Thomson. Then Compton in 1923 discovered that X-ray photons could also loose energy when scattered. In tribute to Thomson, the regime where the scattering is almost elastic ($\epsilon_1 \approx \epsilon$) that corresponds to a photon of energy negligible compared to the mass energy of the electron ($\epsilon \ll 1$) is called the Thomson regime. In this regime, the scattering cross-section is given by:

$$\frac{\mathrm{d}\sigma}{\mathrm{d}\Omega} = \frac{r_e^2}{2}(1 + \cos^2\theta) \tag{2.23}$$

But in the general case, the complete cross-section of the scattering is more complex. Its formulation has been derived later by Heitler (1954):

$$\left(\frac{\mathrm{d}\sigma}{\mathrm{d}\Omega}\right) = \frac{r_e^2}{2}\left(\frac{\epsilon_1}{\epsilon}\right)^2\left(\frac{\epsilon_1}{\epsilon} + \frac{\epsilon}{\epsilon_1} - \sin^2\theta\right) \tag{2.24}$$

The attentive reader can tell that in the Thomson regime ($\epsilon_1 \approx \epsilon$), the complete cross-section simplify in the Thomson cross-section of equation (2.23). When outside of the Thomson regime, one enters in the Klein-Nishina regime and the cross-section drops rapidly - it is then given by equation 2.24.

The scattered photon energy ϵ_1 can be known thanks to equation 2.22. By injecting its value and integrating over solid angles, one can get the total Compton cross-section:

$$\sigma = \sigma_{Th}\frac{3}{4}\left\{\frac{1+\epsilon}{\epsilon^3}\left[\frac{2\epsilon(1+\epsilon)}{1+2\epsilon} - \ln(1+2\epsilon)\right] + \frac{1}{2\epsilon}\ln(1+2\epsilon) - \frac{1+3\epsilon}{(1+2\epsilon)^2}\right\} \tag{2.25}$$

A plot of the total cross-section is given in figure 2.4.

Two approximations can be made:

- In the Thomson regime, when $\epsilon \ll 1$, one has:

$$\sigma = \sigma_{Th}\left(1 - 2\epsilon + \frac{26\epsilon^2}{5}\right) \tag{2.26}$$

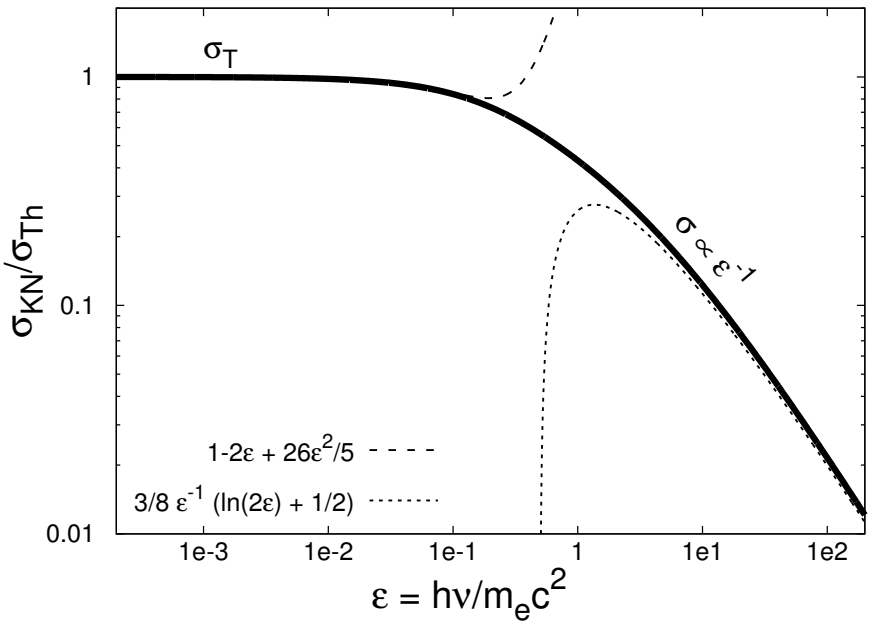

Figure 2.4: Evolution of the integrated cross-section as a function of the incoming photon energy in the particle rest frame. In the Thomson regime ($\epsilon \ll 1$), $\sigma_{KN} \approx \sigma_{Th}$. In the Klein-Nishina regime, $\sigma_{KN} \propto \epsilon^{-1}$

- In the deep Klein-Nishina regime ($\epsilon > 1$) however, one has:

$$\sigma = \sigma_{Th} \frac{3}{8} \epsilon^{-1} \left(\ln 2\epsilon + \frac{1}{2} \right) \tag{2.27}$$

2.3.2 Compton scattering by relativistic particles

Suppose now that the particle is moving at relativistic speed in the observer frame. The Compton scattering as seen previously stay unchanged in the particle rest frame. Nevertheless, in the observer rest frame, the particle initial energy is greater than the initial energy of the incoming photon. In this case, the transfer of energy goes from the particle to the photon. This so-called inverse Compton effect is a very efficient process to produce high-energy photons given the presence of high-energy particles.

Expression 2.22 is valid in the particle rest frame $\mathbf{R}'$ and expresses as:

$$\epsilon'_1 = \frac{\epsilon'}{1 + \epsilon'(1 - \cos\Phi')} \tag{2.28}$$

with Φ' the angle between the incoming photon and the scattered photon in the particle rest frame (see figure 2.5). It can be expressed as a function of the angles θ', θ'_1, φ' and φ'_1:

$$\cos\Phi' = \cos\theta' \cos\theta'_1 + \sin\theta' \sin\theta'_1 \cos(\varphi'_1 - \varphi') \tag{2.29}$$

Frame transformations seen in section 2.1.1 are valid and useful here. The relations between photon energies are:

$$\epsilon' = \epsilon\gamma(1 - \beta\cos\theta) \qquad \epsilon = \epsilon'\gamma(1 + \beta\cos\theta') \tag{2.30}$$

$$\epsilon'_1 = \epsilon_1\gamma(1 - \beta\cos\theta_1) \qquad \epsilon_1 = \epsilon'_1\gamma(1 + \beta\cos\theta'_1) \tag{2.31}$$

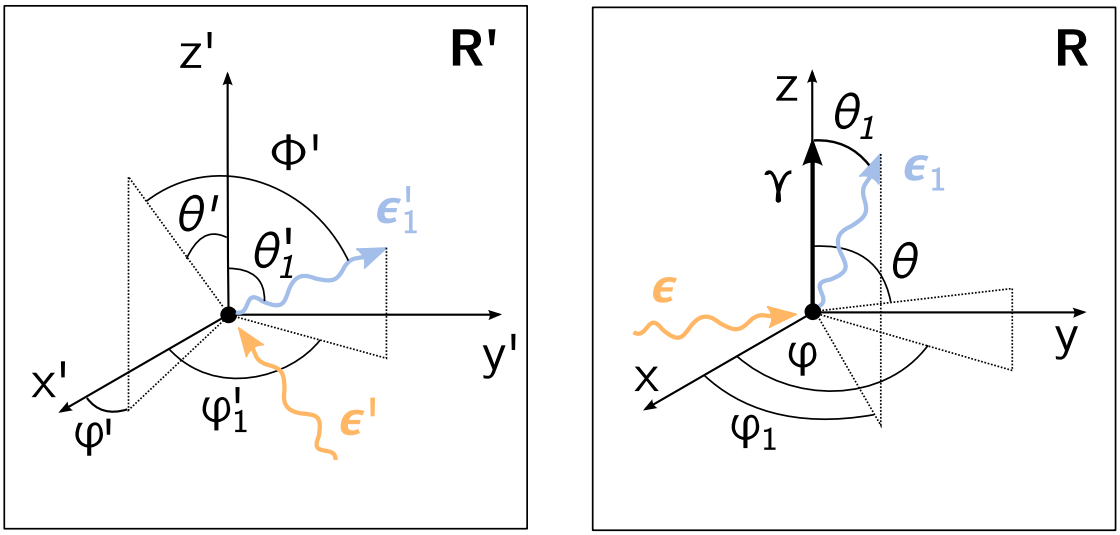

Figure 2.5: Inverse Compton scattering in the particle rest frame $\mathbf{R}'$ (left panel) and in the observer rest frame $\mathbf{R}$ (right panel). An incoming photon of energy ϵ is scattered into a photon of energy ϵ_1 by a particle of total energy $E = \gamma mc^2$ moving along the Z axis.

And the relations between angles are:

$$\cos\theta' = \frac{\cos\theta - \beta}{1 - \beta\cos\theta} \qquad \cos\theta = \frac{\cos\theta' + \beta}{1 + \beta\cos\theta'} \tag{2.32}$$

$$\sin\theta' = \frac{\sin\theta}{\gamma(1 - \beta\cos\theta)} \qquad \sin\theta = \frac{\sin\theta'}{\gamma(1 + \beta\cos\theta')} \tag{2.33}$$

Note that φ and φ_1 are in the plane perpendicular to the particle movement and are therefore untouched by frame transformation.

2.3.3 Inverse Compton spectra

We will now consider the resulting spectrum from the scattering of soft photons on relativistic particles. Consider an incoming flux of photon with a specific intensity $I'_{\nu'}$ [erg.s^{-1}.Hz^{-1}.m^{-2}.sr^{-1}] reaching the particle in its rest frame with an incident solid angle $\mathrm{d}\Omega'_i$.

$$I'_{\nu'} = ch\nu' \frac{\mathrm{d}n}{\mathrm{d}\nu'\mathrm{d}\Omega'_i} = ch\epsilon' \frac{\mathrm{d}n'}{\mathrm{d}\epsilon'\mathrm{d}\Omega'_i} \tag{2.34}$$

The number of scattered photons of energy $\epsilon'_1 = h\nu'_1/m_e c^2$ per element of time, per energy, per energy of the incoming photon ϵ' and per elementary solid angle $\left(\frac{\mathrm{d}N}{\mathrm{d}t'\mathrm{d}\nu'\mathrm{d}\nu'_1\mathrm{d}\Omega'_1}\right)$ is equals to the number of photons $\left(\frac{I'_{\nu'}}{h\nu'}\right)$ at the energy $\epsilon' = h\nu'$ verifying equation (2.28) times their probability to scatter in an emission solid angle $\mathrm{d}\Omega'_1$ (see Jones (1968)):

$$\frac{\mathrm{d}N'_1}{\mathrm{d}t'\mathrm{d}\epsilon'_1\mathrm{d}\epsilon'\mathrm{d}\Omega'_1} = \int \left(\frac{\mathrm{d}\sigma}{\mathrm{d}\Omega_1}\right)' \frac{1}{h}\frac{I'_\nu}{m_e c^2 \epsilon'} \delta\left(\epsilon'_1 - \frac{\epsilon'}{1 + \epsilon'(1 - \cos\Phi')}\right) \mathrm{d}\Omega'_i \tag{2.35}$$

2.3.4 The case of a mono-energetic beam

In the case of a mono-energetic and mono-directional plane wave,

$$I_\nu = ch\epsilon_0 n_0 \,\delta\left(\epsilon - \epsilon_0\right)\delta\left(\Omega - \Omega_0\right) \tag{2.36}$$

with n_0 being the photon density.
Introducing the notation $\mu_0 = \cos\theta_0$, we get:

$$\frac{\mathrm{d}N_1'}{\mathrm{d}t'\mathrm{d}\epsilon_1'\mathrm{d}\epsilon'\mathrm{d}\Omega_1'} = \frac{r_e^2 ch}{2hm_e c^2} n_0\gamma(1-\beta\mu_0)$$
$$\int \left(\frac{\epsilon_1'}{\epsilon'}\right)^2 \left(\frac{\epsilon_1'}{\epsilon'} + \frac{\epsilon'}{\epsilon_1'} - \sin^2\Phi'\right)\delta\left(\epsilon_1' - \frac{\epsilon'}{1+\epsilon'(1-\cos\Phi')}\right)\delta\left(\epsilon'-\epsilon_0'\right)\delta\left(\Omega'-\Omega_0'\right)\mathrm{d}\Omega' \tag{2.37}$$

Dubus et al. (2008) as shown that the final spectrum in the observer frame can be written as:

$$\frac{\mathrm{d}N}{\mathrm{d}t\mathrm{d}\epsilon_1} = \frac{\pi r_e^2 c(1-\beta\mu_0)n_0}{\gamma(1-\beta x)} K\left[1 + \left(\frac{x-\beta}{1-\beta x}\right)^2 \mu_0'^2 + \frac{\gamma^2\epsilon_1^2\left[1+\beta\mu_0' - (\beta+\mu_0')x\right]^2}{1-\gamma\epsilon_1\left[1+\beta\mu_0'-(\beta+\mu_0')x\right]}\right] \tag{2.38}$$

with

$$K = \frac{\left[1-\gamma\epsilon_1\left(1+\beta\mu_0' - (\beta+\mu_0')\mu_1\right)\right]^2}{\left|\beta\gamma\epsilon_1 + \epsilon_1^2\mu_0'\right|} \tag{2.39}$$

and

$$x = \frac{1 - \frac{\epsilon_0}{\epsilon_1}(1-\beta\mu_0) + \frac{\epsilon_0}{\gamma}}{\beta + \frac{\epsilon_0}{\gamma}\mu_0} \tag{2.40}$$

Equations 2.30 and 2.31 can be used to impose limits on the observed spectrum. One can show that $\epsilon_- \leq \epsilon_1 \leq \epsilon_+$ with

$$\epsilon_\pm = \frac{(1-\beta\mu_0)\epsilon_0}{1 + \frac{\epsilon_0}{\gamma} \mp \left[\beta^2 + 2\beta\mu_0\left(\frac{\epsilon_0}{\gamma}\right) + \left(\frac{\epsilon_0}{\gamma}\right)^2\right]^{1/2}} \tag{2.41}$$

Simplification in the Thomson regime

In the Thomson regime, one has $\epsilon_0' \ll 1$ and $\epsilon_0' \approx \epsilon_1'$ and the cross section is given by equation (2.23). The expression of the emitted spectrum given above simplifies and one gets:

$$\frac{\mathrm{d}N}{\mathrm{d}t\mathrm{d}\epsilon_1} = \frac{\pi r_e^2 c}{2\beta\gamma^2\epsilon_0}\left[3 - \mu_0'^2 + \left(3\mu_0'^2 - 1\right)\frac{1}{\beta^2}\left(\frac{\epsilon_1}{\gamma^2\epsilon_0(1-\beta\mu_0)} - 1\right)^2\right] \tag{2.42}$$

with

$$\frac{1-\beta\mu_0}{1+\beta} < \frac{\epsilon_1}{\epsilon_0} < \frac{1-\beta\mu_0}{1-\beta} \tag{2.43}$$

2.3.5 Inverse Compton emitted power

The emitted power by inverse Compton scattering can be computed from the integral over energies:

$$\frac{\mathrm{d}E}{\mathrm{d}t} = \int \epsilon_1 m_e c^2 \frac{\mathrm{d}N}{\mathrm{d}t\mathrm{d}\epsilon_1}\mathrm{d}\epsilon_1 \tag{2.44}$$

But this calculation cannot be done analytically in the general case. Fortunately, the emitted power in the Thomson regime can be evaluated. The details of the calculation are done in Rybicki and Lightman (1986) and I will just give here the main steps. Given a soft photon density $\frac{\mathrm{d}n}{\mathrm{d}\epsilon}$ in the energy range $\mathrm{d}\epsilon$, the total emitted power in the electron's rest frame is:

$$\frac{\mathrm{d}E'_1}{\mathrm{d}t'} = c\sigma_T \int \epsilon'_1 \frac{\mathrm{d}n'}{\mathrm{d}\epsilon'}\mathrm{d}\epsilon' \tag{2.45}$$

Thanks to the relativistic invariants $\frac{\mathrm{d}n}{\mathrm{d}\epsilon}$ and the power and relations (2.6), one can write:

$$\frac{\mathrm{d}E_1}{\mathrm{d}t} = c\sigma_T \int \frac{\mathrm{d}n}{\mathrm{d}\epsilon}\gamma^2(1-\beta\cos\theta)^2\epsilon\mathrm{d}\epsilon \tag{2.46}$$

With an isotropic distribution of photons of energy density $U_{ph} = \int \epsilon \frac{\mathrm{d}n}{\mathrm{d}\epsilon}\mathrm{d}\epsilon$, one finally gets:

$$P_{compt} = \frac{\mathrm{d}E_1}{\mathrm{d}t} = \frac{4}{3}\sigma_T c\gamma^2\beta^2\, U_{ph} \tag{2.47}$$

In the Klein-Nishina regime, the cross-section is much smaller and the emitted power will be as well.

Thanks to equation (2.19)[3], it is very easy to compare synchrotron and inverse Compton emitted power as it is equivalent to comparing the energy densities of the photon field and of the magnetic field:

$$\frac{P_{synch}}{P_{compt}} = \frac{U_B}{U_{ph}} \tag{2.48}$$

2.3.6 Inverse Compton cooling time

The inverse Compton cooling time can be evaluated through

$$t_{IC} \approx \frac{\gamma}{\dot{\gamma}} \tag{2.49}$$

with $\dot{\gamma} = \frac{P_{compt}}{m_e c^2}$.

P_{compt} can be evaluated thanks to equation (2.47) and one gets:

$$t_{IC} \approx \frac{3m_e c^2}{4c\sigma_T \gamma U_{ph}} \tag{2.50}$$

[3]Interestingly, the synchrotron emission here appears as an inverse Compton emission on an imaginary photon field created by the magnetic field

In inner regions of AGNs, the soft photon field mainly comes from the accretion disc. Therefore, one can evaluate the soft photon density at a distance Z in the jet as

$$U_{ph} \approx \frac{L_{disc}}{4\pi Z^2 c} \tag{2.51}$$

If we introduce the soft photon compactness:

$$l_s = \frac{L\sigma_T}{4\pi m_e c^3 Z} = \frac{m_p}{m_e}\frac{L_{disc}}{L_{edd}}\frac{R_g}{Z} \tag{2.52}$$

the cooling time finally writes:

$$t_{IC} \approx \frac{3}{4}\frac{1}{\gamma l_s}\frac{Z}{c} \tag{2.53}$$

In the most powerful AGNs, one has $L_{disc} \approx L_{edd}$. Therefore, in the inner parts, the compactness is much larger than unity and one can expect $\gamma_e \gg 1$ to produce high-energy photons. As a consequence, this proves that the inverse Compton cooling time is very short, much shorter than the dynamical time:

$$t_{IC} \ll \frac{Z}{c} = t_{dyn} \tag{2.54}$$

This result has strong consequences for particles in AGNs jets. Firstly, it implies that the inverse Compton process is very efficient to cool them and without a source of energy to heat them, they cool in a few gravitational radii. Secondly, it has consequences on the dynamics of leptons. When they scatter photons (through the inverse Compton process) anisotropically[4], they recoil (while they cool down). This recoil, called Compton drag effect, is well known as a way to decelerate jets (Phinney (1982),Sikora et al. (1996), Ghisellini and Tavecchio (2010)).

In the two-flow paradigm however, we will see that this result has even stronger consequences in section 7.

[4]the emitted radiation can be anisotropic because the particle distribution is anisotropic or because the incident photon distribution is anisotropic in the plasma rest frame

2.4 *[En résumé]* Processus radiatifs

Ce chapitre présente les différents processus d' émission non thermique en jeu dans la modélisation des NAG.

Aberrations relativistes et transformations de Lorentz

Dans la partie 2.1, je présente les bases nécessaires à la description de l'émission de sources relativistes, en commençant par les transformations de Lorentz. Ces transformations (équation 2.1) permettent de décrire le passage de quantitées physiques d'un référentiel à un autre suivant la théorie de la relativité restreinte.

Je décris ensuite les effets d'aberration relativistes qui sont les changements de direction apparente et d'énergie des photons lors de changements de référentiel. Une équivalence newtonienne de cet effet peut être donné avec l'exemple du cycliste sous la pluie. Même si les gouttes de pluie tombent perpendiculairement au sol (sans vent), le visage du cycliste infortuné se trouvera trempé tandis que son dos pourrait rester sec. Ceci est du au changement de direction apparente des gouttes d'eau dans le référentiel du cycliste qui paraissent venir de plus en plus horizontalement tandis que la vitesse du cycliste augmente. De plus, l'énergie avec laquelle ces gouttes arriveront sur le visage du cycliste va également augmenter avec la vitesse de ce dernier. Des effets similaires vont affecter les photons émis ou reçus par des particules relativistes (equations (2.4), (2.5) et (2.6)). Une illustration de ce phénomène est donné figure 2.2.

Processus d'émission

L'émission synchrotron résulte de l'accélération d'une particule chargée dans un champ magnétique. Celle-ci va alors perdre de l'énergie par rayonnement synchrotron. Je présente ensuite quelques considérations utiles sur la puissance émise et le temps démission caractéristique.

L'effet Compton est la diffusion d'un photon sur une particule chargée. Avec une particule au repos, il en résulte une diminution de l'énergie du photon qui en transfert une partie à la particule. L'effet Compton inverse en revanche, survient lorsque la particule est en mouvement et possède une énergie supérieure à celle du photon. Dans ce cas, c'est la particule qui va céder une partie de son énergie au photon. Ce processus est à l'origine de l'émission haute énergie observée dans de nombreux objets astrophysique, et en particulier dans les NAG. Dans la suite, je décris plus en profondeur ce processus en détaillant les équations le décrivant. Le spectre résultant de ce processus est donné par l'équation (2.35).

Chapter 3

Inverse Compton scattering of a thermal photon distribution

Contents

In this chapter I will present in greater details the inverse Compton scattering of soft photon following a thermal distribution. This process is of great importance in astrophysics as many sources of soft photons are thermal or can be approximated by a thermal distribution.

Take an ideal body that completely absorbs all electromagnetic radiation reaching it. At thermal equilibrium, its absorption is equal to its emissivity, $\alpha_\nu(T) = \varepsilon_\nu(T)$, and it emits isotropic radiation described by Planck's law:

$$I_\nu(\nu, T) = B_\nu(\nu, T) = \frac{2h\nu^3}{c^2} \frac{1}{\exp\left(\frac{h\nu}{k_b T}\right) - 1} \tag{3.1}$$

If not ideal, an object can be "grey". A grey-body follows the same law as a black-body but with an emissivity less than 1. Its specific intensity is therefore given by $I_\nu(\nu, T) = \varepsilon\, B_\nu(\nu, T)$.

Planck's law can be approximated in two different regimes:

- At low energies, for $h\nu \ll k_B T$, it becomes the Rayleigh-Jeans law:

$$B_\nu(T) \approx \frac{2\nu^2}{c^2} k_B T \tag{3.2}$$

- At high energy however, when $h\nu \gg k_B T$, Planck's law tends to Wien's law:

$$B_\nu(T) = \frac{2h\nu^3}{c^2} \exp\left(-\frac{h\nu}{k_B T}\right) \tag{3.3}$$

3.1 The modified Wien law: an approximation of the Planck law

An approximation of Planck's law that conserve both low and high energies descriptions can be made. As we will see in the next section, this approximation will greatly simplify the calculation of the inverse Compton scattering. I call this approximation the modified Wien's law whose specific intensity is described by equation (3.4).

$$\boxed{W_\nu(\nu, T) = A(T)\, \nu^2 \exp\left(-\frac{\nu}{\bar{\nu}(T)}\right)} \tag{3.4}$$

with $A(T)$ and $\bar{\nu}(T)$ parameters to determine.

One can see the modified Wien's law as a mix of Rayleigh-Jeans law and of Wien's law. An (arbitrary) criteria to determine $A(T)$ and $\bar{\nu}(T)$ is to conserve the total emitted power and the position of the peak:

$$\begin{cases} \iint B_\nu(\nu, T) \mathrm{d}\nu \cos(\theta) \mathrm{d}\Omega = \iint W_\nu(\nu, T) \mathrm{d}\nu \cos(\theta) \mathrm{d}\Omega \\ \nu_P^{max} = \nu_W^{max} \end{cases} \tag{3.5}$$

The integral of $B_\nu(\nu, T)$ is well known and its result is given by Stefan-Boltzmann law:

$$\iint B_\nu(\nu, T) \mathrm{d}\nu \cos(\theta) \mathrm{d}\Omega = \sigma T^4 \tag{3.6}$$

And ν_P^{max} is given by Wien's displacement law:

$$\nu_P^{max} = \frac{\alpha}{h} k_B T \approx \left(5.879 \times 10^{10}\, \mathrm{Hz}\, K^{-1}\right) T \tag{3.7}$$

with $\alpha \approx 2.821$ a numerical constant.

On the other hand, one can show that:

$$\iint W_\nu(\nu, T) \mathrm{d}\nu \cos(\theta) \mathrm{d}\Omega = 2\pi A \bar{\nu}^2(T) \tag{3.8}$$

and that

$$\nu_W^{max} = 2\bar{\nu} \tag{3.9}$$

Thanks to equations (3.6), (3.7), (3.8) and (3.9), the criterion given by equation (3.5) leads to:

$$\bar{\nu}(T) = \frac{\alpha}{2h} k_B\, T \qquad\qquad A(T) = \frac{2\sigma h^2}{\pi k_b^2 \alpha^2} T^2 \tag{3.10}$$

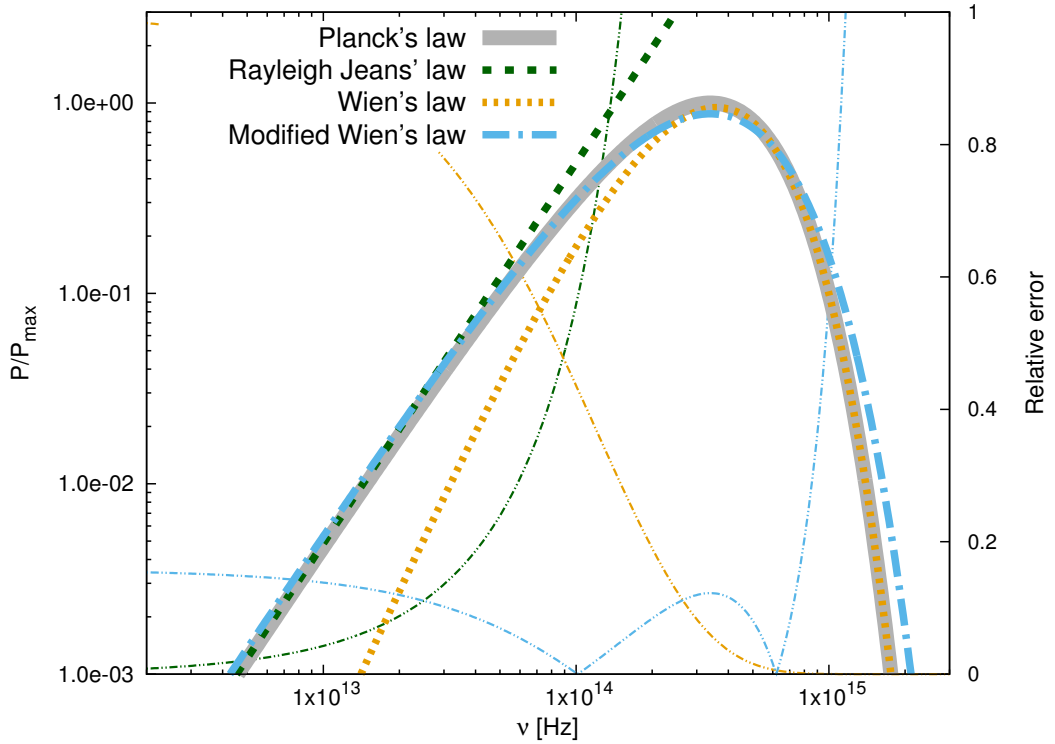

Figure 3.1: Planck's law and its approximations in relative power as a function of frequency for a black-body temperature T=5780K. Parameters for the modified Wien's law are given by equation 3.10. Planck's law in gray, Rayleigh Jeans' law in dark green, Wien's law in orange and modified Wien's law in blue. Relative errors are also represented as thin lines with corresponding colors.

With this choice of parameters, one can compute the modified Wien's law and compare it to Planck's law. This is done figure 3.1

In figure 3.1 is given an example of Planck's law and its approximations for a black-body at a temperature $T = 5780K$[1]. In this figure, the parameters for the modified Wien's law are the ones given by equation (3.10).

3.2 Analytical calculation: case of a single particle

The analytical computation of the inverse Compton scattering of a thermal photon distribution can not be done directly. Some approximations need to be done. Integration over incoming photons energies could be done numerically but combined with other integrations, it could cost a lot of numerical resources and computing time. In this part, I will propose an analytical integration over energies of the incoming photons following a thermal distribution. This analytical integration is based on the modified Wien's law approximation seen previously.

[1]Temperature of the Sun photosphere

3.2.1 General case

Let's consider a plane wave following the energy distribution described by the modified Wien's law. Replacing $I_\nu(\nu, T)$ by $W_\nu(\nu, T)$ (equation 3.4) in equation 2.35, we obtain:

$$\frac{\mathrm{d}N_1'}{\mathrm{d}t'\mathrm{d}\epsilon_1'\mathrm{d}\epsilon'\mathrm{d}\Omega_1'} = \frac{r_e^2}{2hm_ec^2}\int\left(\frac{\epsilon_1'}{\epsilon'}\right)^2\left(\frac{\epsilon_1'}{\epsilon'}+\frac{\epsilon'}{\epsilon_1'}-\sin^2\Phi'\right)\delta\left(\epsilon_1'-\frac{\epsilon'}{1+\epsilon'(1-\cos\Phi')}\right) \times\left(\frac{m_ec^2}{h}\right)^2 A'\epsilon'\exp\left(-\frac{\epsilon'}{\bar{\epsilon}'}\right)\delta\left(\Omega'-\Omega_0'\right)\mathrm{d}\Omega' \quad (3.11)$$

Then use the relations

$$\delta\left(\epsilon_1'-\frac{\epsilon'}{1+\epsilon'(1-\cos\Phi')}\right)\mathrm{d}\epsilon_1' = \delta\left(\epsilon_1-\frac{\epsilon'\gamma(1+\beta\cos\theta_1')}{1+\epsilon'(1-\cos\Phi')}\right)\mathrm{d}\epsilon_1 \quad (3.12)$$

and

$$\delta\left(\epsilon_1-\frac{\epsilon'\gamma(1+\beta\cos\theta_1')}{1+\epsilon'(1-\cos\Phi')}\right) = \frac{\gamma(1+\beta\cos\theta_1')}{\left[\gamma(1+\beta\cos\theta_1')-\epsilon_1(1-\cos\Phi')\right]^2} \times\delta\left(\epsilon'-\frac{\epsilon_1}{\gamma(1+\beta\cos\theta_1')-\epsilon_1(1-\cos\Phi')}\right) \quad (3.13)$$

One obtains:

$$\frac{\mathrm{d}N_1'}{\mathrm{d}t'\mathrm{d}\epsilon_1\mathrm{d}\epsilon'\mathrm{d}\Omega_1'} = \frac{A'r_e^2m_e^2c^4}{2h^3}\times\int\left(\frac{\epsilon_1'}{\epsilon'}\right)^2\left(\frac{\epsilon_1'}{\epsilon'}+\frac{\epsilon'}{\epsilon_1'}-\sin^2\Phi'\right)\epsilon'\exp\left(-\frac{\epsilon'}{\bar{\epsilon}'}\right) \times\frac{\gamma(1+\beta\cos\theta_1')}{\left[\gamma(1+\beta\cos\theta_1')-\epsilon_1(1-\cos\Phi')\right]^2} \times\delta\left(\epsilon'-\frac{\epsilon_1}{\gamma(1+\beta\cos\theta_1')-\epsilon_1(1-\cos\Phi')}\right)\delta\left(\Omega'-\Omega_0'\right)\mathrm{d}\Omega' \quad (3.14)$$

We will note $x = \dfrac{\epsilon_1}{\gamma}$ hereafter. Thanks to relation 2.31 and after integration over ϵ', one gets:

$$\frac{\mathrm{d}N_1'}{\mathrm{d}t'\mathrm{d}\epsilon_1\mathrm{d}\Omega_1'} = \frac{A'r_e^2m_e^2c^4}{2h^3}\int\frac{x}{\gamma\left[(1+\beta\cos\theta_1')-x(1-\cos\Phi')\right](1+\beta\cos\theta_1')} \times\left(1+\cos^2\Phi'-\frac{x(1-\cos\Phi')}{1+\beta\cos\theta_1'}+\frac{x(1-\cos\Phi')}{(1+\beta\cos\theta_1')-x(1-\cos\Phi')}\right) \times\exp\left(-\frac{x}{\left[(1+\beta\cos\theta_1')-x(1-\cos\Phi')\bar{\epsilon}'\right]}\right)\delta\left(\Omega'-\Omega_0'\right)\mathrm{d}\Omega' \quad (3.15)$$

One can show that:

$$\cos\Phi' = \cos\theta_1'\cos\theta' + \sin\theta'\sin\theta_1'\cos(\phi_1'-\phi')$$

In the highly relativistic approximation ($\gamma \gg 1$), one can assume that:

$$\begin{aligned}\cos\Phi' &= \frac{\cos\theta_1-\beta}{1-\beta\cos\theta_1}\frac{\cos\theta-\beta}{1-\beta\cos\theta}+\frac{\sin\theta}{\gamma(1-\beta\cos\theta)}\frac{\sin\theta_1}{\gamma(1-\beta\cos\theta_1)}\cos(\phi_1'-\phi') \\ &\approx \cos\theta_1'\cos\theta'\end{aligned}$$

With the notation $\mu'_1 = \cos\theta'_1$ and $\mu'_0 = \cos\theta'_0$, one gets after integration over $\mathrm{d}\Omega' = 2\pi \mathrm{d}\mu'$:

$$\frac{\mathrm{d}N'_1}{\mathrm{d}t'\mathrm{d}\epsilon_1\mathrm{d}\Omega'_1} = \frac{A' r_e^2 m_e^2 c^4}{2h^3} \frac{x \exp\left(-\frac{x}{\left[(1+\beta\mu'_1)-x(1-\mu'_1\mu'_0)\bar{\epsilon}'\right]}\right)}{\gamma\left[(1+\beta\mu'_1)-x(1-\mu'_1\mu'_0)\right](1+\beta\mu'_1)} \times \left(1+\mu_1'^2\mu_0'^2 - \frac{x(1-\mu'_1\mu'_0)}{1+\beta\mu'_1} + \frac{x(1-\mu'_1\mu'_0)}{(1+\beta\mu'_1)-x(1-\mu'_1\mu'_0)}\right) \quad (3.16)$$

In the highly relativistic case, one can also use the head-on approximation (Blumenthal and Gould (1970)) $\mu'_0 \approx -1$. We have also $t = \dfrac{t'}{\gamma}$ and $A' = \dfrac{A}{\gamma(1-\beta\cos\theta_0)}$ due to frame transformation.

Finally, on gets:

$$\boxed{\frac{\mathrm{d}N_1}{\mathrm{d}t\mathrm{d}\epsilon_1} = \frac{m_e^2 c^4 r_e^2 A \epsilon_1 \pi}{h^3\gamma^4(1-\beta\cos\theta_0)} \quad \mathcal{I}_{\mu'_1}} \quad (3.17)$$

with

$$\mathcal{I}_{\mu'_1} = \int_{-1}^{1} \frac{\left(1 - x\frac{1+\mu'_1}{(1+\beta\mu'_1)} + x\frac{(1+\mu'_1)}{(1+\beta\mu'_1)-x(1+\mu'_1)} + \mu_1'^2\right)}{[(1+\beta\mu')-x(1+\mu'_1)](1+\beta\mu'_1)} \exp\left(-\frac{x}{[(1+\beta\mu'_1)-x(1+\mu'_1)]\bar{\epsilon}'}\right) \mathrm{d}\mu'_1$$

3.2.2 Analytical simplification of the integral

The highly relativistic approximation yields $\beta \approx 1$ and thanks to the substitution $w = \frac{\mathcal{H}}{1+\beta\mu'_1}$ with $\mathcal{H} = \frac{x}{\bar{\epsilon}'(1-x)}$, the integral can be rewritten:

$$\mathcal{I}_{\mu'_1} = \frac{1}{\mathcal{H}(1-x)} \left\{ \int_{\mathcal{H}/2}^{2\gamma^2\mathcal{H}} \left(2 + \frac{x^2}{1-x}\right) e^{-w}\mathrm{d}w + \int_{\mathcal{H}/2}^{2\gamma^2\mathcal{H}} \frac{\mathcal{H}^2}{w^2} e^{-w}\mathrm{d}w - 2\mathcal{H}\int_{\mathcal{H}/2}^{2\gamma^2\mathcal{H}} \frac{1}{w} e^{-w}\mathrm{d}w \right\}$$

which gives :

$$\mathcal{I}_{\mu'_1} = \frac{1}{(1-x)} \left\{ \left(\frac{2}{\mathcal{H}} + 2 + x\bar{\epsilon}'\right) \exp(-\mathcal{H}/2) - (2+\mathcal{H})\left(E_1(\mathcal{H}/2) - E_1(2\gamma^2\mathcal{H})\right) \right\} \quad (3.18)$$

where $E_1(x) = \displaystyle\int_x^\infty \frac{\exp(-t)}{t}\mathrm{d}t$ is the exponential integral which can be easily computed by any numerical package.

Finally, the emitted spectra is given by:

$$\boxed{\begin{aligned}\frac{\mathrm{d}N}{\mathrm{d}t\mathrm{d}\epsilon_1} =& \frac{m_e^2 c^4 r_e^2 A \epsilon' \pi}{h^3\gamma^4(1-\beta\cos\theta_0)} \frac{1}{(1-x)} \\ & \times \left\{ \left(\frac{2}{\mathcal{H}} + 2 + x\bar{\epsilon}'\right) \exp(-\mathcal{H}/2) - (2+\mathcal{H})\left(E_1(\mathcal{H}/2) - E_1(2\gamma^2\mathcal{H})\right) \right\}\end{aligned}} \quad (3.19)$$

3.3 Approximations in the Thomson regime

In the Thomson regime, expression (3.19) can be simplified, especially with:

$$x \ll 1$$
$$x\epsilon_1' \ll \frac{2x}{\epsilon_1'} \approx \frac{2}{\mathcal{H}}$$

We get:

$$\boxed{\left(\frac{\mathrm{d}N}{\mathrm{d}t\mathrm{d}\epsilon_1}\right)_{Th} = \frac{m_e^2 c^4 r_e^2 A\epsilon'\pi}{h^3\gamma^4(1-\beta\cos\theta_0)} f_{Th}(\mathcal{H})} \tag{3.20}$$

with

$$f_{Th}(\mathcal{H}) = \left\{\left(\frac{2}{\mathcal{H}}+2\right)\exp(-\mathcal{H}/2) - (2+\mathcal{H})E_1(\mathcal{H}/2)\right\} \tag{3.21}$$

Therefore, the spectra in the Thomson regime is a function of a single variable and this will be used in the next section.

3.3.1 Thomson regime and pile-up particle energy distribution

In a realistic case, particle energy distributions are rarely mono-energetic and one has to integrate the kernel above over particle energies.

In the case of a pile-up distribution[2] $n_e(\gamma) = \frac{N_e}{2\bar{\gamma}^3}\gamma^2\exp\left(-\gamma/\bar{\gamma}\right)$ for the particles, this integration shows to be quite simple.

The integration over γ writes:

$$\frac{\mathrm{d}N_1}{\mathrm{d}t\mathrm{d}\epsilon_1} = \frac{\pi m_e^2 c^4 r_e^2 A\epsilon_1}{h^3}\int_1^\infty N_e \frac{1}{\gamma^2(1-\beta\mu_0)} f_{Th}(H)\exp\left(-\gamma/\bar{\gamma}\right)\mathrm{d}\gamma \tag{3.22}$$

With the substitution $u = \gamma/\bar{\gamma}$ and the approximation $\gamma \gg 1$, one gets:

$$\begin{aligned}\frac{\mathrm{d}N_1}{\mathrm{d}t\mathrm{d}\epsilon_1} &= \frac{\pi m_e^2 c^4 r_e^2 A\epsilon_1}{h^3}\frac{N_e}{2\bar{\gamma}^4(1-\mu_0)}\int_0^\infty \frac{1}{u^2} f_{Th}(H)\exp\left(-u\right)\mathrm{d}u \\ &= \frac{\pi m_e^2 c^4 r_e^2 A\epsilon_1}{h^3}\frac{N_e}{2\bar{\gamma}^4(1-\mu_0)}\,\chi(s)\end{aligned} \tag{3.23}$$

with

$$\chi(s) = \int_0^\infty \frac{1}{u^2} f_{Th}\left(\frac{s}{u^2}\right)\exp\left(-u\right)\mathrm{d}u \tag{3.24}$$

$\chi(s)$ is a single variable function. As such, it can be computed once, tabulated and interpolated over when required. This way, the computation of the inverse Compton spectra from the scattering of a thermal soft photon field on a pile-up distribution of electrons can be done much faster than usually with complete numerical integration.

3.4 Validating the analytical approximation

In the following, I will present a step by step validation of the analytical Compton scattering spectrum on a thermal photon field presented previously.

[2] see section 4.3 for an explanation of why we are interested in a pile-up distribution, besides the fact that it provides a nice analytical calculation

3.4.1 Analytical approximation compared to numerical integration over a modified Wien law

The first thing we want to verify is the validity of the analytical approximations and calculations. Let's consider an external photon field described by the modified Wien's law and compare the analytical spectrum given by equation (3.19) with a numerical integration over the soft photon energies with the kernel given by equation (2.38). This is shown in figure 3.2 for several mono-energetic particle distribution of energy $\gamma\, m_e c^2$ and for a temperature of the soft photon field $T = 5780K$.

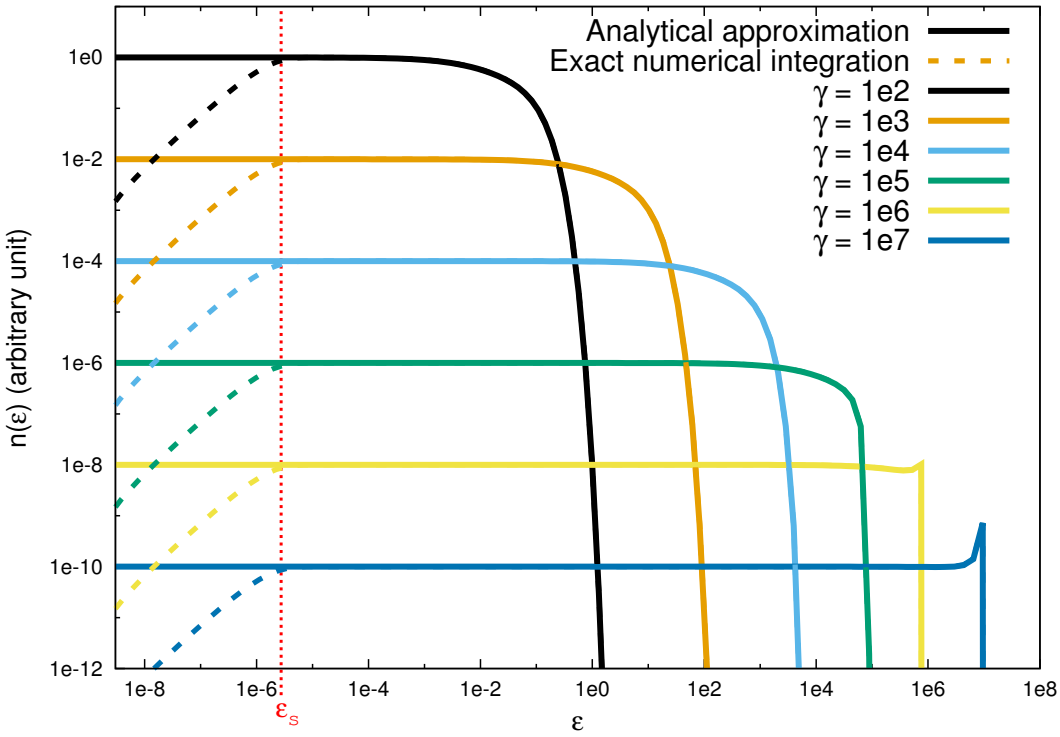

Figure 3.2: Comparison of the analytical integration with the numerical integration of the inverse Compton spectra for a photon field described by the modified Wien's law (T=5780K) and for several mono-energetic particle distribution

We can see that the analytical calculation is valid for most of the integration domain. It starts diverging at energies lower than $\epsilon_s = \frac{\alpha}{h} k_B T$ (see equation 3.7) due to our approximations on the limits of the integration.[3]

Fortunately, this will not have major consequences in our study. First, note that here were represented the number of photons enhancing the role of low energies photons whereas they contribute very little in term of power. Second, the error is done bellow ϵ_s where the emission from the soft photon source will largely dominate over the inverse Compton emission (see figure 3.3).

[3]We should also expect an error at high energies in the Thomson regime corresponding to approximations in the upper limit of the integral but these errors are even smaller and do not appear here. In the Klein-Nishina regime, the energy of the scattered photons is limited by the particle energy.

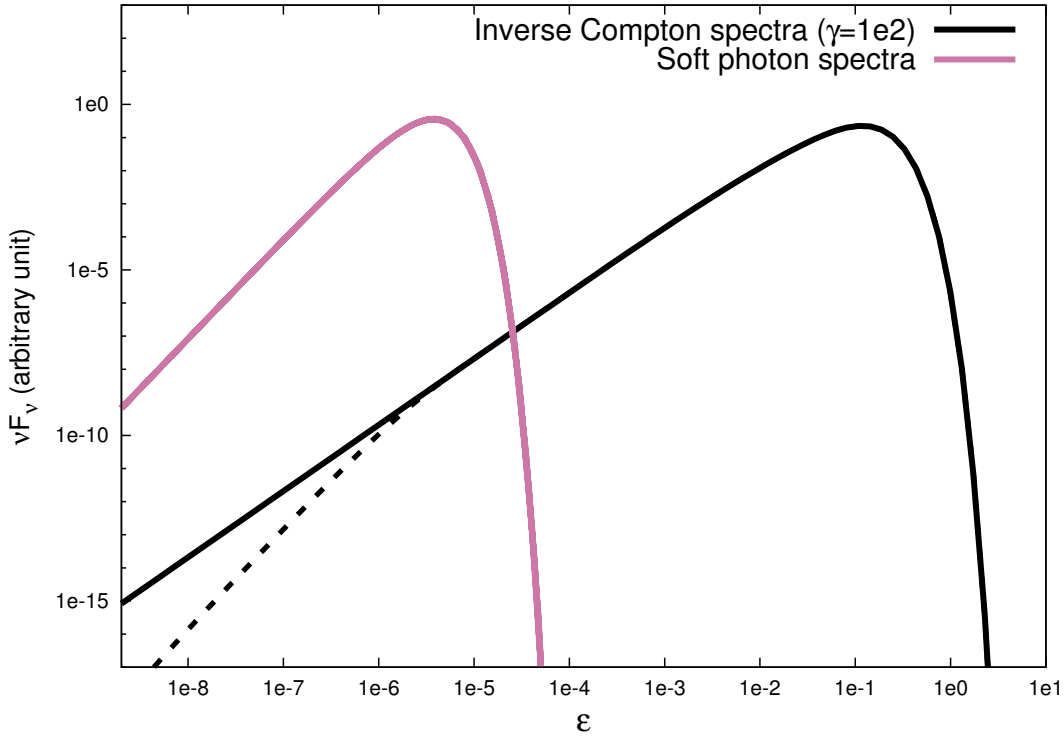

Figure 3.3: The analytical inverse Compton spectrum (thick black line) and the true inverse Compton spectrum (dotted black line) compared to the soft photon spectrum.

3.4.2 Is the modified Wien's law a good approximation of Planck's law?

As we saw in section 3.1, the modified Wien's law can be quite a good approximation of Planck's law given that we choose its parameters A and $\bar{\nu}$ correctly. Nevertheless, our goal here is not to reproduce correctly the soft photon spectra but its Compton scattering on relativistic particles. It might be interesting to choose A and $\bar{\nu}$ differently so that the inverse Compton spectra is better reproduced.

The choices here are to keep:

- the same emitted power after scattering in the Thomson regime
- the peak position of the emitted spectra in the Thomson regime

This work has been done by Begue (2010) and the resulting values are:

$$\bar{\epsilon} = 1.31\frac{k_B T}{m_e c^2} \qquad A = 2.90\frac{k_B T}{c^2} \tag{3.25}$$

The result is displayed figure 3.4.

The relative error is lower than 4% on the middle range but increases rapidly at low energies and at high energies after the emission peak. The principal error at low energies comes from the analytical integration and is not important as said previously. At high energies, there is a substantial error coming from the modified Wien's law approximation but at this point the emission drops exponentially and the error committed here will not affect greatly the total emission. Moreover, the error will be even less important when

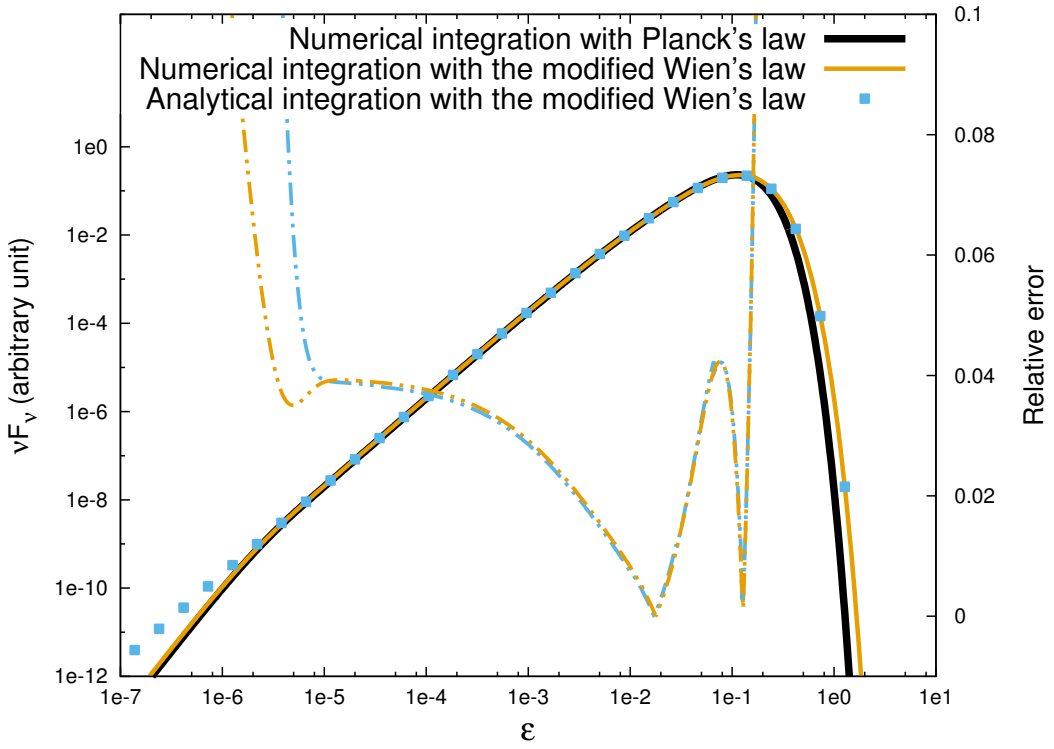

Figure 3.4: Comparison of the different inverse Compton spectra of a thermal soft photon field (T=5780K) scattering on a mono-energetic particle distribution of Lorentz factor $\gamma = 1e2$ with the relative errors. In black the numerically integrated spectra with the thermal distribution described by Planck's law. In orange, the numerically integrated spectra with the thermal distribution described by the modified Wien's law. In blue, the analytically integrated spectra with the thermal distribution described by the modified Wien's law (given by equation 3.19)

integrated over a distribution of black-bodies such as the multi-color accretion disc (see section 6).

3.4.3 Comparison to other analytical work

At the same time I developed these calculations, other work were published to perform analytical calculation of the inverse Compton scattering on a thermal photon distribution (Zdziarski and Pjanka (2013) - hereafter ZP13 and Khangulyan et al. (2014)).

In this part I will compare our results with the one from ZP13 where the scattering rate of a photon beam from direction $\mathbf{\Omega}$ into direction $\mathbf{\Omega_1}$ integrated over blackbody is:

$$\frac{\mathrm{d}\dot{n}}{\mathrm{d}\epsilon_1 \mathrm{d}\gamma \mathrm{d}\Omega_1 \mathrm{d}\Omega} = \frac{3\sigma_T c A}{4\gamma^2} \frac{\mathrm{d}N(\gamma)}{\mathrm{d}\Omega_1} \left[(1+\epsilon_1\epsilon_m y)\theta^2 f_1\left(\frac{\epsilon_m}{\theta}\right) + 2\epsilon_m^2 f_{-1}\left(\frac{\epsilon_m}{\theta}\right) - 2\epsilon_m \theta f_0\left(\frac{\epsilon_m}{\theta}\right) \right] \tag{3.26}$$

with the following notations:

$$y = 1 - \mathbf{\Omega}\cdot\mathbf{\Omega_1} \qquad \epsilon_m = \frac{\epsilon_1}{2y\gamma(\gamma-\epsilon_1)} \qquad \theta = \frac{k_b T}{m_e c^2} \tag{3.27}$$

$$A = 2\left(\frac{m_e c}{h}\right)^3 \tag{3.28}$$

$$f_0(x) = -\ln\left(1-\exp(-x)\right) \tag{3.29}$$

$$f_1(x) = Li_2[\exp(-x)] - x\ln[1-\exp(-x)] = \frac{\pi^2}{6} + \frac{x^2}{2} + Li_2(1-\exp x) \tag{3.30}$$

$$f_{-1}(x) = \begin{cases} g_1(q,3) - g_1(x,3) + g_0, & x \le q, \\ \\ g_h(x,3), & x > q \end{cases} \quad \text{with } q = 2.257 \tag{3.31}$$

$$g_0 = 0.0366377 \tag{3.32}$$

$$g_1(x,N) = -x^{-1} - \frac{\ln x}{2} + \sum_{k=1}^{N} \frac{x^{2k-1} B_{2k}}{(2k-1)(2k)!} \tag{3.33}$$

We see that the solution proposed by ZP13 is in overall better than ours with a relative error bellow 0.1% in the medium range. The emission peak is also closer from the complete calculation.

Nevertheless, our calculation presents the advantage to be faster than the one from ZP13. In our simulations it showed to be more than twice as fast in the case studied here. Moreover, another huge gain of computation time is also done with the one variable function in the case of a pile-up distribution in the Thomson regime (see section 3.3.1). Let's note that the error made compared to the exact numerical integration will be smoothed in the complete model as the spectra will be convolved on several parameters and on the integration along the jet.

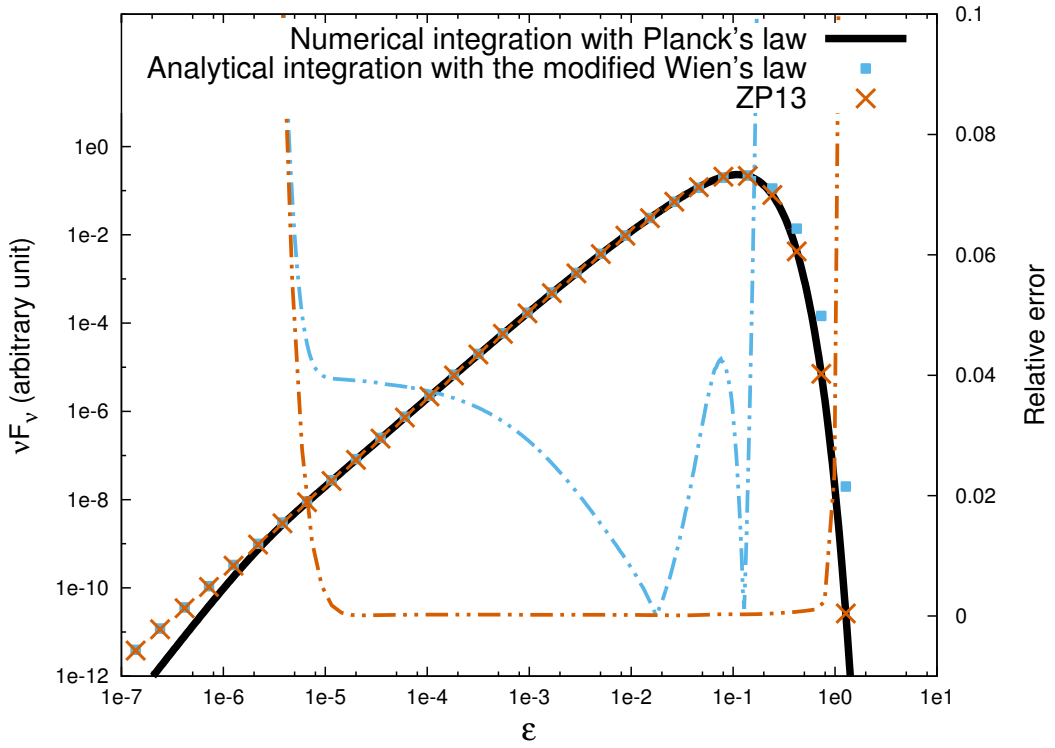

Figure 3.5: Same as figure 3.4 but compared to the scattering rate computed by ZP13

3.5 *[En résumé]* Diffusion Compton inverse sur une distribution thermique de photons

Dans ce chapitre, je présente en détail la diffusion Compton inverse de photons suivant une distribution thermique. Ce processus est extrêmement important en astrophysique car de nombreuses sources de photons suivent un distribution thermique qui est alors donnée par la loi de Planck (équation (3.1)). La loi de Planck peut être approchée par la loi de Rayleigh-Jeans (équation (3.2)) pour les faibles énergies de photon et par la loi de Wien (équation (3.3)) pour les grandes énergies de photon. Je propose ici une nouvelle approximation de la loi de Planck que j'appelle loi de Wien modifiée. Cette nouvelle description, donnée par l'équation (3.4) et représentée figure 3.1, me permet de développer une nouvelle approximation analytique pour le calcul du spectre Compton inverse. Le résultat final de cette approximation est donné par l'équation (3.19). Je montre ensuite que cette approximation est valide sur une grande partie du spectre Compton inverse (figure 3.5) avec une erreur inférieur à quelques pourcents. L'énorme avantage de cette approximation réside dans l'éfficacité de calcul numérique qu'elle permet avec un temps de calcul réduit d'un facteur 10^5 dans le meilleur des cas.

Part II

Modeling in the two-flow framework

Chapter 4

The two-flow: another paradigm

Contents

In section 1 were presented the current important questions and issues with our understanding of AGN. In particular, models have trouble reproducing their broadband emission without assuming had-oc hypothesis. The two-flow model aims at providing a global understanding of AGN based on physical arguments. In the following, I will present the hypothesis of this theory and how they are grounded in observations or physical reasons.

4.1 Hypothesis

The two-flow paradigm is based on an original idea from Sol et al. (1989). The model has evolved since then but the core hypothesis stays the same: an AGN "jet" is actually made of two interacting flows.

The outer one is a MHD jet, or wind, fueled by the accretion disc. It originates from the process described in Blandford and Payne (1982) (BP mechanism) and is much alike the jets found in other objects such as young stars or neutron stars. It is therefore mass loaded by the disc and as such baryonic and midly relativistic ($\beta \approx 0.5$). On the rotation axis, where the angular momentum tends to zero, it is expected that the density also tends to zero because there is no MHD force counteracting the gravity from the central object, thus leaving an empty funnel.

In this empty funnel is supposed to arise a lighter jet made of leptons (electrons/positrons) which are created through $\gamma - \gamma$ interaction between the soft and high-energy photons. This leptonic plasma travels at highly relativistic speeds and is accelerated through the

Compton rocket effect as we will see further. It is confined and collimated by the MHD jet.

The interaction of these two jets is supposed to produce turbulence. The Aflven waves created at the interface of the two flows carry energy that will accelerate particles in the spine. These processes are known under the term of second order Fermi processes. In that picture, because the MHD sheath carries most of the power, it can be seen as an energy reservoir constantly giving energy to the particles through turbulence. This continuous source of energy give rise to two very interesting processes. The first one is the Compton rocket process which is quite inefficient as shown by Phinney (1982) if the pairs are not reaccelerated by an external mechanism (here the turbulence), I will present further this process in section 7. The second one is the large pair creation process. As pairs are created through $\gamma - \gamma$ absorption, the new pairs are also accelerated through turbulence. As they get to high energies, they can emit γ-rays that will create more pairs. Starting from a very low density of pairs, copious amount of new pairs can be created this way, therefore making the spine. Moreover, this pair creation process is very effective and highly non-linear. Above a certain threshold of energy, the process can runaway and give rise to episodes of rapid flares. This has been demonstrated by Renaud (1999), Saugé and Henri (2004) and Boutelier et al. (2008). I will present more details about the pair creation process in section 5.2.

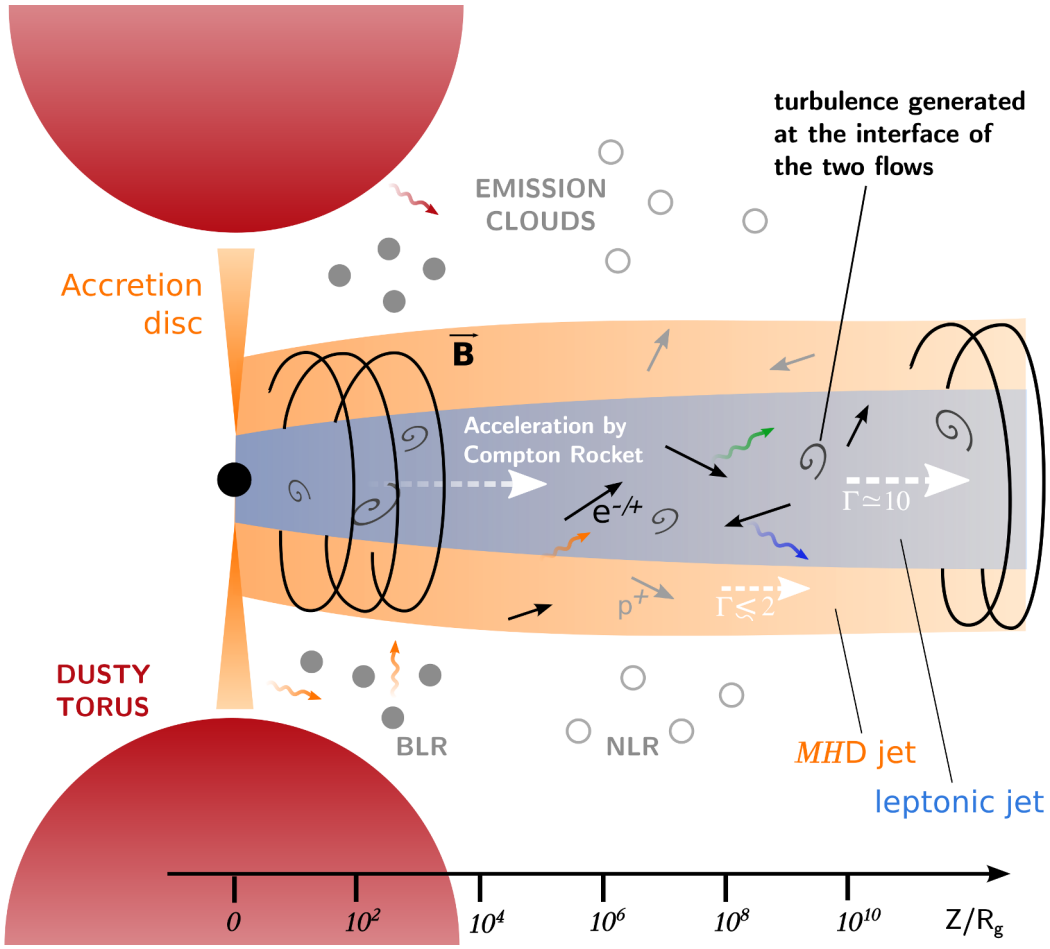

Figure 4.1: Schematic view of the two-flow paradigm.

4.2 Theoretical interest of these hypothesis & link with the observations

4.2.1 About jet velocities

Having two flows with different velocities has many benefits. The main one is that it provides a very natural explanation to the discrepancies in observed velocities in jets and could solve the unification problem between BL Lacs and FR I objects (see section 1.2.2).

More recent theoretical works have also adopted a structured geometry with two layers and different velocities. Chiaberge et al. (2000) proposed such a structure to solve unification problem and has been followed by the spine/sheath structure from Ghisellini et al. (2005) (hereafter Gh05) which was proposed with the same intention. The idea is that one could observe the boosted emission from the highly relativistic flow in BL Lacs while in FR I objects, seen at greater angles, the emission from slower parts would be preferentially observed.

A structured jet not only allow us to observe different speeds, it can also help solving the bulk Lorentz factor crisis (Henri and Saugé (2006)) by reducing the required Lorentz factors. Georganopoulos and Kazanas (2003) showed that an ad-hoc deceleration between the inner parts and the parsec scale of the jet could explain the differences in measured and required Doppler factor as well as reducing the required Doppler factor thanks to the extra radiation coming from the slow jet and seen by the inner parts as Doppler boosted. The spine/sheath scenario developed by Gh05 benefits from the same advantage. In addition for accounting for the discrepancy in jet velocities with a fast spine and a slow sheath[1], the radial structure also allow a mutual boosting of the emission. The emission from the inner spine being enhanced by the extra radiation of the slow jet (here the sheath), the inferred bulk Lorentz factor can be lowered.

The two-flow paradigm is very similar to the spine/sheath scenario and would probably benefit from the same advantages. As it is convenient to speak of the spine for the inner jet and of the sheath for the outer jet, I will borrow this terminology from Gh05 keeping in mind that only the jet layered structure is comparable but not their composition nor physical properties.

From an observational point of view, very recent kinematics studies of M87 (Mertens et al. (2015)) reveal a stratified flow with a midly relativistic layer ($\beta \approx 0.5$) and more relativistic field lines going from $\gamma \approx 2.5$ to $\gamma \approx 6$. This structure is present at the very base of the jet and support very well the view of the two-flow where the spine would be present everywhere in the jet.

4.2.2 About jet composition & emission processes

The composition of jets is still a matter of strong debates. As stated in section 1.2.2, protons always pose a problem of required power. If they take part in the emission (hadronic processes), the required power are tremendous compared to leptonic models (Böttcher et al. (2013) or Zdziarski and Böttcher (2015)) and are therefore more difficult to explain.

But even when protons are cold and just a part of the flow (leptons are responsible for the observed emission), the problem of required power remain as heavy protons should be accelerated to bulk relativistic speed. Statistical study from Ghisellini et al. (2014) suggest that jets composed of 50% of leptons and 50% of protons require powers of the order or even larger than the accretion power. Of course, this would be impossible if the

[1] here the slow external layer is supposed to arise because of the interaction with the ambient medium

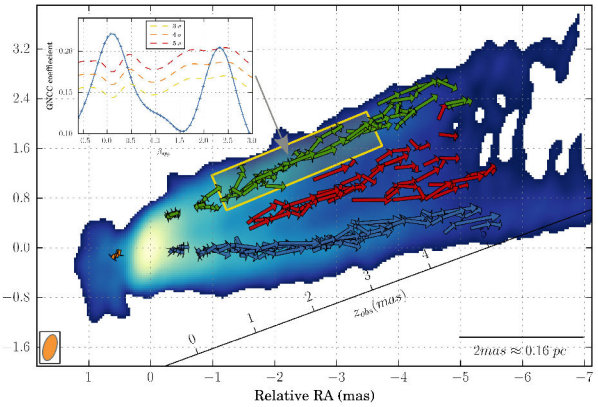

Figure 4: *Velocity field in the jet of M87. Three main flow patterns are detected in a southern (blue) and northern (green) rail and a central region (red). The component found in the inner part of the counter jet (orange), is used to constraint the viewing angle (θ ~ 18°). SCC analysis (inset) reveals velocity stratification with two main velocity components present in all three regions of the jets: a slow mildly relativistic speed (β ~ 0.5 c) and a faster relativistic speed (γ ~ 2.5). The spine in the center of the jet is deboosted and a maximum Lorentz factor can be estimated using the intensity ratio between the sheath and the spine (γ ~ 6).*

Figure 4.2: Courtesy of Mertens et al. (2015). Kinematics study of the inner jet of M87 reveal the presence of a two-flow structure with speeds ranging from $0.5c$ on the edges to $\Gamma \approx 6$ in the spine.

accretion power was the only source of energy but can still be explained thanks to the BZ mechanism (Blandford and Znajek (1977)) where energy is extracted from the black-hole rotation.

In the two-flow paradigm, it is expected that jets would require less energy. Since only hot leptons are accelerated to highly relativistic bulk motion as opposed to protons which are kept at moderate speeds in the external sheath, the required power would be lower. Of course, this is coherent with the fact that the MHD jet is supposed to arise from the BP mechanism and therefore, the accretion power might be sufficient[2].

4.2.3 Acceleration & confinement of a highly relativistic flow

The confinement of highly relativistic flows is also a though question in AGN theory whereas the confinement of slower winds is easily achieved by numerical simulations (see section 1).

In the two-flow paradigm, the confinement of the MHD wind is realized by magnetic pressure. Being more massive and more powerful, the wind can then confine the spine by ram pressure. This interaction between the spine and the sheath provides confinement of the relativistic flow but indirectly also its acceleration.

Indeed, it is through this interaction that instabilities arise, causing a transfer of energy to pairs in the spine that will ultimately induce acceleration of all the spine through the Compton rocket effect. This process will be described in more details in section 7.

4.2.4 Limb brightening

Limb brightening is the presence of a persistent observed luminosity on the edge of the jet. It has been observed in several AGNs the past fifteen years such as M87 (Biretta et al. (1999)), Mrk 501 (Giroletti et al. (2008)), Mrk 421 (Piner et al. (2010)), 1144+35 (Giovannini et al. (1999)) and 3C 84 (Nagai et al. (2014) - hereafter NA14). As explained by NA14, this limb brightening finds quite a natural explanation in the spine/sheath model where the emission on the edges would corresponds to the sheath. Moreover, in NA14,

[2] A more precise evaluation of the total power should be done but would require a complete study of the MHD jet which carry most of the power

the limb brightening corresponds to a regain of activity of the jet with an increase of luminosity jet in the radio band (Abdo et al. (2009)) in 2005 followed by an increase of luminosity of the 3C 84 in the γ-ray band after 2009. Ridge brightening appeared in a low γ ray state whereas the limb brightening appeared in a high γ-ray state. Moreover, assuming uniform radial brightness distribution, they argue that the limb brightening corresponds to a change in the apparent transverse structure of the jet. Indeed, at great angles, the slower sheath can be Doppler boosted or at least less de-boosted than the rapid spine. Therefore, a transition from ridge brightening to limb brightening could be explained by an increase in the spine velocity but no physical explanation of why the jet would accelerate during a high γ-ray state is provided in this study.

In the two-flow paradigm, the limb brightening find the same explanation as in the spine/sheath scenario. But limb brightening is also expected as the transfer of energy takes place at the interface between the spine and the sheath. One can speculate that a resumption of turbulent activity will transfer more energy to the pairs in the spine. This would naturally produce a limb brightening but could also trigger a high γ-ray state correlated with an enhancement of the Compton rocket effect - that will be presented in section 7 - and therefore an increase of the spine velocity, exactly what is observed in NA14. Thus, we see that the limb brightening finds a natural explanation here but additional correlated observations could come as natural consequences in the two-flow paradigm.

4.2.5 Diffuse emission

AGNs jets show diffuse emission from radio to X-ray wavelengths. If one supposes a synchrotron origin for this emission[3], one can compute the characteristic cooling time thanks to equation (2.20)[4]. As the cooling time is proportional to $\frac{1}{\gamma}$ and the synchrotron frequency ν_s is proportional to $\gamma^2 B$, one can see that for a fixed magnetic field:

$$t_{syn} \propto \nu_s^{-1/2} \tag{4.1}$$

Therefore, the synchrotron cooling time at X-ray energies is 10^4 times shorter than the synchrotron cooling time at radio energies. If it is possible to argue that electrons emitting radio are accelerated somewhere and then radiate and cool down slowly as they move further in the jet, this assumption is impractical for X-rays for which electrons basically emit where they are accelerated. The only possibility to explain the X-ray diffuse emission is then a diffuse acceleration mechanism, existing on kilo-parsec scales. If such a mechanism is present on kilo-parsec scales, one can suppose that it exists everywhere in the jet. The micro-physics of these regions is still beyond our reach but a mechanism to explain distributed acceleration is required. Turbulence or magnetic reconnection are the most probable mechanisms at play here but one could also imagine distributed shocks everywhere in the jet such as the model proposed by Jamil et al. (2010) or Malzac (2014) for X-ray binaries.

[3] Apart from synchrotron emission from TeV particles, the only leptonic models proposed to explain the X-ray emission at kilo-parsec scales was the IC/CMB model that has been ruled out recently in several objects by Meyer and Georganopoulos (2013), Cara et al. (2013) and Meyer et al. (2015).

[4] One also needs to suppose a value for the magnetic field. It is usually the equipartition value that is used.

4.2.6 Minor clues

On the necessity of a black-hole

It is indispensable for AGNs to be powered by accretion of matter into a black-hole, whatever the jet creation mechanism may be. Nevertheless, one can argue about the necessity of the black-hole to produce the jet we see and this debate crystallize around the BP mechanism versus BZ mechanism discussion. On the one hand, as stated previously and depending on the jet composition, one may require the BZ mechanism to extract more power from the system than allowed only by the accretion of matter. On the other hand, jets exist in other system without black-holes, proving that at least one jet production mechanism (if not the BP mechanism) works without the help of a black-hole but solely from the accretion disc. An argument to settle this would be to look at the black-hole spin in jetted system as the jet power is directly proportional to the square of the spin in the BZ mechanism whereas it is not necessarily correlated in the BP mechanism. Of course such observations are very difficult by nature but current studies does not show any correlation between the presence of jets and black-hole spin - study from Reynolds (2013) could even point in the opposite direction.

Compton bump

The scattering of an ambient photon field by cold particles should not give rise to a new component, except if they move with a relativistic bulk motion. This is the so called bulk comptonization process which has been proposed first by Begelman et al. (1987). The emergence of this extra component called Compton bump (or Sikora bump) in the spectral energy distribution of AGNs would allow an evaluation of two very important unknowns of jets: their composition and their bulk Lorentz factor (Sikora and Madejski (2000) and Celotti et al. (2007)). Unfortunately, no such feature has been detected so far, putting constraints of the unknowns cited above. In the two-flow paradigm, no such features is expected since only hot pairs are accelerated to highly relativistic bulk motion. On the contrary, a clear detection of the Compton bump would be a strong evidence against the two-flow as it would imply cold particles moving at highly relativistic speeds.

4.3 The pile-up: a natural distribution

Most of the emission models suppose a power-law particle energy distribution. This is very convenient as the spectral energy distributions of the observed emission are often power-laws. Moreover, such a distribution naturally arises when dealing with shock acceleration (Bell (1978)). However, in the two-flow paradigm, even if shocks are present (as well as magnetic reconnection), they are not the main vector of particle acceleration, but turbulence rather is. In the case of stochastic acceleration and without pair creation or bulk flow, the evolution of the distribution in the phase space is governed by the Fokker-Planck equation:

$$\frac{\partial}{\partial t} n(\gamma) = \frac{\partial}{\partial \gamma} A \gamma^2 n(\gamma) + \frac{\partial}{\partial \gamma} \gamma^2 D(\gamma) \frac{\partial}{\partial \gamma} \frac{n(\gamma)}{\gamma^2} \tag{4.2}$$

where $A = \frac{4}{3} \sigma_T \, c \, n_s \, \epsilon_s$ in the case of an isotropic soft photon field of density n_s and mean energy ϵ_s (in electron mass energy unit) (Henri and Pelletier (1991)) and D the

diffusion coefficient given by a simple power-law (Lacombe (1977)):

$$D = D_0 \gamma^r \tag{4.3}$$

Schlickeiser (1984) showed that the solution of this equation was a pile-up distribution:

$$n(\gamma) \propto \gamma^2 \exp\left(-\left(\frac{\gamma}{\bar{\gamma}}\right)^{3-r}\right) \tag{4.4}$$

where $\bar{\gamma}$ is the typical internal energy of the pair plasma.

This distribution can be understood as the competition between cooling and heating. A typical cooling time is the synchrotron one (see equation 2.20) and we have:

$$t_{cool} \propto \gamma^{-1} \tag{4.5}$$

By definition of the diffusion coefficient,

$$D \approx \frac{<\delta\gamma^2>}{\delta t} \tag{4.6}$$

The diffusion time, corresponding to the accelerating time, is:

$$t_{acc} = \frac{\gamma^2}{D} \propto \frac{\gamma^{2-r}}{D_0} \tag{4.7}$$

Thereby, as a particle with initial energy $\gamma m_e c^2$ gains more energy, its acceleration time increases. When it reaches an energy $\gamma_{crit} m_e c^2$ defined as $t_{cool}(\gamma_{crit}) = t_{acc}(\gamma_{crit})$, the cooling is too strong and the particle reaches its equilibrium[5] energy $\gamma_{eq} \approx \gamma_{crit} \approx \bar{\gamma}$.

For the sake of simplicity, we choose a value of $r = 2$. And by setting $N_e = \int n_e(\gamma) \mathrm{d}\gamma$, we obtain the pile-up distribution that we will use in our modeling:

$$\boxed{n_e(\gamma) = N_e \frac{\gamma^2}{2\bar{\gamma}^3} \exp\left(-\frac{\gamma}{\bar{\gamma}}\right)} \tag{4.8}$$

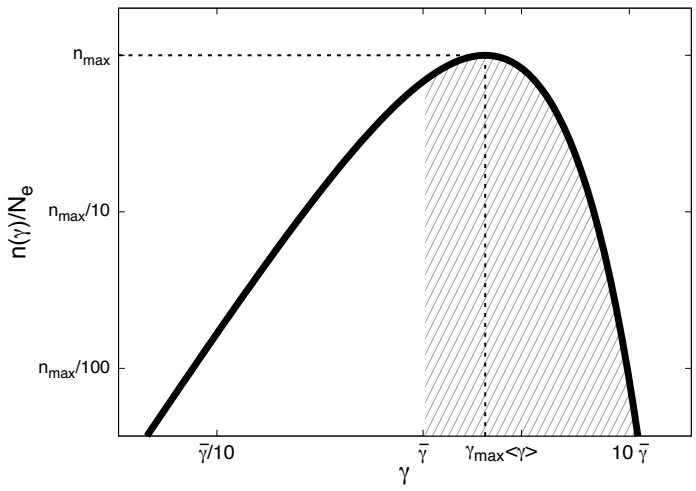

Figure 4.3: A pile-up distribution described by equation (4.8) in log-log.
Maximum arises at (γ_{max}, n_{max})
Filled area represents more than 92% of the particles and more than 98% of the total energy.

With the followings:
$\gamma_{max} = 2\bar{\gamma}$
$n_{max} = 2e^{-2}/\bar{\gamma}$
$< \gamma >= 3\bar{\gamma}$

[5] of course, this is an equilibrium only because of continuous acceleration

4.4 *[En résumé]* Le paradigme du jet à deux fluides

Dans ce chapitre, je présente le paradigme du jet à deux fluides (*two-flow*) proposé pour la première fois par Sol et al. (1989) et aujourd'hui développé à l'IPAG.

Dans ce paradigme, le jet est en réalité composé de deux fluides intriqués, à la manière d'un cable et d'une gaine. La gaine est un jet ou un vent magnétohydrodynamique (MHD) généré par le disque d'accrétion. Ce vent faiblement relativiste transporte de la matière provenant du disque (protons et électrons). A l'intérieur de cette gaine, un jet léger, composé uniquement de leptons (électrons et positrons). Ce jet se déplace à des vitesses relativistes et est confiné par le jet MHD l'entourant.

A l'interface de ces deux jets se créé de la turbulence. Les ondes d'Alven ainsi générées transporte de l'énergie et peuvent accélèrer les leptons de la colonne centrale. Dans cette représentation, le jet MHD transporte la plus grande partie de la puissance et agit ainsi comme un réservoir d'énergie pour la colonne, majoritairement responsable de l'émission non thermique observée.

Le transfert d'énergie entre la gaine et la colonne étant continu, le processus d'accélération par fusée Compton (voir chapitre 7) peut accélérer efficacement la colonne à des vitesses relativistes. Un schéma récapitulatif du paradigme est donné figure 4.1.

Intérêt d'un tel paradigme

Ce nouveau paradigme a l'avantage de proposer une version globale et cohérente des jets de NAG. En particulier, la présence de deux fluides différents permet d'expliquer très facilement les très grandes dispersions de vitesses observées dans les jets de NAG. Cette structure de jet allie de manière intéressante un plasma purement leptonique, et donc léger, pouvant être facilement accélerer à de grands facteurs de Lorentz et un plasma MHD, plus lent mais transportant plus d'énergie sur de grandes distances. De plus, cette gaine MHD permet le confinement de la colonne relativiste alors que l'auto-confinement d'un jet relativiste semble être impossible et est inexpliqué dans de nombreux modèles ne présentant pas de structure à deux fluides.

Du côté observationnel, de très récentes observations confirment une structure de jets transverse (par exemple par le "limb brightening") avec potentiellement des vitesses beaucoup plus importantes dans la colonne centrale (4.2). L'émission diffuse, observée dans de nombreux NAG, joue aussi en faveur de processus d'accélérations des particules non localisés, en accord avec la turbulence.

La distribution en *pile-up*

La distribution d'énergie en *pile-up* (équation 4.8) pour les particules découle de l'hypothèse d'une accélération turbulente. Elle sera utilisée par la suite dans le modèle numérique.

Chapter 5

Evolution of the physical conditions along the jet

Contents

The physical modeling of the jet structure being now described, I will present the numerical modeling of the inner jet (spine). From now on, I will refer to the inner jet simply as "the jet" as it is supposed to be responsible for the non-thermal emission that we want to reproduce and is therefore the only one modeled in this work.

Essential parameters of the emission are the magnetic field B, the particle distribution $n(\gamma)$, the emission site size - characterized here by the radius of the jet R and the Doppler factor δ - characterized by the bulk Lorentz factor Γ and the viewing angle of the observer i_{obs} relative to the jet axis (see equation 2.7).

The approach here is to be, as much as possible, driven by the physics and therefore to avoid any ad hoc hypothesis or description. This has two main implications:

- the particle distribution, chosen to be a pile-up (see section 4.3) can not evolve freely but must be the result of some energy injection and of the cooling from radiation processes. The computation of its parameters is explained in section 5.3.

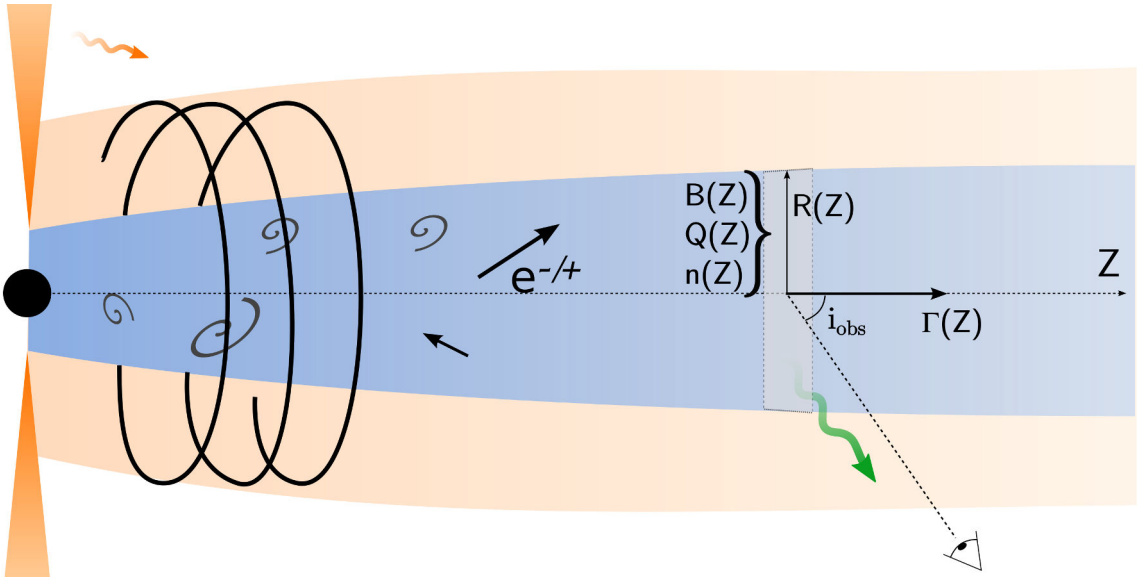

Figure 5.1: Modeling of the inner jet (in blue) with the parameterization of the required physical parameters as a function of Z.

- the bulk Lorentz factor is also not a free parameter but results from the Compton rocket process and therefore depends mainly on the external sources geometry. More details on this process, its computation and resulting values of Γ will be given in section 7.

However, some parameters are left free. It is the case of the magnetic field, the jet shape and the energy Q injected in the particles from the turbulence generated at the interface of the two-flows.

Diffuse acceleration along the jet immediately implies a stratified emission which forces us to model the whole jet. However, to simplify, the jet is supposed to be a one dimensional system along the jet axis Z.

I will start by presenting the numerical computation of the emission processes and of the associated pair creation. Taking into account the pair creation, I will then present the evolution of the particle distribution. Finally, I will describe the evolution of the remaining parameters.

5.1 Synchrotron & Inverse Compton radiation

5.1.1 Synchrotron emission

Blumenthal and Gould (1970) showed that the power per unit of frequency and solid angle emitted through synchrotron radiation by a particle of energy $\gamma m_e c^2$ and making an angle θ with the magnetic field direction is:

$$\frac{\mathrm{d}E}{\mathrm{d}t\mathrm{d}\nu\mathrm{d}\Omega} = \frac{\sqrt{3}e^3 B \sin\theta}{4\pi m_e c^2} F_{syn}\left(\frac{\nu}{\nu_c \sin\theta}\right) \tag{5.1}$$

with $\nu_c = \frac{3}{4\pi}\frac{eB\gamma^2}{m_e c}$ the critical synchrotron frequency and F_{syn} the synchrotron kernel:

$$F_{syn}(x) = x\int_x^\infty K_{5/3}(x)\mathrm{d}x \tag{5.2}$$

with K_n the n-order MacDonald function.

In the case of a pile-up distribution, Saugé (2004) showed that the synchrotron emissivity was equal to:

$$j_\nu = \frac{\sqrt{3}}{16\pi}\frac{e^3 B}{m_e c^2} N_e y\, \Lambda(y) \tag{5.3}$$

with $\bar{\nu}_c = \dfrac{3}{4\pi}\dfrac{eB\bar{\gamma}^2}{m_e c}$, $y = \nu/\bar{\nu}_c$ and

$$\Lambda(y) = \frac{1}{y}\int_0^\infty x^2 \exp(-x) F_{syn}\left(\frac{y}{x^2}\right) \mathrm{d}x \tag{5.4}$$

Approximations of the function $\Lambda(y)$ can de done in different regimes:

- A development in Taylor series for small y gives:

$$\Lambda(y) = \frac{8\pi}{9\sqrt{3}}\left(\frac{y}{2}\right)^{-2/3} \qquad \text{for} \quad y \ll 1 \tag{5.5}$$

- Mahadevan et al. (1996) proposed an approximation for intermediates values of y:

$$\Lambda(y) = 2.5651\left(1 + \frac{1.8868}{y^{1/3}} + \frac{0.9977}{y^{2/3}}\right)\exp\left(-1.8899 y\right) \qquad \text{for intermediates } y \tag{5.6}$$

- For great values of y, with a saddle-point method, Saugé (2004) obtains:

$$\Lambda(y) = \frac{2\pi}{\sqrt{6}}\exp\left[-\left(2^{1/3} + 2^{-2/3}\right) y^{1/3}\right] \qquad \text{for} \quad y \gg 1 \tag{5.7}$$

Finally, one obtains the specific intensity of a portion of jet of radius R in the optically thin regime:

$$\boxed{I_\nu^{thin}(\nu) = R j_\nu = \frac{\sqrt{3}}{16\pi}\frac{e^3 B R}{m_e c^2} N_e y\, \Lambda(y)} \tag{5.8}$$

But an emitting medium also creates an absorption to its own radiation. In the case of a pile-up emitting synchrotron radiation, Saugé (2004) showed that the specific intensity of a portion of jet of radius R in the optically thick regime is given by:

$$\boxed{I_\nu^{thick}(\nu) = 2\bar{\gamma} m_e \nu^2} \tag{5.9}$$

And the optical depth is given by:

$$\boxed{\tau_\nu \approx \frac{I_\nu^{thin}(\nu)}{2\bar{\gamma} m_e \nu^2}} \tag{5.10}$$

The transition between the optically thin and the optically thick regime happens at the frequency ν_{abs} defined by $\tau_\nu(\nu_{abs}) = 1$ which is equivalent to:

$$\frac{I_\nu(\nu_{abs}/\bar{\nu}_c)}{\nu_{abs}} = \frac{12 m_e c}{2\pi e^2 R N_e} \tag{5.11}$$

This equation has an analytical solution only when $\nu_{abs} \ll \bar{\nu}$:

$$\nu_{abs} = \left[\frac{2\pi e^2}{27 m_e c} R N_e \bar{\nu}_c^{2/3}\right]^{3/5} \tag{5.12}$$

Synchrotron spectrum from a pile-up distribution

The synchrotron radiation from a pile-up distribution has finally three regimes:

- $\nu < \nu_{abs}$: the medium is optically thick and the spectrum follows a power-law

$$\boxed{F_\nu = \frac{8\pi m_e}{R}\bar{\gamma}\nu^2} \tag{5.13}$$

- $\nu_{abs} < \nu < \bar{\nu}_c$: the medium is optically thin and the spectrum is described by a power-law of index $-1/3$

$$\boxed{F_\nu = \frac{16\pi^2 2^{2/3}}{27}\frac{e^2 N_e \bar{\gamma}}{c}\left(\frac{\nu}{\bar{\nu}_c}\right)^{-1/3}} \tag{5.14}$$

- $\nu > \bar{\nu}$: the emission drops exponentially

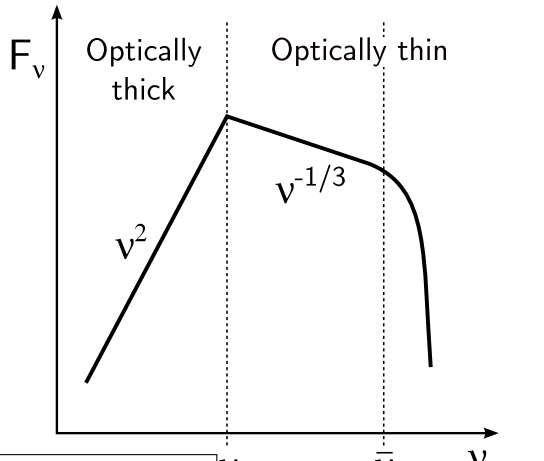

Figure 5.2: Schematic synchrotron spectrum produced by a pile-up

5.1.2 Inverse Compton radiation

Inverse Compton radiation has two components depending on the origin of the incoming soft photon. Synchrotron self-Compton (SSC) refers to the scattering of soft photons originating from the synchrotron emission whereas external Compton (EC) refers to the scattering of soft photons external to the considered medium.

Synchrotron self-Compton

In the case of SSC radiation, approximations can be done as the SSC is co-spatial with the synchrotron. Saugé (2004) considered separately the Thomson and the Klein-Nishina regime. In this section, we consider the dimensionless energy (as introduced before) $\epsilon = h\nu/m_e c^2$

\# The emission photon rate in the Thomson regime is given by the function:

$$\frac{\mathrm{d}n^{Th}(\epsilon_1)}{\mathrm{d}t} = \frac{3}{4}\sigma_{Th}\,\frac{N_e}{2\bar{\gamma}^2}\,\tilde{G}\left(\frac{\epsilon_1}{\bar{\gamma}^2}\right) \tag{5.15}$$

with the function

$$\tilde{G}(x) = \int \frac{\mathrm{d}n_{ph}}{\mathrm{d}\epsilon}\frac{2}{3}\exp\left(-\sqrt{\frac{x}{4\epsilon}}\right)\left[1+\sqrt{\frac{x}{4\epsilon}}+\frac{x}{4\epsilon}\exp\left(\sqrt{\frac{x}{4\epsilon}}\right)E_i\left(\sqrt{\frac{x}{4\epsilon}}\right)\right]\frac{\mathrm{d}\epsilon}{\epsilon} \tag{5.16}$$

and the exponential function

$$E_i(x) = \Gamma(0,x) = \int_x^\infty \frac{\exp(-t)}{t}\,\mathrm{d}t \tag{5.17}$$

As one can see, in equation (5.15), the function $\tilde{G}$ depends only on the ratio $\epsilon_1/\bar{\gamma}^2$. This function can therefore be evaluated and tabulated to decrease the computing time.

The computation of the emission photon rate in the Klein-Nishina regime is a bit more complicated and we need to introduce several functions:

$$g_{th}(\epsilon_1,\epsilon) = \frac{N_e}{4\bar{\gamma}^3}\,\epsilon_1^{1/2}\,\epsilon^{-3/2}\,\exp\left(-\sqrt{\frac{\epsilon_1}{\epsilon\bar{\gamma}^2}}\right) \tag{5.18}$$

$$g_{kn}\,(\epsilon_1,\epsilon) = \frac{3N_e}{16\bar{\gamma}^3}\frac{\ln(2\epsilon_1\epsilon)+1/2}{\epsilon}\epsilon_1\exp(-\epsilon_1/\bar{\gamma}) \tag{5.19}$$

In the Klein-Nishina regime, Saugé (2004) showed that SSC photon rate depends on the position of the energy relative to the absorption energy:

- If $\epsilon_{abs} \ll 1/\epsilon_1$

$$\frac{\mathrm{d}n^{kn}(\epsilon_1)}{\mathrm{d}\epsilon_1\mathrm{d}t} = c\sigma_{Th}\left[\int_{\epsilon_{min}}^{\epsilon_{abs}}\frac{\mathrm{d}n_{ph}}{\mathrm{d}\epsilon}g_{th}(\epsilon_1,\epsilon) + \int_{\epsilon_{abs}}^{1/\epsilon_1}\frac{\mathrm{d}n_{ph}}{\mathrm{d}\epsilon}g_{th}(\epsilon_1,\epsilon) + \int_{1/\epsilon_1}^{\bar{\epsilon}_c}\frac{\mathrm{d}n_{ph}}{\mathrm{d}\epsilon}g_{kn}(\epsilon_1,\epsilon)\right] \tag{5.20}$$

- If $\epsilon_{abs} \gg 1/\epsilon_1$

$$\frac{\mathrm{d}n^{kn}(\epsilon_1)}{\mathrm{d}\epsilon_1\mathrm{d}t} = c\sigma_{Th}\left[\int_{\epsilon_{min}}^{1/\epsilon_1}\frac{\mathrm{d}n_{ph}}{\mathrm{d}\epsilon}g_{th}(\epsilon_1,\epsilon) + \int_{1/^e ps_1}^{\epsilon_{abs}}\frac{\mathrm{d}n_{ph}}{\mathrm{d}\epsilon}g_{kn}(\epsilon_1,\epsilon) + \int_{\epsilon_{abs}}^{\bar{\epsilon}_c}\frac{\mathrm{d}n_{ph}}{\mathrm{d}\epsilon}g_{kn}(\epsilon_1,\epsilon)\right] \tag{5.21}$$

Finally the continuity between the two regimes is done with the following connection:

$$\boxed{\frac{\mathrm{d}n(\epsilon_1)}{\mathrm{d}\epsilon_1\mathrm{d}t} = \frac{\dfrac{\mathrm{d}n^{Th}(\epsilon_1)}{\mathrm{d}\epsilon_1\mathrm{d}t} + x^n\dfrac{\mathrm{d}n^{kn}(\epsilon_1)}{\mathrm{d}\epsilon_1\mathrm{d}t}}{1+x^n} \qquad \text{with} \quad x = \epsilon_1\bar{\epsilon}_c} \tag{5.22}$$

External Compton

The three external sources of photons that I considered in this work are the accretion disc, the dusty torus and the broad line region. These sources, as I will show in section 6 can be modeled as black-body sources (or sum of black-bodies). Therefore, approximations developed in part 3 can be used to compute their Compton scattering by a pile-up distribution of leptons. Given an external source of photons described by its temperature, its solid angle $\mathrm{d}\Omega$ and the direction under which it is seen from the scattering medium, the external Compton emission can be computed. In the Thomson regime, we can use equation (3.23) which allows a fast computation of the emission. In the Klein-Nishina regime however, we must integrate equation (3.19) over the pile-up distribution.

5.2 Absorption and pair creation

When matter and anti-matter interact, they annihilate to create photons. Through this process, pairs in the inner jet can annihilate and create photons but due to the low densities implied here, the process of annihilation is not very important. However, the inverse process, i.e. the creation of new pairs via the interaction of two photons is crucial. It can indeed induce a strong absorption of high-energy photons locally as well as along the path to the observer. Moreover, the local absorption, through the induced pair creation,

is the mechanism at the origin of the inner jet (see section 4). Here, I will detail the calculation of the pair creation process through $\gamma - \gamma$ interaction and then present the different sources of absorption as well as the pair creation engendered.

When dealing with processes implying electrons and positrons, it is interesting to make all calculations with dimensionless energies $\epsilon = h\nu/m_e c^2$. That way, the total energy of two photons of energies $\epsilon_{1,2}$ in their inertial frame is given by:

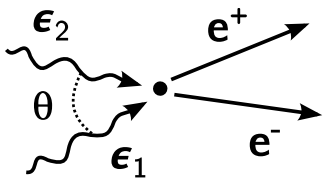

$$\epsilon_{tot}^2 = (\epsilon_1 + \epsilon_2)^2 = 2\epsilon_1\epsilon_2(1-\mu) \tag{5.23}$$

where $\mu = \cos\theta$ is the cosine of the incident angle.

For the interaction to be possible, it is necessary that the total energy is at least the mass energy of one electron and one positron. This condition can be written $\epsilon_{tot} \geq 2$ which gives:

$$\epsilon_1\epsilon_2 \geq \frac{2}{1-\mu} \tag{5.24}$$

The cross section for this interaction is given by (Gould and Schréder (1967)):

$$\sigma(\beta) = \frac{3\sigma_{Th}}{16}(1-\beta^2)\left[(3-\beta^4)\ln\left(\frac{1+\beta}{1-\beta}\right) - 2\beta(2-\beta^2)\right] \tag{5.25}$$

with β the relative velocity in the inertial frame of the two particles:

$$\beta(\epsilon_1, \epsilon_2, \mu) = \sqrt{1 - \frac{2}{\epsilon_1\epsilon_2(1-\mu)}} \tag{5.26}$$

The cross section reaches its maximum σ_{max} in $\beta_{max} = \sqrt{2}/2$. At this point, the relation between incoming photons energies is deduced from equation 5.26:

$$\epsilon_1\epsilon_2 = \frac{4}{1-\mu} \geq 2 \tag{5.27}$$

If we compare this to equation (5.24), we see that the maximal cross section happens just above the pair creation threshold. Therefore, MeV photons will preferentially interact with MeV photons to produce pairs while γ-ray photons at TeV energies will preferentially interact with infrared photons.

5.2.1 Computation of the opacity

For a photon of energy ϵ_1 in a photon field of photon density per solid angle and per dimensionless energy $n_{ph}(\epsilon_2, \Omega)$, its probability to interact with a soft photon on a length $\mathrm{d}l$ is given by:

$$\frac{d}{\mathrm{d}l}\tau_{\gamma\gamma}(\epsilon_1) = \int \frac{1-\mu}{2}\,\sigma(\beta)\,n_{ph}(\epsilon_2, \Omega)\,\mathrm{d}\epsilon_2\,\mathrm{d}\Omega \tag{5.28}$$

If we are able to compute $\mathrm{d}\tau_{\gamma\gamma}/\mathrm{d}l$ in every point of the photon path l_o, then we can integrate along that path to compute the optical depth at any energy:

$$\tau_{\gamma\gamma}(\epsilon_1) = \int_{l_o} \frac{\mathrm{d}\tau_{\gamma\gamma}}{\mathrm{d}l}\mathrm{d}l \tag{5.29}$$

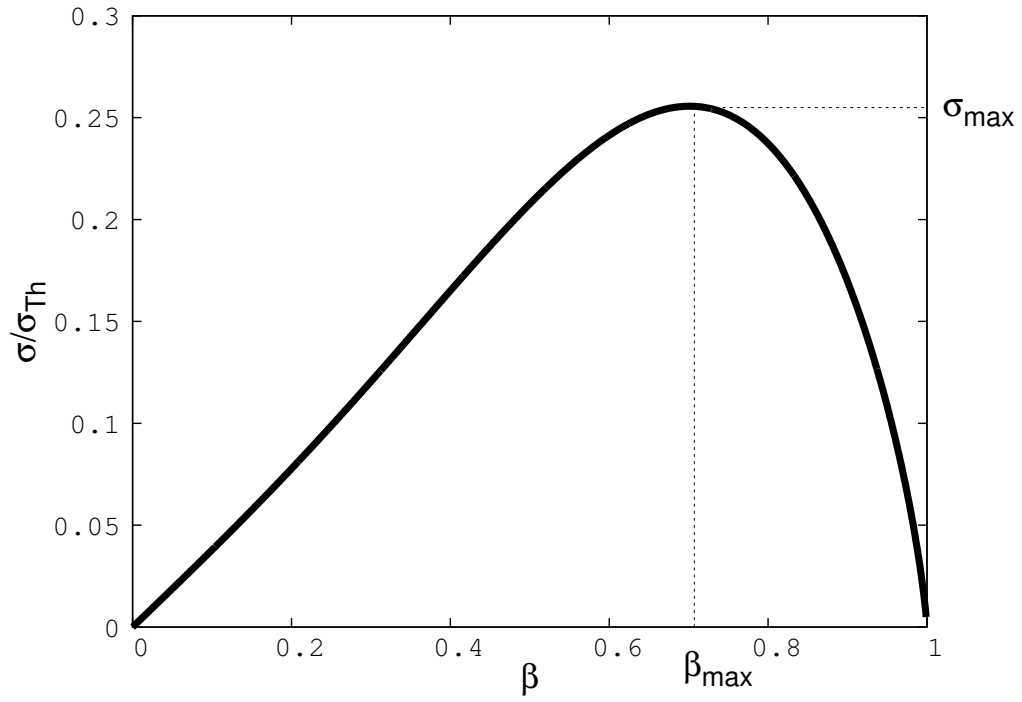

Figure 5.3: $\gamma - \gamma$ cross section as a function of the relative velocity of the two emerging particles in the inertial frame

In the case of an isotropic soft photon field, the integration simplifies and one gets:

$$\frac{\mathrm{d}}{\mathrm{d}l}\tau_{\gamma\gamma}(\epsilon_1) = \frac{3}{4}\sigma_{Th}\int \mathrm{d}\epsilon_2 n_{ph}(\epsilon_2)\mathscr{R}_{pp}(\epsilon_1\epsilon_2) \tag{5.30}$$

with the pair creation rate averaged over angles $\mathscr{R}_{pp}$ given by:

$$\mathscr{R}_{pp}(x) = \frac{4}{3}\frac{1}{\sigma_{Th}}\int_{-1}^{\mu_{crit}} \mathrm{d}\mu \frac{1-\mu}{2}\sigma(\beta) \qquad \text{with} \quad \mu_{crit} = \max\left(-1, 1-\frac{2}{x}\right) \tag{5.31}$$

Here, μ_{crit} corresponds to the condition (5.24) and ensures that β is defined (see equation 5.26). The integral can be computed and one gets:

$$\mathscr{R}_{pp}(x) = \frac{1}{x^2}\psi\left(\frac{1+\sqrt{1-1/x}}{1-\sqrt{1-1/x}}\right)\Theta(x-1) \tag{5.32}$$

with

$$\begin{aligned}\psi(x) = {} & 2\mathrm{Li}_2(-x) - \frac{1}{2}\ln^2(x) - \frac{x}{2} + \frac{1}{2x} - \frac{2}{1+x} + 1 + \frac{\pi^2}{6} \\ & + \left[\frac{2x(2+x)}{(1+x)^2} + \frac{x}{4} - \frac{2x}{1+x} + 2\ln(1+x) - \frac{1}{2} + \frac{1}{4x}\right]\ln(x)\end{aligned} \tag{5.33}$$

The function $\mathscr{R}_{pp}$ is represented here and as one can see, it is very peaked around its maximum with the following values:

$$x_{max} = 3.5563$$
$$\mathscr{R}_{pp}^{max} = 0.2830$$

This allows us to make a dirac approximation of this function, saving a lot of computing time:

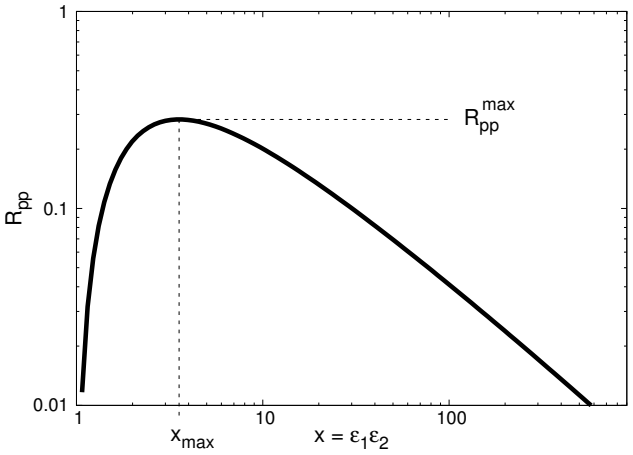

$$\mathscr{R}_{pp} = \mathscr{R}_{pp}^{max}\delta(x - x_{max}) \tag{5.34}$$

With this approximation, the integration simplifies and one gets:

$$\frac{\mathrm{d}}{\mathrm{d}l}\tau_{\gamma\gamma}(\epsilon_1) = \frac{3}{4}\frac{\sigma_{Th}}{\epsilon_1}n_{ph}\left(\frac{x_{max}}{\epsilon_1}\right) \tag{5.35}$$

5.2.2 Origins of the $\gamma - \gamma$ absorption

$\gamma - \gamma$ absorption in AGNs can be very important in the TeV range as the photon density in the infrared band can be very high, with several potential sources:

- The local synchrotron radiation from particles. In this case, high-energy photons are absorbed in the source itself which becomes opaque at the absorbed energies for the observer.
- External radiation from sources in the BH environment such as the accretion disc, the dusty torus, the broad line region or the narrow line region. These sources emit in the infrared and the ultraviolet and can produce a very high photon density for the most luminous sources, making the inner parts of such AGNs totally opaque to very high-energies as we will see in section 6.4.
- External radiation from the host galaxy. Stars from the host galaxy could also provide radiation at energies suitable for the absorption of TeV photons. However, the photon density is too low to be considered and to have an actual effect.
- Photons between the host galaxy of the AGN and the observer which form the Extragalactic Background Light (EBL). It is composed of several sources.
  - First and most famous is the radiation from the cosmic microwave background (CMB).This radiation at $T \approx 2.73K$ (microwaves) is also very diffuse. But, contrary to the host galaxy radiation, it is everywhere between the source and the observer and can therefore constitute a very important integrated absorption. The more distant a source is, the larger the absorption.
  - The second one is the diffuse UV-optical background from 2500Å to 1μm which is the product of the integrated emission from luminous AGNs and stellar nucleosynthesis at $z < 7$.

– The diffuse infrared background from 1μm to 1000μm composed of the emission from stars photospheres and of the thermal emission from dust. Here again, the more distant a source is, the larger the absorption. This sets a maximal distance beyond which we cannot observe very-high energy photons from Earth (e.g $z_{max} \approx 0.1$ for TeV sources - cf figure 5.4).

We will first focus on the absorption occurring outside of the jet. It concerns the EBL and local sources. One needs to compute the local absorption coefficient $\mathrm{d}\tau/\mathrm{d}l$ at every point along the optical path of the high-energy photons and then to integrate along that path to get the optical depth $\tau_{\gamma\gamma}$. For a source at a redshift z_s, one has:

$$\tau_{\gamma\gamma}(\epsilon_0, z_s) = \int_0^{z_s} \frac{\mathrm{d}l}{\mathrm{d}z}\frac{\mathrm{d}}{\mathrm{d}l}\tau_{\gamma\gamma}(\epsilon, z)\,\mathrm{d}z \qquad \text{with} \quad \epsilon_0 = \frac{\epsilon}{1+z} \tag{5.36}$$

where $\mathrm{d}l/\mathrm{d}z$ is an element of the comobile distance. For a flat universe:

$$\frac{\mathrm{d}l}{\mathrm{d}z} = \frac{c}{H_0(1+z)}\left[(1+z)^2(1+z\Omega_m) - z(z+2)\Omega_\Lambda\right]^{-1/2} \tag{5.37}$$

with $\Omega_m = \rho_m/\rho_{crit}$ the normalized mass density of the universe at present time and $\Omega_m = \Lambda/3H_0^2$ the cosmological constant.

Then, radiative transfer equations show that the specific intensity reaching the observer is given by:

$$I_{obs}(\epsilon_0) = I_{jet}(\epsilon)\mathscr{P}_{esc}(\epsilon_0) \tag{5.38}$$

with

$$\mathscr{P}_{esc}(\epsilon_0) = \exp(-\tau_{\gamma\gamma}(\epsilon_0)) \tag{5.39}$$

the probability for a photon to reach the observer.

The computation of $\mathscr{P}_{esc}$ requires the knowledge of the photon density of the soft photon sources. For local sources (accretion disc, BLR, torus), the photon density obviously depends on the modeling. Its computation will be presented in section 6.4.

Concerning the EBL, the complete photon density is a sum of different sources and its computation can be quite complicated. Fortunately, a lot of work has been done in this respect and the EBL is fairly well known. Franceschini et al. (2008) presents a model taking into account the evolution of the CMB with the redshift as well as the other components of the EBL. We will then use tables from Franceschini et al. (2008) to compute the absorption from the EBL (see figure 5.4).

5.2.3 Absorption in the jet and pair creation

The absorption within the jet is particular as it is at the origin of the jet by pair creation, an essential mechanism of our model. High-energy photons emitted by the jet can interact with synchrotron photons as well as photons from external photon sources to generate pairs. If we use the result from equation (5.35) and if we assume that the absorption coefficient is constant at a given altitude Z in the jet of radius $R(Z)$, the opacity is easily calculated:

$$\tau_{jet} = \tau_{jet}^{sync} + \tau_{jet}^{ext} \tag{5.40}$$

$$= R(Z)\left(\frac{\mathrm{d}\tau_{jet}^{sync}}{\mathrm{d}l}(\epsilon_1, Z) + \frac{\mathrm{d}\tau_{jet}^{ext}}{\mathrm{d}l}(\epsilon_1, Z)\right) \tag{5.41}$$

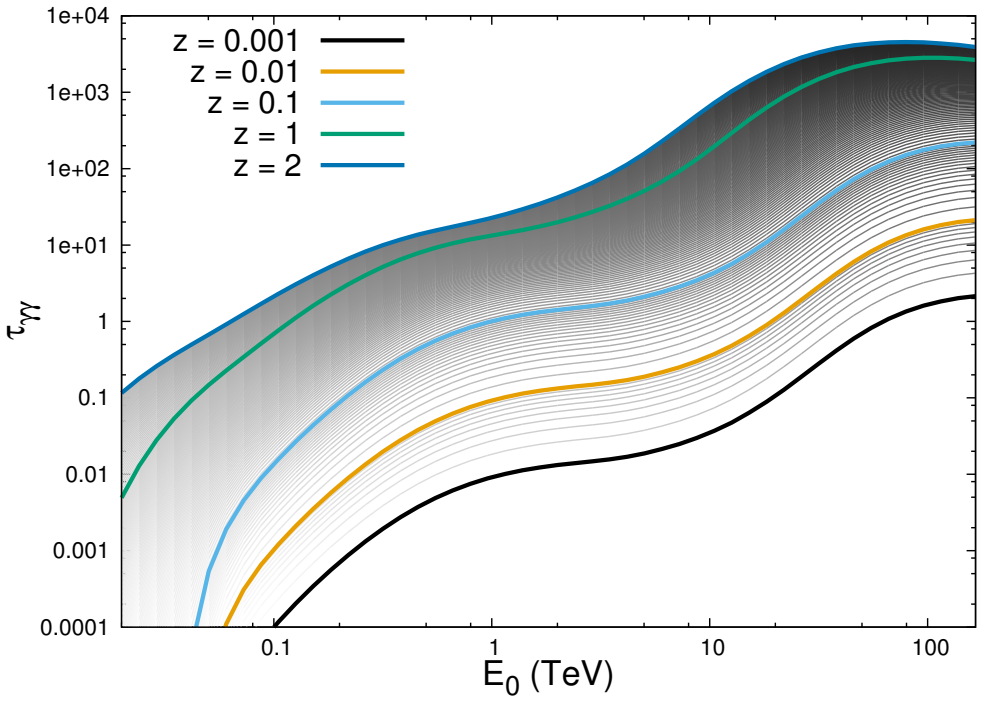

Figure 5.4: Optical depth $\tau_{\gamma\gamma}$ of the EBL as a function of the observed photon energy E_0 and of the redshift z. These results are extracted from Franceschini et al. (2008)

In the case of external sources, the escape probably is given by equation (5.39). In the case of synchrotron radiation however, as the production of high-energy photon is co-spatial with the synchrotron radiation, radiative transfer equations show that the escape probability is:

$$\mathscr{P}_{esc}^{sync} = \frac{1 - \exp(-\tau_{jet}^{sync})}{\tau_{jet}^{sync}} \tag{5.42}$$

Marcowith et al. (1995) showed that once high-energy photons have left the jet, they can still interact with the synchrotron radiation which is not confined to the jet on a characteristic distance $R(Z)$. This introduces an additional term $\exp\left(-\tau_{jet}^{sync}\right)$ to the absorption. The total escape probability of photons produced in the jet is then given by:

$$\mathscr{P}_{esc}^{jet} = \left(\frac{1 - \exp(-\tau_{jet}^{sync})}{\tau_{jet}^{sync}}\right) \exp\left(-\tau_{jet}^{sync}\right) \exp\left(-\tau_{jet}^{ext}\right) \tag{5.43}$$

From there, one can compute the probability that a high-energy photon has to be absorbed:

$$\mathscr{P}_{abs} = 1 - \mathscr{P}_{esc} \tag{5.44}$$

When a high-energy photon of dimensionless energy ϵ_1 interacts with a low energy photon of dimensionless energy $\epsilon_2 \approx 2/\epsilon_1 \ll \epsilon_1$, it creates two particles (one positron and one electron) of dimensionless energy $\gamma \approx \epsilon_1/2$ each. If we know the production rate $\dfrac{\mathrm{d}n(\epsilon_1)}{\mathrm{d}\epsilon_1 \mathrm{d}t}$ of high-energy photons (from SSC and EC radiation), one can compute the pair production rate:

$$\begin{aligned}\frac{\mathrm{d}\dot{n}_{prod}}{\mathrm{d}\gamma}(\gamma) &= 2\left.\frac{\mathrm{d}\dot{n}_{abs}}{\mathrm{d}\gamma}\right|_{\epsilon_1=2\gamma} \\ &= 2\left.\frac{\mathrm{d}n(\epsilon_1)}{\mathrm{d}\epsilon_1\mathrm{d}t}\right|_{\epsilon_1=2\gamma}\mathscr{P}_{abs}(2\gamma)\end{aligned} \tag{5.45}$$

To obtain the total density of pair created, one needs to integrate over γ:

$$\begin{aligned}\dot{n}_{prod} &= \int \mathrm{d}\gamma\frac{\mathrm{d}\dot{n}_{prod}}{\mathrm{d}\gamma} \\ &= 2\int \mathrm{d}\epsilon_1\frac{\mathrm{d}n(\epsilon_1)}{\mathrm{d}\epsilon_1\mathrm{d}t}\left[1-\left(\frac{1-\exp(-\tau_{jet}^{sync})}{\tau_{jet}^{sync}}\right)\exp\left(-\tau_{jet}^{sync}\right)\exp\left(-\tau_{jet}^{ext}\right)\right]\end{aligned} \tag{5.46}$$

5.3 Evolution of the particle distribution

The pile-up distribution (see equation 4.8) of the particles is determined by two parameters: the particle density N_e and the particle characteristic energy $\bar{\gamma}m_ec^2$. These two parameters, instead to be free parameters of the model, are computed depending on the physical conditions in the jet.

5.3.1 Particles mean energy

Particles being submitted to two opposite phenomena, the heating from the turbulence and the cooling from the emission, their energy can be computed as the balance between these two processes. Then, the energy equilibrium for each particle in the comoving frame writes:

$$\frac{\partial}{\partial t}\left(\gamma m_ec^2\right) = \delta_b\left(Q_{acc}m_ec^2 - P_{cool}\right) \tag{5.47}$$

with $Q_{acc}m_ec^2$ the power per particle extracted from the turbulence and P_{cool} the radiative cooling power.

Then one needs to evaluate P_{cool} from the two main radiative processes, the synchrotron and the inverse Compton.

Synchrotron emission cooling: For an isotropic magnetic field, the power emitted by synchrotron in the Thomson regime can be written (from equation (2.19)):

$$P_{cool}^{syn} = \frac{4}{3}c\sigma_{Th}U_B\beta^2\gamma^2 \tag{5.48}$$

with $U_B = \dfrac{B^2}{8\pi}$ for synchrotron radiation.

Inverse Compton emission cooling: As we saw in section 2.3, the inverse Compton cross section quickly drops in the Klein-Nishina regime. Therefore, the cooling of the particle is much more efficient in the Thomson regime and radiation in the KN regime can be neglected concerning the cooling.

Inverse Compton emission has two origins depending on the source of the soft photons: the synchrotron self-Compton and the external Compton.

- As the synchrotron emission is isotropic and co-spatial with the synchrotron self-Compton, one can use the equation (2.47) to deduce the SSC cooling:

$$P_{cool}^{ssc} = \frac{4}{3} c \sigma_{Th} U_{syn} \beta^2 \gamma^2 \tag{5.49}$$

with the effective synchrotron photon energy density in the Thomson regime:

$$U_{syn} = \frac{4\pi}{c} \int_0^{\nu_{kn}} I_\nu^{sync}(\nu)\, \mathrm{d}\nu\, \mathrm{d}\Omega \qquad \text{with} \quad \nu_{kn} = \frac{m_e c^2}{h \gamma_0} \tag{5.50}$$

- On the contrary, the external soft photon field is not isotropic, even in the plasma rest frame. Therefore, one can not use equation 2.47 to compute the emitted power but needs to integrate the emitted spectrum in the plasma rest frame:

$$P_{EC} = \iiint \frac{\mathrm{d}N'}{\mathrm{d}t' \mathrm{d}\epsilon_1' \mathrm{d}\Omega_1'} \mathrm{d}\epsilon_1' \mathrm{d}\Omega_1' \frac{\mathrm{d}\Omega_0'}{4\pi} \tag{5.51}$$

This computation would be very time consuming. To avoid it, I made the approximation that the average external emission was equal to the emission in the direction perpendicular with the jet axis. Then one has:

$$\begin{aligned} P_{EC} \approx & P_{EC}|_{\mu_1'=0} \\ = & \int \frac{\mathrm{d}N'}{\mathrm{d}t' \mathrm{d}\epsilon_1'}\Big|_{\mu_1'=0} \mathrm{d}\epsilon_1' \end{aligned} \tag{5.52}$$

One can write an effective photon density for the external Compton emission:

$$U_{ext} = \frac{3}{4\, c\, \sigma_{Th} \beta^2 \gamma^2} P_{EC} \tag{5.53}$$

Total emission cooling is then given by:

$$P_{cool}^{tot} = \frac{4}{3} c \sigma_{Th} U_{tot} \beta^2 \gamma^2 \tag{5.54}$$

with U_{tot} the total photon energy density:

$$U_{tot} = U_B + U_{sync} + U_{ext} \tag{5.55}$$

Finally, by considering the characteristic energy of the pile-up distribution as the parameter for the equilibrium, we obtain:

$$\boxed{\frac{\partial}{\partial t} \bar{\gamma}(Z,t) = \delta_b(Z) \left[Q_{acc}(Z) - \frac{4}{3} \frac{\sigma_T}{m_e c} \left(U_B + U_{sync}(\bar{\gamma}) + U_{ext}(\bar{\gamma}) \right) \left(\bar{\gamma}^2 - 1 \right) \right]} \tag{5.56}$$

5.3.2 Particles density

The second parameter of the pile-up distribution is the particle density. As the particles move forward in the jet with a bulk speed $\beta_b c$, one can apply flux conservation to compute the evolution of the density along the jet, taking into account the pair production.

For a particle given by its position quadri-vector (t, r, ϕ, z) and its velocity quadri-vector $u^i = \Gamma_b(1, 0, 0, \beta_b)$, the quadri-vector flux-density is defined as $n^i = n'_e u^i$ with n'_e the particle density in the plasma rest frame. By generalizing the standard continuity equation, Boutelier (2009) showed that for a stationary jet structure, one gets:

$$\boxed{D_{\beta_b}\Phi_e = \frac{\partial}{\partial t}\Phi_e + c\beta_b \frac{\partial}{\partial z}\Phi_e = \beta_b S \dot{n}'_{prod}} \tag{5.57}$$

with $S(Z) = \pi R^2(Z)$ the section of the jet, $\dot{n}'_{prod}$ the pair production rate and $\Phi_e = n'_e \beta_b \Gamma_b S$ the particle flux. As one can see, without pair creation along the jet, the flux is conserved.

5.4 Parametrization

In order to compute the evolution of the particle distribution along the jet as explained in the previous section, one needs to know in addition to the local photon field three physical parameters for every altitude in the jet: the jet radius $R(Z)$, the magnetic field $B(Z)$ and the particle acceleration term $Q_{acc}(Z)$. To simplify, they are parameterized by power-laws. They are parameterized so that the initial conditions are given at any distance Z_0 in the jet.

5.4.1 Jet geometry

In the model, we assume that the jet structure is parabolic and stationary. Its radius evolution is given by:

$$\boxed{R(z) = R_0 \left[\frac{Z}{Z_0} + \left(\frac{R_i}{R_0} \right)^{1/\omega} \right]^{\omega}} \tag{5.58}$$

This law describes a parabola with a radius R_i at $Z = 0$ which is the smallest radius of the jet[1] and a radius R_0 at a distance Z_0 from the black-hole. The parabola is displaced by the constant R_i to avoid divergence issues when Z tends to 0. The index w defines the jet opening. One must have $w < 1$ to keep the jet collimated.

5.4.2 Magnetic field

The magnetic field is supposed to be homogeneous and isotropic at every altitude Z in the plasma rest frame. Its evolution is described by:

$$\boxed{B(z) = B_0 \left(\frac{R(Z)}{R_0} \right)^{-\lambda}} \quad \text{with} \quad 1 < \lambda < 2 \tag{5.59}$$

The index λ gives the structure of the magnetic field and is confined by two extrems:

[1] R_i is set at the gravitational radius $R_g = GM_{bh}/c^2$

- $\lambda = 1$ corresponds to a pure toroidal magnetic field as the conservation of the magnetic field circulation gives $B \sim 1/R$
- $\lambda = 2$ corresponds to a pure poloidal magnetic field as the conservation of the magnetic flux in this case gives $B \sim 1/R^2$

5.4.3 Particle acceleration

The particle acceleration is a central part of the two-flow model as it is assumed that the particles are continuously heated by the outer MHD structure (which act as an infinite reservoir here), opposing radiation losses. Due to the lack of a precise expression for the acceleration rate per particle, Q_{acc}, we use this expression:

$$\boxed{Q_{acc}(z) = Q_0 \left[\frac{Z}{Z_0} + \left(\frac{R_i}{R_0} \right)^{1/\omega} \right]^{-\zeta} \exp\left(-\frac{Z}{Z_c} \right)} \tag{5.60}$$

The particle acceleration decreases as a power-law of index ζ until an altitude $Z = Z_c$ where it drops exponentially. This physically corresponds to the end of the turbulence in the jet.

Because of the exponential cut-off, the index ζ could take any value and the energy would still be finite. However, as Z_c could be as large as desired (even as large as the jet), it would be physically more satisfactory with $\zeta > 1$. This way, even an integration to infinity of Q_{acc} would converge.

Similarly to the radius (equation (5.58)), the constant R_i/R_0 avoids numerical issues when Z tends to 0.

5.5 *[En résumé]* Evolution des conditions physiques dans le jet

Dans ce chapitre je présente le détail du modèle numérique et l'évolution des conditions physiques dans le jet. Ici les conditions physiques (telles que le champ magnétique B, la densité de particules n ou le rayon du jet R) dépendent de l'altitude dans le jet, Z (voir figure 5.1).

Le jet émet alors de façon continue de sa base à son extrémité va les processus synchrotron et Compton inverse.

Les conditions physiques sont calculées de manière cohérente avec cette émission. En effet, l'énergie caractéristique des particules, donnée par le paramètre de la distribution en *pile-up* $\bar{\gamma}$, est calculée comme résultant de l'équilibre entre chauffage (par le terme de chauffage turbulent $Q(Z)$ et refroidissement via les différents processus d'émission (équation (5.56)).

Le facteur de Lorentz (et donc la vitesse) du jet dépend elle aussi de l'altitude et est le résultat de l'effet fusée Compton (voir chapitre suivant), entièrement déterminé par les sources de photons externes.

La densité de photon basse énergie peut être relativement importante dans les NAG. Il y a plusieurs sources potentielles pour ces photons: l'émission synchrotron locale, l'émission des sources externes (chapitre 6), l'émission de la galaxie hôte et le fond diffus extragalactique (figure 5.4). Ces photons *mous* peuvent interagir avec les photons de hautes énergies via l'interaction $\gamma - \gamma$. En dehors du jet, ceci créé une certaine opacité, empêchant les radiations de plus hautes énergies de sortir du système. Dans le jet, cette interaction prend un intérêt supplémentaire car elle est responsable de la création de nouvelles paires qui, accélérées par la turbulence, peuvent à nouveau émettre. La densité de particule $n(Z)$ dans le jet est déterminée par la conservation du flux de particules et par la création de paires.

Les paramètres physiques imposés suivent des lois de puissances donnés par les équations (5.58), (5.60) et (5.59). A partir de conditions initiales à la base du jet, on peut donc déterminer l'ensemble des conditions physiques partout dans le jet ainsi que l'émission observée, et ce de façon entièrement cohérente.

Chapter 6

External sources modeling

Contents

The modeling of external sources of soft photons is relevant for two reasons:

- To compute the high-energy emission from the jet through inverse Compton scattering
- To compute the absorption from these sources as explained in section 5.2

Several external sources of soft photons are present in AGNs. The main one is of course the accretion disc. If not always detected, it is a requirement to produce jets and huge luminosities as it is the main source of power (through accretion). Other possible sources of external photons include the dusty torus (DT), the broad line region (BLR), the narrow line region (NLR), the host galaxy and the cosmological background (CMB).

One can discriminate between sources and determine whether they are worth modeling or not. As the inverse Compton emitted power is proportional to the energy density (equation 2.47) of the photon source and the absorption is proportional to the photon density (equation 5.28), we need to evaluate these two quantities for each source:

From these rapid evaluations, one can conclude that the only sources of external soft photons worth considering for the computation of the inverse Compton here are the accretion disc, the dusty torus and the broad line region as the photon energy density of other sources is at least 6 orders of magnitude lower.

The absorption coefficient is proportional to the soft photon density n_{ph} but one must be careful that $\tau_{\gamma\gamma}$ is the integrated optical depth on the path followed by the photons. Local (in the host galaxy) sources act on lengths of the same order. However, the photon density of the NLR and of the host galaxy are much lower than the ones from the disc, the DT or the BLR. Therefore, these two sources can be neglected for the computation of the absorption. The CMB photon density is also very weak but it is present everywhere

Source	$< h\nu >$ (eV)	U_{ph} (eV.cm^{-3})	$n_{ph}(cm^{-3})$
Disc ($< T > \approx 10^4 K$)	1	10^{12}	10^{12}
DT ($< T > \approx 10^3 K$)	0.1	$>10^{10}$	$> 10^{11}$
BLR ($< T > \approx 10^5 K$)	10	$> 10^{10}$	$> 10^9$
NLR ($< T > \approx 10^5 K$)	10	10^4	10^3
Host Galaxy ($< T > \approx 5 \times 10^3 K$)	0.5	10^3	2×10^3
CMB ($< T > \approx 3K$)	5×10^{-4}	0.1	2×10^2

Table 6.1: Evaluation of the external sources photon energy density U_{ph} and photon density n_{ph} in the reference frame

between the source and the observer and one integrated on the photon path, its absorption is important for great redshifts - as discussed in section 5.2.

Then we limit the local modeling to the three main sources (accretion disc, BLR and torus) and obtain the final picture given figure 6.1.

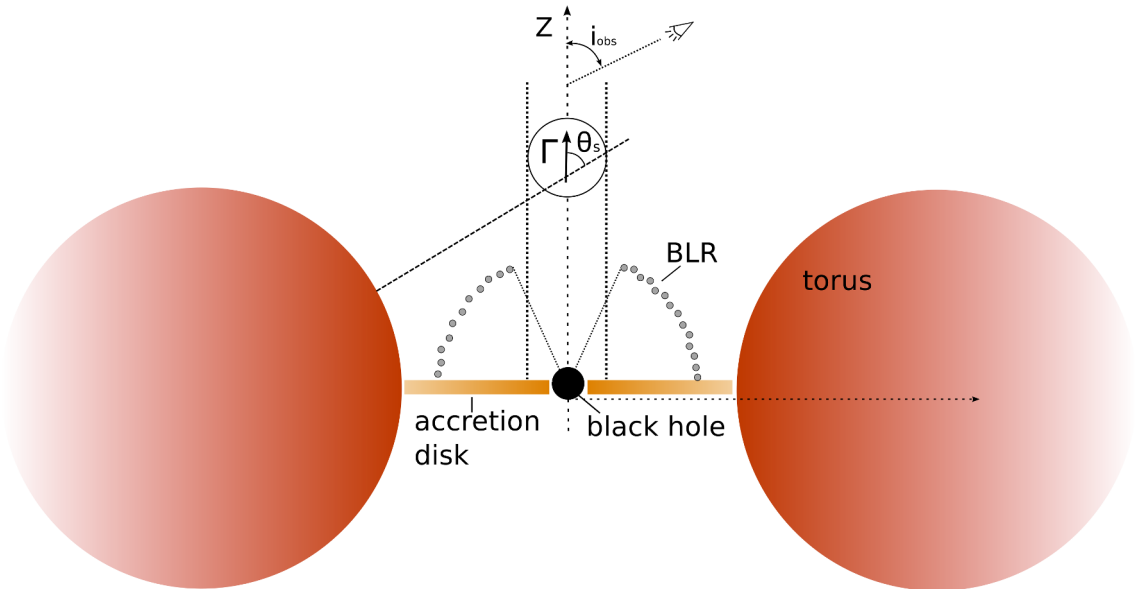

Figure 6.1: The big picture: sketch edge on of the global model geometry (not to scale) with the accretion disk, the dusty torus and the BLR. i_{obs} is the observer viewing angle and θ_s is the angle between the incoming radiation from a source and the jet axis.

The anisotropy of the photon sources will be taken into account in the numerical scheme by slicing the different sources into a set of small independent sources modeled as grey-bodies in radiative equilibrium, i.e. with a Planck spectrum but with a possible smaller emissivity. This discretization is done in three dimensions. Even for an axisymmetric source, an azimuthal discretization is still required to compute accurately the Compton external emission towards the observer line of sight. Indeed, since the object is seen under a certain angle, the axisymmetry is always broken with respect to the line of sight.

Each slice of the discretization is then described by 4 numbers:

- $\mu_s = \cos\theta_s$ with θ_s the angle between the incoming light wave and the jet axis (see figure 6.1)

- $\mathrm{d}\Omega$ the solid angle under which it is seen from the altitude Z
- its temperature T
- its emissivity ε

The slices emission characterized by these numbers is given by its specific intensity I_ν $(erg.s^{-1}.cm^{-2}.sr^{-1}.Hz^{-1})$ (see equation 2.10)

6.1 The accretion disc

Theory of accretion disc finds its origin in the understanding of the formation of the Solar system but had a great confirmation with the discovery of AGNs that can be fueled only by the colossal power allowed by accretion onto a compact object. Shakura and Sunyaev (1976) developed a model of accretion disc to explain the emission from X-ray binaries. This model became the standard accretion disc (SAD). Since then, other theoretical models (with poetics names) of accretion discs have been developed to describe more accurately the accretion disc (e.g. ADAF, ADIOS, JED, MAD...).

The geometry of the disc is described by its internal radius R_{in} and its external radius R_{out}. It is then sliced along its radius r (with a logarithmic discretization) and its azimuthal angle φ (with a linear discretization).Therefore, each slice has a surface $\mathrm{d}S = \mathrm{d}\varphi\left(r\mathrm{d}r + \frac{\mathrm{d}r^2}{2}\right)$. Seen from the axis at an altitude z, each slice is seen under an angle

$$\theta_s = \arccos\left(\frac{r}{\sqrt{r^2+z^2}}\right) \tag{6.1}$$

and a solid angle

$$\mathrm{d}\Omega = \mathrm{d}S\frac{z}{(r^2+z^2)^{3/2}} \tag{6.2}$$

The temperature and specific intensity of the disc highly depend on the type of disc we want to model. Here for the sake of simplicity[1], the disc is a standard accretion as described by Shakura and Sunyaev (1976). Then every part of the disc is a black-body ($\varepsilon = 1$) with $I_\nu = B_\nu$ described by equation (3.1) with a temperature given by:

$$T_{disc}(r) = \left[\frac{3GM\dot{M}}{8\pi\sigma}\frac{1}{r^3}\left(1-\sqrt{\frac{3R_S}{r}}\right)\right]^{1/4} \tag{6.3}$$

with G the gravitational constant, σ the Stefan-Boltzmann constant, M the black-hole mass, $\dot{M}$ its accretion rate, r the radius and R_S the Schwarzschild radius.

With this description, the luminosity of one face of the disc for $R_{in} = 3R_S$ and $R_{out} \gg R_{in}$ can be computed thanks to Stefan-Boltzmann law[2]:

$$L_{disc} = \int_{R_{in}}^{R_{out}} \sigma T_{disc}^4(r)\, 2\pi r\, \mathrm{d}r \approx \frac{\dot{M}c}{24} \tag{6.4}$$

[1]Note that the code is very flexible on this regard and another temperature description of the disc could be easily implemented

[2]here we find again the efficiency for a Schwarzschild black-hole under Newtonian approximation of 1/12 in total (both faces)

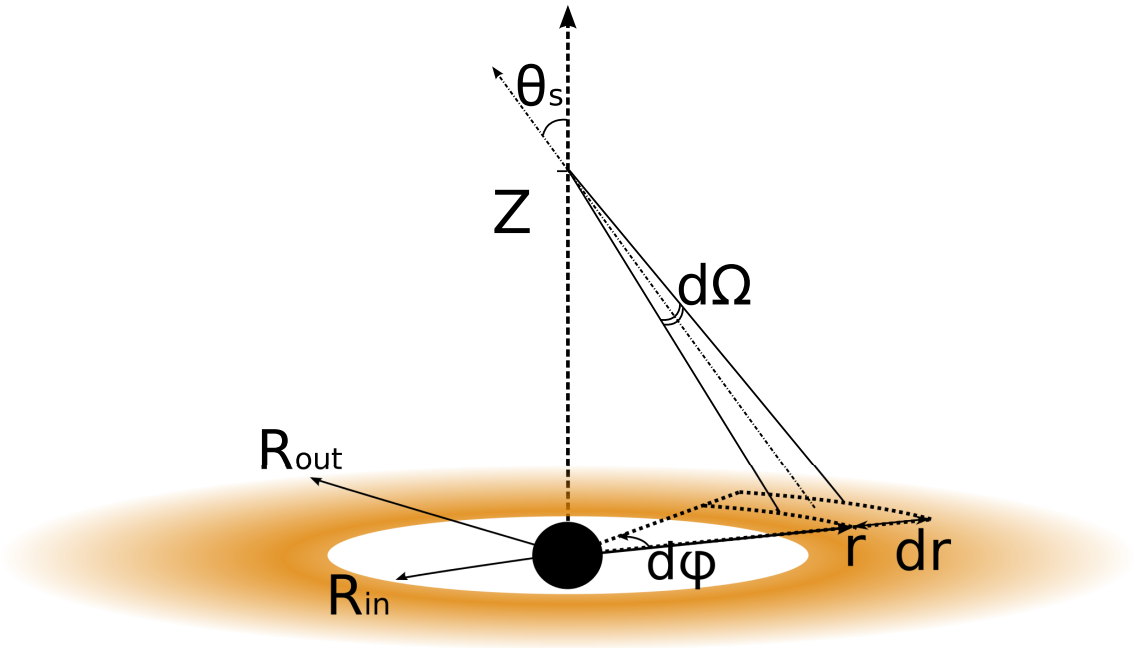

Figure 6.2: Sketch of the disc radial and azimuthal splitting. A slice at $(r, \varphi) \in ([R_{in}, R_{out}], [0, 2\pi])$ is seen under a solid angle $d\Omega$ from the jet at an altitude z.

6.2 The dusty torus

The idea of a dusty torus finds its origin in the dichotomy between Seyfert 1 and Seyfert 2 galaxies. The observational differences between these two types of AGNs lies in emission lines. While strong narrow forbidden lines are common in both types of Seyfert, broad optical permitted lines are not directly observed in Seyfert 2 galaxies. They are however observed in the polarized spectrum. A generally accepted explanation is that the polarized emission corresponds to the emission of the central object scattered at larger scales and that it is not seen in the un-polarized spectrum because of an obscuring medium along the line of sight. However, a simple sphere along the line of sight (figure 6.3a) would intercept only the light coming from a precise direction and the average polarization from all scattered light would be null. Therefore, the simplest geometry that one can assume to explain the observations is an obscuring torus (figure 6.3b) intercepting all light at great angles.

More recent observations have confirmed (and even imaged) the presence of an axisymmetric absorber at large scale (from parsec to hundreds of parsecs) even if its structure is far less simple than first imagined. Our intent is not to give a very accurate modeling of the external sources but to reproduce their general properties. Therefore, as a first approach, I have modeled the dusty torus as a simple optically thick geometrical torus.

In the same way as the disk, the torus is sliced in different parts that will radiate as grey-bodies. Slices follow a linear discretization and are located with their coordinates (θ_t, φ) at the surface of the torus (see figure 6.4). Each slice of the torus is assumed to be in radiative equilibrium with the luminosity received from the accretion disk.

To simplify, we make the assumption that all the energy from the disk comes from its inner parts and that $R_{in} \ll (D_t - R_t)$ so that the source of energy is point-like seen from the torus. The power

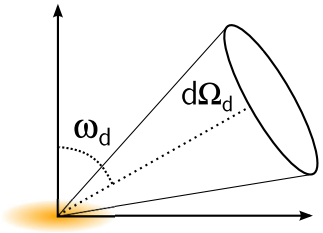

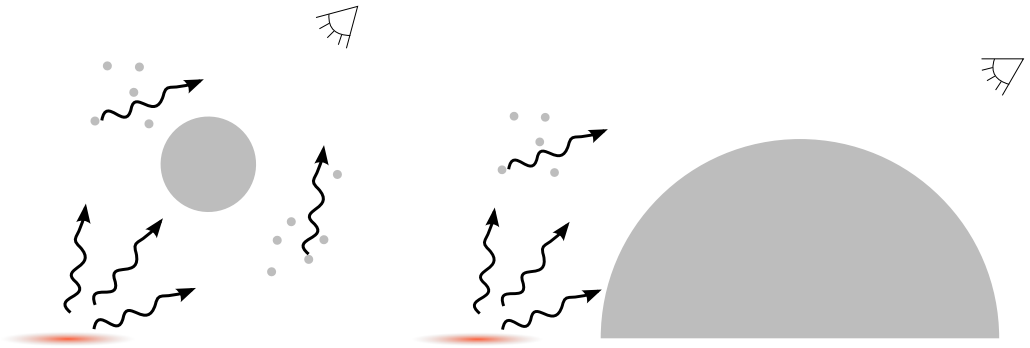

(a) Scattered light around an obscuring sphere

(b) Scattered light on top of an obscuring torus

Figure 6.3: Comparison between two obscuring geometries

emitted from the disc in a cone $\mathrm{d}\Omega_d$ is given by $I_d \,\mathrm{d}\Omega_d \, S_d \, \cos\omega_d$.

At radiative equilibrium, the received luminosity by a slice of the torus surface $\mathrm{d}S_t(\theta_t)$ equals the emitted luminosity so that:

$$I_d \,\mathrm{d}S_d \,\mathrm{d}\Omega_d \, \cos\omega_d = \varepsilon(\theta)\sigma T^4_{torus}(\theta_t)\mathrm{d}S_t(\theta_t) \tag{6.5}$$

From this equality and with the parameter $a = \dfrac{R_t}{D_t} \leq 1$, one can obtain the surface brightness density of the torus:

$$\begin{aligned} P_{S_t} &= \sigma T^4_{torus}(\theta_t)\, \varepsilon_t(\theta_t) \\ &= \frac{L_{disc}}{\pi D_t^2} \, \frac{(\cos\theta_t - a) a \sin\theta_t}{(1 - 2a\cos\theta_t + a^2)^2} \\ &= \frac{L_{disc}}{\pi D_t^2} \, \zeta(a,\theta) \end{aligned} \tag{6.6}$$

From there, one can either fix a constant temperature or a constant emissivity and compute the other parameter in function of θ_t. Figure 6.5 displays a polar representation of $\zeta(a,\theta)$ which gives the angular repartition of the brightness density on the surface of the torus (equation 6.6). $\zeta(a,\theta) = 0$ for $\theta_t = 0$ because here the torus does not receive any radiation from the disc which is seen edge on ($\cos\omega_d$ term in (6.5)). $\zeta(a,\theta)$ is also null for $\cos\theta \leq a$, as this angle corresponds to a tangent radiation from the disc, and therefore a non-illumination.

6.3 The broad line region

The broad line region (BLR) is the name given to the region responsible for the broad emission lines observed in the optical/UV and for the absorption observed in the UV/X-ray. The nature itself of the BLR, as well as its spatial description are still unknown, mainly because this region is not spatially resolved by observations. However, the BLR emission probably corresponds to a reprocessing of the disc emission corresponding to a temperature $T \approx 10^4 K$ (Blandford et al. (1990)) which corresponds to the photoionization equilibrium. It comes from correlated variability between the emission lines and the

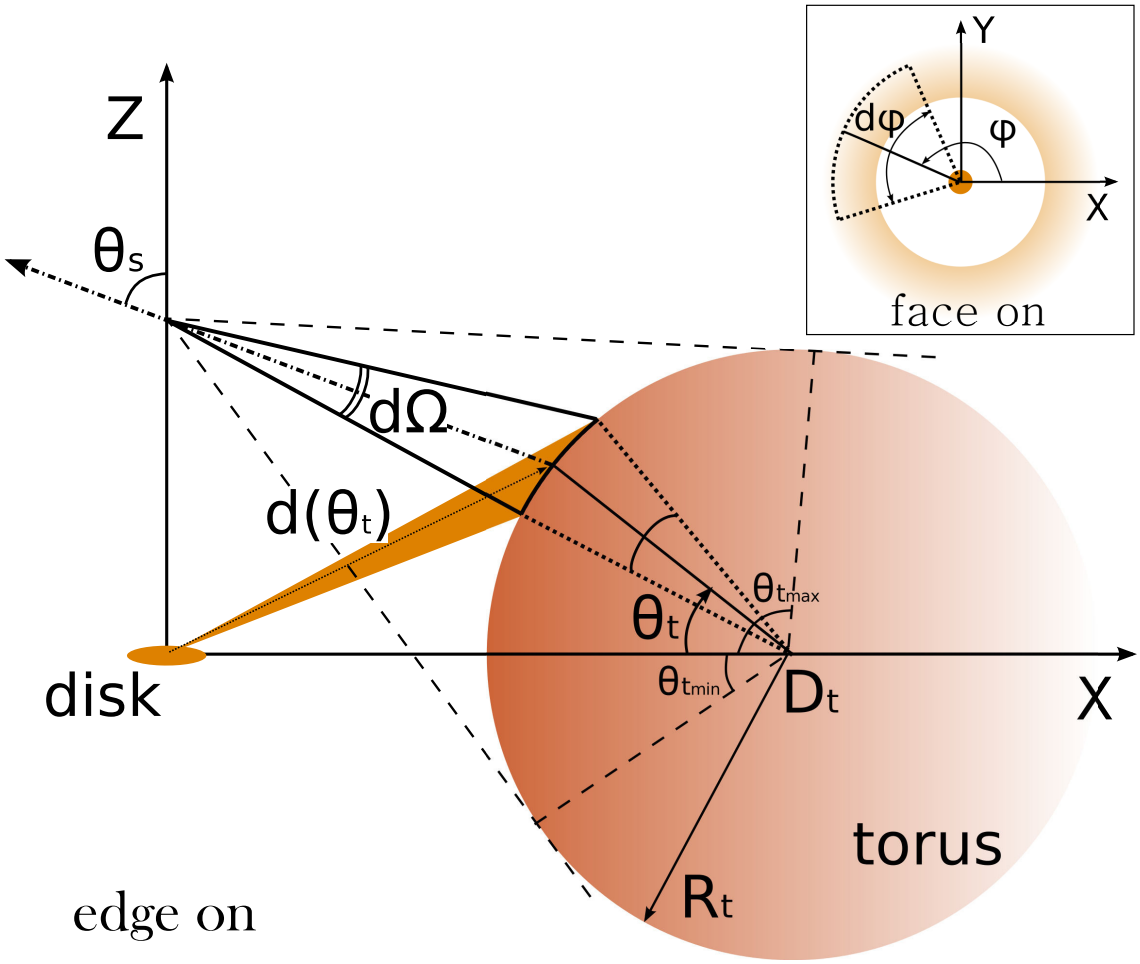

Figure 6.4: The dusty torus seen from an altitude z in the jet under a solid angle $d\Omega$. The torus is sliced according to $\theta_t \in [\theta_{t_{min}}, \theta_{t_{max}}]$ and $\varphi \in [0, 2\pi]$. Each slice is illuminated by the disk and is in radiative equilibrium. It emits as a grey-body with a temperature $T_t(\theta_t, \varphi)$ and an emissivity $\varepsilon(\theta_t, \varphi)$.

continuum on short time scales coupled with light-travel time arguments that the BLR must be fairly small. The size of the BLR inferred by reverberation mapping in Seyfert galaxies extend from 10^3 to $10^4 R_g$ ($\leq$ 1 parsec) (Peterson (2006)).

The broad line here is modeled by an isotropic, optically and geometrically thin shell of clouds situated at a distance R_{blr} from the central black-hole. Like other sources, it is sliced into different parts in order to make the numerical integration. I chose a linear discretization along $\omega \in [\omega_{max}, \omega_{min}]$ and along $\varphi \in [0 : 2\pi]$.

Observed BLR display a complex emission with a continuum and broad absorption lines but Tavecchio and Ghisellini (2008) showed that modeling the spectrum of the BLR with a grey-body spectrum at $T = 10^5 K$ provides un good approximation to the resulting inverse Compton spectrum. We followed this idea using a temperature of $T_{blr} = 10^5 K$ and an overall luminosity being a fraction α_{blr} of the disk luminosity.

Here we can assume two different hypothesis: either the BLR is locally in radiative equilibrium (as it was done for the torus) and, as different parts, at different ω, do not receive the same amount of energy from the disc, it is anisotropic. Or, we assume it is completely isotropic, meaning that the emissivity does not depend on ω.

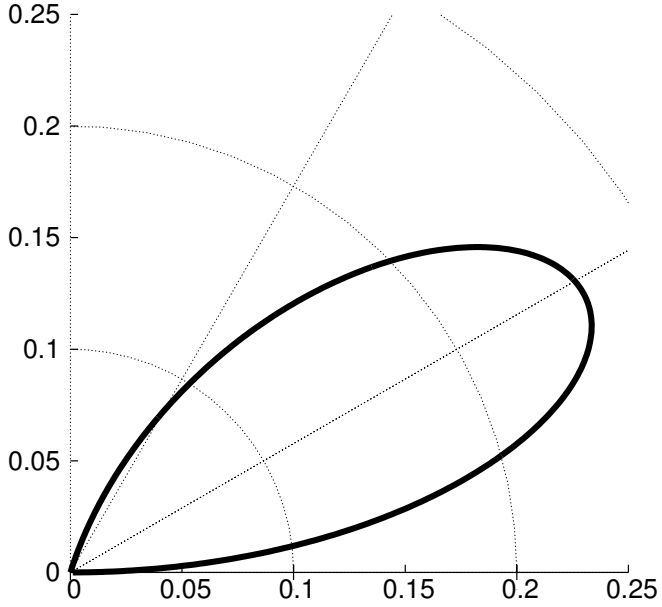

Figure 6.5: Polar representation of the function $\zeta(a,\theta)$ for $a = 0.3$. The surface brightness density is proportional to $\zeta(a,\theta)$ and therefore is null at $\theta = 0$ and $\cos\theta = a$

Isotropic shell of clouds

If we suppose the BLR isotropic (ε constant), then:

$$\begin{aligned} L_{blr} &= \alpha_{blr} L_d \\ &= \int_{blr} \varepsilon_{blr} \sigma T_{blr}^4 \mathrm{d}S \\ &= \varepsilon_{blr} \sigma T_{blr}^4 2\pi R_{blr}^2 (\cos\omega_{max} - \cos\omega_{min}) \end{aligned} \tag{6.7}$$

From which we deduce the emissivity of the BLR:

$$\varepsilon = \frac{\alpha_{blr} L_d}{\sigma T_{blr}^4 2\pi R_{blr}^2 (\cos\omega_{max} - \cos\omega_{min})} \tag{6.8}$$

Note that equation 6.7 implies $R_{blr} \propto L_d^{1/2}$, which is coherent with observations showing that $R_{blr} \propto L_{obs}^{\alpha}$ with $0.55 \lesssim \alpha \lesssim 0.7$ depending on the observation energy band (Kaspi et al. (2000) and Kaspi et al. (2005)).

Local radiative equilibrium

As for the torus, one can write a local radiative equilibrium. A proportion α' of the power emitted in the direction ω_d by the disc is absorbed by the elementary surface $\mathrm{d}S_{blr}$ and re-emitted:

$$\alpha' I_d \, \cos\omega_d \, \mathrm{d}\Omega_d \, S_d = \varepsilon(\omega) \, \sigma T_{blr}^4 \, \mathrm{d}S_{blr} \tag{6.9}$$

From that, one can compute the total BLR luminosity:

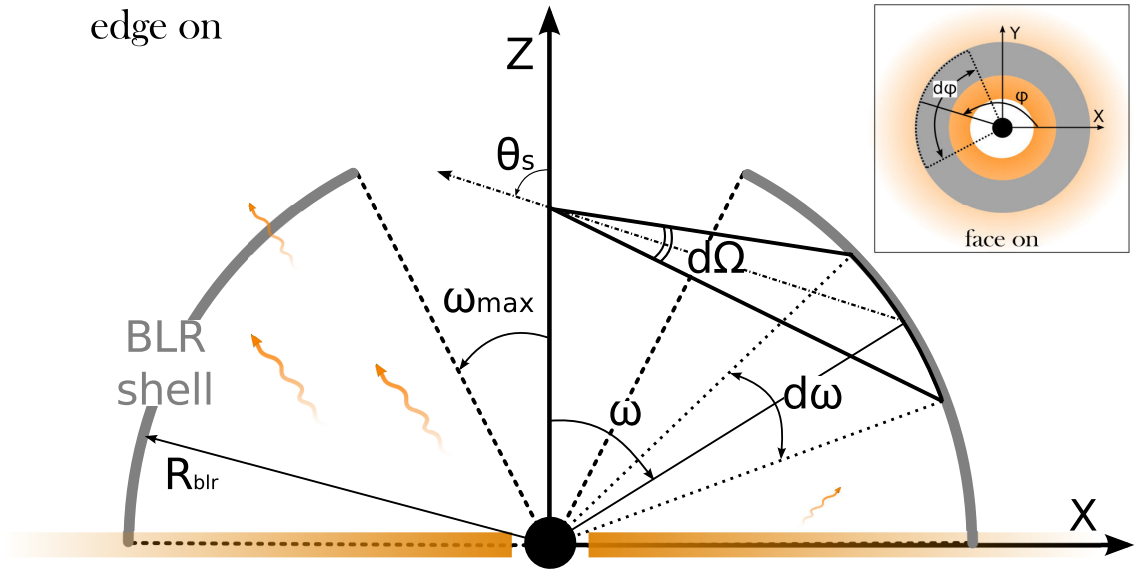

Figure 6.6: The BLR, an optically and geometrically thin shell of clouds seen from an altitude Z in the jet under a solid angle dΩ. The BLR is sliced according to $\omega \in [\omega_{max}, \pi/2]$ and $\varphi \in [0, 2\pi]$. The BLR absorbs and re-emits part of the disk luminosity.

$$\begin{aligned} L_{blr} &= \int_{blr} \varepsilon(\omega)\sigma T_{blr}^4 \mathrm{d}S \\ &= \int_{\omega_{min}}^{\omega_{max}} \alpha' I_d S_d \cos\omega \,\mathrm{d}\Omega\, S_d \\ &= \alpha' L_d(\cos\omega_{max}^2 - \cos\omega_{min}^2) \qquad \text{as } L_d = \pi I_d S_d \\ &= \alpha_{blr}\, L_d \qquad \text{by definition of } \alpha_{blr} \end{aligned} \tag{6.10}$$

Therefore, one has:

$$\alpha = \alpha'(\cos\omega_{max}^2 - \cos\omega_{min}^2) \leq (\cos\omega_{max}^2 - \cos\omega_{min}^2) \tag{6.11}$$

and the emissivity:

$$\varepsilon(\omega) = \frac{\alpha' L_d \cos\omega}{\pi\sigma T_{blr}^4 R_{blr}^2} = \frac{\alpha_{blr} L_d}{\pi\sigma T_{blr}^4 R_{blr}^2} \frac{\cos\omega}{(\cos^2\omega_{max} - \cos^2\omega_{min})} \tag{6.12}$$

6.4 External absorption

As described in section 5.2, soft photons from external sources induce an opacity for high-energy photons. To compute the absorption coefficient $\tau_{\gamma\gamma}$ experienced by a photon emitted from an altitude Z_0 in the jet, one needs to integrate $\frac{\mathrm{d}\tau_{\gamma\gamma}}{\mathrm{d}l}(M)$ (from equation 5.28) over the path followed by the photon from Z_0 to infinity (here M relates to the position along that path). The result of this integration is given in figure 6.7 for a photon traveling along the jet axis.

The opacity is very important ($\tau_{\gamma\gamma} \gg 1$) close from the central engine. In an object emitting at the Eddington luminosity, no photon of energy larger than 10 GeV and emitted at $Z_0 < R_{blr}$ can escape the system. It gets even worse for photons of energies higher than

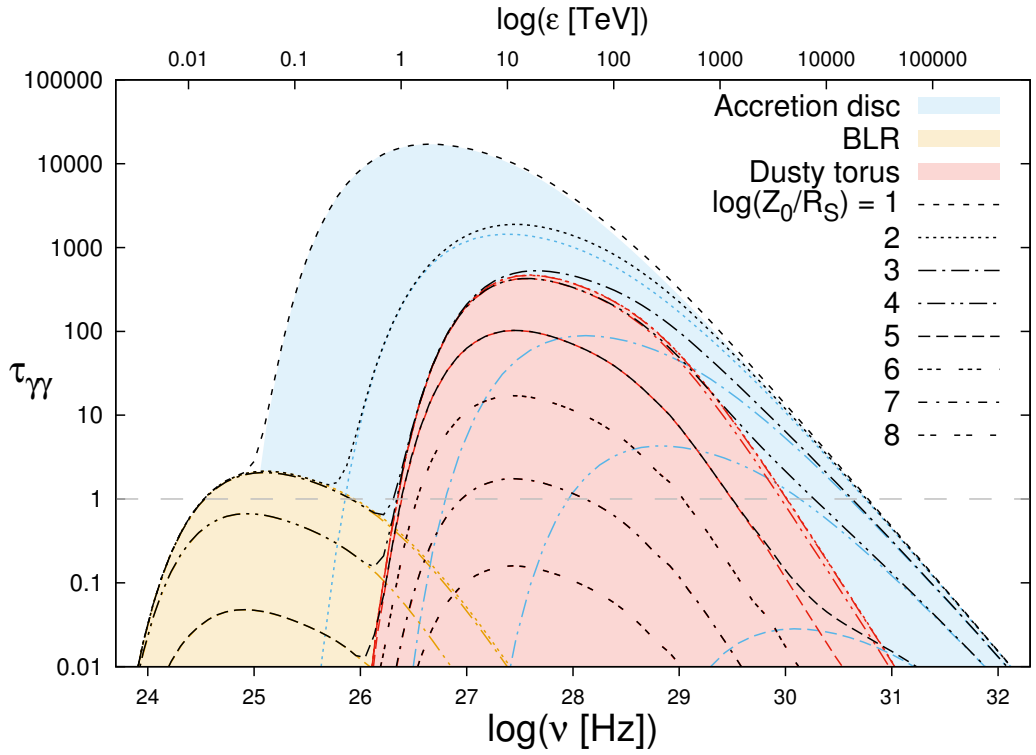

(a) $\tau_{\gamma\gamma}$ created by the three external sources (disc, torus, BLR) and experienced by a photon of frequency ν leaving the jet from an altitude Z_0 and traveling along the jet axis

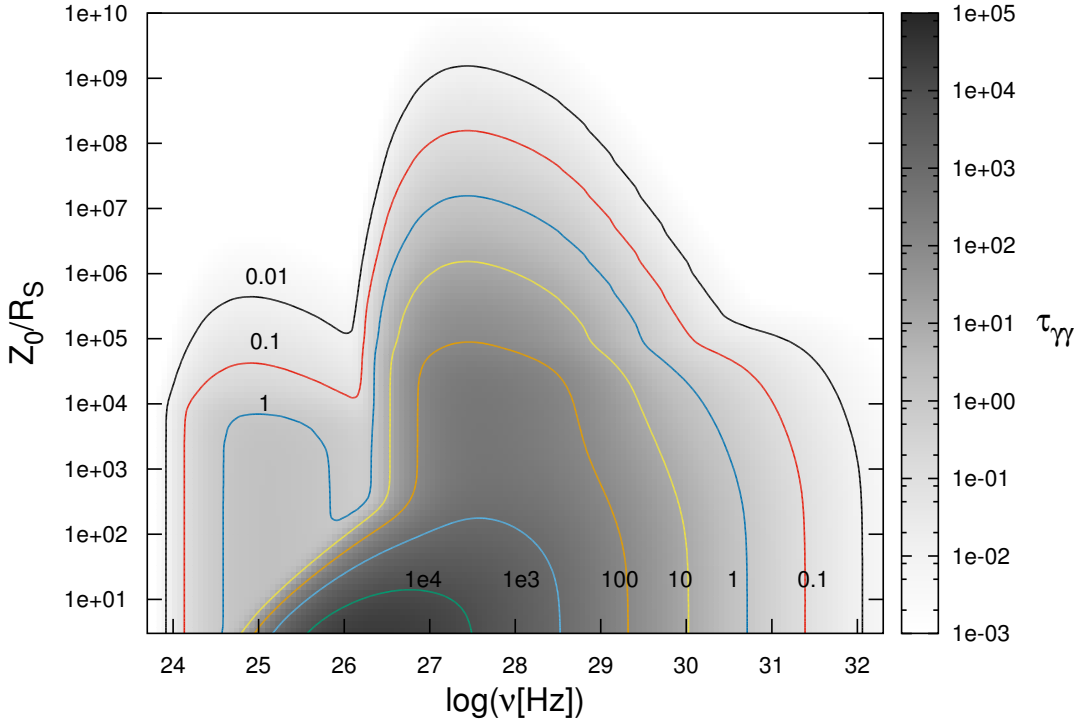

(b) Map of $\tau_{\gamma\gamma}$ created by the three external sources (disc, torus and BLR) for a photon of frequency ν leaving the jet from an altitude Z_0 and traveling along the jet axis

Figure 6.7: Integrated $\tau_{\gamma\gamma}$ from external sources experienced by a photon leaving the jet at Z_0 and going to infinity. Parameters of the sources: *Disc:* $L_d = 0.2L_{edd}$, $R_{in} = 3R_S$ and $R_{out} = 5e4R_S$. *Torus:* $R_t = 5e4R_S$ and $D_t = 1e5R_S$. *BLR:* $R_{blr} = 8e3R_S$, $\omega \in [0 : \pi/2]$, $\alpha_{blr} = 0.01$

10 TeV but as seen in section 5.2, the EBL absorption prevent us to detect AGNs at these energies anyway.

6.4.1 Effect of the observational angle

It is also interesting to see the changes in the opacity for a photon traveling outside the jet toward an observer at an angle i_{obs} with the axis. To simplify, we will interest ourself only to the absorption from the disc here (see figure 6.8).

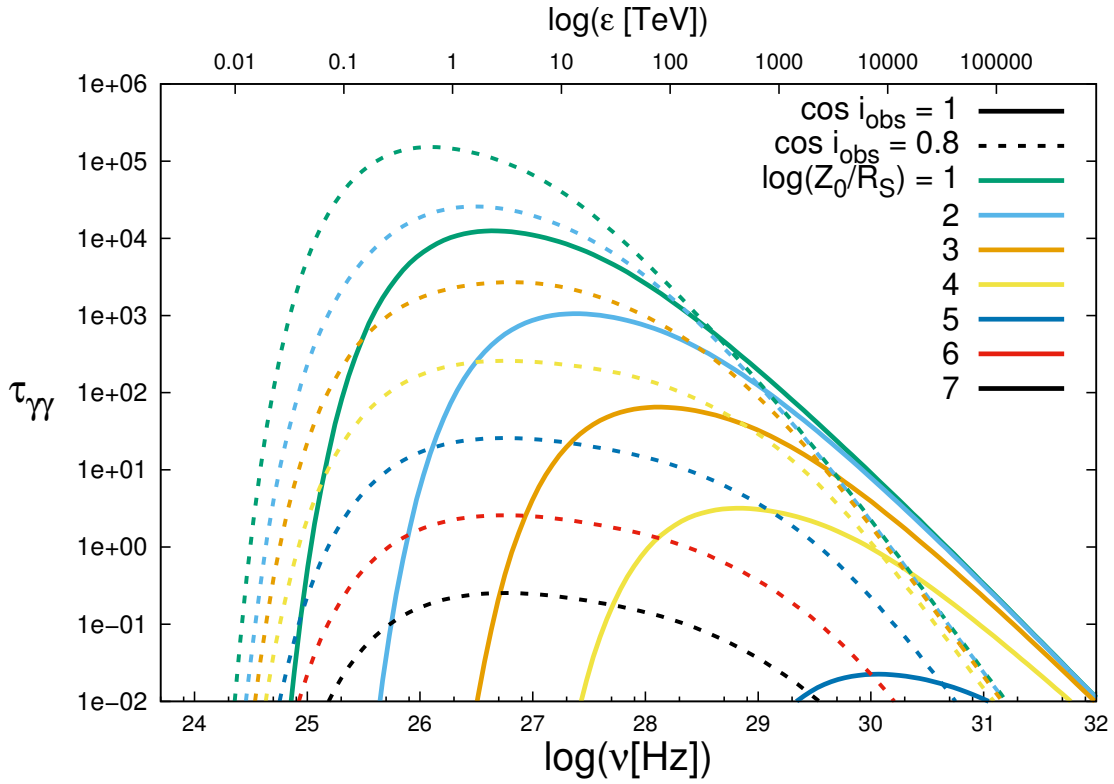

Figure 6.8: Integrated $\tau_{\gamma\gamma}$ from external sources experienced by a photon leaving the jet at Z_0 and going to infinity. The thick lines here represents the same situation as in the figure 6.7 with the disc only. The dotted lines show the opacity $\tau_{\gamma\gamma}$ for the same disc but for a photon traveling in the direction $i_{obs} = \arccos(0.8)$ with the jet axis.

The first and obvious result is that the opacity increases (here by 1 or 2 orders of magnitude) when the angle increases. This is mainly because the length of the path in the photon field of the disc increases. A more subtle change is that the absorption peak in frequency depends less on the altitude Z_0. This is an effect of the changes on the incident angles. These effects can be important when studying orientation effects of AGNs and are well taken into account in the numerical simulation.

6.5 *[En résumé]* Modélisation des sources de photons externes

Les sources de photons externes correspondent à la matière dans l'environnement proche du trou noir central et émettant des radiations. Les trois sources principales de radiations sont le disque d'accrétion, le tore de poussière et la "Broad Line Region (BLR)"[3]. Un schéma récapitulatif de la disposition de ces trois sources est donné figure 6.1. Je présente dans ce chapitre la modélisation de ces trois sources qui est essentielle pour deux raisons :

- calculer l'émission Compton inverse provenant de la diffusion des photons de ces sources externes sur les particules relativistes du jet
- calculer l'absorption induite par le champ de photon de ces sources qui peut rendre les régions internes des AGN opaques (voir section 5.2)

Le disque d'accrétion est modélisé par un disque troué plat (sans hauteur) s'étendant entre son rayon interne R_{in} et son rayon externe R_{out} (voir figure 6.2). Il est découpé en sections suivant son rayon et l'angle azimuthal φ afin de permettre l'intégration numérique sur sa géométrie. Chaque section du disque émet comme un corps noir dont la température est déterminée par la loi de Shakura and Sunyaev (1976) (voir l'équation 6.3). La luminosité totale du disque est alors déterminée par l'équation 6.4.

Le tore de poussière est modélisé par un tore géométrique de section πR_t^2 centrée en $(D_t, 0)$. A l'instar du disque, il est découpé en sections, ici suivant les angles θ_t et φ (voir figure 6.4). On considère chaque section du tore comme un corps gris en équilibre radiatif avec l'illumination provenant du disque d'accrétion. L'équation (6.5) donne alors une relation entre la luminosité du disque, l'émissivité et la température d'une section. La densité surfacique de puissance est alors déterminée par la luminosité du disque et la fonction géométrique $\zeta(a, \theta)$ (cf équation 6.6 et figure 6.5).

La BLR est un ensemble de nuages de gaz en orbite autour du trou noir central dont la distribution spatiale est l'objet de nombreuses recherches. Ces nuages produisent des raies d'émission dans l'optique et les UV et une absorption dans les UV et les rayons X. Ici j'ai choisi de modéliser la BLR par une coquille sphérique de rayon R_{blr} (voir figure 6.6). Cette coquille est découpée suivant les angles ω et φ. Chaque section intercepte une partie du rayonnement provenant du disque d'accrétion et le réémet. L'émission de la BLR est relativement complexe mais Tavecchio and Ghisellini (2008) ont montré qu'elle pouvait être modélisée par celle d'un corps gris de température $T_{blr} = 10^5 K$. En suivant cette idée, on peut déterminer l'émissivité de la BLR dans le cas d'une BLR isotrope (équation 6.8) et dans le cas d'une BLR en équilibre radiatif local (équation 6.12).

Le champ de photons induit par les sources décrites ici absorbe les photons de plus hautes énergies. La description géométrique des sources étant faite, on peut déterminer le coefficient d'absorption $\tau_{\gamma\gamma}$ pour chacun d'entre elles. Un exemple est donné figure 6.7 en fonction de la fréquence et de l'altitude dans le jet du photon émis. Lorsque $\tau_{\gamma\gamma} > 1$, on considère que le milieu est complètement opaque.

[3] comme on peut le voir dans le tableau 6.1, d'autres sources de photons peuvent être considérées mais sont négligeables devant le disque d'accrétion, le tore de poussière et la BLR

Chapter 7

Relativistic jet acceleration: the Compton rocket

Contents

7.1 How to rocket a plasma?

When a plasma of particles emits anisotropicaly in its comoving frame, a recoil force arises on this plasma, much like rockets move forward by throwing stuff backward[1]. O'dell (1981) showed that this effect could be of importance in the case of a hot plasma of leptons emitting through inverse Compton (IC) process. He demonstrated that the induced radiation force was greater on a hot (relativistic) plasma than on a cold ($\gamma \ll 1$) one[2] by a factor $\left[1+\frac{2}{3}(\beta\gamma)^2\right]$. Such an IC anisotropic emission can have two origins: an anisotropic distribution of particles or an anisotropic incident radiation.

Moreover, as we saw in section 2.3, the inverse Compton cooling time is much smaller than the dynamical time in the inner part of luminous AGNs. This means that the Compton rocket force acts much faster than any MHD force, which necessarily act on dynamical times. Therefore, a plasma of hot leptons in the vicinity of an AGN must be dynamically driven by the Compton rocket.

This result applies directly in the two-flow model where the inner jet is composed of a pure plasma of hot leptons.

[1] note that this is a rough shortcut, the plasma global motion being the average of particles motions, the later losing more momentum in the direction of emission

[2] a cold plasma being only pushed by radiation pressure

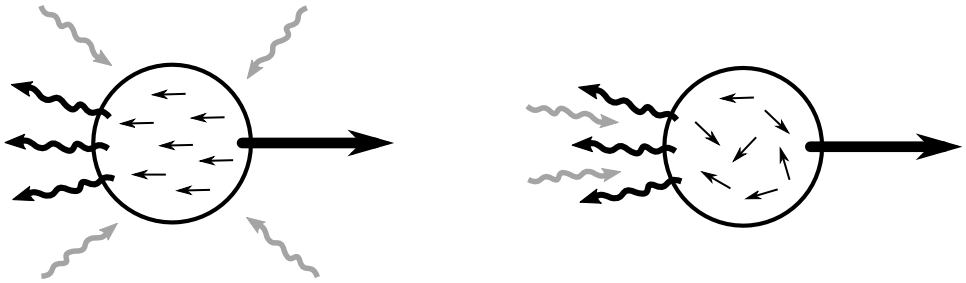

Figure 7.1: Illustration of the Compton rocket effect: A plasma of hot leptons (straight arrows) scatter an incident radiation (gray wave arrows). *Left:* Anisotropic particle distribution. *Right:* Anisotropic incident radiation. Both cases result in an anisotropic scattering (to the left) inducing a radiation force (to the right).

The force resulting from the Compton rocket effect depends on the photon field Eddington momenta in the plasma rest frame J', H' and K'. with:

$$\begin{aligned} J &= \frac{1}{4\pi}\int I_\nu\left(\Omega_s\right)\mathrm{d}\Omega_s\mathrm{d}\nu_s \\ H &= \frac{1}{4\pi}\int I_\nu\left(\Omega_s\right)\mu_s\mathrm{d}\Omega_s\mathrm{d}\nu_s \\ K &= \frac{1}{4\pi}\int I_\nu\left(\Omega_s\right)\mu_s^2\mathrm{d}\Omega_s\mathrm{d}\nu_s \end{aligned} \tag{7.1}$$

Given an external photon field, one can compute the resulting force and thus the resulting equilibrium bulk Lorentz factor of the plasma, Γ_{eq}. As long as the plasma is driven by the Compton rocket, if it travels faster than its equilibrium speed ($\Gamma_b > \Gamma_{eq}$ with Γ_b its bulk Lorentz factor), then the flow must decelerates whereas on the contrary, when $\Gamma_b < \Gamma_{eq}$, the flow must accelerates.

7.2 Compton rocket in a complex photon field: resulting Γ_b and implications

The resulting equilibrium Lorentz factor shows variations as a function of the distance in the jet Z (see figure 7.2 as an example) which can have interesting influence on the observed emission. The details of this study and the implication on the observed emission are given in the following article Vuillaume et al. (2015).

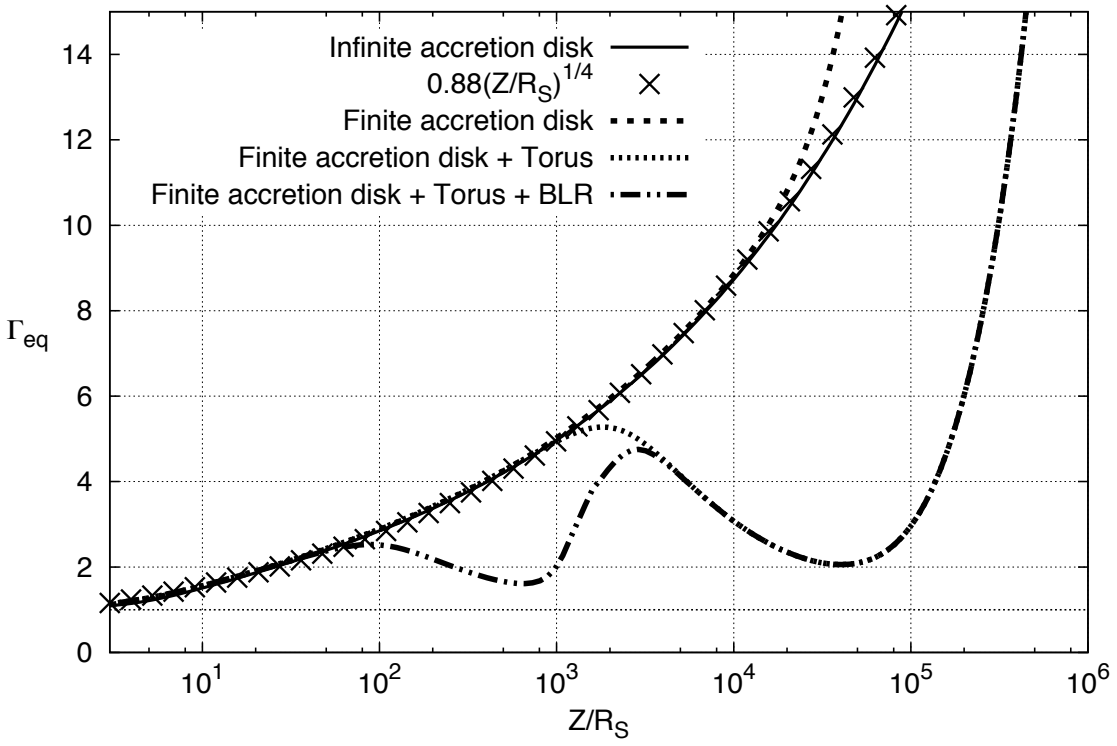

Figure 7.2: Equilibrium bulk Lorentz factor resulting of the external Compton emission for different external photon sources. The geometry is described in section 6 with the following parameters : finite and infinite accretion disk have an inner radius $R_{in} = 3R_S$. The finite disk has an outer radius $R_{out} = 5\times10^4 R_S$. $D_{torus} = 10^5 R_S$, $R_{torus} = 5\times10^4 R_S$, $R_{BLR} = 10^3 R_S$ and $\cos\omega_{max} = 0.9$

A&A 581, A18 (2015)
DOI: 10.1051/0004-6361/201525972

Astronomy & Astrophysics

Variation of bulk Lorentz factor in AGN jets due to Compton rocket in a complex photon field

T. Vuillaume, G. Henri, and P.-O. Petrucci

Institut de Planétologie et d'Astrophysique de Grenoble, 414 rue de la Piscine, 38400 St.-Martin d'Hères, France
e-mail: thomas.vuillaume@obs.ujf-grenoble.fr

Received 26 February 2015 / Accepted 30 June 2015

ABSTRACT

Radio-loud active galactic nuclei are among the most powerful objects in the universe. In these objects, most of the emission comes from relativistic jets getting their power from the accretion of matter onto supermassive black holes. However, despite the number of studies, a jet's acceleration to relativistic speeds is still poorly understood. It is widely known that jets contain relativistic particles that emit radiation through several physical processes, one of them being the inverse Compton scattering of photons coming from external sources. In the case of a plasma composed of electrons and positrons continuously heated by the turbulence, inverse Compton scattering can lead to relativistic bulk motions through the Compton rocket effect. We investigate this process and compute the resulting bulk Lorentz factor in the complex photon field of an AGN composed of several external photon sources. We consider various sources: the accretion disk, the dusty torus, and the broad line region. We take their geometry and anisotropy carefully into account in order to numerically compute the bulk Lorentz factor of the jet at every altitude. The study, made for a broad range of parameters, shows interesting and unexpected behaviors of the bulk Lorentz factor, exhibiting acceleration and deceleration zones in the jet. We investigate the patterns of the bulk Lorentz factor along the jet depending on the source sizes and on the observation angle and we finally show that these patterns can induce variability in the AGN emission with timescales going from hours to months.

Key words. galaxies: jets – galaxies: active – radio continuum: galaxies – radiation mechanisms: non-thermal – scattering – plasmas

1. Introduction

It is now widely known that AGN jets hold relativistic flows. The first evidence of this goes back to the 1960s with the interpretation of brightness temperatures of quasar radio emission exceeding the Compton limit by Rees (1966). This was beautifully confirmed by the observation of superluminal motions with the achievement of the very long base interferometry (VLBI) technique (Cohen et al. 1971). These superluminal events are only possible for actual speeds larger than $0.7c$. Relativistic velocities are also required to avoid strong $\gamma - \gamma$ absorption by pair production, the high-energy photons being able to escape thanks to beamed radiation (see Baring 1994).

Relativistic flows are characterized by their bulk Lorentz factor $\Gamma_\mathrm{b} = \left(1 - \beta_\mathrm{b}^2\right)^{-1}$ rather than their speed V_b with $\beta_\mathrm{b} = V_\mathrm{b}/c$. However, there are several pieces of evidence that this bulk Lorentz factor is not homogeneous throughout the flow. The spatial distribution of the relativistic motion in the jet is still a matter of discussion. Two types of variations are possible: radial and longitudinal (or a combination of both). The variations of longitudinal bulk Lorentz factor have often been parametrized by power laws with an accelerating and/or a decelerating phase (Marscher 1980; Ghisellini et al. 1985; Georganopoulos & Marscher 1998; Li & Wang 2004; Boutelier et al. 2008). Even though an initial accelerating phase appears necessary to achieve relativistic speeds, decelerating flows have also been invoked at larger scales, for example, to unify BL Lacs and radiogalaxies. In the unification scheme, BL Lacs and FR I radio galaxies are the same type of objects seen at different angles. However, BL Lacs models with constant jet velocities need very high bulk Lorentz factors to produce the observed spectral energy distribution (SED), which is in contradiction with the FR I models and the observed jet velocities at subparsec scales in the TeV BLacs Mrk 421 and Mrk 501 (Marscher 1999). In their work, Georganopoulos & Kazanas (2003) showed that deceleration of the jet allows photons emitted in the inner parts of it to be scattered by the upper parts. In this case, radiation from fast regions of the jet would be highly beamed and thus correspond to BL Lacs objects, while radiation from slower regions would be emitted in a wider cone and would correspond to radio galaxies. Implications of a bulk velocity structure for the observed SED has been studied by Yang et al. (2009).

In addition, a radial distribution of velocity is possible and has been particularly studied in the case of a double-jet structure, the so-called spine/layer jet. Here too, the idea was proposed as a solution to the unification issue between BL Lac objects and radiogalaxies (see Chiaberge et al. 2000). In this framework, Ghisellini et al. (2005) explain the rapid variability of the TeV emission without requiring huge Doppler factors, and Tavecchio & Ghisellini (2014) are able to reproduce the SED of NGC 1275. Recent observations (Giovannini et al. 1999; Swain et al. 1998; Giroletti et al. 2004) also bring evidence of such structures.

The idea of a two-flow structure was first proposed by Sol et al. (1989) for theoretical reasons. In this paradigm, the jet is assumed to be made of two components: a mildly relativistic sheath composed of e^-/p^+ and driven by magnetohydrodynamical (MHD) forces, which transports most of the kinetic energy, and an ultra-relativistic spine composed of e^-/e^+ pairs, which is responsible for most of the emission. A detailed description

A&A 581, A18 (2015)

of the formation of such a pair beam has been developed in Marcowith et al. (1995) and following works (e.g., Renaud & Henri 1998; Henri & Saugé 2006; Boutelier et al. 2008). In this model, the outer jet acts as an energy reservoir for the particles of the spine. Starting from an initial injection of some relativistic particles (possibly created in the surrounding of a rotating black hole), these particles will emit copious amounts of high-energy radiation, which will be converted into pairs. These pairs will be in turn continuously reaccelerated along the jet via the second-order Fermi process through the turbulence triggered by various instabilities in the outer MHD jet. Observations of diffuse X-ray emission in type 1 Fanaroff-Riley objetcs are in favor of this view of distributed particle acceleration rather than localized shocks (Hardcastle et al. 2007).

In leptonic models, X-ray and gamma-ray emission is thought to arise from inverse Compton (IC) process on soft photons. These photons can be provided by synchrotron emission (called the synchrotron self-Compton (SSC) process), or by external sources such as an accretion disk, the broad line region, or a dusty torus. All these sources will give a locally anisotropic photon field on the axis of the jet. Under these conditions, the emitted radiation will also be highly anisotropic, which produces a strong momentum transfer between the relativistic plasma and the emitted radiation, the so-called Compton rocket effect (see O'dell 1981, Melia & Konigl 1989, or more recently Renaud & Henri 1998).

For a relativistic e^-/e^+ pair plasma, this force is dominant and will drive the bulk motion to relativistic velocities. As is detailed in Sect. 2, this effect will saturate when the velocity (or equivalently the bulk Lorentz factor) of the plasma reaches a characteristic value for which the net radiation flux vanishes in the comoving frame as a result of the aberration of the photon momentum. Thus, a plasma submitted to this radiation force will tend to reach this equilibrium velocity, which can be viewed as the average velocity of the photon "wind". The Compton rocket effect can also be found under the name of Compton drag effect. Even though they are exactly the same mechanism, the drag denomination comes from an a priori assumption of a very high bulk Lorentz factor, higher than that imposed by the external radiation and the Compton rocket effect: in this case, the inverse Compton rocket (more appropriately called a "retrorocket" effect in this case) will result in a deceleration of the flow or a limitation of its velocity (Sikora et al. 1996; and Ghisellini & Tavecchio 2010).

The Compton rocket effect has often been dismissed as a cause of relativistic motion because it is also a cooling process. This means that an isolated relativistic pair plasma will also be quickly cooled and will generally be unable to reach the high bulk Lorentz factors ($\approx$10) needed to explain superluminal motions (Phinney 1982 and also Madau & Thompson 2000). However, this objection is not valid in the two-flow model, since the relativistic pair plasma is supposed to be continuously reheated by the surrounding MHD flow.

Under these conditions, a pure electron-positron pair plasma can be coupled to the radiation field over a much larger distance. It will then stick to the equilibrium velocity (which is generally variable), until the radiation field weakens enough for the decoupling to occur. The plasma will then essentially follow a ballistic motion at the terminal velocity, which depends on the location of the decoupling. In the following, we will only study the value of the equilibrium velocity, which depends only on the radiation field and not on the characteristics of the plasma in the Thomson regime. On the other hand, the location of the decoupling, and hence the terminal velocity, depends on these plasma characteristics, as is discussed in Sect. 6.

In summary, we investigate this paradigm and propose to study the evolution of the resulting bulk Lorentz factor (presented in Sect. 2) due to the Compton rocket effect in a complex photon field including three main external sources of soft photons present in quasars, the accretion disk, the dusty torus, and the broad line region (BLR; presented in Sect. 3). By computing accurately the equilibrium bulk Lorentz factor along the jet in the Thomson regime (Sects. 4 and 5), we can study what effect it might have on the observed emission (Sects. 5 and 7).

In the rest of the paper, the "jet" refers to the inner spine of the two-flow model which is subject to the Compton rocket effect and is the flow moving at relativistic bulk speeds. Primed quantities are expressed in the comoving frame and unprimed quantities are expressed in the lab frame (i.e., the external source frame of the AGN).

2. $\Gamma_{\rm bulk}$ and equilibrium

We assume a static bulk of relativistic leptons following an isotropic distribution in an anisotropic photon field. Owing to the Doppler effect, particles moving towards the main light source will scatter photons of higher energy and with a higher rate than those moving outwards. This will naturally lead to an anisotropic inverse Compton emission, most of it going back to the main photon source. This anisotropic emission will result in a transfer of momentum on the emitting plasma, the so-called Compton rocket effect first described by O'dell (1981). A hot plasma could be driven to relativistic bulk motion through this mechanism. The force depends on the anisotropy of the soft photons seen in the comoving frame. When relativistic motion is taken into account, the photon field in the comoving frame will be affected by the bulk Doppler factor, resulting in a more isotropic photon distribution, until the Compton rocket force vanishes. The plasma then reaches an equilibrium velocity, or equivalently, an equilibrium bulk Lorentz factor $\Gamma_{\rm eq}$.

In the Thomson regime, $\Gamma_{\rm eq}$ depends only on the external radiation field through the Eddington parameters (J, H, K)

$$\begin{aligned} J &= \frac{1}{4\pi}\int I_{\nu_{\rm s}}(\Omega_{\rm s})\mathrm{d}\Omega_{\rm s}\mathrm{d}\nu_{\rm s} \\ H &= \frac{1}{4\pi}\int I_{\nu_{\rm s}}(\Omega_{\rm s})\mu_{\rm s}\mathrm{d}\Omega_{\rm s}\mathrm{d}\nu_{\rm s} \\ K &= \frac{1}{4\pi}\int I_{\nu_{\rm s}}(\Omega_{\rm s})\mu_{\rm s}^2\mathrm{d}\Omega_{\rm s}\mathrm{d}\nu_{\rm s} \end{aligned} \tag{1}$$

with $I_{\nu_{\rm s}}$ the specific intensity of the emitting source, $\Omega_{\rm s}$ the solid angle, and $\theta_{\rm s} = \arccos\mu_{\rm s}$ the angle under which the source is seen by the pair plasma (see Fig. 1).

In the Thomson regime, the saturation of the Compton rocket effects happens when the second Eddington parameter, H', vanishes in the comoving frame (see Marcowith et al. 1997, for more details). With the factor $\zeta = \dfrac{J+K}{2H}$, one obtains the equilibrium equation

$$H' = H\,\Gamma_{\rm eq}^2\left(\beta_{\rm eq}^2 - 2\zeta\beta_{\rm eq} + 1\right) = 0, \tag{2}$$

whose solution is

$$\beta_{\rm eq} = \zeta - \sqrt{\zeta^2 - 1}. \tag{3}$$

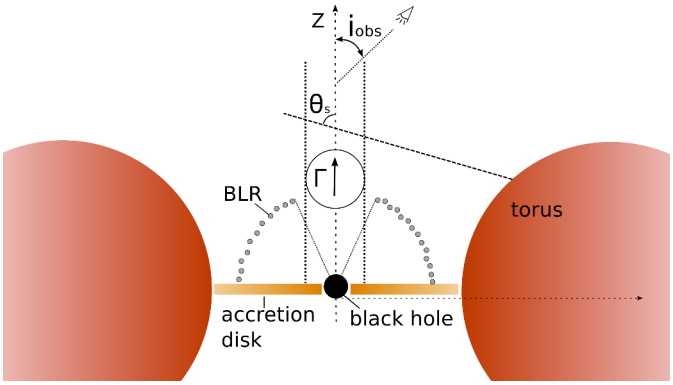

Fig. 1. The big picture: edge-on view of the global model geometry (not to scale) with the accretion disk, the dusty torus, and the broad line region (BLR). i_{obs} is the observer's viewing angle and θ_s is the angle between the incoming radiation from a source and the jet axis.

It is interesting to note again that, as long as the plasma is hot, this result does not depend on the jet model in the Thomson regime, but only on the external photon field (see Eq. (2)). The Compton rocket effect will also take place in the Klein-Nishina (KN) regime, but in this case the computation of the equilibrium velocity is a bit more complex and depends on the energy distribution of the pair (see Renaud & Henri 1998). Moreover, one can expect that the resulting Γ_{eq} will not vary much from that computed in the Thomson regime as long as we are not deep in the KN regime, as the recoil in the Thomson regime is much more efficient. Then Γ_{eq} could be sensitive to KN correction for the most extreme objects (>100 GeV; see Sect. 7). In the following, we suppose that conditions always meet the Thomson regime. The goal of this paper is to compute the resulting equilibrium bulk Lorentz factor Γ_{eq}, in a complex environnement, taking into account the angular and spectral distribution of various sources of photons in a realistic model of AGNs.

3. Modeling the AGN

We will consider the effect of several possible external sources of photons, namely the accretion disk, the dusty torus, and the broad line region (see Fig. 1). We note that because the synchrotron radiation is produced in the comoving frame with a zero net flux, it does not interfere with the bulk motion as long as the SSC is treated in a local approximation. This could change, however, if the particles scatter synchrotron photons produced in other parts of the jet, but this problem is much more complex since it involves the knowledge of the whole structure of the jet. We will not address this issue in this work.

3.1. Discretization of the sources

The anisotropy of the photon sources will be taken into account in the numerical scheme by slicing the different sources into a set of small independent parts modeled as graybodies in radiative equilibrium, i.e., with a Planck spectrum but with a possible smaller emissivity. This discretization is done in three dimensions. Even for an axisymmetric source, an azimuthal discretization is still required to accurately compute the Compton external emission towards the observer's line of sight. Since the object is seen under a certain angle, the axisymmetry is always broken with respect to the line of sight.

Each slice of the discretization is then described by four numbers:

- $\mu_s = \cos\theta_s$ with θ_s the angle between the incoming light wave and the jet axis (see Fig. 1),
- $\mathrm{d}\Omega$ the solid angle under which it is seen from the altitude Z,
- its temperature T,
- its emissivity ε.

The slice emission characterized by these numbers is given by its specific intensity I_ν $\left(\mathrm{erg\,s^{-1}\,cm^{-2}\,sr^{-1}\,Hz^{-1}}\right)$, defined as the emitted energy $\mathrm{d}E$ by normal surface $\mathrm{d}\Sigma$, time $\mathrm{d}t$, frequency band $\mathrm{d}\nu$, and solid angle $\mathrm{d}\Omega$: $\mathrm{d}E = I_\nu\,\mathrm{d}\Sigma\,\mathrm{d}t\,\mathrm{d}\Omega\,\mathrm{d}\nu$ (Rybicki & Lightman 1979). The specific intensity of a graybody is given by Planck's law (Eq. (4)):

$$I_{\nu_s} = \varepsilon \frac{2h\nu^3}{c^2} \frac{1}{\exp\left(\frac{h\nu}{k_B T} - 1\right)}. \tag{4}$$

A blackbody is a graybody with an emissivity $\varepsilon = 1$.

Here below, we detail the computation of each photon source.

3.2. Standard accretion disk

The accretion disk is assumed to be an optically thick standard accretion disk as described by Shakura & Sunyaev (1973) extending from R_{in} to R_{out}. Each point of the disk is a blackbody with a temperature given by the distance to the central black hole (BH), assumed to be non-rotating, following the relation

$$T_{disk}(r) = \left[\frac{3GM\dot{M}}{8\pi\sigma}\frac{1}{r^3}\left(1 - \sqrt{\frac{3R_S}{r}}\right)\right]^{1/4} \tag{5}$$

with G the gravitational constant, σ the Stefan-Boltzmann constant, M the BH mass, $\dot{M}$ the accretion rate, $R_S = 2\frac{GM}{c^2}$ the Schwarzschild radius, and r the distance from the center of the BH.

To model this accretion disk, we sliced it in different parts, each being a blackbody with its own temperature $T_{disk}(r, \varphi)$. The discretization follows a logarithmic scale along r and a linear scale along φ. Given an altitude Z in the jet, a slice of the disk is seen under a solid angle $\mathrm{d}\Omega = Z\,\mathrm{d}S/(r^2 + Z^2)^{3/2}$, where $\mathrm{d}S = \mathrm{d}\varphi(r\mathrm{d}r + \mathrm{d}r^2/2)$ is the surface of the slice. Photons coming from this slice make an angle $\theta_s = \arccos(Z/\sqrt{r^2 + Z^2})$ with the axis (see Fig. 2).

The luminosity of one face of the disk, for $R_{in} = 3R_S$ and $R_{out} \gg R_{in}$, is given by the relation

$$L_{disk} = \int_{R_{in}}^{R_{out}} \sigma T_{disk}^4(r)\, 2\pi r\,\mathrm{d}r \approx \frac{\dot{M}c}{24}. \tag{6}$$

3.3. Dusty torus

The dusty torus is modeled by a torus shape structure whose major radius is D_t and minor radius R_t (see Fig. 3).

In the same way as the disk, the torus is sliced in different parts that will radiate as blackbodies (so $\varepsilon = 1$ for the torus). Slices follow a linear discretization and are located with their coordinates (θ_t, φ) at the surface of the torus.

Each slice of the torus is assumed to be in radiative equilibrium with the luminosity received from the accretion disk. To

A&A 581, A18 (2015)

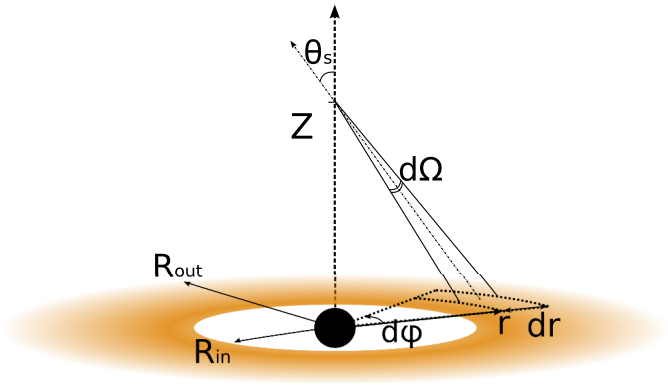

Fig. 2. Disk radial and azimuthal splitting. A slice at $(r, \varphi) \in ([R_{\rm in}, R_{\rm out}], [0, 2\pi])$ is seen under a solid angle dΩ from the jet at an altitude Z.

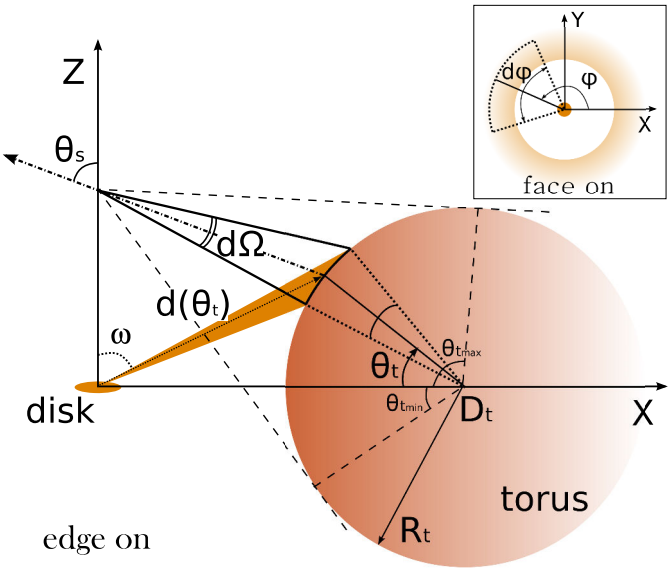

Fig. 3. Dusty torus seen from an altitude Z in the jet under a solid angle dΩ. The torus is sliced according to $\theta_{\rm t} \in \left[\theta_{t_{\rm min}}, \theta_{t_{\rm max}}\right]$ and $\varphi \in [0, 2\pi]$. Each slice is illuminated by the disk and is in radiative equilibrium with a temperature $T(\theta_{\rm t}, \varphi)$ and emits as a blackbody ($\varepsilon = 1$).

simplify, we make the assumption that all the energy from the disk comes from its inner parts and that $R_{\rm in} \ll (D_{\rm t} - R_{\rm t})$ so that the source of energy is point-like when seen from the torus. With the parameter $a = \dfrac{R_{\rm t}}{D_{\rm t}} \leq 1$, the torus temperature is given by

$$T_{\rm tor}(\theta_{\rm t}) = \begin{cases} \left[\dfrac{D_{\rm t}(\cos\theta_{\rm t} - a)}{2\pi\sigma {\rm d}(\theta_{\rm t})^3} L_{\rm disk} \sin\omega\right]^{1/4} & \text{for } \cos\theta_{\rm t} \in [-a{:}a] \\ 0 & \text{otherwise} \end{cases} \tag{7}$$

with ${\rm d}(\theta_{\rm t})$ the distance between the slice center and the point-like source,

$${\rm d}(\theta_{\rm t}) = D_{\rm t}\left[(1 - a\cos\theta_{\rm t})^2 + a^2 \sin^2\theta_{\rm t}\right]^{1/2}, \tag{8}$$

and ω the angle between the Z-axis and the emission direction from the disk:

$$\sin\omega = \frac{a\sin\theta}{(1 + a^2 - 2a\cos\theta)^{1/2}}. \tag{9}$$

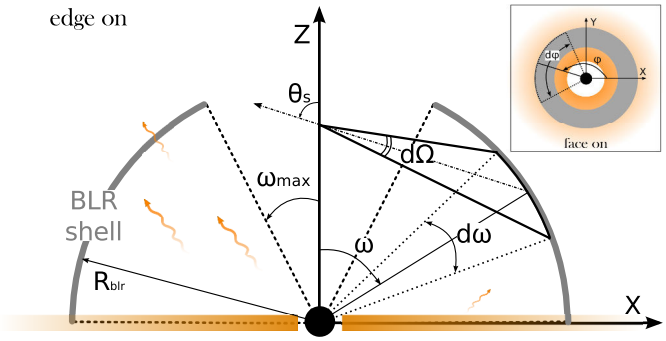

Fig. 4. The BLR, an optically and geometrically thin shell of isotropic clouds seen from an altitude Z in the jet under a solid angle dΩ. The BLR is sliced according to $\omega \in [\omega_{\rm max}, \pi/2]$ and $\varphi \in [0, 2\pi]$. The BLR absorbs and re-emits part of the disk luminosity.

From an altitude Z in the jet, the torus is seen under a certain solid angle which is delimited by $\theta_{t_{\rm min}}$ and $\theta_{t_{\rm max}}$ (see Fig. 3). These values can be determined from geometrical considerations:

$$\theta_{t_{\rm min}} = \arctan\left(\frac{Z}{D_{\rm t}}\right) - \arccos\left(\frac{R_{\rm t}}{\sqrt{Z^2 + D_{\rm t}^2}}\right), \tag{10}$$

$$\theta_{t_{\rm max}} = \arctan\left(\frac{Z}{D_{\rm t}}\right) + \arccos\left(\frac{R_{\rm t}}{\sqrt{Z^2 + D_{\rm t}^2}}\right).$$

However, in the case of a continuum between the accretion disk and the dusty torus ($D_{\rm t} = R_{\rm t} + r_{\rm out}$), $\theta_{t_{\rm min}}$ will be chosen equal to 0.

3.4. Broad line region

The broad line region is modeled as an optically and geometrically thin shell of isotropically emitting clouds situated at a distance $R_{\rm blr}$ from the central black hole and extending up to an angle $\omega_{\rm max}$ above the accretion disk plane (see Fig. 4).

Tavecchio & Ghisellini (2008) showed that modeling the spectrum of the BLR with a blackbody spectrum at $T = 10^5$ K provides a good approximation of the resulting inverse Compton spectrum. We followed this idea using a temperature of $T_{\rm blr} = 10^5$ K and an overall luminosity being a fraction $\alpha_{\rm blr}$ of the disk luminosity. To achieve this, the BLR is modeled as a graybody at $T_{\rm blr}$ with an emissivity

$$\varepsilon_{\rm blr} = \frac{\alpha_{\rm blr} L_{\rm disk}}{2\pi R_{\rm blr}^2 \sigma T_{\rm blr}^4} \cos\omega_{\rm max}. \tag{11}$$

Thus the total luminosity of the BLR is given by

$$L_{\rm blr} = \int_{\rm blr} \varepsilon_{\rm blr}(\omega)\, \sigma T_{\rm blr}^4 {\rm d}S = \alpha_{\rm blr} L_{\rm disk}. \tag{12}$$

Like the torus, the BLR is divided linearly into slices along ω and φ.

4. $\Gamma_{\rm eq}$ in the jet

4.1. Parameter values

We have presented the description of the source modeling, and we can now choose the values for the different parameters.

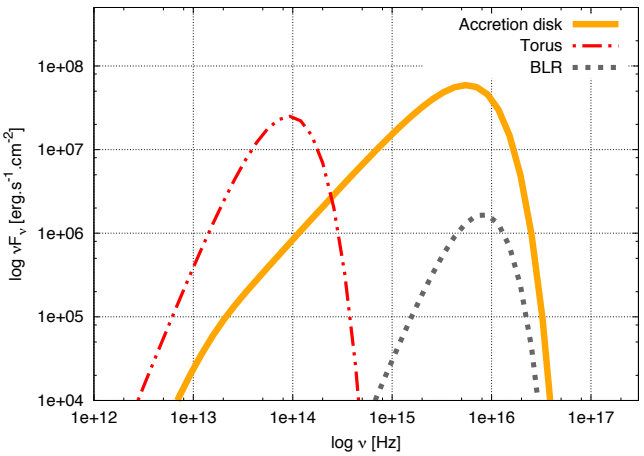

Fig. 5. Spectra of the three external soft photons sources seen at an altitude $Z = 10^5\ R_S$ on the jet axis in the sources frame.

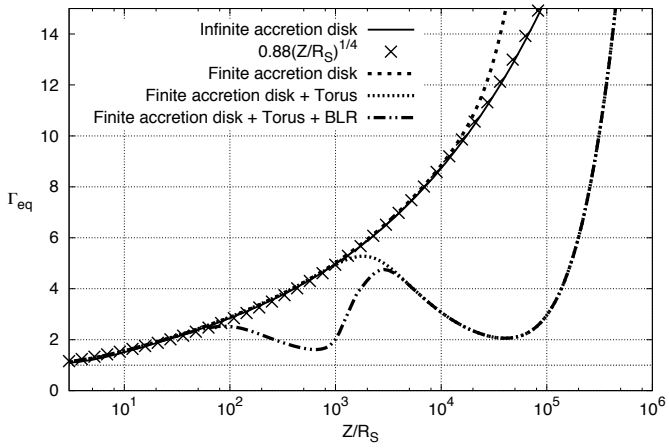

Fig. 6. Equilibrium bulk Lorentz factor resulting of the external Compton emission for different external photon sources. The geometry is described in Fig. 1 with the following parameters: finite and infinite accretion disk have an inner radius $R_{in} = 3R_S$; the finite disk has an outer radius $R_{out} = 5 \times 10^4 R_S$; $D_{torus} = 10^5 R_S$, $R_{torus} = 5 \times 10^4 R_S$, $R_{BLR} = 10^3 R_S$, and $\cos \omega_{max} = 0.9$.

Table 1. Parameters of the external sources.

Parameter	Symbol	Value
Black hole mass	M	$5 \times 10^8\ M_\odot$
BH accretion rate	$\dot{M}$	$1\ \dot{M}_{edd}$
Disk inner radius	R_{in}	$3R_S$
Disk outer radius	R_{out}	$5 \times 10^4 R_S$
Disk emissivity	ε_{disk}	1
Number of disk slices	$N_{r_{disk}} \times N_{\varphi_{disk}}$	18×3
Torus center	D_t	$10^5 R_S$
Torus radius	R_t	$5 \times 10^4 R_S$
Torus emissivity	ε_t	1
Number of torus slices	$N_{r_{tor}} \times N_{\varphi_{tor}}$	6×3
BLR radius	R_{blr}	$10^3 R_S$
BLR angular opening	$\cos \omega_{max}$	0.9
BLR temperature	T_{blr}	10^5 K
BLR absorption	α_{blr}	0.1
Number of BLR slices	$N_{r_{blr}} \times N_{\varphi_{blr}}$	6×3
Derived characteristic	**Symbol**	**Value**
Schwarzschild radius	R_S	5.9×10^{13} cm
Disk temperature	T_{disk}	[280:10^6] K
Disk total luminosity	L_{disk}	1.0×10^{46} erg s^{-1}
Torus equilibrium temperature	T_{tor}	[580:1345] K
Torus total luminosity	L_{tor}	1.4×10^{45} erg s^{-1}
BLR total luminosity	L_{blr}	1.0×10^{45} erg s^{-1}

Notes. The values indicated in the right column are those used in this paper.

They are listed in Table 1. If not specified otherwise, these parameters are set for the rest of the study. Some characteristic values of the model are also derived in Table 1.

With these parameters the external source spectra can be derived. An illustration of these spectra seen at an altitude $Z = 10^5\ R_s$ in the jet is provided in Fig. 5.

4.2. Resulting Γ_{eq}

We can now compute the resulting equilibrium bulk Lorentz factor Γ_{eq} all along the jet. This has been done for different set-ups of external sources (infinite accretion disk or finite accretion disk alone, finite disk + torus or finite disk + torus + BLR) and the results are given in Fig. 6. In this plot, one can distinguish the effect of each external source.

We start with the case of an infinite accretion disk ($R_{out} = \infty$). For an emission zone in the jet, the inner parts of the accretion disk are always seen from below. As explained earlier, for a static source, this would lead to a Compton emission mainly directed toward the disk. This causes a transfer of momentum and a thrust forward on the plasma. However, as soon as the plasma accelerates, the photons coming from the outer part (for $\mu_s < \beta^{-1}$) of the disk seem to travel backward in the comoving frame and produce a drag on the plasma. At every altitude, the equilibrium velocity is reached when the two effects balance. Analytical computation from Marcowith et al. (1995) showed that in the case of an infinite accretion disk, one should have $\Gamma_{eq} = 1.16 \left(\frac{Z}{R_i}\right)^{1/4}$. With $R_i = 3R_S$, this gives $\Gamma_{eq} = 0.88 \left(\frac{Z}{R_S}\right)^{1/4}$, which is in agreement with our numerical results (see bold solid line compared to crosses in Fig. 6).

If we now consider a finite accretion disk ($R_{out} = 5 \times 10^4 R_S$), we note the same behavior: at low altitudes the disk seems to be infinite seen from the axis. Once an altitude $Z \gtrsim R_{out}$ is reached, the drag effect from the outer parts of the disk ceases and then the entire disk will imply a thrust on the bulk. As long as the acceleration is effective, Γ_{eq} will follow a law in Z/R_{out} (Renaud & Henri 1998).

We can have the same reasoning concerning the effect of the dusty torus. As seen from the jet axis, the radiation from the torus comes at greater angles than the one from the accretion disk. Therefore, when the plasma accelerates, the torus radiation seems to come forward, which will tend to drag the flow. Nevertheless, in the lowest altitude the accretion disk radiation dominates and the resulting Γ_{eq} is unchanged from the previous case. It is only from a certain altitude ($Z \approx 10^3 R_S$ in our study) that the effect of the torus radiation starts to dominate and that the flow will actually slow down. Of course, the equilibrium velocity will never reach zero, as the radiation in the lab frame is never isotropic and always has a preferred direction upward. At one point ($Z \approx R_t$ in our study), most of the radiation from the

A&A 581, A18 (2015)

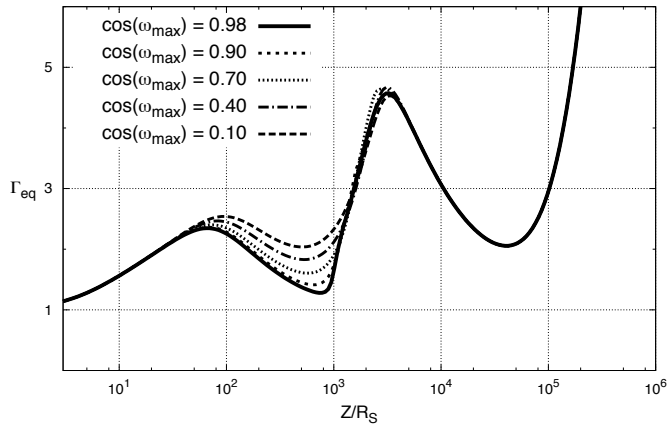

Fig. 7. Equilibrium bulk Lorentz factor for several BLR opening angles $\cos \omega_{\rm max}$. Values of the other geometrical parameters can be found in Table 1.

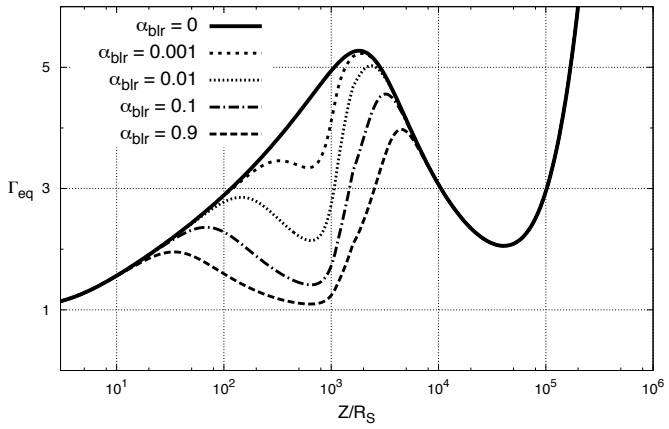

Fig. 8. Equilibrium bulk Lorentz factor for several BLR absorption α. Values of the other geometrical parameters can be found in Table 1.

torus moves forward in the comoving frame. This leads to a thrust on the flow and $\Gamma_{\rm eq}$ increases again with the same accelerating slope as in the finite accretion disk case.

The BLR photon field shows the same kind of effects with a deceleration regime inside the BLR (from $10^2 R_{\rm S}$ to $10^3 R_{\rm S}$ in our study), followed by an accelerating regime once the bulk leaves the BLR. At some point, the torus photon field becomes predominant and controls $\Gamma_{\rm eq}$ as explained previously.

We note that the computation is done for a hot electron-positron plasma in the Thomson regime. For very hot plasmas, KN corrections will affect the rate of momentum transfer and the bulk Lorentz factor will differ in a way that is difficult to predict. Indeed, the Compton rocket is less efficient in the KN regime, but photons coming from larger incident angles are more likely to be in the KN regime and are precisely the ones dragging the flow.

Moreover, far from the external photon sources, the relaxation time to the equilibrium will become larger than the dynamical time z/c. At this point, the acceleration will stop, leading to an asymptotic value of the bulk Lorentz factor. The blob will then follow a ballistic motion. However, The point where this decoupling occurs depends on the absolute luminosity of the disk and the average energy of the plasma. A study of this phenomenon is presented in Sect. 6.

5. Influence of parameters on the equilibrium bulk Lorentz factor

In this section we study the influence of the model parameters on $\Gamma_{\rm eq}$ with the model composed of the accretion disk, the dusty torus at thermal equilibrium, and the BLR. If not otherwise stated, the parameters keep the values given in the previous section (Table 1).

5.1. Influence of the BLR on $\Gamma_{\rm eq}$

5.1.1. Influence of the BLR opening angle $\omega_{\rm max}$

The influence of the BLR opening angle on $\Gamma_{\rm eq}$ is shown in Fig. 7. The smaller $\omega_{\rm max}$, the bigger the BLR, and the stronger the effect.

When $\omega_{\rm max}$ increases, parts of the BLR at small ω are suppressed. For the plasma inside the BLR ($Z < R_{\rm blr}$), radiation from these parts moved backward in the comoving frame. The suppression of this radiation means less dragging effect and thus a higher $\Gamma_{\rm eq}$ for the flow inside the BLR. Thus, the differences between the different opening angles are important at $Z < R_{\rm blr}$.

However, for the plasma outside the BLR ($Z > R_{\rm blr}$), radiation from these parts moved forward in the comoving frame. The suppression of this radiation means less thrust on the plasma, but the radiation from the parts of the BLR at greater ω, which seems to move forward in the comoving frame, is still present and so is the dragging effect. This is why the differences between the different cases at $Z > R_{\rm blr}$ are not so important. Much of the thrust is given by the disk itself, even at altitudes close to the outer border of the BLR.

5.1.2. Influence of the BLR absorption $\alpha_{\rm blr}$

The effect of the BLR absorption $\alpha_{\rm blr}$ is shown in Fig. 8. The effect is similar to the opening angle effect. The stronger the absorption, the stronger the emissivity and thus the stronger the luminosity from the BLR, and consequently, the stronger the drag effect.

However, unlike in the opening angle $\omega_{\rm max}$ case, differences in the acceleration regime outside the BLR are noticeable. Indeed, with a reduction of the absorption, the drag and the thrust change, which was not the case previously.

5.1.3. Influence of the BLR radius

The effect of the BLR radius is shown in Fig. 9. The BLR radius is now going from $R_{\rm blr} = 10^3 R_{\rm S}$ to $R_{\rm blr} = 10^4 R_{\rm S}$. Other parameters are fixed to the values given in Table 1.

The effect of the source radius sizes is a bit different as it increases the amplitude of the drag or thrust, but also shifts the different regimes in altitude . We note that when the BLR radius increases, its acceleration zone moves to higher Z. At one point (when $R_{\rm blr}$ tends to $D_{\rm t} - R_{\rm t}$), the radiation from the torus dominates and controls $\Gamma_{\rm eq}$.

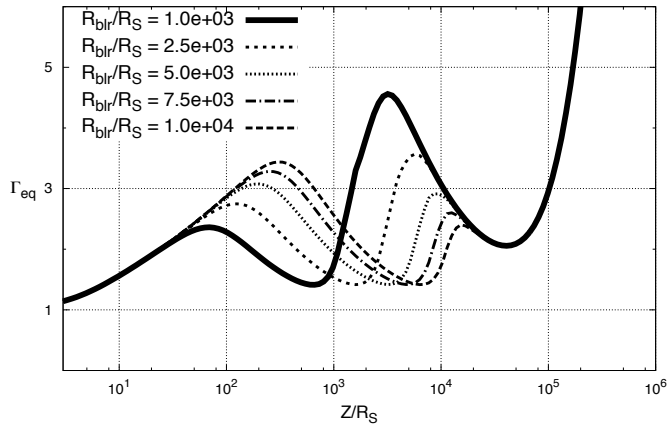

Fig. 9. Equilibrium bulk Lorentz factor for several BLR radius $R_{\rm blr}$. Values of the other geometrical parameters can be found in Table 1.

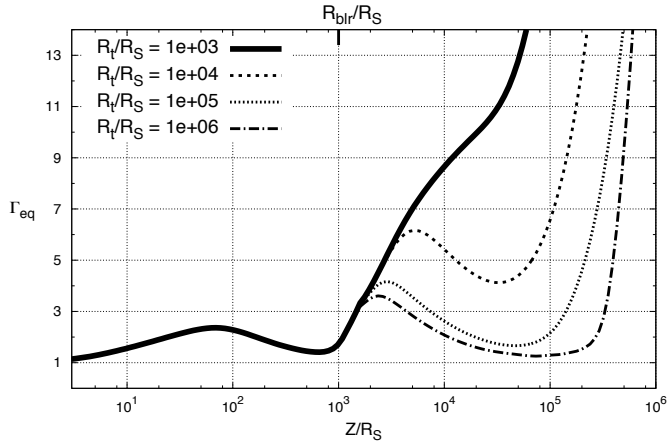

Fig. 10. Equilibrium bulk Lorentz factor for several torus sizes. $R_{\rm t}$ changes as a free parameter as $D_{\rm t} = r_{\rm out} + R_{\rm t}$. The values of the other parameters can be found in Table 1.

5.2. Influence of the torus on $\Gamma_{\rm eq}$

We study here the influence of varying $R_{\rm t}$, but always assume that $D_{\rm t} = r_{\rm out} + R_{\rm t}$. The results are shown in Fig. 10.

The torus acts farther in the jet than does the BLR. Its radius effect is similar to the BLR's: the bigger the radius, the stronger the drag, and the lower in the jet it occurs. With a smaller torus, higher $\Gamma_{\rm eq}$ are reached closer to the black hole. Therefore, the emission from the lowest parts of the jet (at subparsec scale) will be strongly influenced by the torus size through the induced Doppler boosting.

5.3. Observation angle and Doppler factor

The relativistic bulk Doppler factor is defined as

$$\delta_{\rm b} = \frac{1}{\Gamma_{\rm b}\,(1 - \beta_{\rm b}\,\mu_{\rm obs})} \tag{13}$$

with $\mu_{\rm obs} = \cos i_{\rm obs}$ (see Fig. 1 for a definition of $i_{\rm obs}$). As $\frac{I_\nu}{\nu^3}$ is a relativistic invariant (Rybicki & Lightman 1979), the specific

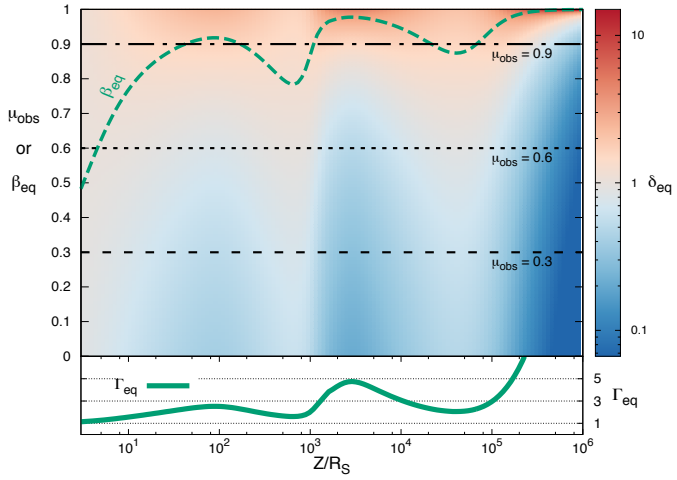

Fig. 11. *Upper panel*: equilibrium bulk Doppler factor $\delta_{\rm eq}$ in the jet plane altitude $Z/R_{\rm s}$ vs. observational angle $i_{\rm obs}$ ($\mu_{\rm obs} = \cos i_{\rm obs}$). The color scale is shown on the right. The green dashed line represents the corresponding $\beta_{\rm eq}$. *Bottom panel*: $\Gamma_{\rm eq}$ as a function of the jet altitude. The geometry is described in Sect. 3 and the source parameters are listed in Table 1.

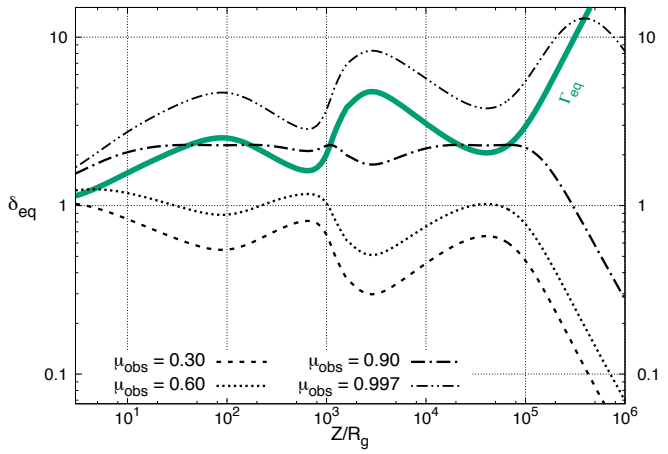

Fig. 12. Examples of equilibrium bulk Doppler factor as a function of the altitude for different observational angles $i_{\rm obs}$ ($\mu_{\rm obs} = \cos i_{\rm obs}$). The green solid line represents the corresponding $\Gamma_{\rm eq}$. The geometry is described in Sect. 3 and the source parameters are listed in Table 1.

intensity in the lab frame is given by $I_\nu = I'_\nu\,\delta_{\rm b}^3$. It can be shown that most of the emission is emitted within a characteristic emission cone of aperture angle $\approx 1/\Gamma$. This led to the idea that the same object seen from a different angle will show a different broadband spectrum and led to the AGN unification scheme (Blandford & Rees 1978; Orr & Browne 1982; and Barthel 1989).

For a given function $\Gamma_{\rm eq}(Z)$, it is possible to compute the function of the equilibrium bulk Doppler factor $\delta_{\rm eq}(Z, \mu_{\rm obs})$, which depends on the altitude and on the observer viewing angle. Figure 11 shows the function $\delta_{\rm eq}(Z, \mu_{\rm obs})$ in false colors, corresponding to the $\Gamma_{\rm eq}$ (see also Fig. 11) computed in Sect. 4 with the source parameters given in Table 1. Figure 12 shows the same $\delta_{\rm eq}$ as a function of the altitude, but for four chosen observation angles.

An observer situated at a constant $\mu_{\rm obs}$ sees the emission along the jet modulated by $\delta_{\rm eq}(Z)$. It can be seen in Figs. 11 and 12 that $\delta_{\rm eq}(Z)$ shows several extrema at a constant $\mu_{\rm obs}$. This means that certain zones of the jet are preferentially seen depending on the jet viewing angle $i_{\rm obs}$.

A few remarks can be made for peculiar values of $\delta_{\rm b}$.

a. $\delta_{\rm b} = 1$ is an important value for the observer because it marks the limit between an increase and a decrease in the observed flux compared to the flux in the comoving frame. As $\Gamma_{\rm eq}(Z)$ varies in the observer frame, so does $\delta_{\rm eq}$, and the same observer can be in the emission cone of certain parts of the jet and out of the emission cone of other parts of the jet. With the bulk Lorentz factor computed in Sect. 4, a value of $\delta_{\rm eq} = 1$ is possible for $0.52 < \mu_{\rm obs} < 0.96$.

b. Extrema of $\delta_{\rm eq}$ are found at Z verifying

$$\frac{\partial \delta_{\rm eq}}{\partial Z} = 0 \Leftrightarrow \left.\frac{\partial \delta_{\rm b}}{\partial \Gamma}\right|_{\Gamma_{\rm eq}} \left(\frac{\partial \Gamma_{\rm eq}}{\partial Z}\right) = 0.$$

We are then left with two possibilities:

- $\dfrac{\partial \Gamma_{\rm eq}}{\partial Z} = 0.$
  The solutions to this equation correspond to the $\Gamma_{\rm eq}$ extrema. In our case, they are approximately at $Z = 134\,R_{\rm S}$, $Z = 656\,R_{\rm S}$, $Z = 1.73 \times 10^3\,R_{\rm S}$, and $Z = 3.61 \times 10^4\,R_{\rm S}$.
- $\left.\dfrac{\partial \delta_{\rm b}}{\partial \Gamma}\right|_{\Gamma_{\rm eq}} = 0.$

It can be shown that this always happens for $\beta_{\rm b} = \mu_{\rm obs}$, or equivalently for $\delta_{\rm b} = \Gamma_{\rm b}$. These $\delta_{\rm b}(Z)$ extrema can be assimilated to a way in or out of the emission cone by the observer at $\mu_{\rm obs}$. In our particular case, Fig. 11 shows that this is possible for $\min(\beta_{\rm eq}) = 0.45 \lesssim \mu_{\rm obs} \lesssim 1 = \max(\beta_{\rm eq})$. Moreover, it can be confirmed for the cases $\mu_{\rm obs} = 0.6 - 0.9 - 0.997$ that the altitudes where $\beta_{\rm eq} = \mu_{\rm obs}$ in Fig. 11 correspond to the altitudes where $\delta_{\rm eq}$ reaches an extremum and where $\delta_{\rm eq} = \Gamma_{\rm eq}$ in Fig. 12.

However, $\Gamma_{\rm eq}$ extrema can correspond to $\delta_{\rm eq}$ minima or maxima depending on $\mu_{\rm obs}$. In the case $\beta_{\rm eq} < \mu_{\rm obs}$ (blazar-type objects), $\delta_{\rm eq}$ maxima are correlated with $\Gamma_{\rm eq}$ maxima. In consequence, for these objects an observer will preferentially see jet zones where $\Gamma_{\rm eq}$ is at a maximum since the jet emission will be more boosted. On the contrary, for $\beta_{\rm eq} > \mu_{\rm obs}$ (radio-galaxy-type objects), $\delta_{\rm eq}$ maxima are correlated with $\Gamma_{\rm eq}$ minima. This means that an observer will not see the zones of the jet that have the highest speed, but – on the contrary – the jet emission will be dominated by the slowest zones.

It is also interesting to note that there is a class of objects that will present very low modulation of the jet emission along Z. These objects are characterized by $\mu_{\rm obs} \approx \beta_{\rm eq}$ and thus $\dfrac{\partial \delta_{\rm eq}}{\partial Z} \approx 0$ almost everywhere in the jet. An example of this is shown by the case $\mu_{\rm obs} = 0.9$ in Fig. 12, where $\delta_{\rm eq}$ is almost constant from $Z = 10 R_{\rm S}$ to $Z = 10^5 R_{\rm S}$. Of course other sources of variations can still produce an important variability for these sources.

Similarly, different processes could dominate at different altitudes, only due to $\Gamma_{\rm eq}$ evolution. In particular, external and synchrotron self-Compton emissions do not have the same beaming pattern for a given Doppler factor as shown by Dermer (1995). This author showed that synchrotron self-Compton follows a general beaming pattern $\propto \delta_{\rm b}^{3+\alpha}$ (with α the energy spectral index of the radiation) whereas external Compton follows a beaming pattern $\propto \delta_{\rm b}^{4+2\alpha}$ because the Comptonized photon field is isotropic in the plasma rest frame in the SSC case whereas it depends on $\delta_{\rm b}$ in the external Compton case.

Moreover, the computation in Dermer (1995) assumed an external isotropic radiation and a pre-assumed bulk Lorentz factor. Both of these assumptions are no longer valid in our framework. This could have some consequences on the beaming statistics of these objects, but an exhaustive study of these effects could not be done without a complete modeling of the jet, which is not the purpose of this paper.

6. Dependence of $\Gamma_{\rm b}$ on the energetics

As stated previously, in the two-flow paradigm the Compton rocket process finds its energy in the turbulence from the outer MHD jet through the relativistic particle emission. It is therefore understandable that the energetics of the particles will limit the influence of the Compton rocket effect on the actual value of Γ. To compute the actual value of Γ, one can solve the following differential equation (Renaud & Henri 1998),

$$\frac{\partial \Gamma_{\rm b}(Z,\gamma_{\rm e})}{\partial Z} = \frac{F'^{z}}{\rho'} \frac{1}{\left(1 + \frac{1}{3\Gamma_{\rm b}^2}\right)} \tag{14}$$

$$\text{with } F'^{z} = \frac{\sigma_T}{c} 4\pi H' \int \left(1 + \frac{2}{3}\gamma_{\rm e}'^2 \beta_{\rm e}'^2\right) n_{\rm e}'(\gamma')\mathrm{d}\gamma'$$

$$\text{and } \rho' = \int \gamma' m_{\rm e} c^2 n_{\rm e}'(\gamma')\mathrm{d}\gamma'.$$

Here, it can be seen that the complete calculation of $\Gamma_{\rm b}(Z,\gamma_{\rm e})$ depends on the particle energy distribution. For the sake of simplicity, here we choose a Dirac distribution:

$$n_{\rm e}(\gamma) = N_{\rm e}\,\delta(\gamma - \gamma_{\rm e}). \tag{15}$$

In this case, the following results are obtained:

$$F'^{z} = \frac{\sigma_T}{c}\frac{8\pi}{3} N_{\rm e} \gamma_{\rm e}^2 H' \tag{16}$$

and

$$\rho' = N_{\rm e}\gamma_{\rm e} m_{\rm e} c^2. \tag{17}$$

For bulk Lorentz factors close to the equilibrium value, H' can be evaluated with a linear expansion:

$$H'(\Gamma_{\rm b}) \approx H'(\Gamma_{\rm eq}) + \frac{\mathrm{d}H'}{\mathrm{d}\Gamma_{\rm b}}\left(\Gamma_{\rm b} - \Gamma_{\rm eq}\right). \tag{18}$$

By definition $H'(\Gamma_{\rm eq}) = 0$, and it can be shown that

$$H' \approx -\frac{H}{\beta_{\rm eq}^3 \Gamma_{\rm eq}^3}\left(\Gamma_{\rm b} - \Gamma_{\rm eq}\right). \tag{19}$$

Finally, the following differential equation is solved:

$$\frac{\partial \Gamma_{\rm b}(Z,\gamma_{\rm e})}{\partial Z} = -\frac{1}{l(Z,\gamma_{\rm e})}\left(\Gamma_{\rm b}(Z,\gamma_{\rm e}) - \Gamma_{\rm eq}(Z)\right) \tag{20}$$

$$\text{with } l(Z,\gamma_{\rm e}) = \frac{3 m_{\rm e} c^3}{8\pi\sigma_T}\frac{\beta_{\rm eq}^3 \Gamma_{\rm eq}^3}{\gamma_{\rm e} H}\left(1 + \frac{1}{3\Gamma_{\rm eq}^2}\right).$$

As an example, we solve this equation and compute the actual value of $\Gamma_{\rm b}$ for several values of $\gamma_{\rm e}$ in two different cases: the accretion disk alone and the complete case seen Sect. 4.2 with

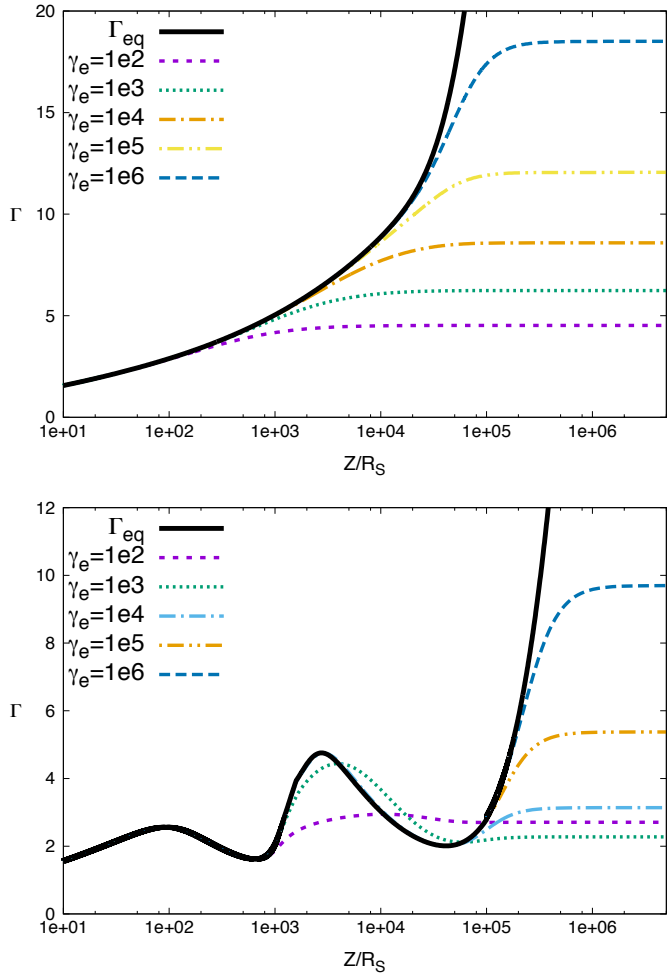

Fig. 13. Actual value of Γ_b as a function of the altitude in the jet Z/R_S for several values of γ_e. *Top*: standard accretion disk alone with an outer radius of $4e5R_s$. *Bottom*: accretion disk, dusty torus, and broad line region with parameter values from Table 1.

the accretion disk, the dusty torus, and the broad line region. In this study, we suppose γ_e constant along the jet. Of course, this is a simplistic assumption and a complex evolution of γ_e along the jet can be expected in a more complete modeling, but as we will see, it has very little influence on the evolution of Γ_b in the lowest part of the jet.

Here the Compton rocket appears as a restoring force on the plasma with a stiffness constant $\frac{1}{l(Z,\gamma_e)}$. The relaxation length towards the equilibrium value, $l(Z,\gamma_e)$, is inversely proportional to γ_e (i.e., the higher γ_e is, the stronger the force is and the longer the plasma will actually follow $\Gamma_{eq}(Z)$) , but the coupling is effective in the lowest parts of the jet, no matter the value of γ_e. At some distance (of the order of $l(Z,\gamma_e)$), the Compton rocket force slowly stops acting on the plasma. The bulk Lorentz factor then reaches a final Lorentz factor $\Gamma_b = \Gamma_\infty$ and follows a ballistic motion. It can be seen that in both cases in Fig. 13, high values of Γ_∞ can be achieved with reasonable values of γ_e. The value of Γ_∞ also depends strongly on the source geometry. Without the drag from the torus, it is easier for the jet to reach higher values of Γ_∞. Nevertheless, even with a strong torus, the computed values of Γ_∞ are entirely compatible with observed values by Lister et al. (2013) for the highest values of γ_e that are totally compatible with the observed high-energy emission.

7. Variation in the emission

The aim of this section is not to create a realistic model of a jet nor to explain all the variability of a single object, but to illustrate what type of variations would be induced by a variation of Γ_{eq}. We assume a jet composed of spherical emitting zones called blobs moving forward (see, e.g., Katarzynski et al. 2001; Boutelier et al. 2008; or Hervet et al. 2015, for *blob-in-jet* models). The emergence of a blob at the base of the jet would then correspond to a flare. In our framework, this blob moves forward in the jet with an imposed bulk Lorentz factor Γ_{eq}. Because of the variation of Γ_{eq} inducing variations of δ_{eq} for an observer, the blob emission will show some interesting changes. Therefore, a single flare will induce a complex variability as it moves along the jet, displaying associated peaks in the emission that we call echoes. To show and study these effects, we will set up a very simple jet model where we compute the synchrotron radiation (SYN), the synchrotron-self Compton (SSC), and the external Compton (EC) radiations. The following results are just examples of variations. A different model, or a complete modeling of the jet, would obviously show different results, but we can expect the variations to keep the same general features.

7.1. Jet modeling

To compute the emission, we first need to model the jet. The jet radius is fixed at a constant value $R_{jet} = 5\times10^2 R_S$. The magnetic field follows a power law $B = B_0\left(\frac{Z}{R_S}\right)^{-1}$ with $B_0 = 6.8\times10^{-2}G$ for the whole study. These values ensure that the same global evolution is kept between the magnetic energy density and the photon field energy density so we can compare the SCC emission and the EC emission along the jet.

We have chosen a pile-up distribution for the energy distribution. It has the advantage of presenting one parameter less than a power-law distribution and concurs better with the idea of particles accelerated through the second-order Fermi process. It can be written as

$$n(\gamma) = \frac{\gamma^2}{2\bar{\gamma}^3}\exp\left(-\frac{\gamma}{\bar{\gamma}}\right). \quad (21)$$

Particles have to be energetic enough to explain the high-energy emission of AGNs, but we also assumed the Thomson regime to compute Γ_{eq}. The Thomson condition can be expressed as $\gamma\epsilon_s(1-\cos\theta_s) \ll 1$ in the bulk frame. Using the sources parameters given in Table 1, the computation of $\epsilon_S(1-\cos\theta_S)$ along the jet in the rest frame of a flow at Γ_{eq} gives a maximum value of 10^{-4} for the photons coming from the BLR, of 10^{-5} for the photons coming from the disk, and of 10^{-6} for the photons coming from the torus. The pile-up distribution has a mean value $\langle\gamma\rangle = 3\,\bar{\gamma}$ and drops rapidly at higher γ because of the exponential term. Setting a value of $\bar{\gamma} = 10^5$ allows us to stay in the Thomson regime almost everywhere along the jet and to obtain a $\Gamma_\infty > 5$. Therefore, one can presume $\Gamma = \Gamma_{eq}$ to compute the emission at every altitude in the jet.

Pursuing what was said in the previous sections, each slice of the external emitting regions is a different source characterized by four numbers: $\mu_s = \cos\theta_s$ with θ_s the incoming angle and $d\Omega$ the solid angle both described in Figs. 1 and 2; the temperature T; and the emissivity ε. These parameters seen in the bulk frame depend on $\delta_b = \Gamma(1-\beta_b\mu_s)$ and are given by (parameters

A&A 581, A18 (2015)

in the bulk rest frame are denoted by a prime)

$$T' = \delta_b T \qquad d\Omega' = \frac{1}{\delta_b^2} d\Omega \qquad (22)$$

$$\mu'_s = \frac{\mu - \beta_b}{1 - \beta_b \mu_s} \qquad \varepsilon' = \varepsilon.$$

7.2. Computation of the emission along the jet in two energy bands

The model being set, we were able to compute broadband emission (including SYN, SSC, and EC) at every altitude along the jet for a flow at $\Gamma_b = \Gamma_{eq}$. From this, we computed the total emitted power at every altitude $\left(\frac{dP}{d\Omega}\right)_{eq}$ in two characteristic energy bands:

- Infrared: [1 meV−1 eV].
- γ-rays: [20 MeV−300 GeV].

This allows us to study the evolution of the emission as a blob of particles moves forward in the jet. Nevertheless, the emission $\frac{dP}{d\Omega}$ depends on Γ_b but also on the jet model. In order to decouple the variations of emission due to the jet model from the emission due to the variations of Γ_{eq}, we computed $\left({}^{dP}/_{d\Omega}\right)_{eq}$, i.e., the emission with $\Gamma_b = \Gamma_{eq}$, and $\left({}^{dP}/_{d\Omega}\right)_5$, i.e., the emission with $\Gamma_b = 5$. This way, the function $\frac{(dP/d\Omega)_{eq}}{(dP/d\Omega)_5}(Z)$ is only modulated by the variations of Γ_{eq}, excluding other sources of variability.

7.3. Time dependance of the emission in the case of a single blob moving in the jet

In the case of a single blob traveling along the jet, we can convert the altitude into time, but owing to light time travel effects, the time between two events in the observer frame is different from the time between these two events in the lab frame. In the case of a single blob moving along the jet, the relation between Z and the observation time is given by

$$t_{obs} = \int_{Z_0}^{Z_f} \frac{1}{\beta_{eq} c} \left(1 - \beta_{eq}\, \mu_{obs}\right) dZ. \qquad (23)$$

An example of the dependance of the altitude on the observed time is given in Fig. 14 for several observation angles. The parameters to compute Γ_{eq} are the same as those used Sect. 5.3.

7.4. Emission variability as a function of model parameters

In order to compare the evolution of the emission to the evolution of Γ_{eq} = along the jet, the study has been performed with the parameters given in Table 1. The results are shown in Figs. 15 and 16.

The variations are simultaneous in infrared (IR) and in γ rays and follow the variations of Γ_{eq} studied in Sect. 5. The conclusions regarding the variations are quite similar to those on Γ_{eq}. The first echo lasting several hours is due to the acceleration of the flow followed by a deceleration due to the dragging effect from the BLR. The jet is then reaccelerated by the disk and the BLR before being dragged again by the torus, giving a second echo.

However, as the flow moves more quickly, the time contraction increases resulting in different variation timescale.

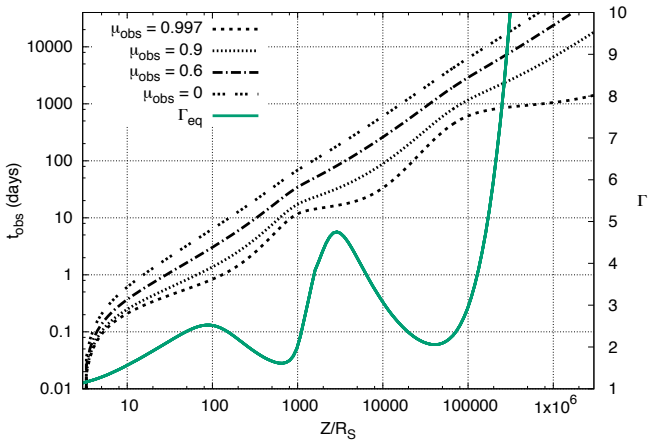

Fig. 14. Example of evolution of the observation time as a function of the altitude in the jet for different observation angles. The solid line is the Γ_{eq} curve, the value of Γ is in the scale shown on the right.

These timescales depend on the sizes of the different sources of external emission. Because it is closer to the base of the jet, the BLR is responsible for the short timescale variations (from some hours to some days in our study). The torus, however, is responsible for variations at larger timescales (from several days to years).

7.4.1. Influence of the BLR parameters

Figure 15 shows the influence of the BLR parameters on the time lag effects. The upper plot in Fig. 15 concerns the geometrical repartition of the BLR (through its opening angle ω_{max}) at constant total luminosity $L_{blr} = 0.1 L_{disk}$. One can see that effects are more important with a larger covering factor because parts of the BLR closer to the jet axis have more influence on the Compton rocket.

The influence of total luminosity of the BLR (given by α_{blr}) is more important (middle panel). For an ineffective BLR ($\alpha_{blr} = 0$), there is only one echo around day 4 imposed by the torus, but as the BLR becomes more important, two echoes appear, the first lasting several hours and the second a few days. We note that the greater the BLR, the more separated these two echoes are and the more peaked they are. Whereas the first echo always occurs around day 1, the second occurs later and later, from a few days to a hundred days.

Last panel concern the BLR radius. The radius has almost the same effect as α_{blr} as it can delay the second echo. It is also worth noting that the first and second echoes are inversely important. As the BLR grows bigger, the first echo arises later and is more important (because Γ_{eq} is). The second echo also arises later but because it is limited by the influence of the torus, its amplitude is diminished.

Depending on the geometry and on the total luminosity of the BLR, we see that different behaviors in the time modulation of the emission are possible, which could lead to very different time variability in different objects.

7.4.2. Influence of the torus parameters

We can see the influence of the torus size in Fig. 16. The radius of the torus evolves while we keep the continuity between the accretion disk and the torus so $D_t = r_{out} + R_t$.

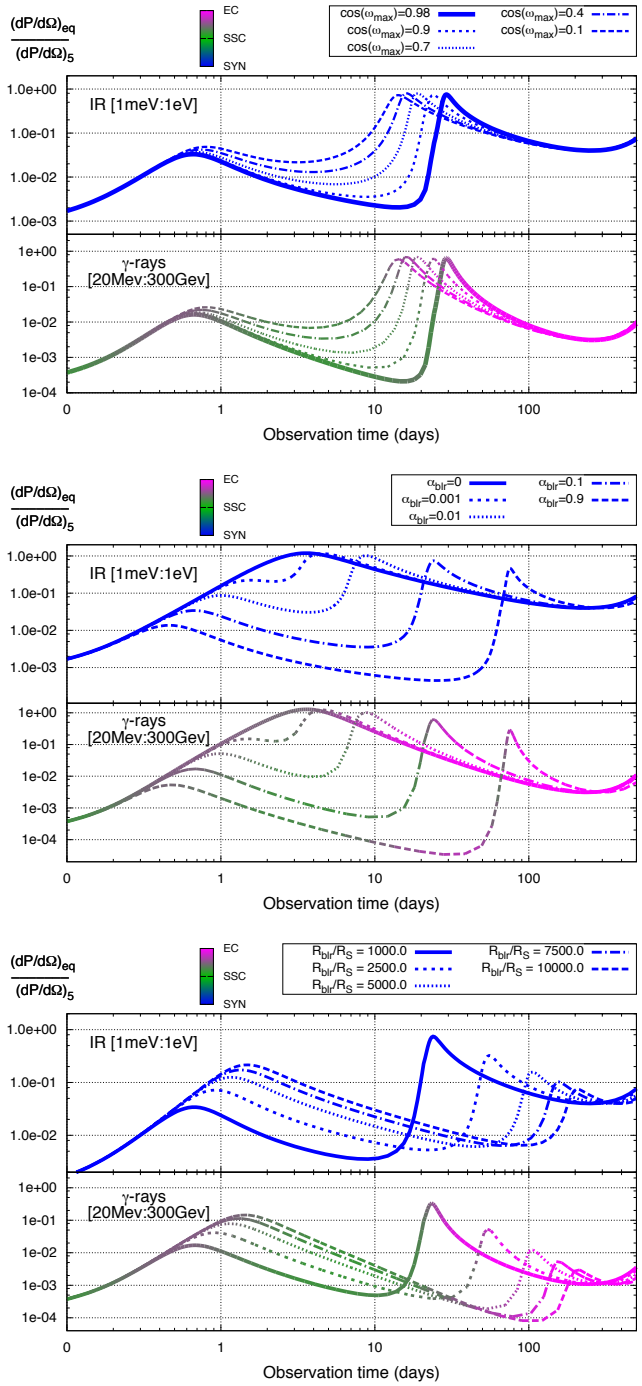

Fig. 15. Evolution of the emission in the direction of the observer ($\cos i_{\rm obs} = 0.997$) as a function of observed time for a range of BLR parameters. The emission of the blob following $\Gamma_{\rm eq}$, $(dP/d\Omega)_{\rm eq}$ is normalized by the emission of a blob at $\Gamma = 5$, $(dP/d\Omega)_5$. Values of all parameters are listed in Table 1. The color scale indicates the dominant emission process.

Here, we see again the two echoes imposed by the BLR and the drag from the torus after the flow crossed the BLR. As we can see, the second echo (which has timescale of at least ten days), is driven by the torus size. With a greater torus size, the echo arises sooner, but is more tamed. On the contrary, a smaller torus allows the flow to reach a larger velocity, implying a stronger echo here.

At a certain point, as explained in Sect. 2, the flow only accelerates, increasing the emission, but when the observer leaves

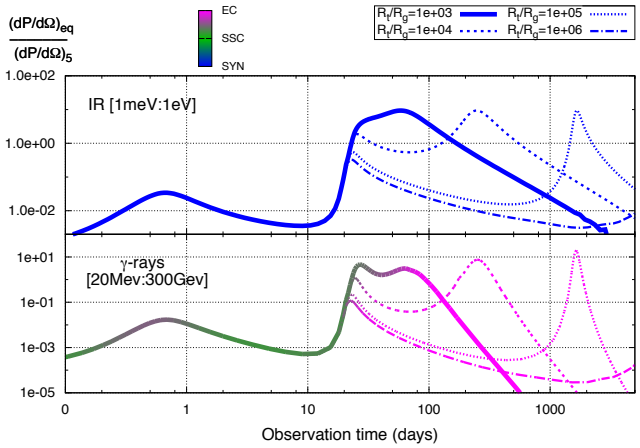

Fig. 16. Evolution of the emission in the direction of the observer ($\cos i_{\rm obs} = 0.997$) as a function of observed time for a range of torus parameters. The emission of the blob following $\Gamma_{\rm eq}$, $(dP/d\Omega)_{\rm eq}$ is normalized by the emission of a blob at $\Gamma = 5$, $(dP/d\Omega)_5$. Values of all parameters are given in Table 1. The color scale indicates the dominant emission process.

the emission cone (which is highly dependent on the observation angle), the observed emission will decrease, giving the last echo. Here too, the torus size has a huge impact on the timescale of the variability. The smaller the torus, the sooner this echo arises (around day 100 here). When the torus size increases, this last echo gets delayed (up to day 2000 here), but its extent does not increase accordingly which makes it comparatively steeper. It is also interesting to note that the maximum observed value of the emission does not depend on the torus size for this kind of echo.

8. Conclusion

The question of the acceleration of AGN jets is still a matter of discussion as we do not know the underlying processes or the precise speeds of the flows. The solution implied by the Compton rocket effect, viable in the two-flow paradigm, is elegant as it can naturally lead to relativistic speeds. In this work, we embrace this framework and study the influence of several external photon sources (the accretion disk, the dusty torus, and the broad line region) on the Compton rocket effect and on the induced bulk Lorentz factor. To do so, we carefully computed the resulting equilibrium bulk Lorentz factor, $\Gamma_{\rm eq}$, of a flow driven by the Compton rocket effect taking into account the anisotropy of the emission. With several external sources, $\Gamma_{\rm eq}$ will show important changes along the jet, leading to acceleration and deceleration phases. We studied the influence of the external sources on these patterns and the induced Doppler factor as a function of the observation angle. We also showed that the emission of a flow following this $\Gamma_{\rm eq}$ will experience correlated variations and that a single flare could be echoed several times. This could take part in the time-variation of these very variable objets and so we computed some examples of observed emission to illustrate our discussion. Even though these effects could not explain all the AGN variability alone, we find some interesting and non-trivial effects that could be part of the observed variability. This work could have some influence on the statistical study of AGNs and on their modeled variability. It will be followed by a more complete and more realistic model, applied to real objects to understand more precisely the role of the Compton rocket in the AGN variability.

Acknowledgements. We acknowledge funding support from the French CNES agency. We also thank the referee as well as the editor for useful comments and corrections which greatly improved the manuscript.

References

Baring, M. G. 1994, ApJSS, 90, 899
Barthel, P. D. 1989, ApJ, 336, 606
Blandford, R. D., & Rees, M. J. 1978, in Pittsburgh Conf. on BL Lac Objects, 328
Boutelier, T., Henri, G., & Petrucci, P.-O. 2008, MNRAS, 390, L73
Chiaberge, M., Celotti, A., Capetti, A., & Ghisellini, G. 2000, A&A, 358, 104
Cohen, M. H., Cannon, W., Purcell, G. H., et al. 1971, ApJ, 170, 207
Dermer, C. D. 1995, ApJ, 446, L63
Georganopoulos, M., & Kazanas, D. 2003, ApJ, 594, L27
Georganopoulos, M., & Marscher, A. P. 1998, ApJ, 506, 621
Ghisellini, G., & Tavecchio, F. 2010, MNRAS, 409, L79
Ghisellini, G., Maraschi, L., & Treves, A. 1985, A&A, 146, 204
Ghisellini, G., Tavecchio, F., & Chiaberge, M. 2005, A&A, 432, 401
Giovannini, G., Taylor, G. B., Arbizzani, E., et al. 1999, ApJ, 522, 101
Giroletti, M., Giovannini, G., Feretti, L., et al. 2004, ApJ, 600, 127
Hardcastle, M. J., Kraft, R. P., Sivakoff, G. R., et al. 2007, ApJ, 670, L81
Henri, G., & Saugé, L. 2006, ApJ, 640, 185
Hervet, O., Boisson, C., & Sol, H. 2015, A&A, 578, A69
Katarzynski, K., Sol, H., & Kus, A. 2001, A&A, 367, 809
Li, H., & Wang, J. 2004, ApJ, 617, 162
Lister, M. L., Aller, M. F., Aller, H. D., et al. 2013, AJ, 146, 120
Madau, P., & Thompson, C. 2000, ApJ, 534, 239
Marcowith, A., Henri, G., & Pelletier, G. 1995, MNRAS, 277, 681
Marcowith, A., Pelletier, G., & Henri, G. 1997, A&A, 323, 271
Marscher, A. P. 1980, ApJ, 235, 386
Melia, F., & Konigl, A. 1989, ApJ, 340, 162
O'dell, S. L. 1981, ApJ, 243, L147
Orr, M. J. L., & Browne, I. W. A. 1982, MNRAS, 200, 1067
Phinney, E. S. 1982, MNRAS, 198, 1109
Rees, M. J. 1966, Nature, 211, 468
Renaud, N., & Henri, G. 1998, MNRAS, 300, 1047
Rybicki, G. B., & Lightman, A. P. 1979, in Radiative processes in astrophysics (New York: Wiley-Interscience), 393
Shakura, N. I., & Sunyaev, R. A. 1973, A&A, 24, 337
Sikora, M., Sol, H., Begelman, M. C., & Madejski, G. M. 1996, MNRAS, 280, 781
Sol, H., Pelletier, G., & Asseo, E. 1989, MNRAS, 237, 411
Swain, M. R., Bridle, A. H., & Baum, S. A. 1998, ApJ, 507, L29
Tavecchio, F., & Ghisellini, G. 2008, MNRAS, 386, 945
Tavecchio, F., & Ghisellini, G. 2014, MNRAS, 443, 1224
Yang, J., Wang, J., Dai, B., & Gao, X. 2009, PASJ, 61, 1153

7.3 Γ_∞ - complete calculation and approximation

As explained previously, $\Gamma_b(Z) = \Gamma_{eq}(Z)$ as long as the plasma is coupled with the soft radiation field. The decoupling occurs when the inverse Compton emission time becomes greater than the dynamical time in the plasma rest frame.

By considering the conservation of the stress-energy tensor, Renaud and Henri (1998) showed that the actual value of $\Gamma_b(Z)$ could be computed by solving the differential equation:

$$\frac{\partial \Gamma_b(Z,\gamma_e)}{\partial Z} = \frac{F'^z}{\rho'} \frac{1}{\left(1+\frac{1}{3\Gamma_b^2}\right)} \tag{7.2}$$

with $F'^z = \frac{\sigma_T}{c} 4\pi H' \int \left(1+\frac{2}{3}\gamma_e'^2\beta_e'^2\right) n_e'(\gamma')\mathrm{d}\gamma'$ the force exerted on the pair plasma and $\rho' = \int \gamma' m_e c^2 n_e'(\gamma')\mathrm{d}\gamma'$ the energy density of the plasma.

It is assumed here that the continuous acceleration required for the Compton rocket to be effective on great distances is isotropic in the plasma rest frame so it does not intervene in the force expression.

As shown in the section 7.2, equation (7.2) can be approximated to:

$$\boxed{\frac{\partial \Gamma_b(Z,\gamma_e)}{\partial Z} = -\frac{1}{l(Z,\gamma_e)}\left(\Gamma_b - \Gamma_{eq}\right)} \tag{7.3}$$

with

$$l(Z,\gamma_e) = \frac{\rho' H'}{F'^z} \frac{\beta_{eq}^3 \Gamma_{eq}^3}{H} \left(1+\frac{1}{3\Gamma_{eq}^2}\right) \tag{7.4}$$

In equation (7.3), $\frac{1}{l(Z,\gamma_e)}$ acts as a stiffness constant, pulling Γ_b to its equilibrium value on a relaxation length $l(Z,\gamma_e)$. When the relaxation length is short compared to the dynamical length, the plasma is strongly tight to the radiation, it is driven by the Compton rocket effect and has a bulk Lorentz factor very close (or equal) to the equilibrium one Γ_{eq}.

In the study in section 7.2, I made the calculation of F'^z and ρ' for a particle Dirac distribution but one can also make it for a power-law and a pile-up distribution:

For a power-law distribution $n_e(\gamma) = N_e^* \gamma^{-s}$ from γ_{min} to γ_{max} with $N_e^* = \frac{s-1}{\left(\gamma_{min}^{1-s} - \gamma_{max}^{1-s}\right)} N_e$ and $s \neq 1$, one has:

- For $s = 2$

$$\begin{cases} F'^z = \frac{8\pi}{3}\frac{\sigma_T}{c} H' N_e^* \left[\frac{\gamma^{3-s}}{3-s}\right]_{\gamma_{min}}^{\gamma_{max}} \\ \rho' = m_e c^2 N_e^* \left[\ln\gamma\right]_{\gamma_{min}}^{\gamma_{max}} \end{cases} \tag{7.5}$$

So

$$\boxed{l(z,\gamma) = \left(1+\frac{1}{3\Gamma_{eq}^3}\right) \frac{\beta_{eq}^3 \Gamma_{eq}^3}{H} \frac{3 m_e c^3}{8\pi\sigma_T} \frac{1}{(\gamma_{max}-\gamma_{min})} \ln\left(\frac{\gamma_{max}}{\gamma_{min}}\right)} \tag{7.6}$$

- For $s = 3$

$$\begin{cases} F'^z = \dfrac{8\pi}{3}\dfrac{\sigma_T}{c} H' N_e^* \left[\ln\gamma\right]_{\gamma_{min}}^{\gamma_{max}} \\ \rho' = m_e c^2 N_e^* \left[\dfrac{\gamma^{2-s}}{2-s}\right]_{\gamma_{min}}^{\gamma_{max}} \end{cases} \tag{7.7}$$

So

$$\boxed{l(z,\gamma) = \left(1 + \frac{1}{3\Gamma_{eq}^3}\right) \frac{\beta_{eq}^3 \Gamma_{eq}^3}{H} \frac{3 m_e c^3}{8\pi\sigma_T} \frac{\left(\gamma_{max}^{-1} - \gamma_{min}^{-1}\right)}{\ln\left(\dfrac{\gamma_{max}}{\gamma_{min}}\right)}} \tag{7.8}$$

- Otherwise

$$\begin{cases} F'^z = \dfrac{8\pi}{3}\dfrac{\sigma_T}{c} H' N_e^* \left[\dfrac{\gamma^{3-s}}{3-s}\right]_{\gamma_{min}}^{\gamma_{max}} \\ \rho' = m_e c^2 N_e^* \left[\dfrac{\gamma^{2-s}}{2-s}\right]_{\gamma_{min}}^{\gamma_{max}} \end{cases} \tag{7.9}$$

So

$$\boxed{l(z,\gamma) = \left(1 + \frac{1}{3\Gamma_{eq}^3}\right) \frac{\beta_{eq}^3 \Gamma_{eq}^3}{H} \frac{3 m_e c^3}{8\pi\sigma_T} \left(\frac{\gamma_{max}^{2-s} - \gamma_{min}^{2-s}}{\gamma_{max}^{3-s} - \gamma_{min}^{3-s}}\right) \left(\frac{3-s}{2-s}\right)} \tag{7.10}$$

For a pile-up distribution $n_e(\gamma) = N_e \dfrac{\gamma^2}{2\bar{\gamma}^3} \exp\left(-\gamma/\bar{\gamma}\right)$, one has:

$$F'^z = \frac{\sigma_T}{c} 32\pi H' \bar{\gamma}' N_e \qquad \& \qquad \rho' = 3 m_e c^2 \bar{\gamma}' N_e \tag{7.11}$$

So

$$\boxed{l(z,\bar{\gamma}) = \frac{3 m_e c^3}{32\pi\sigma_T \bar{\gamma}} \left(1 + \frac{1}{3\Gamma_{eq}^2}\right) \frac{\beta_{eq}^3 \Gamma_{eq}^3}{H}} \tag{7.12}$$

7.3.1 Approximation of Γ_∞ for a pile-up distribution

As explained in the section 5.3, we use a pile-up distribution in the numerical code. The integration of the differential equation (7.3) to find $\Gamma_b(Z)$ can be very time consuming. However, the altitude when $\Gamma_b(Z)$ decouple from $\Gamma_{eq}(Z)$ can be approximated. As explained in the article section 7.2, $l(Z,\bar{\gamma})$ acts as a stiffness constant, pulling back $\Gamma_b(Z)$ to $\Gamma_{eq}(Z)$ and corresponds to the dynamical length. Therefore, $\Gamma_b(Z)$ should decouple from $\Gamma_{eq}(Z)$ when $l(Z,\bar{\gamma})$ is of the order of Z. Numerically I found that the value of $\Gamma_{eq}(Z)$ when $\dfrac{l(Z,\bar{\gamma})}{Z} \approx 0.6$ is not far from the asymptotic value $\Gamma_b(Z \to \infty)$ (see figure 7.3. Therefore, in the code we simplify the computation of $\Gamma_b(Z)$ by computing $\Gamma_b(Z) = \Gamma_{eq}(Z)$ until it reached its asymptotic value:

$$\Gamma_b(Z) = \begin{cases} \Gamma_{eq}(Z) & \text{for} Z < Z_{lim} \\ \Gamma_{eq}(Z_{lim}) & \text{for} Z \geq Z_{lim} \end{cases} \tag{7.13}$$

with Z_{lim} such as $\dfrac{l(Z_{lim},\bar{\gamma})}{Z_{lim}} = 0.6$

One can compare the approximation with the complete calculation of Γ_∞ for the disc only and all sources (disc+torus+blr) (see figure 7.3). The estimated error for the asymptotic value is less than 4%. However, there is a range of altitude Z for which the error is greater (between the altitude corresponding to the decoupling between Γ_{eq} and the actual Γ_b and the altitude where Γ_b converges to its asymptote. The maximal error on Γ_b can reach 25 to 30% here, but only on a short length. We consider this error acceptable considering the important gain in computing time realized.

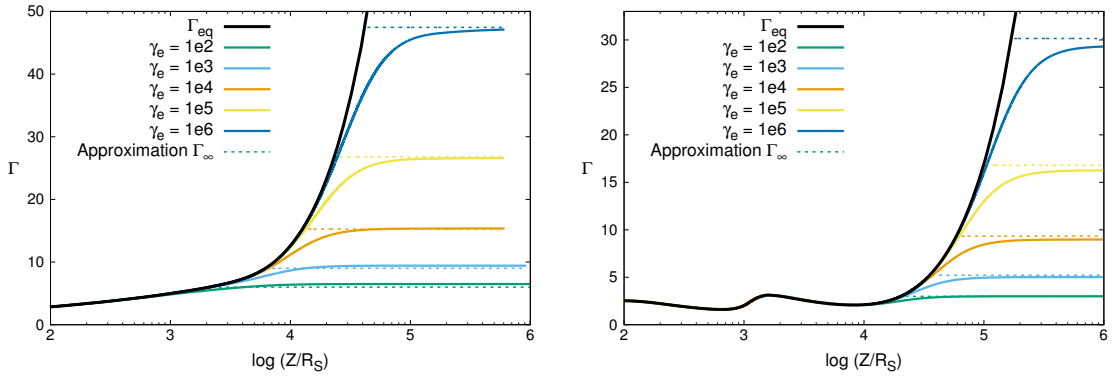

Figure 7.3: Comparison of the compete calculation of Γ_∞ (thick colored lines) with its approximation given by equation (7.13) (dotted lines with corresponding colors) for several γ_e. *Left:* Accretion disc alone. *Right:* Accretion disc, torus and BLR. The computation is done for $M_\bullet = 5\times10^8 M_\odot$ and $\dot{M} = \dot{M}_{edd}$. $R_{in} = 3R_S$ & $R_{out} = 10^4 R_S$. $D_t = 2\times10^4 R_S$ & $R_t = 10^4 R_S$. $R_{blr} = 10^3 R_S$, $\alpha_{blr} = 0.1$ & $\cos\omega_{max} = 0.9$.

7.4 A whole range of observed Γ

Observations show very different values of the bulk Lorentz factor from objects to objects. It ranges from a few to 40 for the fastest jets (Lister et al. (2013)). Therefore, it is interesting to see if the Compton rocket process can reproduce such a broad range of values. In the Thomson regime, the evolution of $\Gamma_{eq}(Z)$ depends only on the geometrical distribution of the external sources. However, the asymptotic value depends on the energetics of the system, namely the accretion rate $\dot{M}$ and the particle energy γ_e. The asymptotic value would actually correspond to measurements of Γ in jets as they are done at distance greater than 1 parsec in most jets[3]. In the following, the computation are made for a pile-up distribution (see equation (7.12)) of parameter γ_e.

7.4.1 Influence of energetics

The stiffness parameter given by equation (7.12) depends on the particles mean energy $\bar{\gamma}$ and on the photon flux in the sources frame H. However, the photon flux directly depends on the the reduced accretion rate $\dot{m} = \dfrac{L_{disc}}{L_{edd}}$ which can therefore be used as variable to study the evolution of Γ_∞.

[3]minus a few exceptions such as M87 for which observations can now access the inner parts of the jet (Kovalev et al. (2007))

This is done for a standard accretion disc (SAD) alone in figure 7.4 showing that we obtain values of Γ_∞ ranging from 1 to 50 for the most extreme objects. The study is limited to $\bar{\gamma} < 10^6$ here as it corresponds to the Klein-Nishina limit for photons from the SAD in the bulk rest frame. The corrections from these results in the KN regime is not easy to predict but one could expect values of Γ_∞ of the same order as the one obtained here (see section 7.5 for a discussion about the KN regime).

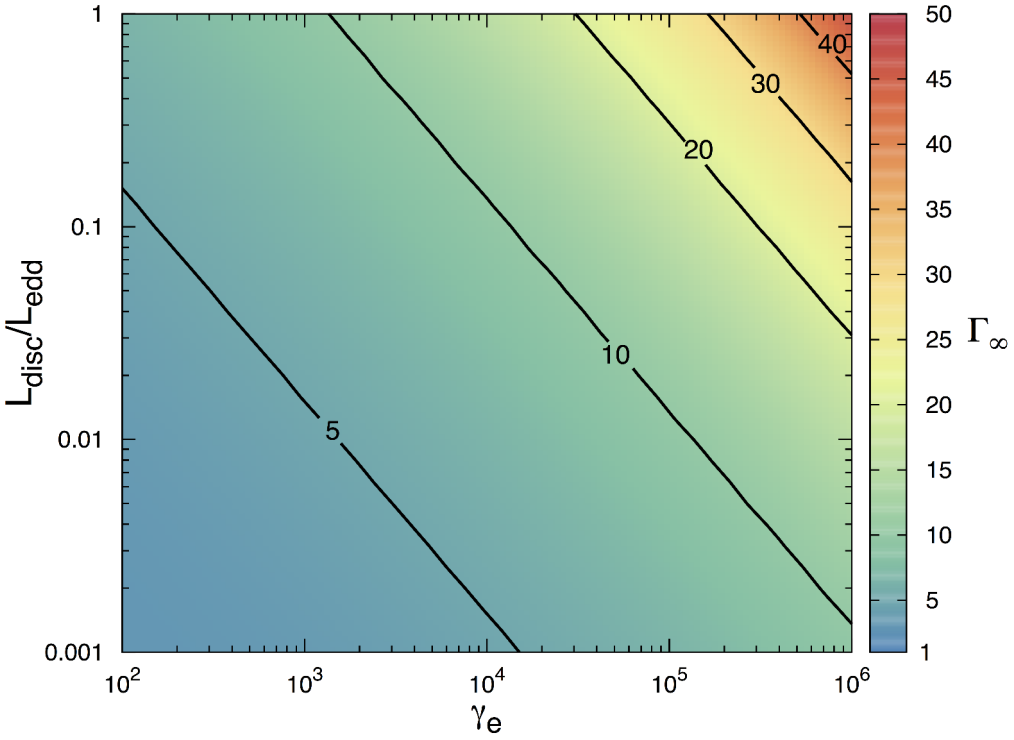

Figure 7.4: Γ_∞ for an accretion disc alone in function of γ_e for a pile-up distribution and $\dot{m} = \frac{L_{disc}}{L_{edd}}$. Parameters for the disc are $R_{in} = 3R_S$ and $R_{out} = 1e4R_S$ for $M_\bullet = 5 \times 10^8 M_\odot$

It is worth noting that the range of values obtained here is in perfect agreement with observations. Observed or expected values of L_{disc} and γ_e easily give values of Γ_∞ between a few and 20, which represent most of the measured values in jets (Lister et al. (2013), hereafter Li13). More extreme objects can reach values of Γ_∞ as high as 40 to 50, here also in agreement with observations. Li13 has also showed that intrinsically more powerful jets tend to be faster. Our results are in good agreement with these observations as more powerful jets are expected to have higher energy particles and extract energy from an important accretion rate. Finally, it is also known from Kellermann et al. (2007), Onuchukwu and Ubachukwu (2013) and Li13 that BL Lacs have the slowest jets, which can be easily explained here by their smaller disc luminosity, leading them to smaller values of Γ_∞.

As seen previously (in section 7.2), the $\Gamma_{eq}(Z)$ is quite different when other external sources of photon are added. Therefore, one can expect very different results for Γ_∞ as well. The same study has been realized with a BLR ($R_{blr} = 10^3 R_S, \alpha_{blr} = 0.1, \cos\omega_{max} = 0.9$) and a torus ($D_t = 2 \times 10^4 R_S$ and $R_t = 10^4 R_S$).

Because the accelerating phase is less direct and happens on greater length with a more complex photon field than with only an accretion disc (see section 7.2), the plasma

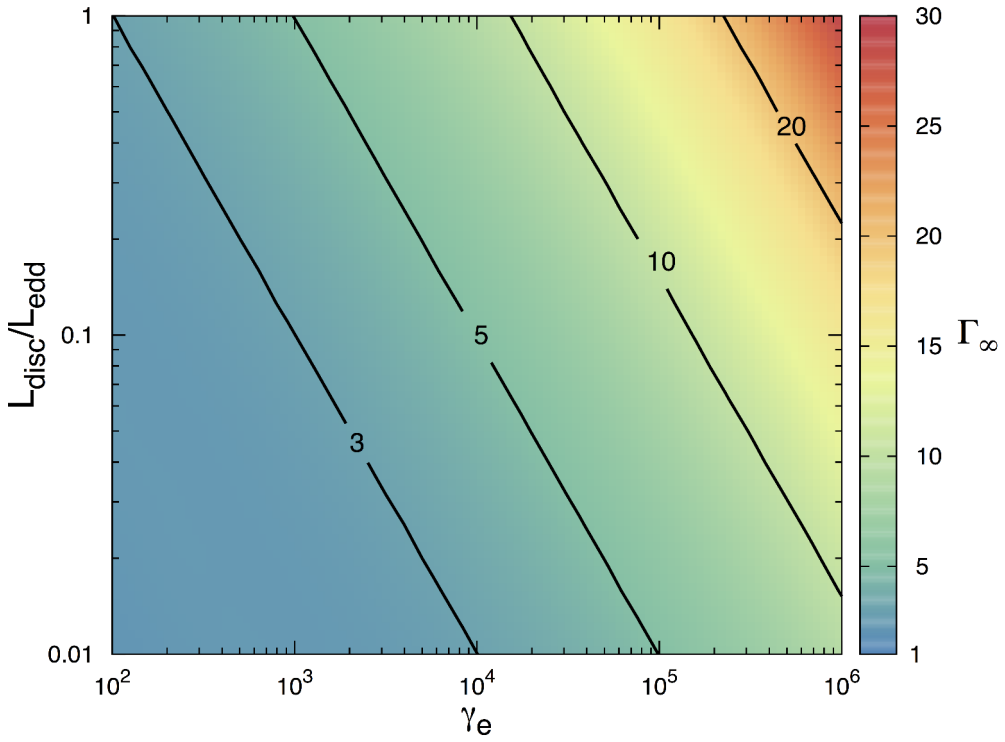

Figure 7.5: Γ_∞ in the case (SAD + Torus + BLR) in function of γ_e for a pile-up distribution and $\dot{m} = \frac{L_{disc}}{L_{edd}}$. Parameters for the sources are $R_{in} = 3R_S$ and $R_{out} = 10^4 R_S$.

requires more distance to reach high Γ. As a result, values reached by Γ_∞ are smaller than in the SAD case and do not exceed 30 in the best case. One still obtains relativistic speeds of the order of the one observed in jets but it can be difficult to explain the fastest jets in objects showing strong external sources such as a BLR or a dusty torus. This is studied in further details in the next section.

7.4.2 Explaining the fastest jets

In the previous section, we saw that a general study can explain the broad range of Lorentz factor measured in jets. However, we also saw that the drag from the torus and the BLR could be a brake to reach the highest values of Γ_b. In this section, I will look more precisely at the fastest known AGN, PKS 1510-089 to see if the Compton rocket process can explain such an extreme object. PKS 1510-089 is a very intriguing and extreme FSRQ. It is located at a redshift $z = 0.361$, has shown very high emission (up to the TeV, H.E.S.S. Collaboration et al. (2013)) and is the host of very fast motion, with apparent speeds up to 46c (Jorstad et al. (2005) - hereafter J05). The black-hole mass has been estimated at $M_\bullet \approx (1.16 - 1.98) \times 10^8 M_\odot$ by Dai et al. (2002) and at $M_\bullet \approx 4.47 \times 10^8 M_\odot$ by Woo and Urry (2002). The "big blue bump" attributed to the emission of the accretion disc (Pian and Treves (1993)) is well visible in the SED and its luminosity is evaluated at $L_{disc} = 5 \times 10^{45}$erg.s^{-1} (Nalewajko et al. (2012)). For $M_\bullet = 2 \times 10^8 M_\odot$, this luminosity corresponds to a standard accretion disc with $\dot{m} = 0.4$. Broad emission lines have been detected first by Malkan and Moore (1986) and then confirmed by Tadhunter et al. (1993). It is not clear whether a thermal emission from dust has been detected (Tanner et al. (1996)), however Kataoka et al. (2008) required a thermal emission corresponding to the

torus with a luminosity $L_{torus} = 3.7 \times 10^{45}$erg.s^{-1} to explained the broadband emission with their emission model. To study the resulting Γ_b of PKS 1510-089 system, I used the following values given in table 9.2.

Case	$\bar{\gamma}$	$M_\bullet$	$\dot{m}$	R_{in}	R_{out}	R_{blr}	α_{blr}	R_t	D_t
1	10^6	$2 \times 10^8 M_\odot$	0.4	$3R_S$	$10^4 R_S$	$10^3 R_S$	0.1	$10^4 R_S$	$2 \times 10^4 R_S$
2	10^6	$2 \times 10^8 M_\odot$	0.4	$3R_S$	$10^4 R_S$	$10^3 R_S$	0.1	-	-
3	10^6	$2 \times 10^8 M_\odot$	1	$3R_S$	$10^4 R_S$	$10^3 R_S$	0.1	-	-
4	10^6	$2 \times 10^8 M_\odot$	0.4	$3R_S$	$10^3 R_S$	$10^3 R_S$	0.1	-	-

Table 7.1: Parameters used for the study of Γ_∞ in PKS150-089.

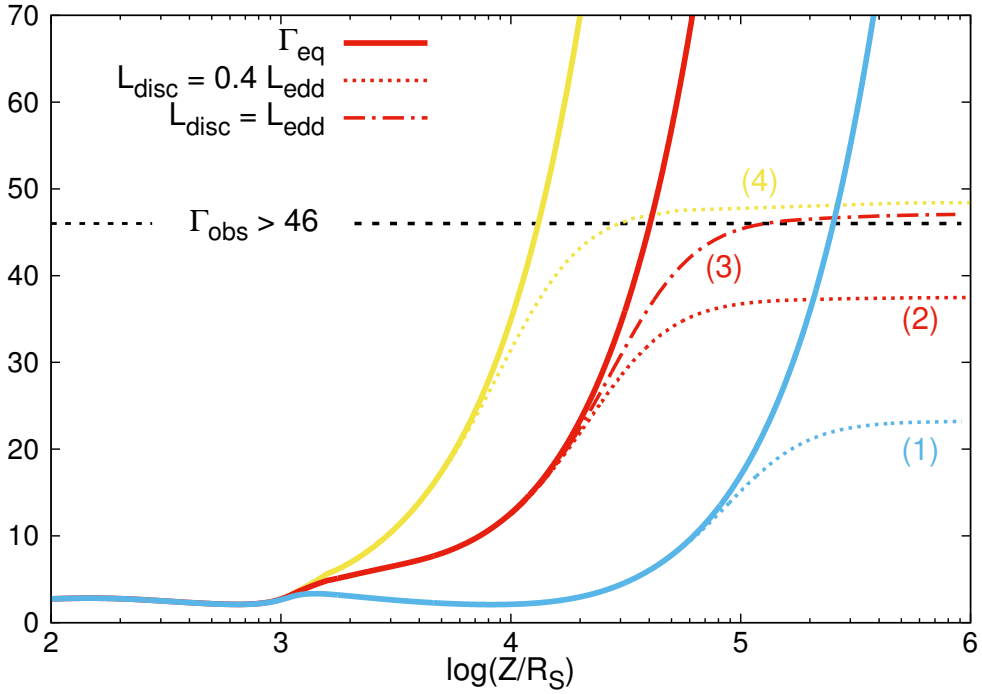

Figure 7.6: Computation of Γ_b in the case of PKS 1510-089 for different sources and accretion rates. Thick lines always represent Γ_{eq} while dotted lines represent Γ_b for different accretion rate. The numbers and colors correspond to the cases whose parameters are given in table 9.2.

In figure 7.6 are represented different solution for Γ_b for different geometry and accretion rates.

- Case 1: Starting with the sources required by Kataoka et al. (2008) to fit the overall SED of PKS 1510-089, in blue here, one can see that Γ_b only reaches $\Gamma_\infty \approx 21$, which is not enough to explain the measured value by J05. This is of course in agreement with figure 7.5. However, the torus was a model necessity in this case but is not actually confirmed by data. Therefore, one can see what happens without the torus.

- Cases 2 & 3: The solution with a SAD and a BLR with the same as previsouly sizes. The values reached by Γ_b are then higher but an accretion rate of $0.4\dot{M}_{edd}$ is not sufficient. With this geometry, an accretion rate $\dot{M} = \dot{M}_{edd}$ is required to obtain $\Gamma_\infty \approx 46$.

- Case 4: Another possibility to reach higher Γ_b is to reduce the sources sizes. Indeed, with a more compact disc and BLR, the fast acceleration happens at lower altitude in the jet, allowing a decoupling from Γ_{eq} sooner but also at higher Γ_b. Here, one can see in yellow that with a smaller SAD ($R_{out} = 10^3 R_S$) but with luminosity still coherent with observations (the external parts of the disc contribute very little to the total luminosity of the disc) one gets $\Gamma_\infty \approx 49$, enough to explain the observed values of $\Gamma = 46$.

PKS 1510-089 is undoubtedly an extreme object and the Compton rocket process reaches its limits there but is still able to explain the fastest jet observed.

7.5 Conclusion & Perspectives on the Compton rocket

In this section I studied the evolution of the equilibrium Lorentz factor in complex photon fields. I showed that variation of $\Gamma_{eq}(Z)$ could be expected, leading to non trivial emission patterns, in space as well as in time. I also showed that the Compton rocket process is able to explain the whole range of observed values for Γ with reasonable physical parameters. Good agreements between observation[4] and theoretical results can be summarized here:

- Jets accelerate on parsec to deca-parsec scales ✓
- Jets can reach $\Gamma \approx 50$ ✓
- But usually have values between a few and 20 ✓
- More powerful jets and sources with more luminous discs show faster jets ✓
- Dispersion of speeds are observed within single jets ✓

Of course, these general trends do not prove that the Compton rocket is the actual accelerating mechanism and the same correlations are expected in other accelerating mechanism (there is nothing surprising in the fact that more powerful sources have more powerful jets) but good agreements are worth noting.

Let us remind that every calculation here has been done assuming the Thomson regime for the inverse Compton emission. In the Klein-Nishina regime, the cross-section drops, making the Compton rocket much less efficient. It is not clear how different the solution would be in this case, as different soft photon sources (or even different parts of the same source) can interact in different regimes with the plasma, modifying the Lorentz factor, which can in turn make a source enter or leave the Thomson regime. The soft photons most likely to scatter in the KN regime come from the BLR for parts of the jet inside the BLR as the limit is around $\gamma_e \approx 10^4$ whereas it is around $\gamma_e \approx 10^6$ for the disc or the torus. Therefore, for such a hot plasma, the influence of the BLR on Γ_{eq} might disappear. Also, external parts of the disc might enter in the KN regime at lower particle energies than the inner parts as their incident angle is lower. This might make the disc artificially

[4] all statistical information on jet dynamics given here come from Li13

appear smaller, inducing a faster jet (see the example of PKS 1510-089, figure 7.6).

Finally, other sources of soft photons could be considered for the calculation of Γ_{eq}. In particular, the MHD jet (section 4) might be luminous enough to take part in the process. One could also consider the synchrotron photons emitted all along the pair jet. The calculation of the resulting Γ_{eq} would be highly non-linear in this case, as the perceived synchrotron emission in one zone of the jet depends on the Lorentz factor of the complete jet, the same Lorentz factor depending on the synchrotron emission from all the jet.

More investigation can be done on the Compton rocket process and the resulting Γ_b and effects for AGN jets.

7.6 *[En résumé]* Accélération d'un jet relativiste par effet fusée Compton

Lorsque un plasma de particules émet de façon anisotropique, cela créé une force de recul sur ce plasma, de manière semblable aux fusées qui émettent de la matière dans une direction pour se déplacer dans la direction opposée. O'dell (1981) a montré que cet effet pouvait être important dans le cas de plasmas chauds émettant via le processes Compton inverse. Un plasma chaud peut émettre de façon anisotropique pour deux raisons : soit la distribution de particules est anisotropique, soit le champ de photons incident est anisotropique (voir l'illustration figure 7.1). Dans le cas d'une distribution de particules isotropique et dans le régime d'émission Thomson, le calcul de la force de recul ne dépend que de la distribution spatiale du champ de photons externes dans le référentiel en mouvement via les paramètres d'Eddington (équation 7.1). Puisque la distribution spatiale du champ de photon dans le référentiel en mouvement change avec la vitesse du plasma (voir les aberrations relativistes chapitre 2), on peut montrer qu'il existe un facteur de Lorentz d'équilibre Γ_{eq} (équivalent à une vitesse d'équilibre) pour lequel le champ de photon dans le référentiel en mouvement est isotrope - la force de recul est alors nulle.

Dans ce chapitre, je m'intéresse au calcul du facteur de Lorentz d'équilibre dans l'environnement complexe d'un AGN. En considérant les différentes sources de photons décrites dans le chapitre précédent, j'ai pu calculer l'évolution du facteur de Lorentz d'équilibre en fonction de l'altitude (distance au trou noir central) dans le jet. Un exemple de résultat est donné figure 7.2. On voit que le facteur de Lorentz d'équilibre change avec l'altitude Z/R_s et que les différentes sources peuvent avoir des influences différentes, accélérant ou freinant alternativement le plasma. Cet effet peut avoir d'importantes conséquences sur la dynamique des jets ainsi que sur l'émission observée, car celle-ci est fortement dépendente du facteur de Lorentz via les effets d'aberration relativiste. Cette étude a été publiée dans le journal Astronomy & Astrophysics (voir article joint).

Je montre ensuite que le facteur de Lorentz réel ne peut être égal au facteur de Lorentz d'équilibre indéfiniment et atteint une limite Γ_{inf}. Cette limite dépend en particulier de l'énergie des particules et de la luminosité du disque d'accrétion. Je propose ensuite un calcul approché de cette limite (équation 7.13) et détermine Γ_∞ dans différentes situations (figure 7.3). En faisant varier l'énergie des particules et la luminosité du disque, je montre que Γ_∞ peut varier dans une grande plage de valeurs, de 1 à 50 (figures 7.4 et 7.5). Il est intéressant de noter que cette plage de valeurs correspond aux valeurs observées dans les jets des AGN.

Ainsi, nous pouvons conclure que l'effet fusée Compton est compatible avec les observations et peut expliquer plusieurs caractéristiques des jets (plus grands facteurs de Lorentz observés, facteurs de Lorentz moyens observés, corrélation avec la luminosité du disque, dispersion des vitesses observées au sein d'un seul jet).

Part III

Comparison to observations

Chapter 8

Model optimization

Contents

Having a numerical model is one thing, fitting observation is another. In this part, I will explain how we can find sets of model parameters able to reproduce an object SED.

8.1 General method to model an object

The first objective of our model is to be able to reproduce the spectral energy distribution (SED) of observed objects.

Therefore, the first step is to get data. Some objects have been extensively observed along the years and we have access to large amounts of data. But the question of what do these data actually mean is not an easy one. Indeed, AGNs are very complex objects evolving on all timescales from minutes to millions of years and on galaxy scale. Because emission could come from very different regions in the jet (and thus have been produced at very different time), one should be very careful with the interpretation of data, even simultaneous ones. This will be discussed further in section 9

Once the "good" data have been selected, we would like to find the "good" parameters for the model to fit the SED, knowing that the complete model has quite a large number (19) of free parameters (see table 8.1).

Parameter name	Parameter symbol	Reference
Black-hole mass	$M_\bullet$	
Mass accretion rate	$\dot{m} = \dfrac{\dot{M}}{\dot{M}_{\rm edd}}$	Equation (6.4)
Viewing angle	i_{obs}	Figure 5.1
Altitude of initial condition	Z_0	
Radius at Z_0	R_0	Equation (5.58)
Magnetic field at Z_0	B_0	Equation (5.59)
Acceleration rate per particle at Z_0	Q_0	Equation (5.60)
Particle density at Z_0	n_0	
Index describing the evolution of R with Z	ω	Equation (5.58)
Index describing the evolution of B with R	λ	Equation (5.59)
Index describing the evolution of Q with Z	ζ	Equation (5.60)
Cut-off distance for Q	Z_c	Equation (5.60)
Redshift	z	
Accretion disc inner radius	R_{in}	Figure 6.2
Accretion disc outer radius	R_{out}	Figure 6.2
Torus small radius	R_t	Figure 6.4
Torus big radius	D_t	Figure 6.4
BLR minimal opening angle	ω_{blr}^{min}	Figure 6.6
BLR maximal opening angle	ω_{blr}^{min}	Figure 6.6
BLR radius	R_{blr}	Figure 6.6
BLR luminosity over disc luminosity	$\alpha_{blr} = \frac{L_{blr}}{L_{disc}}$	Equation (6.7)

Table 8.1: Parameters of the numerical model

We have to take into account that some parameters, such as the black-hole mass, or the viewing angle, can be constrained by observations (sometimes model dependent). Some others though, are very poorly constrained, such as the magnetic field (value and evolution) or the jet geometry. In order to adjust these parameters, it is possible to infer their impact on the simulated SED.

8.1.1 Influence of the parameters on the spectral energy distribution

One can describe the dependence of the emission luminosity and peak frequency for one emitting zone as a function of the local parameters values.

In the Thomson regime, the peaks of the different emission processes are described by:

$$\begin{cases} \nu_{syn} & \propto \gamma^2 B \\ L_{syn} & \propto N\gamma^2 B^2 \end{cases} \qquad \begin{cases} \nu_{ssc} & \propto \gamma^2 \nu_{syn} \propto \gamma^4 B \\ L_{ssc} & \propto N\gamma^2 W_{syn} \propto \dfrac{N^2\gamma^4 B^2}{R^2} \end{cases} \qquad \begin{cases} \nu_{ec} & \propto \gamma^2 \epsilon_s^* \\ L_{ec} & \propto N\gamma^2 \dfrac{L_{disc}}{Z^2} \end{cases} \tag{8.1}$$

with $N = nR^2 \mathrm{d}Z$, the total number of particles in the emitting zone.

Synchrotron dominated cooling regime: In the synchrotron cooling regime, the equation (5.56) at equilibrium simplifies into:

$$0 = Q_{acc} - \frac{4}{3}\frac{\sigma_T}{m_e c} U_B \gamma^2 \tag{8.2}$$

This implies directly $Q_{acc} \propto B^2\gamma^2$. Then we can rewrite relations (8.1) as a function of the model parameters:

$$\begin{cases} \nu_{syn}(Z_0) & \propto \dfrac{Q_0}{B_0} \\ L_{syn}(Z_0) & \propto n_0 R_0^2 Q_0 \end{cases} \quad \begin{cases} \nu_{ssc}(Z_0) & \propto \dfrac{Q_0^2}{B_0^3} \\ L_{ssc}(Z_0) & \propto n_0 R_0^2 \dfrac{Q_0^2}{B_0^2} \end{cases} \quad \begin{cases} \nu_{ec}(Z_0) & \propto \dfrac{Q_0}{B_0^2}\Gamma\epsilon_s \\ L_{ec}(Z_0) & \propto n_0 R_0^2 \dfrac{Q_0}{B_0^2}\dfrac{L_{disc}}{Z_0^2} \end{cases} \tag{8.3}$$

SSC dominated cooling regime: If the SSC dominates the cooling of particles, then the equation (5.56) simplifies into:

$$0 = Q_{acc} - \frac{4}{3}\frac{\sigma_T}{m_e c} U_{syn} \gamma^2 \tag{8.4}$$

Therefore we have $Q_{acc} \propto n\gamma^4 B^2$ and here again we can rewrite relations (8.1) as a function of the model parameters:

$$\begin{cases} \nu_{syn}(Z_0) & \propto \sqrt{\dfrac{Q_0}{n_0}} \\ L_{syn}(Z_0) & \propto \sqrt{Q_0 n_0} B_0 R_0^2 \end{cases} \quad \begin{cases} \nu_{ssc}(Z_0) & \propto \dfrac{Q_0 R_0^2}{B_0 n_0} \\ L_{ssc}(Z_0) & \propto n_0 R_0^2 Q_0 \end{cases} \quad \begin{cases} \nu_{ec}(Z_0) & \propto \sqrt{\dfrac{Q_0}{n_0}}\dfrac{1}{B_0}\Gamma\epsilon_s \\ L_{ec}(Z_0) & \propto \sqrt{\dfrac{Q_0 n_0}{B_0^2}} R_0^2 \dfrac{L_{disc}}{Z_0^2} \end{cases} \tag{8.5}$$

EC dominated cooling regime: If the EC dominates the cooling of particles, then the equation (5.56) simplifies into:

$$0 = Q_{acc} - \frac{4}{3}\frac{\sigma_T}{m_e c} U_{\text{soft}} \gamma^2 \tag{8.6}$$

Therefore we have $Q_{acc} \propto n\gamma^2 \dfrac{L_{disc}}{Z_0^2}$ and here again we can rewrite relations (8.1) as a function of the model parameters:

$$\begin{cases} \nu_{syn}(Z_0) & \propto Q_0 B_0 \dfrac{Z_0^2}{L_{disc}} \\ L_{syn}(Z_0) & \propto Q_0 B_0^2 n_0 R_0^2 \dfrac{Z_0^2}{L_{disc}} \end{cases} \quad \begin{cases} \nu_{ssc}(Z_0) & \propto Q_0^2 B_0 \dfrac{Z_0^4}{L_{disc}^2} \\ L_{ssc}(Z_0) & \propto Q_0^2 B_0^2 n_0^2 R_0^2 \dfrac{Z_0^4}{L_{disc}^2} \end{cases} \quad \begin{cases} \nu_{ec}(Z_0) & \propto Q_0 \epsilon_s \dfrac{Z_0^2}{L_{disc}} \\ L_{ec}(Z_0) & \propto n_0 R_0^2 Q_0 \end{cases} \tag{8.7}$$

Those equations give us a general trend for the model and one can try to adjust the parameters to correctly fit the spectrum. However, practice reveals more difficult as this is only true for the Thomson case and changes of regime change the behaviors described here. Moreover, this is only true where we impose the initial conditions (at $Z = Z_0$)! As the jet is not expected (and does not in most cases) to evolve in a linear way, other emitting zones will behave erratically, making a hand-based fit unrealistic.

8.2 An inverse problem

Therefore, we need to search for a more automatic method to obtain a possible modeling of our observation. In our case we want to reproduce the observed SED of an object with the model. Suppose that we have a SED that we consider to represent the steady-state of an object that the model should reproduce. The objective is to find the set of parameters able to do so and represented by the vector $\mathcal{X}$:

$$\mathcal{X} = \{M_\bullet, \dot{M}, i_{obs}, R_0, B_0, Q_0, n_0, \omega, \lambda, \zeta, R_{in}, R_{out}, R_t, D_t, \varepsilon_t, \omega_{blr}^{min}, \omega_{blr}^{max}, R_{blr}, \alpha_{blr}\} \quad (8.8)$$

This is a recurrent problem in science known as inverse problem, as we want to start from the output of the model and retrieve the input. It requires a way to evaluate the goodness of a fit, so that when an input is tried, the output can be discriminated or not. If this evaluation is done by a mathematical function $f(\mathcal{X})$, the problem is reduce to an optimization problem. The distance function $f(\mathcal{X})$, measuring the error or the distance to our data, must be minimized to find the best fit from the model (as $f(\mathcal{X}) = 0$ corresponds to a perfect fit of the data).

The most general methods for optimization are based on differential calculation (Newton, Levenberg-Marquardt...). Unfortunately, these methods work for function presenting a unique global minimum and no local minimum where the fitting algorithm could converge. Other well known methods are based on Monte-Carlo simulation (MC, Markov-Chain Monte Carlo...). The limitation here is the time consumption of our model. With an average of several minutes to compute a solution (one SED), it is rather impossible to use methods requiring millions of tests. Another approach was necessary here. A general difficulty for all method comes from the number of parameters of the model, which correspond to the dimension of the function to minimize. Larger dimensions usually mean more local extrema and obviously, more dimensions to explore.

I decided to use genetic algorithms to handle this problem. This kind of algorithm presents the advantage of requiring less evaluations of the function to minimize and to work well in hyper-spaces with potentially numerous local minima. I will present their general procedure in the following.

8.2.1 Genetic algorithms

The principle of genetic algorithms (GA) is rather simple and based on biology evolution. These algorithms consider a vector (of parameters) as an individual confronted to the harshness of nature. If the individual is fit, or well-adapted, it should survive, procreate and transmit its genes to the next generation. Here the individual is confronted to the model (hence representing the world, or nature). A well-adapted individual would be one carrying parameters for the model able to reproduce observations (the calculation of the fitness of an individual is important here and I will come back to it later). Generation after generation, the best individual are selected, exchange their genome and mutate to progressively converge to the most adapted population. This method is used in a great variety of fields (in astrophysics for example, it is used in exoplanets research to fit radial velocities) and the details of the methods vary for each problem. Here I will develop the details of the algorithm I develop and what we found to be the best recipe.

The different steps of the GA are the following:

- A set of parameters $\mathcal{X} = \{p_0, p_1, ...\}$ is chosen with bounds for each parameters. These bounds are chosen on physical arguments and/or based on additional observations.

- A population $\mathcal{P}_0$ of $\mathcal{N}_0$ individuals is generated randomly. Each individual is represented by a set of parameters $\mathcal{X}_0^i$ which corresponds to its biological DNA.
- Every individual of the population is tested against the model and for each one, a fitness value is determined.
- Individual fitnesses are compared one another.
- Only a proportion η_e of the population called the elite, corresponding to the best individuals, is conserved. Other individuals die for being less adapted to their environment. This is harsh but necessary.
- These $\eta_e \mathcal{N}$ best-adapted individuals (the elite) can now produce a new generation $\mathcal{P}_i$ of individuals via two means:
  - *Mutations*: the DNA of individuals can mute meaning that a proportion of the parameters see their value changed by a small amount.
  - *Crossover*: Pairs of individual are randomly selected and exchange part of their DNA, creating new individuals (offsprings).
- Go back to point two and start over. The loop can be stopped when the population is good enough or when it has not significantly improved in many generations.

8.2.2 Building a new population: mutations & crossover

When the elite has been selected from the population, they are submitted to mutations and crossovers. These processes can be handled in different ways.

a. Two kinds of mutations

Randomize A proportion $\eta_r\eta_e$ of the elite is randomly selected. For each individual in this subgroup, each parameter has a probability P_r to be randomized in the bounds set at start. When the bounds are separated by more than two orders of magnitude, the draw is realized on the logarithmic values.

Mutations following a normal law A proportion $\eta_m\eta_e$ of the elite is randomly selected. For each individual in this subgroup, each parameter has a probability P_m to be muted following a truncated gaussian law centered on the previous value μ and with a standard deviation $\sigma = 0.1 \times \mu$. The gaussian law is truncated so that the parameter stays in the bounds set by the user.

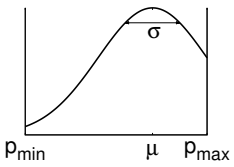

Mutations are basically good for exploring the hyper-space. The first kind of mutation introduce important fluctuations in the DNA of individuals, allowing a global exploration only limited by the bounds of each parameters. The second kind of mutation however, is more intended at a local exploration and at micro-optimization of the parameters.

b. Two kinds of crossover

Contrary to mutations, the crossover helps the convergence by mixing potential "good" parameters.

Standard crossover A proportion $2 \times \eta_{cxs}\eta_e$ of the elite is randomly selected and each individual is uniquely assigned with another to form a faithful couple $(\mathcal{X}^1, \mathcal{X}^2)$. A subset of parameters is randomly selected in the DNA of one parent and exchanged with the corresponding part of the other parent DNA.
Example:

$$\begin{cases} \mathcal{X}^1 = \{p_0^1 \dots \mid p_i^1 \dots p_j^1 \mid \dots p_n^1\} \\ \mathcal{X}^2 = \{p_0^2 \dots \mid p_i^2 \dots p_j^2 \mid \dots p_n^2\} \end{cases} \Rightarrow \begin{cases} \mathcal{X}^1 = \{p_0^1 \dots \mid p_i^2 \dots p_j^2 \mid \dots p_n^1\} \\ \mathcal{X}^2 = \{p_0^2 \dots \mid p_i^1 \dots p_j^1 \mid \dots p_n^2\} \end{cases} \tag{8.9}$$

This kind of crossover is a standard in the GA method and is particularly useful when segments of the DNA can be considered as a whole.

Oriented crossover A proportion $2 \times \eta_{cxor}\eta_e$ of the elite is randomly selected and each individual is uniquely assigned with another to form a faithful couple $(\mathcal{X}^1, \mathcal{X}^2)$. Each parameter of each parent has a probability P_{cxor} to see its value changed to a random value following an uniform distribution between the parent values. When the bounds are separated by more than two orders of magnitude, the draw is realized on the logarithmic values.
Example:

$$\begin{cases} \mathcal{X}^1 = \{4, 2, 1, 2\} \\ \mathcal{X}^2 = \{1, 2, 3, 4\} \end{cases} \Rightarrow \begin{cases} \mathcal{X}^1 = \{1.9 \in [1:4], 2, 1, 2\} \\ \mathcal{X}^2 = \{3.6 \in [1:4], 2, 3, 4\} \end{cases} \tag{8.10}$$

The oriented crossover aims at giving a more adapted crossover here considering that individuals DNA is composed of numerical values: a better value of a parameter might be included between the values from two good parents.

c. The new population

Starting from a population $\mathcal{P}_i$, an elite is selected by fitness selection. Part of this elite is selected to give an offspring by mutations and crossover as described previously. The number of offspring individuals is then $\mathcal{N}_{i+1} = [2 \times (\eta_{cx} + \eta_{cxor}) + (\eta_m + \eta_r)]\,\mathcal{N}_i$. To get the new population $\mathcal{P}_{i+1}$, we complete this number with elite individuals so that the offspring population is at least as large as the parent population. We note the total proportion of mutation $\eta_{mut} = \eta_m + \eta_r$ and the total proportion of crossover $\eta_{cx} = 2(\eta_{cxs} + \eta_{cxor})$. With this definition η_{mut} and η_{cx} respectively represent the proportion of individuals coming from mutation and crossover in the new generation. Then the population grows if the number of offsprings is superior to the number of individuals, which is equivalent to:

$$\eta_{mut} + \eta_{cx} \geq 1 \tag{8.11}$$

Note that the best individual from the parent population is kept in all cases (so the fitness of the population cannot decrease). A graphical representation of this process is given in figure 8.1.

8.2.3 Fitness evaluation

The fitness evaluation f of individuals is a crucial point here as it will drive the GA. Even if the GA will always favor the solution $f(\mathcal{X}) = 0$, a different form of the function f can mean a slower or faster convergence - or in the worst case, a convergence to local minima (as opposed to global) because the hyper-space is not properly covered.

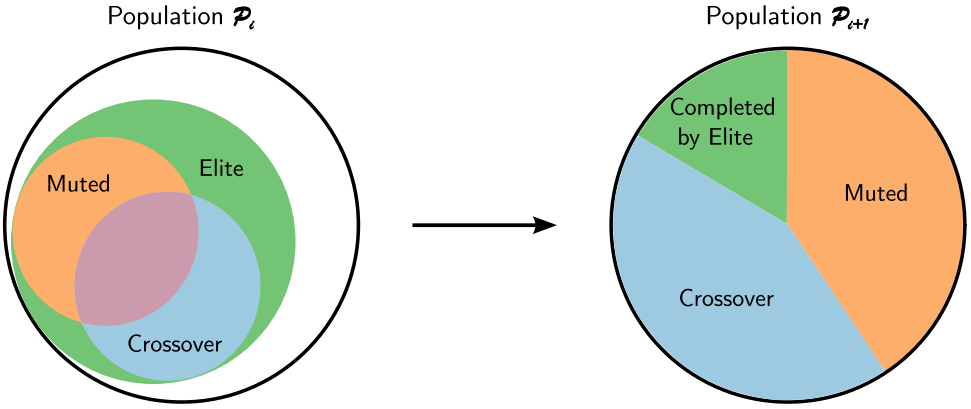

Figure 8.1: Example of distribution of the individuals in the new population. In green the best individuals (elite) selected in the initial population. In orange the proportion of individuals muted and in blue the proportion of individuals getting crossed (both included in the best ones). These two subgroups can intersect (purple subgroup) and some parents give birth to offsprings through mutation and crossover. At right, the new population with the origin of the individuals. As each parents can give birth to several offspring, the population can grow. If not, it can be completed by the best individuals selected in the elite.

The χ^2

The χ^2 test is a statistical test based on the calculation of the sum of squared errors between observations and a model. The computation of the χ^2 is defined by:

$$\chi^2 = \sum_{\nu} \frac{\left[(\nu F_\nu)_i^{obs} - (\nu F_\nu)_i^{th}\right]^2}{\sigma_i^2} \tag{8.12}$$

with the *th* upperscript referring to data points from the model and *obs* upperscript to observational data point with an error σ.

While this is a great tool in many cases, it might not be the best one in our case for two main reasons:

- Because the χ^2 is defined by a sum, the weight of an energy band depends on the number of observation points. It means that an automatic algorithm will preferably fit bands with more data, which are not necessarily the ones carrying the most important information. In AGN case, there is a lot of data available from radio to optical but limited one at high energy. The result of a standard χ^2 test would be to artificially give much more importance to the radio than to high-energies.
- Likewise, the error σ gives a different weighting to different points. Of course, this is great when we do not want to attach too much importance to data point with large error bars. However, in our case, this would give a lot of weigh to optical data, where the observations are very well constrained and almost none to other less constrained band despite the fact that optical does not carry most of the information for a broadband modeling.
- The different orders of magnitude present in the data pose a real challenge to the χ^2 evaluation. Whereas we would like to have a "visually good" fit in a log-log

representation of the SED ($\log(\nu F_\nu) - log(\nu)$), the standard χ^2 causes to always devaluate theoretical model close on a log-log scale but actually of amplitude several times the data. A graphical representation of this is done in figure 8.2.

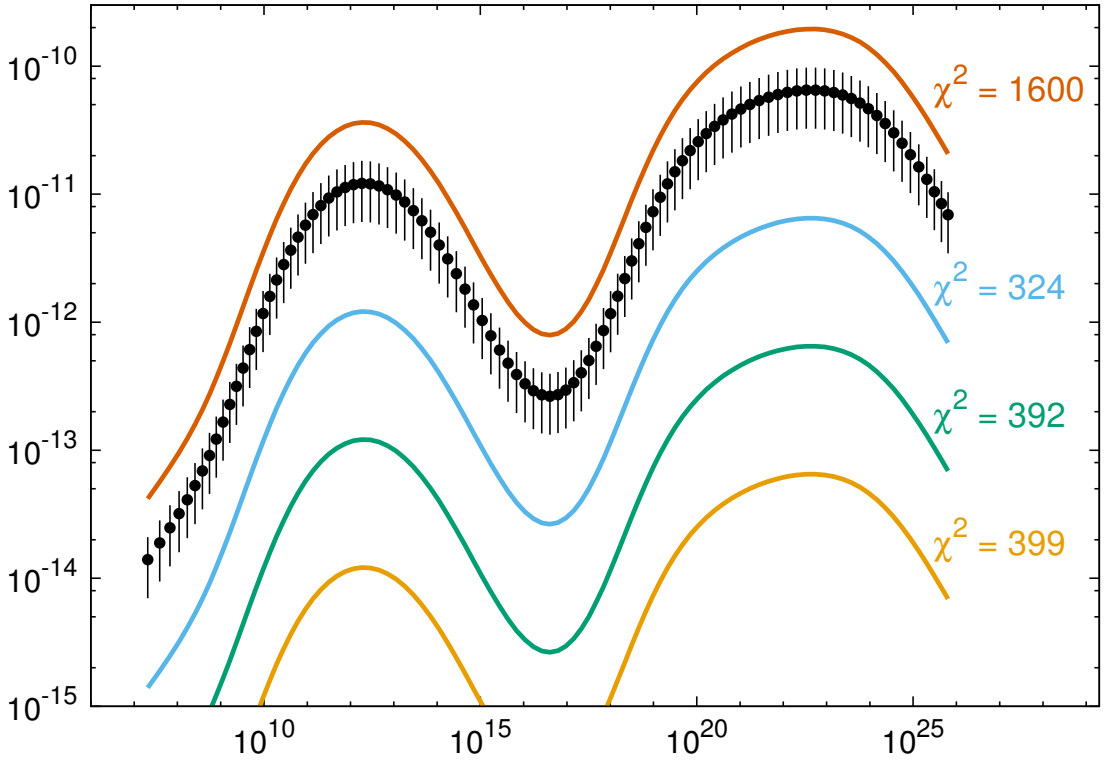

Figure 8.2: What is the "best" model for the data represented by black dots? The standard χ^2 would blindly prefer the models under observational values (blue, green or orange) whereas we might prefer to select the one above (in red).

The two first problems can be avoided by using averaged data equally distributed over all energies so that all energy bands weight the same in the fitness evaluation.

Third and last issue is of course due to the log-log representation versus a standard computation of the fitness on linear values. That is why we decided to use an evaluation of the distance data-model in logarithmic values. I will note it $\chi^2_{\log}$:

$$\chi^2_{\log} = \sum_i \left[\log((\nu F_\nu)_{obs}) - \log((\nu F_\nu)_{th})\right]^2 \tag{8.13}$$

If not stated otherwise, this function will be used for the evaluation of the fitness of a theoretical model in the following.

Note also that the fitness evaluation has a more special signification in the case of genetic algorithm compared to other fitting procedure (such as gradient algorithms) as it drives the evolution of the population by selecting certain kind of individual at the expense of others that could have evolved in a more adapted population. Therefore, there is a risk here to artificially select ranges of parameters in the first generations of the species. As an example, a simple sum of distances (as done here) might select models fitting perfectly

parts of the SED while neglecting solution that we might consider "good" on average[1]. Other fitness evaluation have been considered, for example based on the SED shape.

SED shape

Another possibility to evaluate the goodness of a fit is to compare directly the function form or SED main characteristics. An evaluation based only on 6 criteria has been imagined:

- position of the synchrotron peak (ν_{LE} & $\nu F_{\nu\mathrm{LE}}$)
- index of a power-law fitting the low energy α
- position of the high energy peak (ν_{HE} & $\nu F_{\nu\mathrm{HE}}$)
- full width at half maximum of the high energy bump in $\log(\nu) - \log(\nu F_\nu)$

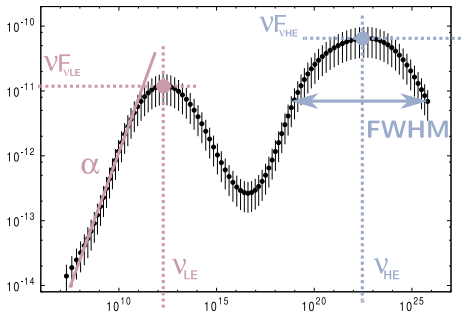

Unfortunately, this type of evaluation has not been tested with the genetic algorithm by lack of time.

8.2.4 Evolution example

As an example of evolution, I will present the fit of a theoretical SED by the GA. For this example, a theoretical SED is computed and the GA must try to fit this theoretical SED (as the SED is theoretical and computed by the model, we are sure there is a solution to the inverse problem). Results from this evolution are compiled in figure 8.3. On the left, the minimum χ^2 of each generation (corresponding to the best individual) as a function of the generation and on the right, the SED of some best individuals. Each generation includes 500 individuals. The best individual randomly generated in the initial population P_0 has a $\chi^2 = 139$ and a SED already quite good at high energy but quite far at low energies (in blue in figure 8.3). Generation after generation, the population improves and the best individuals gets closer from the theoretical SED. The GA has been stopped at generation 92 here for which the best individual has a $\chi^2 \approx 1.41$ and a SED visually very close form the theoretical one.

In table 8.2 are given the free parameters for this example, the corresponding values for the theoretical SED and the final values for the best individual in $\mathcal{P}_{92}$.

	$\cos(i_{obs})$	R_0	B_0	Q_0	N_0	ω	λ	ζ
Theoretical	0.95	200	1.4×10^{-4}	2.9×10^{-3}	2.7×10^{6}	0.4	1.2	1.4
Best fit	0.946	144.5	1.2×10^{-4}	5.4×10^{-3}	4.3×10^{6}	0.39	1.32	1.41

Table 8.2: Values of the free parameters of the model for the theoretical SED and for the best fit obtained after 92 generations (see figure 8.3).

As one can see, the best fit is very close from the theoretical SED, both visually and in parameters values. When such a good fit is obtained, we could pursue with a standard

[1] this phenomenon has been actually observed in tests

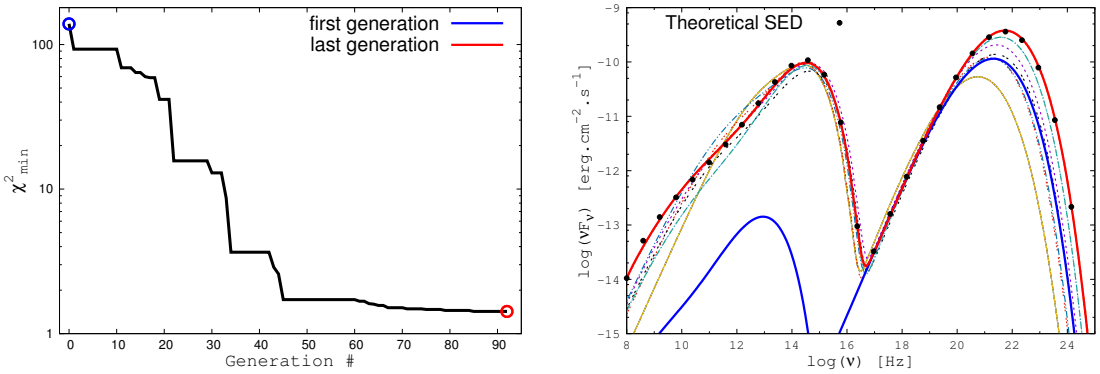

Figure 8.3: Best individual of the population $\mathcal{P}_i$ as a function of generation. *Left:* χ^2 of the best individual. *Right:* SED of the best individual. Note that only one out of seven data point for the theoretical SED is represented here for clarity. In both figures, blue is the best individual of the first generation and red is the best individual of the last generation.

gradient optimizer that would probably converge faster to the exact values and to the perfect fit than the GA.

8.3 Optimizing the optimizer

The GA also has parameters that can be adjusted and change its efficiency: in particular, the different proportion described previously must be chosen and depend on the function (i.e. the model) that we are trying to minimize. To find the optimal values in link with our model, the best way is to try and see what works and what does not. The strategy here has been to build a theoretical SED (the same as the one given in figure 8.3) with the model and use the GA to converge to $f(\mathcal{X}) = 0$ with different values of η. It implies to run the complete GA with a lot of different parameters, which can be very time consuming. In order to simplify the calculation and save a lot of computing resources, a pure SSC version of the model is used here (the external Compton computation being the most demanding in resources) with the assumption that the complete version of the model does not differ significantly from the simplified version in terms of behavior and that the GA will benefit from the same parameters η. Note also that to really test the GA and avoid pure luck at the initial draw ($\mathcal{P}_0$), we explicitly excluded a small region around the actual parameters of the theoretical SED (table 8.2). An example of evolution for $\eta_{css} = 0.1$, $\eta_{cxor} = 0.1$, $\eta_m = 0.1$ and different values of η_r is presented in figure 8.4. The evolution to lower χ^2_{min} of each population differs with the value of η_r.

For practical reasons, the computation has been stopped at the same generation for every simulation. It means that we do not wait for complete convergence and some final individual are actually "bad" fit. What interests us here is the χ^2_{min} of the last population that can be compared to evaluate what values of η favor the quickest convergence.

8.3.1 On the value of mating

It might not be obvious to see the benefit of crossover in accelerating the convergence to a better solution. In figure 8.5, I compare the fitness of the best individual obtained after 70 generations (with a constant population of 500 individuals) as a function of η_{mut} for different value of η_{cx}. The black curve corresponds to an absence of crossover ($\eta_{cx} = 0$) which is basically a Monte-Carlo simulation. There is a clear tendency at improving

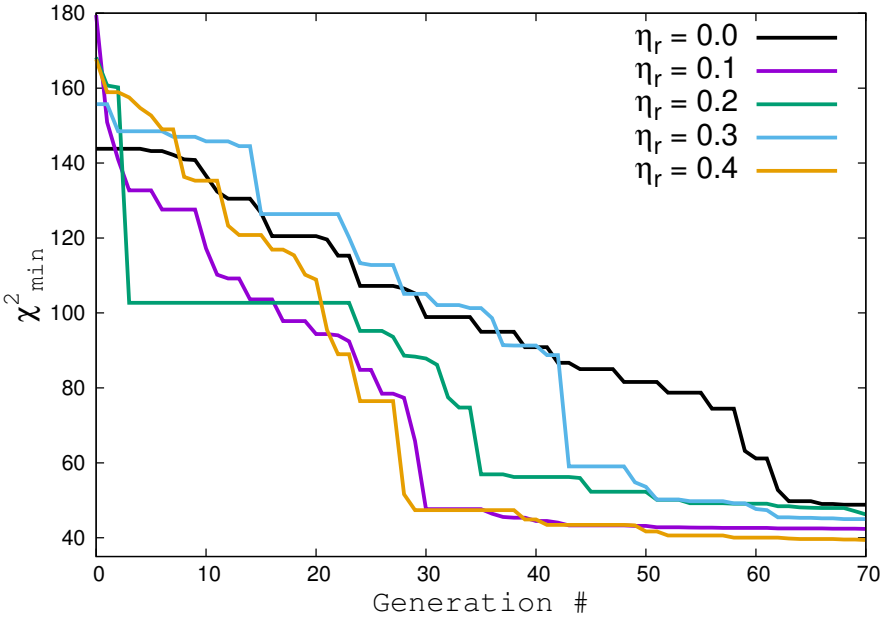

Figure 8.4: Example of evolution of χ^2_{min} for different η_r.

the convergence by increasing η_{mut}. This is not surprising of course, with no crossover, the more the space is covered by mutations, the more chances there is to find a better individual. All other curves are done for increasing values of η_{cx}. One can see that already for a low proportion (10% of the population) of crossover, the convergence is strongly improved and that it is constantly the case for other proportion of crossover.

From this, we can conclude that GA always converge faster than random walk simulations where the hyper-space is covered only on the base of random mutations.

8.3.2 Optimal GA parameters

For those tests, we decided to keep a constant population generation after generation. Therefore, equation (8.11) imposes $\Sigma\eta \leq 1$ which imposes a maximal range of [0:1] for each η. After computing 70 generations respecting these constraints, one can try to find the optimal set of GA parameters. In order to get from 4 dimensions to 2 and be able to represent the result here, I will study the dependance of χ^2 with $\eta_{mut} = \eta_r + \eta_m$ and $\eta_{cx} = 2(\eta_{cxor} + \eta_{css})$.

In figure 8.6, I represented the average χ^2_{min} as a function of η_{mut} and η_{cx} (one needs to average as for a value of η_{mut}, there are many couples of $(\eta_m, \eta_r, \eta_{cxor}, \eta_{cxs})$).

If we look directly at the average χ^2, we might want to pick $\eta_{mut} = 0.4$ and $\eta_{cx} = 0.4$ as they present the minimal $< \chi^2 >$. However, one must be careful that this couple also occurs to be the one concentrating the more couples of η, which can introduce a bias when looking at an average. For example, the best individual overall happened to be at $(\eta_{cxor} = 0.15, \eta_{cxs} = 0, \eta_r = 0.4, \eta_m = 0.2)$. If we look at the 10 best overall individuals (2% of all tested parameters), parameters are closer to an important proportion of mutation and lower proportion of crossover. Finally, there is no magical number here (or finding it will require a lot more computation) and the goal of this section was to find good parameters for the GA. I chose to keep the average parameters on those 10 best which are $\eta_m = 0.25, \eta_r = 0.25, \eta_{cxs} = 0.025, \eta_{cxor} = 0.1$. This set is represented by a black spot on

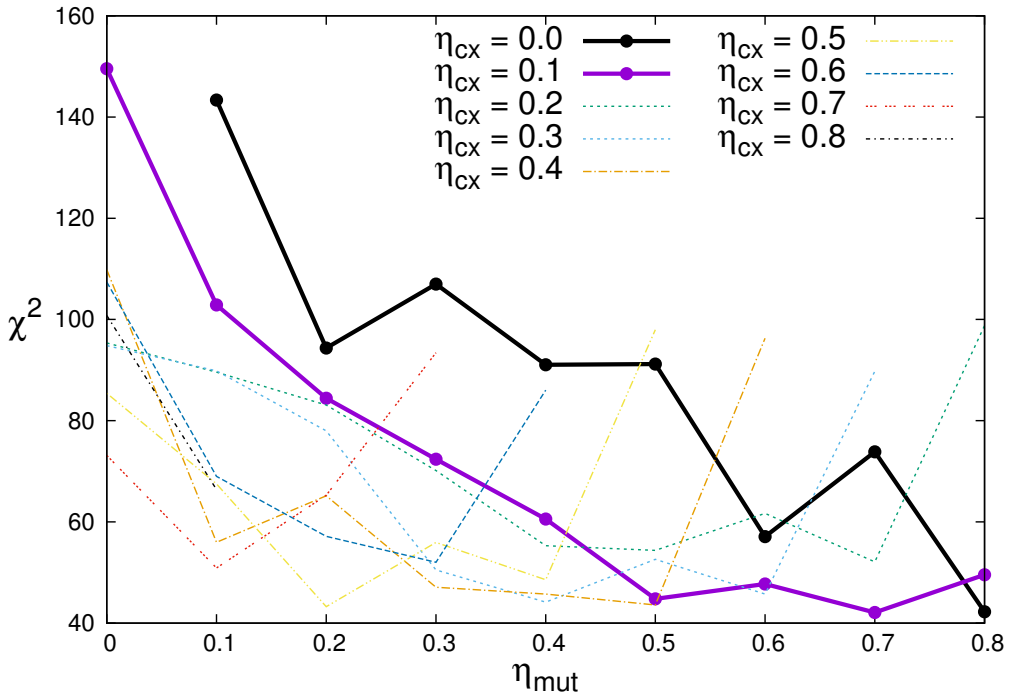

Figure 8.5: The value of mating. The mean value of χ^2 of the best individual obtained after 70 generations for different values of GA parameters η. The black curve represents the results obtained with an exploration based purely on mutations (no crossover). Other curves are obtained for increasing proportion of crossover.

the χ^2 map in figure 8.3.

8.4 Re-parameterization

The model parameters are simply the physical parameters (magnetic field, particle density, etc...). But these are not necessary adapted parameters for optimization. Parameters actually corresponding to the position of the peaks can ease the optimization research. This is true of course for a "hand" optimization as the user can infer the changes on the SED made by changes on parameters but also for an automatic fit such as the genetic algorithms that can exchange "good" parameters having a direct influence on the SED.

Based on section 8.1.1, one can choose a set of new parameters that corresponds to SED features:

$$\begin{array}{lll} \alpha_1 = \dfrac{Q_0}{B_0} & \alpha_2 = \dfrac{Q_0^2}{B_0^3} & \alpha_3 = n_0 Q_0 R_0^2 \\ \alpha_4 = M\dot{m} & \alpha_5 = \dfrac{\dot{m}}{M} & \alpha_6 = R_0 \end{array} \tag{8.14}$$

so that, under the assumption of synchrotron cooling[2]:

- $\alpha_1 \propto \nu_{syn}$ imposes the synchrotron peak frequency

[2]Only α_1, α_2 and α_3 actually require this assumption.

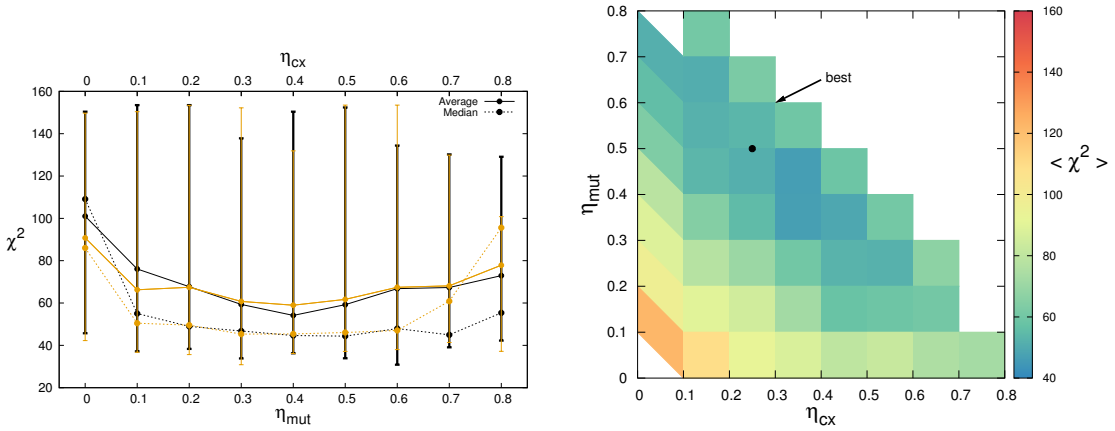

Figure 8.6: *Left:* Average and median of the best χ^2 with errorbars as a function of η_{mut} (black) and η_{cx} (orange). *Right:* Map of χ^2_{min} as a function of η_{cx} and η_{mut}. Arrow points at the best individual overall ($\chi^2 \approx 30$). Black dot represent the final chosen parameters for the GA.

- $\alpha_2 \propto \nu_{ssc}$ imposes the SSC peak frequency
- $\alpha_3 \propto L_{syn}$ imposes the synchrotron luminosity
- $\alpha_4 \propto \dot{M}$ imposes the disc luminosity
- $\alpha_5 \propto \dfrac{\dot{M}}{R_S^2}$ imposes the disc emission peak frequency
- $\alpha_6 \propto R_S$ allows to have a reversible system of parameters

8.5 Using the genetic algorithm

After the study of the genetic algorithm parameters, we are now set up to use the GA to try optimizing our jet model on real SED data. The GA has been developed in order to be very user friendly and takes only one parameter file as entry. This file regroups all physical parameters of the jet model, specifying wether the parameter is free or fixed for the genetic algorithm. If free a range of values must be given for the parameter whereas a single value is given for a fixed parameter. The genetic algorithm is then launched using a single PYTHON function. Options of this function include the possibly to use the re-parameterization described in section 8.4 or not and the number of processor cores that should be used.

Indeed, a valuable advantage of the genetic algorithms compared to other optimizing methods (such as the gradient method) is the possibility to compute individuals independently within one generation. The code developed here is parallel, which allows a computation on any number of cores, up to the number of individuals per generation. The results presented in the next section have been obtained using IPAG's computation server with a maximum of 20 cores only, which eventually limited the computation time: even on these machines, the optimization of one SED takes several days. An utilization on more cores (CIMENT platform in Grenoble for example) in the future would be a possible way to improve the computation efficiency of the algorithm.

8.6 *[En résumé]* Optimisation du modèle

L'objectif premier du modèle développé dans le chapitre 5 est de produire une distribution spectrale d'énergie (SED) comparable à celles observées. Malheureusement, reproduire ces observations n'est pas chose aisée avec un modèle complexe comprenant de nombreux paramètres (voir tableau 8.1) et nécessitant un temps de calcul important. Afin d'automatiser l'adaptation du modèle aux observations, j'ai du développer un algorithme d'optimisation. Afin de résoudre ce problème inverse, j'ai développé une méthode basée sur les algorithmes génétiques.

Le principe de ces algorithmes est plutôt simple et basé sur l'évolution biologique. On considère un vecteur de paramètres du modèle comme un individu confronté à la nature (le modèle). Si l'individu est adapté (les paramètres formant son ADN permette une bonne reproduction des observations par le modèle), il peut survivre, se reproduire et transmettre ses gènes à la génération suivante. Dans ce chapitre je développe les détails de cette méthode. En particulier, les différentes étapes de l'algorithme sont :

- Un ensemble de paramètres $\mathcal{X} = \{p_0, p_1, ...\}$ bornés par des considérations physique est choisi.
- Une population $\mathcal{P}_0$ de $\mathcal{N}_0$ individus est générée aléatoirement. Chaque individu est représenté par un ensemble de paramètres $\mathcal{X}_0^i$ correspondant à son ADN.
- Chaque individu est testé par le modèle et une valeur d'adaptation est déterminée pour chacun d'entre eux.
- Les valeurs d'adaptation sont comparées entre elles
- Seule une proportion de la population, appelée l'élite et correspondant aux meilleurs individus[3], est conservée. Les autres individus sont supprimés, c'est dur mais nécessaire.
- L'élite peut maintenant produire une nouvelle génération d'individus ($\mathcal{P}_{i+1}$) par deux moyens :
  - *Mutations* : l'ADN des individus peut muter, les valeurs de certains paramètres sont légèrement modifiées
  - *Echanges*: Des paires d'individus sont séléctionnées aléatoirement et échangent une partie de leur ADN, générant ainsi de nouveaux individus (descendance).
- Retournez à l'étape numéro deux et recommencez. La boucle peut être stoppée quand la population est suffisamment adaptée ou quand elle ne s'est pas significativement améliorée pendant plusieurs générations.

Un exemple d'évolution est donné figure 8.3 avec l'évolution de la SED et de la valeur d'adaptation (χ^2) du meilleur individu de chaque population en fonction de la génération.

L'algorithme d'optimisation a également du être optimisé afin d'être le plus adapté possible à notre problème en particulier. Pour cela, j'ai déterminé les meilleurs valeurs pour les taux de mutation et déchange (figure 8.6). J'ai également procédé à une reparamétrisation du problème afin que les nouveaux paramètres soient mieux adaptés à la résolution de notre problème (équation 8.14).

[3] ils sont la meilleur valeur d'adaptation

Chapter 9

Objects modeling

Contents

The problem of fitting and of a choice of fit evaluation has been raised in previous section. But in the case of AGN (as in many fields), there is also the problem of what does the data represent compared to our model. First, observations are rarely simultaneous in energy bands, and therefore cannot be the result of one object state (especially as these objects can be highly variable). Moreover, as soon as we abandon the assumption of a single emission zone, even simultaneous for the observer is not synonym of a single state for the object. As jets extend over millions of light years, radiation emitted at two instants separated by millions of years can reach the observer simultaneously. Moreover it is abusive to talk about a single state for an object of this size as information from a part of the jet will need hundred, thousand of years to reach another part and change its state accordingly. It is also important to remind that a lot of bias exist in observations as some observations are for example triggered by flaring states or simply because it is easier to observe high states (with higher flux). Having these limitations in mind, we have tried to fit averaged data and to give a general fit of these data to see if the jet model can reproduce the type of emission observed in FSRQ.

9.1 Blazar 3C 273

3C 273 has been the first blazar ever discovered due to its relative close distance. It has been extensively observed and studied over the past. The average data published by Turler et al. (1998) are more likely to represent the average state of the object and are therefore a good choice for our modeling. Moreover, thermal sources can be well constrained by observations which constrains the Compton rocket. These reasons make the study of 3C 273 a good starting point to test the numerical model.

9.1.1 Observations

3C 273 was the first quasar ever detected. Presence of strong emission lines allowed Schmidt (1963) to determine 3C 273 redshift to $z = 0.158$. Its black-hole mass is subject to discussion and large ranges have been evoked. Peterson et al. (2004) determined a mass of $M_\bullet = (8.8 \pm 1.8) \times 10^9 M_\odot$ using large reverberation mapping database whereas Paltani and Turler (2005) determined $M_\bullet = (5.69 - 8.27) \times 10^9 M_\odot$ using reverberation method on Ly-α and C_{IV} lines and $M_\bullet = (1.58 - 3.45) \times 10^9 M_\odot$ using Balmer lines.

Superluminal motion has been observed in 3C 273 by Pearson et al. (1981), proving the existence of relativistic motion in this jet. The deduced apparent velocity is $v_{app} \approx 7.5c$[1]. This can be used to impose constrains on the observation angle. From equation 1.4 and with the approximation $\beta \approx 1$, one can determine that $i_{obs} < 15^\circ$ (or $\cos i_{obs} > 0.96$).

By studying the lag of the Balmer lines, Paltani and Turler (2005) find a BLR size of $R_{blr}/c = 986 days$.

The SED data used here are the averaged data from Turler et al. (1998) over 30 years of observation. Averaged data over long period of time such as this sample are more likely to represent the average state of the AGN.

9.1.2 Modeling

To achieve the SED model of 3C 273 represented in figure 9.1, a step by step process has been necessary. It was the first object that I tried to fit and the genetic algorithm were not as developed as today. A first and long exploration by hand of the parameters space allowed a restriction of the parameters range. Then the genetic algorithm narrowed further these ranges of parameters, enough to finally use a gradient method in order to achieve the best fit by χ^2 minimization. Therefore, the modeling that I present here is not the result of a clear and linear process and all parameters of the model were free during the research of a best fit.

The mass and the accretion rate were fixed to fit the optical spectrum with a standard accretion disc around a Schwarschild black-hole. The inferred mass of $M_\bullet = 1.3 \times 10^9 M_\odot$ is lower than averages given previously and corresponds to the lowest limit obtained by Paltani and Turler (2005) from the study of Balmer lines. By lack of time I did not obtain satisfactory fits with more massive black-holes but this should be done in the future with a disc temperature profile in agreement with a Kerr black-hole consistent with the optical spectrum. With this black-hole mass, the BLR radius of $5 \times 10^2 R_S$ corresponds to clouds moving at 75 light days from the central engine, here also much lower than the observed value by Paltani and Turler (2005). However, changing the radius of the BLR afterward

[1] In the historical article, they compute an apparent velocity of $\sim 9.5c$ assuming a value for the Hubble constant $H_0 = 55 km.s^{-1}.Mpc^{-1}$ which is now known to be closer to $70 km.s^{-1}.Mpc^{-1}$

does not change the overall SED.

The torus emission is well visible in 3C273 spectrum which constrains its geometrical parameters of our model (see section 6.2) in order to fit the SED. However, there is not a single couple (R_T, D_T) able to reproduce the infrared peak observed in the SED, even though it has a great impact on the resulting Γ_{eq}. With the parameters given in table 9.1, the torus emission peaks in the infrared and explains the additional flux observed in this band. The torus reaches a maximal temperature of about 1170K, just below dust sublimation temperature. The outer radius of the accretion disc is then fixed to make the connection with the torus: $R_{out} = 0.5 \times 10^3 R_S$.

All the parameters are summarized in table 9.1. In the resulting SED (figure 9.1), the different processes are represented with different colors here: blue for synchrotron, green for synchrotron self-Compton (SSC) and purple for external Compton (EC). Dotted lines represent integrated emission for different slices of jet. The torus and the accretion disc emissions are respectively represented in red and orange. Similarly to Seyferts galaxies, 3C 273 presents evidences characteristic of the presence of a hot corona comptonizing the photons from the accretion disc. The resulting emission can be reproduced by a model of thermal comptonization (not included in our model) but is well represented by a power-law with an exponential cut-off. Therefore, the SED obtained here is completed by a power-law of photon index $\Gamma = 1.65$ between 5×10^{15}Hz and 5×10^{19}Hz (0.02-200keV) to represent the hot corona emission (Haardt et al. (1998)).

z	$M_\bullet/M_\odot$	R_S (cm)	$\dot{m}$	R_{blr}/R_S	ω_{max}	α_{blr}
0.158	1.3×10^9	3.8×10^{14}	0.1	5×10^2	35°	0.1
i_{obs}	D_T/R_S	R_T/R_S	R_{in}/R_S	R_{out}/R_S	Z_0/R_S	Z_c/R_S
13°	$1.5 \times 10^4 R_S$	10^4	3	$5 \times 10^3 R_S$	2×10^3	10^9
R_0/R_S	B_0 (G)	$Q_0(s^{-1})$	$n_0(cm^{-3})$	ω	λ	ζ
7.5	1.2	0.03	4.5×10^3	0.50	1.40	1.52

Table 9.1: Parameters corresponding to 3C 273 modeling.

9.1.3 Discussion

Here the model gives a very good reproduction of the broadband SED from radio to γ-rays.

The low energy (radio to optical) is of course produced by the synchrotron process. The synchrotron part of the inner jet (below $10^3 R_S$) emits in the optical and is covered by the emission from the accretion disc and the dusty torus. When moving further in the jet, the synchrotron peaks shift to lower frequencies and the further we go, the more the peak shifts. Finally, the whole jet from $10^3 R_S$ to $10^9 R_S$ is necessary to reproduce the power-law like radio spectrum. Its slope is determined by different factors: the increase of the jet opening (through the jet radius), the decrease of the magnetic field and of the particle heating and the bulk Lorentz factor. 3C 273 spectrum shows a break at $\sim 10^9$ Hz which is not well fitted by our model. It is not clear whether the emission at lower energy comes from the jet or not[2]. If so, such a break can find several reasons: a change

[2]It could be the result of synchrotron emission produced by the extended radio structure (lobe+hot

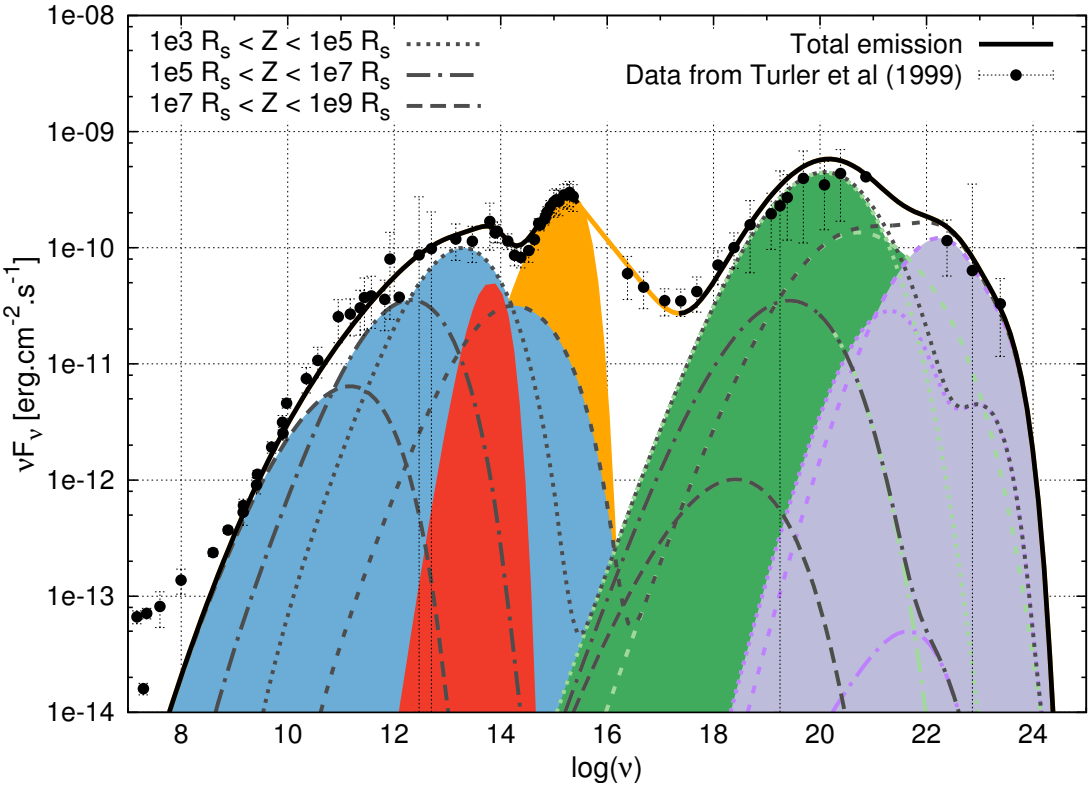

Figure 9.1: Modeling SED of 3C273. In blue the synchrotron emission, in green the SSC and in purple the external Compton. In red is the torus emission and in orange is the multicolor accretion disc completed with a power-law describing the hot corona emission between 0.02 and 200keV. Different emission zones in the jet are represented with different dotted lines.

of geometry, in the magnetic field evolution or in the heating can induce drastic changes in the jet conditions and explain such a break. A break in $\Gamma(Z)$ is also to consider. Such changes are possible through recollimation shocks or changes in the interstellar medium surrounding the jet.

The high energy emission is produced by inverse Compton processes, either on synchrotron (SSC) or on thermal photons (EC). Similarly to the synchrotron, the highest energies are produced close to the central engine and further regions emit at lower energies. In particular, the spectrum at $\nu > 10^{21}$ Hz is produced by regions at $Z < 10^3 R_S$ with a combination of SSC and EC. However, the X-rays and soft γ-rays are produced further, at $Z > 10^3 R_S$ by SSC.

From figure 9.2, one can see that the jet at $Z = 10^4 R_S$ reaches ballistic motion ($\Gamma(Z) = \Gamma_\infty$). From this point, there is no more pair creation, the density decreasing only by dilution (increase of the jet radius) and all parameters follow a very smooth evolution, corresponding to the almost featureless spectrum below 10^{13}Hz.

Concerning the physical parameters, the spine geometry (see equation 5.58) follows a

spot)

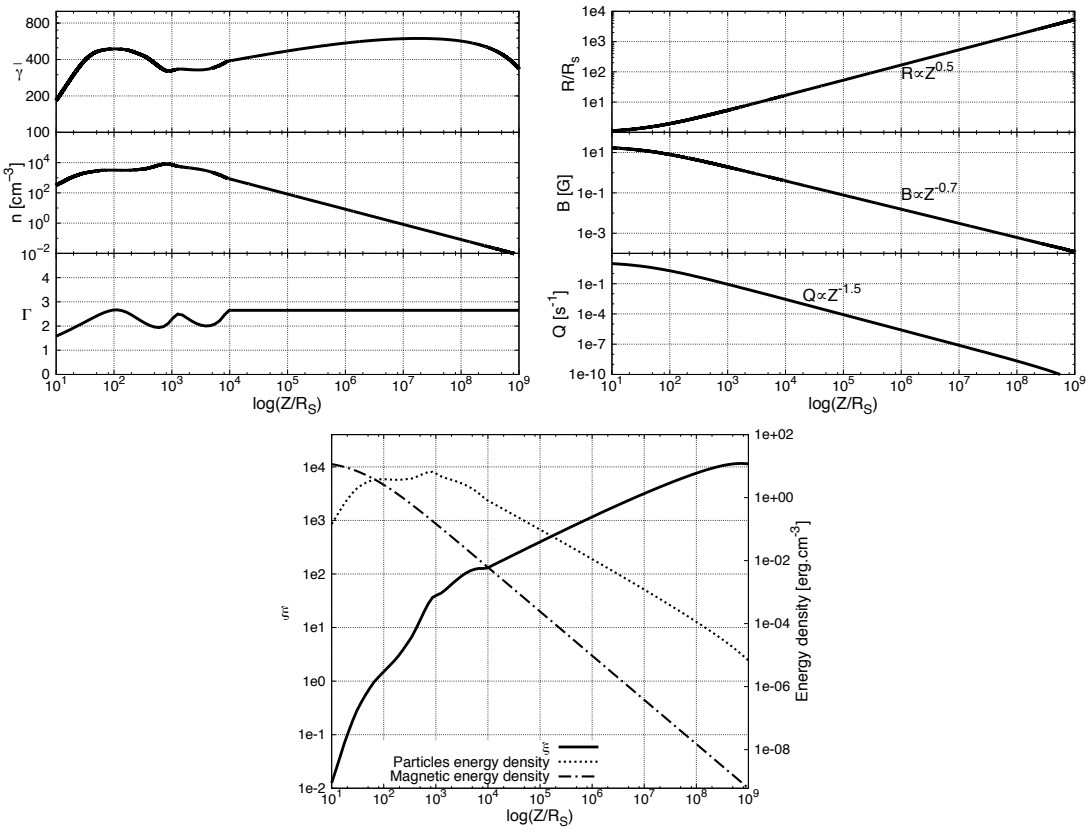

Figure 9.2: Evolution of the physical parameters as a function of the distance in the jet for the modeling of 3C273

parabola with a radius $R(Z) \propto \sqrt{Z}$. The jet opening can be evaluated by $\tan\theta_{jet} = \dfrac{R}{Z}$ and goes from 0.008rad below 1 parsec to about 10^{-5}rad at 1kpc which makes it a very narrow jet (however, do not forget that we are only dealing with the spine jet here which should be collimated by the outer MHD jet in the two-flow paradigm).

The particle density (middle curve of the first plot in the figure 9.2) evolves along the jet and goes through important pair creation under $10^3 R_S$. This part is also the part where the high energy emission is emitted. This is in great agreement with the two-flow paradigm as flares (which can be extremely at high-energies) are explained by intense phases of pair creation. Slight changes in the particle acceleration could induce large changes in the pair creation which is an highly non-linear process, in turn creating flare episodes. A time dependent modeling of 3C 273 would be very valuable in this matter.

The particles mean Lorentz factor ($3\bar{\gamma}$) varies between 600 and 1800. It increases an decreases rapidly below $10^3 R_S$, following changes in the bulk Lorentz factor Γ. This is due to changes in the cooling inferred by changes in Doppler aberration in the plasma rest frame. Further in the jet, $\bar{\gamma}$ slowly increases but note that due to an important decrease in the particle density, the particle energy density also decreases (dotted line in the last plot in figure 9.2).

Last plot in figure 9.2 represents the energy density in the particles and in the magnetic

field as well as the equipartition ratio defined as the ratio of both energy densities:

$$\xi = \frac{n_e < \gamma > m_e c^2}{B^2/8\pi} \tag{9.1}$$

This plot shows that the jet is dominated by the magnetic field very close to the black-hole (below 100 R_S). Then particles carry much more overall energy and bring this energy very far in the jet, allowing for the far synchrotron emission.

Γ varies as a function of the distance in the jet and is equal to $\Gamma_{eq}(Z)$ under $10^4 R_S$. Changes in $\Gamma_{eq}(Z)$ are due to effects discussed in section 7 and are the result of the Compton rocket effect. The jet reaches ballistic motion at $Z = 10^4 R_S$ and then $\Gamma(Z) = \Gamma_\infty$.

On one hand, the value of $\Gamma_\infty \approx 2.8$ is very questionable in this modeling as superluminal motion inferring $\Gamma > 7$ has been observed. Superluminal motion as seen by very long based interferometry (VLBI) corresponds to regions very far from the central engine and is then directly comparable to Γ_∞. As seen in section 7, there are two "easy" ways to increase the value of Γ_∞ by accelerating the jet on longer scales before to reach ballistic motion: to increase the luminosity of the accretion disc or to increase the particles mean energy.

Due to light travel time, there could be a delay between the disc luminosity affecting the jet bulk Lorentz factor and the disc luminosity as seen by the observer. Superluminal motion occurs at least at a few light years from the accretion disc. However, no changes important enough in the disc luminosity have been observed on time scales of several years and this hypothesis seems difficult to justify.

However, a lack of energy in particles is possible and consistent with the fact that particles are quite cold here ($\bar{\gamma} \approx 400$). Figure 9.2 shows that ballistic motion is reached in the accelerating phase out of the torus photon field (see detailed explanation in section 7.2). Therefore, an increase of the particles mean energy would directly imply an increase of Γ_∞.

On the other hand, it is very interesting that the model is able to reproduce the broadband spectrum of 3C 273 with $\Gamma_b(Z) < 3$. As explained in section 1.2.2, there are many evidences pointing to low Lorentz factors in AGN and high Lorentz factor are very difficult to explain if applied to the entire jet. Here we show that with a stratified jet model, high Lorentz factor are not necessary to reproduce the averaged broadband emission and that the stationary state of the object could correspond to very moderate Γ_b. However, an increase of the particles mean energy, corresponding to a state of higher activity (observed in blazar) or flare, could induce higher Γ_∞, as high as the ones observed.

9.2 PKS 1510-089

For the next objects, I used mainly the GA to find a best fit to the SED and did not spend as much time as for 3C 273 trying to narrow the ranges of parameters to “good” values. As I explain later, this may result in less physical modeling.

9.2.1 Observations

PKS 1510-089 is a very powerful FSRQ that I presented in section 7.4.2 as hosting the fastest observed jet. Moreover, it has been observed at almost all wavelengths. As such,

it is a good candidate to test the two-flow model and see if we can reproduce the SED as well as the huge Lorentz factor $\Gamma \gtrsim 46$. The observed luminosity for the disc is evaluated at $L_{\rm disc,obs} = 5 \times 10^{45}{\rm erg.s}^{-1}$. For a black-hole mass of $M_\bullet = 2 \times 10^8 M_\odot$, the Eddington luminosity is $L_{edd} = 1.25 \times 10^{38} \left(\frac{M_\bullet}{M_\odot} \right) {\rm erg.s}^{-1} = 2.5 \times 10^{46} {\rm erg.s}^{-1}$. So the total luminosity of the disc (twice the observed one) corresponds to an accretion rate of $\dot{m} = 0.4$. The apparent velocity of $\beta_{app} = 46$ imposes a maximum viewing angle of 2.5°.

The SED data used here are a compilation of many observations and instruments taken from ASDC (2000) (figure 9.3). It shows a strong variability at high energy which makes the modeling of an hypothetic steady state difficult. The theoretical data used for the genetic algorithm are presented as black dot in figure 9.3. This theoretical data are obtained by locally averaging the low energy emission (below 10^{16}Hz) and by best-fitting the high energy emission with a log-parabola.

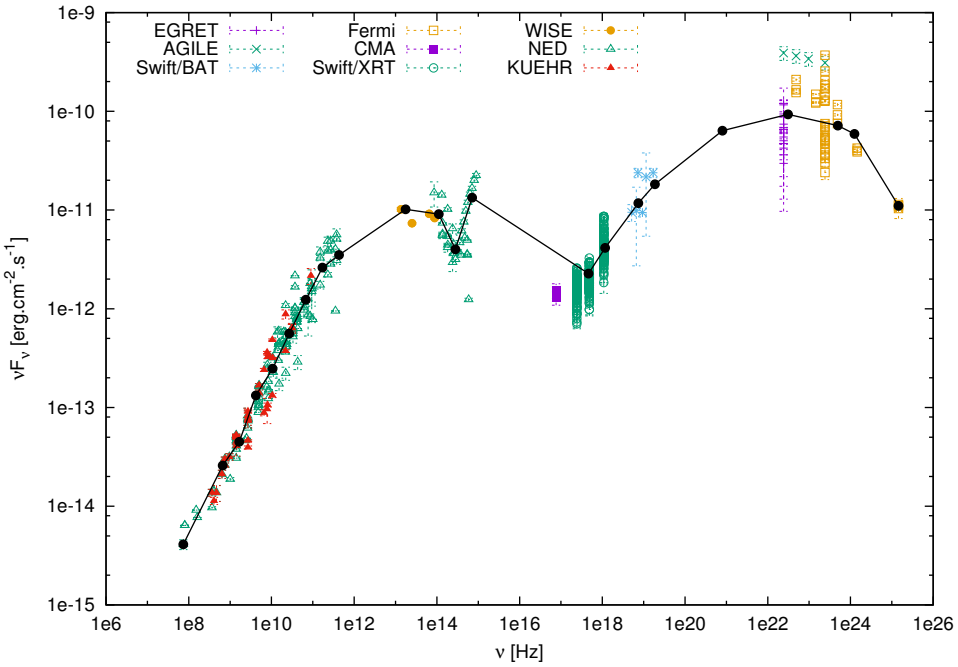

Figure 9.3: Broadband data of PKS 1510-089 taken from ASDC (2000). The different instruments come in different colors. Black dots-line represent the fake data used by the genetic algorithm for the automatic fit.

9.2.2 Modeling

As seen in section 7.4.2, the huge Lorentz factor of PKS 1510-089 cannot be explained by the Compton rocket effect if there is a dusty torus. To stay coherent with this result, I chose not to include any torus in the modeling. Broad emission lines have been observed however, indicating the presence of a broad-line region. Results from section 7.4.2 also showed that the accretion disc and the BLR could not be larger than $10^3 R_S$. I therefore chose sources sizes in consequence - these parameters are fixed and given in table 9.2:

$M_\bullet/M_\odot$	$\dot{m}$	R_{blr}	ω_{max}	α_{blr}	D_T	R_T	R_{in}	R_{out}
2×10^8	0.4	$10^3 R_S$	8°	0.1	-	-	$3R_S$	$10^3 R_S$

Table 9.2: Geometrical parameters used for the modeling of PKS 1510-089. These parameters were fixed for the genetic algorithm.

Research of the best fit by the genetic algorithm

The genetic algorithm is then used to find the best fit of theoretical data presented in figure 9.3 with 8 free parameters (i_{obs}, R_0, Q_0, B_0, n_0, ω, λ, ζ) in this case (see table 9.3) and populations of 500 individuals. A presentation of the evolution of the population is done in figure 9.4. On the left is presented the evolution of the χ^2 of the best individual as a function of the generation. On the right is displayed the SED of the best individuals for some generations showing the evolution of the population.

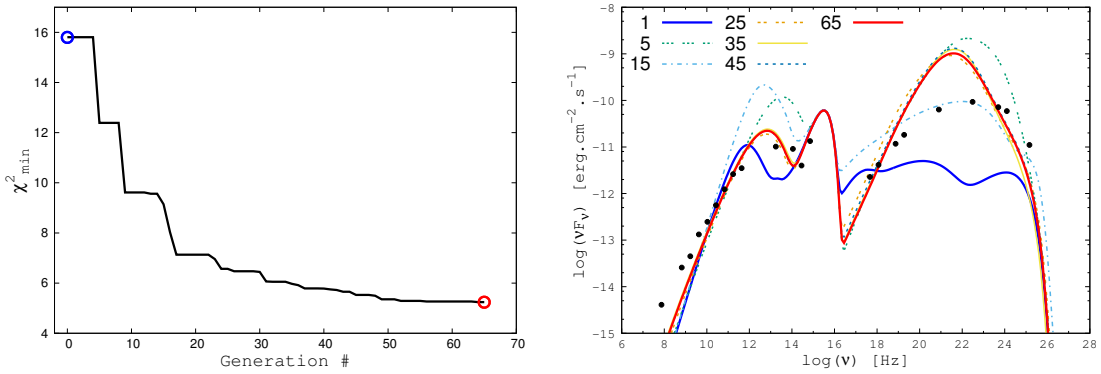

Figure 9.4: Evolution of the population during the fit of PKS 1510-089 with the χ^2 (left) and the SED (right) of the best individual as a function of the generation. In blue the best individual of the first generation, in red the best individual of the last generation. Some best individuals of intermediate generations have also been represented.

Looking only at the SED, one might think that the successive individuals are quite similar. However, the scatter of parameters shows otherwise. The table 9.3 shows the parameters of the best individual for the first and last generation as an example and one can see that the resulting values are very different (B_0 and Q_0 are different by two orders of magnitude and the indexes of the power-laws are completely different, implying a very different evolution of the parameters along the jet). Figure 9.5 shows a scattering plot of the individuals as a function of χ^2 and one physical parameter. This shows that a wide variety of parameters and of combination have been tried by the genetic algorithm to reach a best fit after 72 generations.

9.2.3 Discussion

The best fit SED obtained by the genetic algorithm after 72 generation on a population of 500 individuals is represented on the left in figure 9.6. The parameters corresponding to this solution are represented as dotted lines in figure 9.7. The overall SED of PKS 1510-089 is well reproduced by the model. Note that the resulting spectrum for a standard

Generation	i_{obs}	R_0	Q_0	B_0	n_0	ω	λ	ζ
1	6.8 °	$49R_S$	7.2×10^{-5}	16.4 G	$3.4 \times 10^4 cm^{-3}$	0.81	1.74	0.81
65	6.3 °	$79R_S$	8.6×10^{-3}	$6.4 \times 10^{-2} G$	$7.9 \times 10^3 cm^{-3}$	0.66	1.00	0.99

Table 9.3: Free parameters for the fit of PKS 1510-089 and values for the best individual of the first and last generation. These parameters correspond to the initial condition set at $Z_0 = 2 \times 10^3 R_S$.

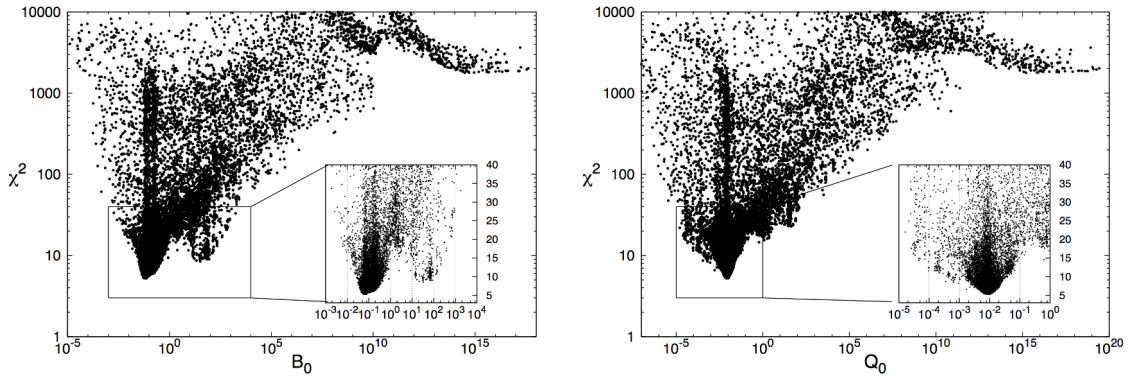

Figure 9.5: Scatter plot of all individuals, generation wise. Each point represent one individual as a function of one parameter (B_0 [G] or Q_0 [s^{-1}]) and χ^2. For clarity issues, the range of χ^2 is limited.

accretion disc around a Schwarschild black hole does not fit very well the optical data but this should not have a very strong impact on the external Compton resulting emission as long as the total luminosity emitted by the disc is respected.

Contrary to 3C 273, the peak frequency of the synchrotron and of the SSC does not clearly decrease with the distance in the jet and the slices emission are less spread over the SED. The radio emission is till produced by far synchrotron however. At high energies also the contributions from each slices are similar and there is still some high-energy emission far in the jet. This is interesting as the location of the γ-ray emission is subject to discussion (Saito et al. (2013), Dotson et al. (2015) & Brown (2013)).

The magnetic field in the inner regions as well as the opening angle ($\theta_{jet} \approx 6°$) can be compared to the ones used by Kataoka et al. (2008) for its fit of PKS 1510-089 broadband SED with a one-zone model. The magnetic field used in this study had a value of $B \approx 1G$ and the opening angle was $\theta_{jet} \approx 2°$ (with slight variations depending on the modeling).

The pair creation is not as important as in 3C 273 and evolution of physical parameters appear much smoother here. This might be due to the absence of dusty torus which makes less variations in $\Gamma_b(Z)$.

As one can see, the bulk Lorentz factor does not reach the very high values observed of $\Gamma \gtrsim 46$ but converge to $\Gamma_\infty \approx 10$. In order to see if a fit compatible with the observation $\Gamma \geq 46$ was possible, I tried to find a best fit with the genetic algorithm with the same fixed and free parameter as before but with an imposed $\Gamma_\infty = 50$ (thus not respecting the decoupling from the photon naturally occuring and the self computation of Γ_∞ - see

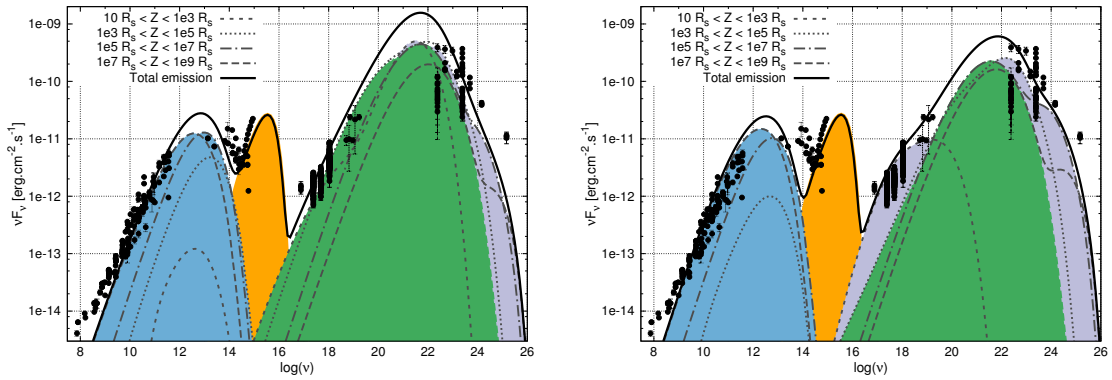

(a) Model fitting with Γ_∞ computed self-coherently

(b) Model fitting with $\Gamma_\infty = 50$ imposed

Figure 9.6: Best SED from the genetic algorithm for the modeling of PKS 1510-089. In orange the accretion disc emission with the choice made to have a luminosity consistent with observations $L_{disc} = 5 \times 10^{45}$erg.s^{-1}. Here the standard accretion disc does not fit very well the optical data. In blue the synchrotron emission, in green the SSC and in purple the external Compton on the disc and the BLR. Different dashed lines show different emission region of the jet.

section 7.2). The best solution obtained is given on the right in figure 9.6 as a comparison.

It is interesting to note that the GA converge to a similar solution, independently of the value of Γ_∞. The broadband SED is well reproduced here also. We can note that the inverse Compton emission is more important in this solution, especially in the X-rays and at very-high energy. The emission at large distances is also enhanced due to the larger Doppler factor.

The power-laws have very similar indexes in both solution indicating that both solution could depict the same jet. However the magnetic field in the second solution ($\Gamma_\infty = 50$) is much lower as well as the heating. The diminution of these two parameters somehow compensate as the particle cooling (through synchrotron and SSC emission) decrease as much as the heating. But the second solution is even further to equipartition than the first one (see last plot in figure 9.7 and equation 9.1 for a definition of ξ). This poses an energetic problem as ultimately, the magnetic field is supposed to be the source of particle acceleration through turbulence. To be closer to equipartition would need to increase the magnetic field. Interestingly a solution with higher B_0 has been explorer by the GA in the research for the first solution and is visible in the left plot of figure 9.5 as the second broad bell at $B_0 \approx 30$G. The SED of this solution is also visible as the best individual of generation 15 in figure 9.4. This solution, explorer by the GA was abandoned for cause of too large synchrotron emission and eventually discriminated when a better individual came along (generation 25 and following).

9.3 Too wild genetic algorithm

Studies similar to the one of PKS 1510-089 have been done for the blazars 3C 454.3, 3C 279 and PKS 1514-241 (aka Ap Librae).

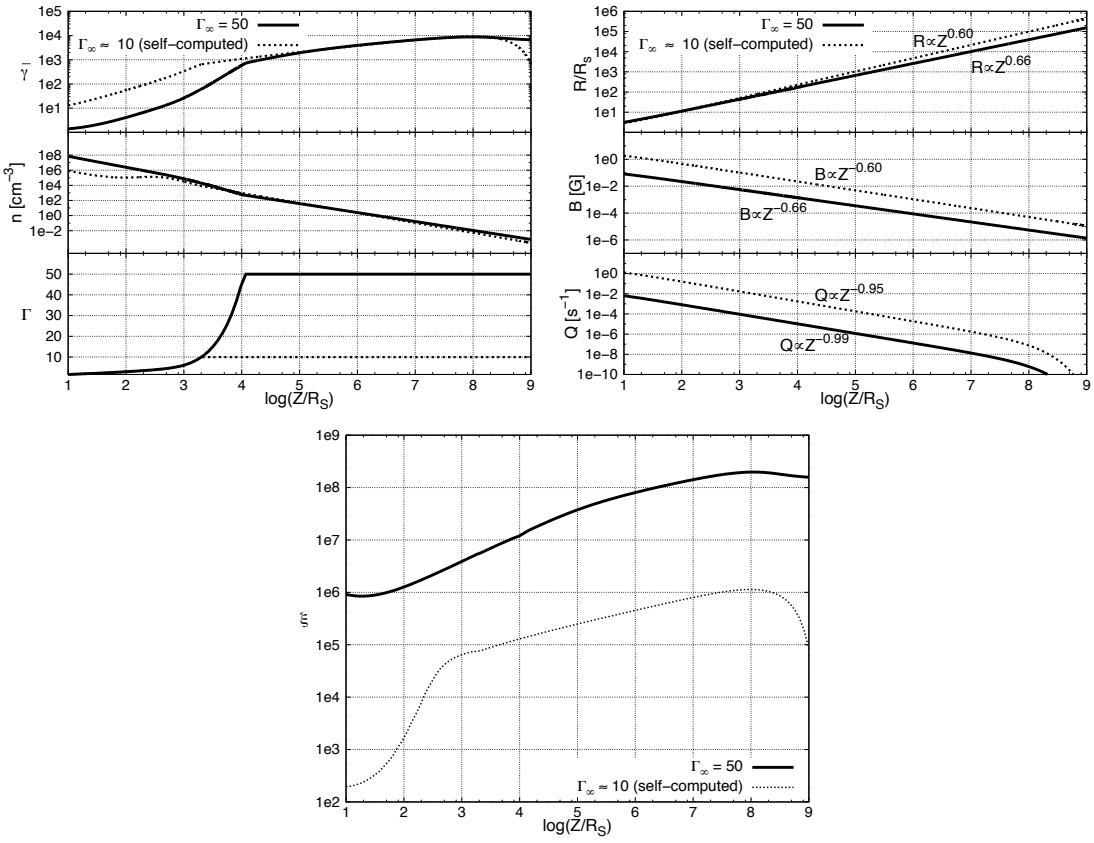

Figure 9.7: Evolution of the physical parameters as a function of the distance in the jet for the two modeling of PKS 1510-089: with Γ_∞ computed self-coherently and with $\Gamma_\infty = 50$ imposed.

9.3.1 Observations

- 3C 454.3 is a blazar at a redshift of $z = 0.859$ Its black-hole mass is constrained to a few $10^9 M_\odot$. Woo and Urry (2002) (Wo02) derived a mass $M_\bullet = 1.48 \times 10^9 M_\odot$ using the relation between the BLR size and the optical luminosity, Gu et al. (2001) (Gu01) derived $M_\bullet = 4.41 \times 10^9 M_\odot$ using H_β line width and Liang and Liu (2003) (Lia03) derived $M_\bullet = 4.99 \times 10^9 M_\odot$ using the $\gamma - ray$ luminosity. Fast superluminal motion has been observed at several positions in the jet of 3C 454.3 by Jorstad et al. (2005) (Jo05) with derived Lorentz factor ranging from 10 to 25 and observation angles ranging from 0.2° to 3.9°. They also derived an half-opening angle $\theta_{jet} = (0.8 \pm 0.2)°$. The BLR is visible in 3C 454.3 and Pian et al. (2005) (Pi05) derived a luminosity of $L_{blr} = 3.3 \times 10^{45} erg.s^{-1}$ and a size $R_{blr} = 223ld = 5.8 \times 10^{17} cm$

- 3C 279 is a FSRQ located at a redshift $z = 0.536$. The black-hole mass derived by the same author and techniques than for 3C 454.3 are $M_\bullet = 2.69 \times 10^8 M_\odot$ for Wu02, $M_\bullet = 8.17 \times 10^8 M_\odot$ for Gu01 and $M_\bullet = 3.98 \times 10^8$ for Lia03. Jo05 also observed superluminal motion at several position in the jet of 3C 279. The derived ranges are (10-18) for Γ and $(0.6 - 3.9°)$ for i_{obs}. The half-opening angle is $\theta_{jet} = (0.4 \pm 0.3)°$. Pi05 derived a BLR luminosity of $2.42 \times 10^{44} erg.s^{-1}$ and a BLR size of $R_{blr} = 36ld = 9.3 \times 10^{16} cm$.

- Ap Librae is a curious FSRQ by its SED and has proved to be difficult to model.

It is located at $z = 0.049$. Wo02 derived a black-hole mass $M_\bullet = 2.69 \times 10^8_\odot$ by direct measurement of stellar velocity dispersion. No superluminal motion has been observed in this AGN and parameters are much less constrained than for the two previous objects. Hervet et al. (2015) recently made a modeling of Ap Librae with an original model of blob in jet. They argue that the raise in the optical band is a sign of the accretion disc emission. Following this argument, the accretion rate is then fixed at $\dot{m} = 0.02$.

These observations motivate the parameters values for the modeling given in table 9.4.

9.3.2 Modeling

The parameters fixed before to run the genetic algorithm are given in table 9.4.

	$M_\bullet/M_\odot$	R_S (cm)	$\dot{m}$	R_{out}/R_S	R_{blr}/R_S	ω_{max}	α_{blr}	R_T/R_S	D_T/R_S
3C 454.3	1.5×10^9	4.5×10^{14}	0.1	5×10^3	2×10^3	37°	0.1	5×10^4	4.5×10^4
3C 279	5×10^8	1.5×10^{14}	0.04	500	500	37°	0.1	-	-
Ap Librae	2.5×10^8	7.4×10^{13}	0.02	500	500	37°	0.1	-	-

Table 9.4: Fixed parameters for the modeling of 3C 454.3, 3C 279 and Ap Librae. The Schwarzschild radius is derived from the black-hole mass are given as information.

For 3C 454.3 and 3C 279, the accretion rate have been chosen so that the accretion disc emission correspond to the lower limit in optical. The genetic algorithm has been used to find the best fit parameters for these objects. Here we use "theoretical" data to avoid the weight problem of the χ^2 computation as described previously. For 3C 454.3 and 3C 279, the theoretical data correspond to local averages below 10^{16} Hz and to a best fit parabola above. For Ap Librae, the real data were provided as a courtesy by Hervet et al. (2015) and are the ones used in their study - it is a compilation of data from Planck, Fermi-LAT, WISE, Swift-UVOT, Swit-XRT and H.E.S.S. We used a linear interpolation on these data to create the theoretical data used by the GA.

The resulting best fits from the GA are given in figure 9.8 with the corresponding parameters.

9.3.3 Discussion

At first sight, the fits give an overall good representation of the broadband SED of these three objects. However, the dependence $\nu_{peak}(Z)$ for the SSC in reversed compared to previous solutions. Indeed, the parts of the jets emit in the X-ray whereas the γ-ray emission is produced at great distances. This is due to an index of the heating power-law ($Q(Z) \propto Z^{-\zeta}$) close to unity ($\zeta \approx 1$) resulting in an important increase of the mean particle energy $< \gamma >$. This kind behavior is in apparent contradiction with rapid variability observed in γ-rays in 3C 454.3 and 3C 279.

Due to light travel time and for causality arguments, the size of the emission zone is limited by the observed variability such that:

$$R_b < c t_{var} \delta_b (1 + z) \tag{9.2}$$

In 3C 454.3, variability in γ-rays has been observed on the timescale of several days (Bonning et al. (2009)) and even lower (Foschini et al. (2010)). A one-day variability

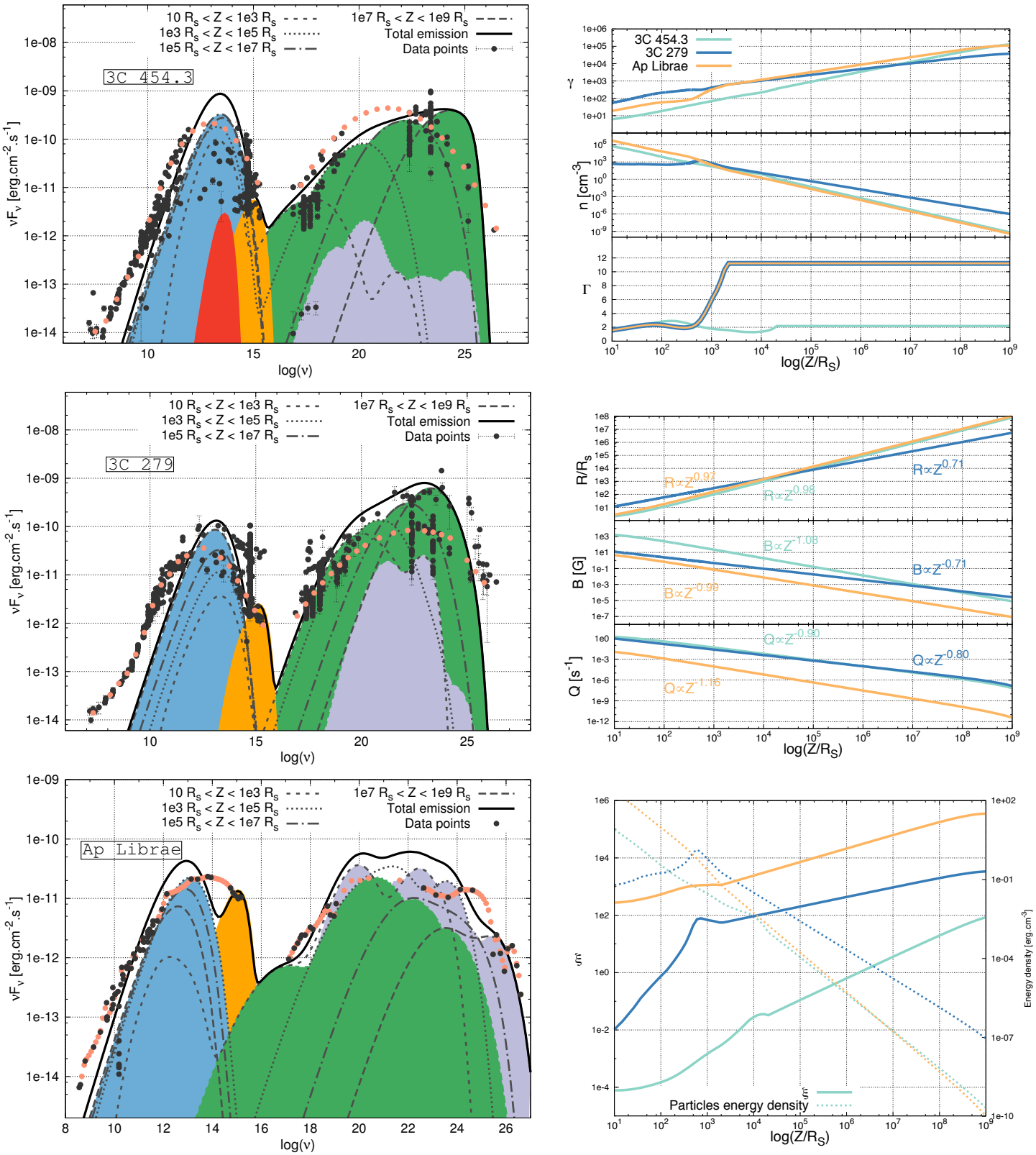

Figure 9.8: Modeling of three blazars with the resulting SED on the left side: *Top:* 3C 454.3. *Center:* 3C 279. *Bottom:* Ap Librae. Black points represent all the data available in archives from ASDC (2000). Orange points represent the "theoretical" data used by the GA to optimize the fit. Colors represent different emission processes: blue is synchrotron, green is SSC, purple is EC. In orange is the accretion disc emission while red is the dusty torus emission. On the right side are displayed the parameters as a function of the distance in the jet Z/R_S.

imposes a size $R_b < \delta_b(4.8 \times 10^{15})$ cm. But in the modeling here, the jet opening gives a jet radius of $R > 4.5 \times 10^{18}$ cm for $Z > 10^5 R_S$. Then the variability would imply a ridiculous value of $\delta_b \geq 10^3$. The same argument applies to 3C 279 with hours variability observed in γ-rays (Hayashida et al. (2015)). This kind of solutions are therefore ruled out for 3C 454.3 and for 3C 279.

To my knowledge, no very fast variability has been detected for Ap Librae to this day. Therefore the question of the γ-ray emission location is still open and a solution with very-high energy emitted at large distances in the jet is still possible.

But we see here the limits of the research of a model by an automatic tool driven only by the best fit of the integrated emission on data points. The blind use of the GA will not provide satisfactory modeling in most cases but must be used as a tool to converge to best solution in an already narrowed space of parameters. Moreover, the examples showed here might also be a demonstration of a wrong selection of data. 3C 454.3 and 3C 279 both show very important variability and the data selected are mostly representative of high activity events or flares. The model aims at reproducing the stationary state of AGN which is certainly closer to their quiescent state. Further studies are being done on these three blazars.

9.4 General discussion

The main result of this study is that the model can reproduce the broadband emission of FSRQ. The SED of 3C 273 has been reproduced in great agreement while it imposes a lot of constraints:

- the broad line region, the accretion disc and the torus are all visible and constrain very much the resulting bulk Lorentz factor $\Gamma_{eq}(Z)$ through the Compton rocket effect
- a lot of data are available and the SED show data points almost without discontinuity from far radio (10^7Hz) to far γ-rays (10^{25}Hz).

While these data bring a lot of constraint, when averaged on long period of times they also give the possibility to have a SED closer to the stationary state and therefore provide an adapted SED to fit with our model.

I showed that reproducing the broadband SED of blazars does not require high Lorentz factor (the SED of 3C 273 is reproduced with a $\Gamma_b(Z) < 3$ and the one of PKS 1510-089 with $\Gamma < 10$). This is possible thanks to the stratification of the jet and to the pile-up distribution of the particles that help overcoming the constraint on self-absorption (Henri and Saugé (2006)). However, this is in contradiction with observed superluminal motion inferring $\Gamma \geq 7$. But these observations made by VLBI does not involve that all the jet move at such speed. It is possible that only some parts of the jets, and only on limited timescales, move with high Lorentz factors. Moreover, Lorentz factor of the order of 7 are very easily reachable in the case of 3C 273 with hotter particles. This result opens a lot of questions and perspectives on the actual speed of jets. Further studies are needed here to see if high activity states in 3C 273, explained by the raise of the particles heating (and consequently of their mean energy) would be coherent with the boost of Γ_∞ required to explain the superluminal motion.

In section 7.4, I showed that observations and limits of Γ inferred by superluminal motion were theoretically reachable with the Compton rocket effect. The next step would be to study if the required conditions are compatible with SED modeling.

It is also possible that our prescription for $Q(Z)$ is not detailed enough and too simple to allow the required heating at $Z > 10^4 R_S$. This is confirmed by observations in other objects showing signs of important re-acceleration at great distances in the jet such as HST-1 in M 87 (Harris et al. (2003), Harris et al. (2006)) or the X-ray emission at kilo-parsec scales in many blazars (Jorstad and Marscher (2006))).

Other improvements on the model could also be done on the jet geometry described by $R(Z)$ as a simple power-law. While this might be a good first approximation, observations show changes in jets geometry (see Jorstad et al. (2005) or Asada and Nakamura (2012) for M 87).

The genetic algorithm that I developed is a powerful tool to explore the hyper-space of parameters and to optimize the fit on data. However, it cannot be used blindly as it does not prevent the convergence to non physical solutions as it is based only on the best fit of the broadband SED. The choice of data to fit is also essential. The model that I developed is stationary and as such, is not adapted to fit broadband SED including flaring states. However, once a quiescent state has been modeled, it is possible to study the implications of slight changes in the parameters (such as heating or magnetic field) to try to reproduce flaring states. This would be the first step to a time dependent modeling. Unfortunately, getting and selecting data is a complicated and long process that must be handled with caution (for the reasons I just mentioned and to avoid observation bias) and I have not had the time to do it.

9.5 *[En résumé]* Modélisation d'objets

Ce dernier chapitre traite de la modélisation de plusieurs objets astrophysiques par le modèle développé dans ce travail de thèse. Le premier objet modélisé est 3C 273, le premier blazar découvert grâce à sa relative proximité. Il a été énormément étudié depuis, et de nombreuses données sont disponibles. J'utilise ici des données moyennées sur 30 ans d'observations (Turler et al. (1998)). 3C 273 est également un bon candidat pour tester le modèle car ses sources de photons externes (le disque d'accrétion, le tore de poussière et la BLR) sont visibles et bien connues. Ceci permet d'imposer une certaine modélisation de ces sources (voir chapitre 6) et donc de l'évolution de $\Gamma_{eq}(Z)$ (voir chapitre 7). La SED obtenue permet une bonne reproduction des données, de la radio aux rayons gamma (voir figure 9.1). On peut y voir le rôle de chaque partie du jet dans la SED finale. En particulier, on voit que les plus hautes énergies sont reproduites par l'émission Compton inverse sur les sources de photons externes, et ce dans les parties les plus internes du jet (pour $10R_s < Z < 10^3 R_s$). Le spectre radio se construit par somme des émissions des parties de plus en plus éloignées dans le jet. L'évolution des paramètres physiques pour cette modélisation est donnée figure 9.2. Cette modélisation de 3C 273 est intéressante car elle permet une bonne reproduction de la SED dans sa globalité, et ce avec un facteur de Lorentz relativement bas ($\Gamma(Z) < 3$). La valeur finale de $\Gamma_\infty \approx 2.8$ est en revanche discutable car elle n'est pas en accord avec certaines observations de mouvements superluminiques indiquant $\Gamma > 7$. Ce décalage avec les observations peut s'expliquer par une insuffisance dans le modèle. Il serait en effet possible d'accélerer le plasma à de plus grandes valeurs de Γ en augmentant l'énergie moyenne des particules (voir chapitre 7).

Le second objet modélisé est PKS 1510-089. C'est un AGN très puissant qui est particulièrement intéressant car il abrite le jet le plus rapide jamais observé. Le résultat de l'application de l'algorithme génétique est représenté figure 9.6 (a). Ici encore le modèle est capable de reproduire assez fidèlement la SED observée mais le facteur de Lorentz résultant est trop faible pour expliquer les observations ($\Gamma_{infty} \approx 10$ contre $\Gamma_{obs} \approx 50$). Une seconde modélisation est réalisée en imposant cette fois ci $\Gamma_\infty = 50$ (figure 9.6 (b)) ; on peut voir que cette modélisation est également capable de reproduire correctement la SED de PKS 1510-089. Ceci montre à nouveau une possible limite du modèle.

Enfin, les modélisations de trois autres objets, 3C 454.3, 3C 279 et Ap Librae, montre les limites de l'algorithme génétique. En effet, ces objets ont des SED plus "complexes" que les deux objets étudiés précédement et l'application aveugle de l'algorithme génétique ne permet pas une bonne reproduction des données. De plus, on peut se rendre compte lors d'une analyse plus fine des solutions obtenues que celles ci ne sont pas physique. On voit ici la limite de l'algorithme qui cherche uniquement à obtenir la meilleur modélisation de la SED sans d'autres considérations physique.

Conclusion

Conclusions & perspectives

Active Galactic Nuclei. Some incredible astrophysical sources that I have discovered and studied in the past three years. In essence, they are the most energetic objects in the universe, powered by super-massive black-holes lying at the center of their host galaxy. The energy released is tremendous and in some cases, allow the formation of plasma jets blasting-off the galaxy at relativistic speeds.

Despite many efforts and more advanced instruments since their discovery less than a century ago, these objects are still widely misunderstood. The subject of my thesis was the modeling of a branch of these jetted active galactic nuclei (AGN), the flat spectrum radio quasars (FSRQ) in the two-flow paradigm developed at IPAG.

The paradigm of the two-flow, based on original ideas but rooted on solid physical ground aims at giving a unified coherent picture of AGN jets. It relies on the assumption that the observed jets are not composed of one, but two interacting plasma jets: a spine composed of a pure leptonic plasma moving at relativistic speed is collimated by an outer MHD sheath. This is supported both by observational facts and theoretical ground.

More and more observations show limb brightening in jets, suggestive of a possible interaction between two flows. In addition, very recent observations show radial velocity stratification in M87 jet with edges slower than center.

On the theoretical side, it has several benefits. First the energy budget is lightened as only a purely leptonic plasma needs to be accelerated to relativistic bulk speeds. The confinement issue of relativistic jets is naturally solved as the MHD jet (sheath) is self-collimated and then confines the relativistic spine. Furthermore, the interaction between the two flows allows a transfer of energy from the sheath to the particles in the spine which in turn, assure the bulk acceleration of the spine through the Compton rocket effect, up to the observed bulk Lorentz factors Γ. Finally, the stratification of the jet, compulsory with a distributed acceleration, reduce the constraints on Γ, providing a potential solution to the bulk Lorentz factor crisis.

In order to study further this paradigm and confront it to observations, a numerical model based on its concept and able to produce observables was necessary. Such a numerical model has been started in a previous work by Boutelier (2009) but lacked a central process: the external Compton emission. This process which is the scattering of thermal photons on relativistic particles is unavoidable in the study of FSRQ. First, it can provide a substantial high-energy emission contributing to the observed luminosities. Second, it produces a strong cooling of the particles, especially close to the central engine, which must be taken into account in any serious physical modeling of these objects. Last but not least, in the two-flow paradigm, it is responsible for the acceleration of the relativistic spine of the jet through the Compton rocket effect.

However, taking completely into account this process is complex and can be very greedy in computing time. To accomplish fast and efficient computation of the external Compton emission, I have had to formulate new analytical approximations of the scattering of a thermal distribution of photons. Numerical development has also been handled with care to avoid any unnecessary waste of computing time. The use of a pile-up as particle energy distribution also fastened the computation by allowing an analytical integration over the particle energy in the Thomson regime.

The complete model of the jet takes into account the synchrotron and the inverse Compton emission processes. Both synchrotron and thermal photons are used as scattering sources for the computation of the inverse Compton. The complete cross-section (in Klein-Nishina regime) is used and a special attention is given to the external Compton (on thermal photons) to take carefully into account the anisotropy of the soft photon sources present in FSRQ (accretion disc, dusty torus, broad line region) and of the emission. Energy of the particles is computed as the result of the cooling due to emission processes and a heating term due to turbulence. Then the bulk Lorentz factor is computed self-consistently based on the soft photon sources and on the energetics of the jet. The photon-photon absorption in the jet, also responsible for the pair creation, as well as out of the jet (from local thermal sources as well as from the extragalactic background) is also carefully computed. All these ingredients are integrated in a structured jet model in which physical conditions are computed consistently all along the jet from initial conditions at its base.

From the precise computation of the equilibrium bulk Lorentz factor (Γ_{eq}) of the pair plasma resulting from the Compton rocket effect in the photon field of a FSRQ, I studied the variation of $\Gamma_{eq}(Z)$ as a function of the distance from the central engine. I showed that the plasma moves through zones of acceleration and deceleration as different sources dominate the photon field. This results in changes in the Doppler boosting, leading to possible variations in the observed emission, both spatially and temporally. This work led to a publication in Astronomy & Astrophysics.

The complete jet model can produce broadband spectral energy distribution (SED) than one can directly compare to observed ones as it takes into account the redshift and the absorption from the distance to the object. However, because of its completeness, the model is also very complex and depends on many parameters. Also, despite many efforts to keep it to a minimum, the computing time is still an obstacle to the use of the model. Both of these drawbacks prohibit the optimization of the model with direct methods (by hand or by gradient methods). In order to circumvent this major issue, I developed an optimizing tool based on genetic algorithms. The study and the refinement of this tool has been the opportunity for me to develop new knowledge and to manage a master student during his internship. The application of this method allowed me to fit successfully the SED of several objects. However, the picture is surely more complex than what the model describe. In particular, the Lorentz factors obtained self-coherently with the computation of the jet are often lower than the observed ones. This is interesting as it demonstrates the possibility to reproduce the broadband SED of FSRQ with low Lorentz factor in a stratified jet, which could bring a solution to the bulk Lorentz factor crisis. However, the final values do not match with the observed ones at great distances in jets by very long based interferometry. This difference can have several origins. Firstly, observed features

moving at large bulk Lorentz factor do not necessarily correspond to the whole flow nor to a stationary state. The Compton rocket might be responsible for these fast motions in flaring state, when the particles mean energy is higher. Secondly, another acceleration mechanism could be at play at great distances when the pair plasma is not coupled with the photon field anymore. Finally, the results presented here are obtained for a certain modeling. The hyperspace of parameters have not been covered and one cannot exclude the possibility that other sets of parameters might be able to reproduce well the observations. It is also important to remember that the prescriptions of the model are relatively simple and that physical conditions in jets are most certainly much more complex.

In the near future, it would be very interesting to study the possibility of accelerating jets to higher bulk Lorentz factor (Γ_∞) during flaring states. Additionally, one could study the influence of a more complex particle energy distribution or of a more complex prescription of the heating term as a function of the distance in the jet on the bulk Lorentz factor.

The second objective would be the modeling of more objects with a deeper test of the model. The lack of convergence to physical solutions by the genetic algorithms on certain objects does not necessarily prove a fail of the model. Therefore, the complete coverage of the parameter hyperspace, even for a single object, would be very valuable and would provide deep insights on the possible modelings and on the limitations of the model.

Another potential study is the investigation of other type of objects. Indeed, the model first aim were FSRQ but it has been designed in a very general and versatile way. In particular, it could be easily applied to BL Lacs by attenuating some of the external sources or to radio galaxies as the anisotropy and the viewing angles are completely taken into account in the modeling. It might even be applicable to micro-quasars, the miniature version of AGN by changing the dusty torus for a star in rotation.

A time-dependent study would be the next big step for the model. A time-dependent version was developed by Boutelier (2009) for the pure SSC modeling and the structure of the numerical code has been thought in this purpose. Indeed, the jet altitude grid is actually an observer time grid. Therefore, starting from a stationary state fitting stationary data, one can try to fit the high-energy in the flaring states by changing only a few parameters (e.g. the heating term or the initial particle density). Then one can sum contributions from the same observing times to retrieve the observed SED.

Finally, it is safe to say that AGN are very complex objects and that their studies will keep the community busy for many years. The two-flow paradigm provides a coherent picture and is able to explain many of the main features observed in AGN. It is only through this kind of models, based on physical arguments and cleaned (as much as possible) of ad hoc hypothesis that we will get meaningful insights on AGN activity. I am grateful I had the opportunity to work on such a model and to study objects beyond imagination. Teaching at university, as well as participating to popularization of astronomy and science in general have also been very stimulating time of my PhD. I have no doubt that the knowledge and experience I have gathered during these last three years will stay with me and will be of great benefit on the road ahead.

[En résumé] Conclusions & perspectives

Pendant ces trois dernières années, j'ai découvert et étudié les noyaux actifs de galaxie. Des objets incroyables, parmi les plus puissant de l'univers et tirant leur énergie de l'accrétion de matière sur un trou noir supermassif siègeant en leur coeur. En dépit de nombreuses études et d'instruments toujours plus performants depuis leur découverte il y a un siècle, beaucoup de questions centrales sont encore ouvertes. Le sujet de ma thèse était la modélisation d'un certain type d'NAG comportant un jet, les FSRQ (pour "Flat Spectrum Radio Quasars") dans le cadre du modèle de "*two-flow*" développé à l'IPAG.

Le paradigme du *two-flow* s'assoie sur des arguments physiques forts et sur plusieurs observations et tente d'apporter une vision unifiée et cohérente des jets de NAG. Il suppose que les jets observés sont en réalitée composés de deux plasmas en interaction : un jet central, purement leptonique et se déplacant à grande vitesse est collimaté par une gaine magnétohydrodynamique (MHD) prenant racine dans le disque d'accrétion. Cette hypothèse se fonde à la fois sur des considérations observationnelles et théoriques.

Afin d'étudier plus en profondeur ce paradigme et de le confronter aux observations, le développement d'un modèle numérique de jet fondé sur ses préceptes était nécessaire. Un tel modèle a en partie été développé par un travail de Boutelier (2009) mais n'incluait pas un processus central : l'émission Compton inverse sur des sources de photons externes au jet. Ce processus est essentiel dans la compréhension et la modélisation des FSRQ. D'une part, il contribue de façon importante à l'émission haute énergie observée. D'autre part, il est responsable d'une partie du refroidissement des particules et doit donc être pris en compte dans toute modélisation physique sérieuse de ces objets. Enfin, dans le paradigme du jet à deux fluides, il est responsable de l'accélération du jet et de sa dynamique par l'intermédiaire de l'effet fusée Compton.

Cependant, prendre en compte de manière précise ce processus est complexe et peut être très couteux en temps de calcul. Afin d'obtenir un calcul rapide et efficace, j'ai du développer de nouvelles approximations analytiques de la diffusion Compton inverse sur une distribution de photons thermiques. Il a également fallu être attentif à l'implémentation numérique de ce processus afin d'aboutir à une modélisation la plus rapide possible.

Le modèle complet de jet prend en compte les émissions synchrotron et Compton inverse dans le jet. Une attention spéciale a été portée à la modélisation spatiale des sources de photons (disque d'accrétion, tore de poussière, la "Broad Line Region" ou BLR) et à la prise en compte de l'anisotropie dans le calcul du Compton inverse. L'énergie des particules est calculée de manière cohérente comme le résultat du refroidissement dû aux processus d'émission et à l'accéleration due à la turbulence. Enfin, le facteur de Lorentz est calculé de façon cohérente avec les sources de photons externes et l'énergie des particules.

L'absorption photon-photon dans le jet (alors responsable de la création de paires) et à l'extérieur du jet est également calculée. Tous ces ingrédients sont intégrés dans un modèle de jet structuré dans lequel les conditions physiques sont calculées de façon cohérente tout au long du jet à partir de conditions initiales à sa base.

A partir du calcul précis de facteur de Lorentz d'équilibre (Γ_{eq}) du plasma de paires dans le champ de photon d'un FSRQ, j'ai étudié les variations de $\Gamma_{eq}(Z)$ en fonction de la distance à l'objet central. J'ai montré que le plasma passe par des zones d'accélération et de décèlération lorsque différentes sources dominent le champ de photon. Ceci provoque des changements dans l'effet Doppler pouvant avoir des répercussions importantes sur l'émission observée. Ce travail a été publié dans la revue *Astronomy & Astrophysics*.

Le modèle complet produit des distributions spectrales d'énergies (SED) comparables aux observations. Cependant, de par sa complexité, son nombre de paramètres et le temps de calcul important, l'application du modèle est difficile. Afin de pallier ce problème, j'ai développé un algorithme d'optimisation basé sur des algorithmes génétiques. Le développement et l'amélioration de cet algorithme a été l'opportunité d'encadrer un étudiant pendant son stage de master. L'application de cette méthode m'a permis de reproduire avec succès la SED de plusieurs objets. Cependant, d'autres difficultés dans la modélisation sont apparues, comme celle de reproduire de grands facteurs de Lorentz. Ceci dénote probablement une insuffisance dans la modélisation et/ou dans la recherche de solutions par l'algorithme qui n'est établi que sur l'optimisation de la SED.

Dans le futur, d'autres études intéressantes pourraient être réalisées grâce au modèle. En particulier, il est possible d'envisager la modélisation d'autres types d'objets comme les BL Lacertae ou les galaxies radios, et même les micro-quasars, ces NAG miniatures. Une modélisation dépendante du temps sera la prochaine grande étape du modèle et apportera de grandes contraintes sur celui-ci.

Pour conclure, on peut dire sans risque que les NAG sont des objets très complexes dont l'étude va continuer pendant encore de nombreuses années. Le modèle du *two-flow* fournit une image cohérente et physique capable d'expliquer de nombreux traits des NAG. C'est seulement par le biais de ce genre de modèle, assis sur de solides arguments physiques et minimisant le nombre d'hypothèse *ad hoc* que l'on pourra vraiment améliorer notre compréhension des NAG. Je suis enchanté d'avoir pu travailler sur un tel modèle et dans un champ de recherche si vaste. Enseigner à l'université et participer à la vulgarisation de la science ont également été des parties extrêmement stimulantes de mon doctorat. Que l'aventure continue...

Bibliography

Abdo, A.A. et al (2009). FERMIDISCOVERY OF GAMMA-RAY EMISSION FROM NGC 1275. *Astrophysical Journal*, 699(1):31–39.

Aharonian, F. et al (2007). An Exceptional Very High Energy Gamma-Ray Flare of PKS 2155-304. *Astrophysical Journal*, 664(2):L71–L74.

Albert, J. et al (2007). Variable Very High Energy γ-Ray Emission from Markarian 501. *Astrophysical Journal*, 669(2):862–883.

Alfvén, H. and Herlofson, N. (1950). Cosmic Radiation and Radio Stars. *Physical Review*, 78(5):616–616.

Antonucci, R. (2012). A panchromatic review of thermal and nonthermal active galactic nuclei. *Astronomical and Astrophysical Transactions*, 27:557–602.

Antonucci, R. (2015). Active Galactic Nuclei and Quasars: Why Still a Puzzle after 50 years? *arXiv.org*.

Antonucci, R.R.J. and Miller, J.S. (1985). Spectropolarimetry and the nature of NGC 1068. *Astrophysical Journal*, 297:621.

Aretxaga, I. et al (1999). Seyfert 1 Mutation of the Classical Seyfert 2 Nucleus NGC 7582. *The Astrophysical Journal*, 519(2):L123–L126.

Asada, K. and Nakamura, M. (2012). THE STRUCTURE OF THE M87 JET: A TRANSITION FROM PARABOLIC TO CONICAL STREAMLINES. *The Astrophysical Journal*, 745(2):L28.

ASDC (2000). Asi Science Data Center (ASDC).

Barkov, M.V., Khangulyan, D.V. and Popov, S.B. (2012). Jets and gamma-ray emission from isolated accreting black holes. *Monthly Notices of the Royal Astronomical Society*, 427(1):589–594.

Barthel, P.D. (1989). Is every quasar beamed? *Astrophysical Journal*, 336:606–611.

Begelman, M.C., Fabian, A.C. and Rees, M.J. (2008). Implications of very rapid TeV variability in blazars. *Monthly Notices of the Royal Astronomical Society: Letters*, 384(1):L19–L23.

Begelman, M.C. et al (1987). Inverse Compton scattering of ambient radiation by a cold relativistic jet - A source of beamed, polarized continuum in blazars? *Astrophysical Journal*, 322:650.

Begue, D. (2010). Modélisation de l'émission gamma des AGNs. *Master thesis*, pages 1–38.

Bell, A.R. (1978). The acceleration of cosmic rays in shock fronts. I. *Monthly Notices of the Royal Astronomical Society*, 182:147–156.

Biretta, J.A., Junor, W. and Livio, M. (1999). Formation of the radio jet in M87 at 100 Schwarzschild radii from the central black hole. *Nature*, 401(6756):891–892.

Blandford, R.D. and McKee, C.F. (1982). Reverberation mapping of the emission line regions of Seyfert galaxies and quasars. *Astrophysical Journal*, 255:419–439.

Blandford, R.D., Netzer, H. and Woltjer, L. (1990). *Active Galactic Nuclei*. Springer Berlin Heidelberg, Berlin, Heidelberg.

Blandford, R.D. and Payne, D.G. (1982). Hydromagnetic flows from accretion discs and the production of radio jets. *Monthly Notices of the Royal Astronomical Society*, 199:883–903.

Blandford, R.D. and Znajek, R.L. (1977). Electromagnetic extraction of energy from Kerr black holes. *Monthly Notices of the Royal Astronomical Society*, 179:433–456.

Blumenthal, G.R. and Gould, R.J. (1970). Bremsstrahlung, Synchrotron Radiation, and Compton Scattering of High-Energy Electrons Traversing Dilute Gases. *Reviews of Modern Physics*, 42(2):237–270.

Blustin, A.J. et al (2005). The nature and origin of Seyfert warm absorbers. *Astronomy and Astrophysics*, 431(1):111–125.

Bogovalov, S. and Tsinganos, K. (2001). Magnetic collimation of relativistic jets. *Astronomical and Astrophysical Transactions*, 20(2):303–309.

Bogovalov, S.V. (2001). Acceleration and collimation of relativistic plasmas ejected by fast rotators. *Astronomy and Astrophysics*, 371(3):1155–1168.

Bonning, E.W. et al (2009). CORRELATED VARIABILITY IN THE BLAZAR 3C 454.3. *Astrophysical Journal*, 697(2):L81–L85.

Böttcher, M. et al (2013). Leptonic and Hadronic Modeling of Fermi-detected Blazars. *The Astrophysical Journal*, 768(1):54.

Boutelier, T. (2009). Modélisation dépendante du temps des blazars du TeV par un modèle de jet stratifié inhomogene. *tel.archives-ouvertes.fr*.

Boutelier, T., Henri, G. and Petrucci, P.O. (2008). An inhomogeneous jet model for the rapid variability of TeV blazars. *Monthly Notices of the Royal Astronomical Society: Letters*, astro-ph(1):L73–L77.

Bowyer, C.S. et al (1970). Detection of X-Ray Emission from 3c 273 and NGC 5128. *Astrophysical Journal*, 161:L1.

Brown, A.M. (2013). Locating the -ray emission region of the flat spectrum radio quasar PKS 1510-089. *Monthly Notices of the Royal Astronomical Society*, 431(1):824–835.

Cara, M. et al (2013). POLARIMETRY AND THE HIGH-ENERGY EMISSION MECHANISMS IN QUASAR JETS: THE CASE OF PKS 1136–135. *Astrophysical Journal*, 773(2):186.

Celotti, A. and Ghisellini, G. (2008). The power of blazar jets. *Monthly Notices of the Royal Astronomical Society*, 385(1):283–300.

Celotti, A., Ghisellini, G. and Fabian, A.C. (2007). Bulk Comptonization spectra in blazars. *Monthly Notices of the Royal Astronomical Society*, 375(2):417–424.

Chiaberge, M. et al (2000). Does the unification of BL Lac and FR I radio galaxies require jet velocity structures? *Astronomy and Astrophysics*, 358:104–112.

Cohen, M.H. et al (1971). The Small-Scale Structure of Radio Galaxies and Quasi-Stellar Sources at 3.8 Centimeters. *Astrophysical Journal*, 170:207.

Collmar, W. (2001). AGN: The High-Energy Status before INTEGRAL.

Compton, A. (1923). A Quantum Theory of the Scattering of X-rays by Light Elements. *Physical Review*, 21(5):483–502.

Dai, B.Z. et al (2002). The Supermassive Black Hole in the Gamma-ray Loud Blazar PKS 1510-089. *eprint arXiv:astro-ph/0205482*.

de Almeida, C. and Saa, A. (2006). The radiation of a uniformly accelerated charge is beyond the horizon: A simple derivation. *American Journal of Physics*, 74(2):154.

Dotson, A. et al (2015). ON THE LOCATION OF THE 2009 GEV FLARES OF BLAZAR PKS 1510–089. *Astrophysical Journal*, 809(2):164.

Dubus, G., Cerutti, B. and Henri, G. (2008). The modulation of the gamma-ray emission from the binary LS 5039. *Astronomy and Astrophysics*, 477(3):691–700.

Fanaroff, B.L. and Riley, J.M. (1974). The morphology of extragalactic radio sources of high and low luminosity. *Monthly Notices of the Royal Astronomical Society*, 167:31P–36P.

Foschini, L. et al (2010). Does the gamma-ray flux of the blazar 3C 454.3 vary on subhour time-scales? *mnras.oxfordjournals.org*.

Fossati, G. et al (1998). A unifying view of the spectral energy distributions of blazars. *Monthly Notices of the Royal Astronomical Society*, 299(2):433–448.

Franceschini, A., Rodighiero, G. and Vaccari, M. (2008). Extragalactic optical-infrared background radiation, its time evolution and the cosmic photon-photon opacity. *Astronomy and Astrophysics*, 487(3):837–852.

Friedman, H. and Byram, E.T. (1967). X-rays from Sources 3C 273 and M 87. *Science*, 158(3798):257–259.

Georganopoulos, M. and Kazanas, D. (2003). Decelerating Flows in TeV Blazars: A Resolution to the BL Lacertae-FR I Unification Problem. *The Astrophysical Journal*, 594(1):L27–L30.

Georganopoulos, M. and Marscher, A.P. (1998). A Viewing Angle–Kinetic Luminosity Unification Scheme for BL Lacertae Objects. *The Astrophysical Journal*, 506(2):621–636.

Ghisellini, G. (2008). Emission and power of blazar jets. *arXiv.org*, (09):1491–1501.

Ghisellini, G. et al (1998). A theoretical unifying scheme for gamma-ray bright blazars. *Monthly Notices of the Royal Astronomical Society*, 301(2):451–468.

Ghisellini, G., Maraschi, L. and Treves, A. (1985). Inhomogeneous synchrotron-self-Compton models and the problem of relativistic beaming of BL Lac objects. *Astronomy and Astrophysics*, 146:204–212.

Ghisellini, G. and Tavecchio, F. (2010). Compton rockets and the minimum power of relativistic jets. *Monthly Notices of the Royal Astronomical Society: Letters*, 409(1):L79–L83.

Ghisellini, G., Tavecchio, F. and Chiaberge, M. (2005). Structured jets in TeV BL Lac objects and radiogalaxies. *Astronomy and Astrophysics*, 432(2):401–410.

Ghisellini, G. et al (2014). The power of relativistic jets is larger than the luminosity of their accretion disks. *Nature*, 515(7527):376–378.

Giovannini, G. et al (1999). B2 1144+35: A Giant Low Power Radio Galaxy with Superluminal Motion. *The Astrophysical Journal*, 522(1):101–112.

Giroletti, M. et al (2008). The jet of Markarian 501 from millions of Schwarzschild radii down to a few hundreds. *Astronomy and Astrophysics*, 488(3):905–914.

Giroletti, M. et al (2004). Parsec-Scale Properties of Markarian 501. *The Astrophysical Journal*, 600(1):127–140.

Gould, R.J. and Schréder, G.P. (1967). Pair Production in Photon-Photon Collisions. *Physical Review*, 155(5):1404–1407.

Greenstein, J.L. and Schmidt, M. (1964). The Quasi-Stellar Radio Sources 3c 48 and 3c 273. *Astrophysical Journal*, 140:1.

Gu, M., Cao, X. and Jiang, D.R. (2001). On the masses of black holes in radio-loud quasars. *mnras.oxfordjournals.org*.

Haardt, F. et al (1998). The hidden X-ray Seyfert nucleus in 3C 273: BeppoSAX results. *Astronomy and Astrophysics*, 340:35–46.

Harris, D.E. et al (2003). Flaring X-Ray Emission from HST-1, a Knot in the M87 Jet. *The Astrophysical Journal*, 586(1):L41–L44.

Harris, D.E. et al (2006). The Outburst of HST-1 in the M87 Jet. *Astrophysical Journal*, 640(1):211–218.

Hayashida, M. et al (2015). RAPID VARIABILITY OF BLAZAR 3C 279 DURING FLARING STATES IN 2013-2014 WITH JOINT FERMI-LAT, NuSTAR, SWIFT, AND GROUND-BASED MULTI-WAVELENGTH OBSERVATIONS. *Astrophysical Journal*, 807(1):79.

Heitler, W. (1954). *The Quantum theory of Radiation*. Oxford University Press, monograph on physics edition.

Henri, G. and Pelletier, G. (1991). Relativistic electron-positron beam formation in the framework of the two-flow model for active galactic nuclei. *Astrophysical Journal*, 383:L7–L10.

Henri, G. and Saugé, L. (2006). The Bulk Lorentz Factor Crisis of TeV Blazars: Evidence for an Inhomogeneous Pileup Energy Distribution? *The Astrophysical Journal*, 640(1):185–195.

Hervet, O., Boisson, C. and Sol, H. (2015). Linking radio and gamma ray emission in Ap Librae. *arXiv.org*.

H.E.S.S. Collaboration et al (2013). H.E.S.S. discovery of VHE γ-rays from the quasar PKS 1510-089. *Astronomy and Astrophysics*, 554:A107.

Homan, D.C. et al (2015). MOJAVE. XII. ACCELERATION AND COLLIMATION OF BLAZAR JETS ON PARSEC SCALES. *Astrophysical Journal*, 798(2):134.

Jamil, O., Fender, R.P. and Kaiser, C.R. (2010). iShocks: X-ray binary jets with an internal shocks model. *Monthly Notices of the Royal Astronomical Society*, 401(1):394–404.

Johnson, H.L. (1964). The Brightness of 3c 273 AT 2.2 μ. *Astrophysical Journal*, 139:1022.

Jones, F.C. (1968). Calculated Spectrum of Inverse-Compton-Scattered Photons. *Physical Review*, 167(5):1159–1169.

Jorstad, S.G. and Marscher, A.P. (2006). The X-ray and radio jets of quasars on kiloparsec scales. *Astronomische Nachrichten*, 327(2-3):227–230.

Jorstad, S.G. et al (2005). Polarimetric Observations of 15 Active Galactic Nuclei at High Frequencies: Jet Kinematics from Bimonthly Monitoring with the Very Long Baseline Array. *The Astronomical Journal*, 130(4):1418–1465.

Kaspi, S. et al (2005). The Relationship between Luminosity and Broad-Line Region Size in Active Galactic Nuclei. *Astrophysical Journal*, 629(1):61–71.

Kaspi, S. et al (2000). Reverberation Measurements for 17 Quasars and the Size-Mass-Luminosity Relations in Active Galactic Nuclei. *Astrophysical Journal*, 533(2):631–649.

Kataoka, J. et al (2008). Multiwavelength Observations of the Powerful Gamma-Ray Quasar PKS 1510-089: Clues on the Jet Composition. *Astrophysical Journal*, 672(2):787–799.

Kellermann, K.I. et al (2007). Doppler boosting, superluminal motion, and the kinematics of AGN jets. *Astrophysics and Space Science*, 311(1-3):231–239.

Kellermann, K.I. and Pauliny-Toth, I.I.K. (1969). The Spectra of Opaque Radio Sources. *Astrophysical Journal*, 155:L71.

Kellermann, K.I. et al (1989). VLA observations of objects in the Palomar Bright Quasar Survey. *The Astronomical Journal*, 98:1195–1207.

Khangulyan, D., Aharonian, F.A. and Kelner, S.R. (2014). Simple Analytical Approximations for Treatment of Inverse Compton Scattering of Relativistic Electrons in the Blackbody Radiation Field. *The Astrophysical Journal*, 783(2):100.

Knight, C.A. et al (1971). Quasars: Millisecond-of-Arc Structure Revealed by Very-Long-Baseline Interferome. *cdsads.u-strasbg.fr*.

Kormendy, J. (1988). Evidence for a supermassive black hole in the nucleus of M31. *Astrophysical Journal*, 325:128.

Kovalev, Y.Y. et al (2007). The Inner Jet of the Radio Galaxy [OBJECTNAME STATUS="LINKS"]M87[/OBJECTNAME]. *Astrophysical Journal*, 668(1):L27–L30.

Lacombe, C. (1977). Acceleration of particles and plasma heating by turbulent Alfven waves in a radiogalaxy. *Astronomy and Astrophysics*, 54:1–16.

Liang, E.W. and Liu, H.T. (2003). The masses of central supermassive black holes and the variability time-scales in gamma-ray loud blazars. *Monthly Notices of the Royal Astronomical Society*, 340(2):632–638.

Lister, M.L. et al (2013). MOJAVE. X. PARSEC-SCALE JET ORIENTATION VARIATIONS AND SUPERLUMINAL MOTION IN ACTIVE GALACTIC NUCLEI. *The Astronomical Journal*, 146(5):120.

Low, F.J. and Johnson, H.L. (1965). The Spectrum of 3c 273. *Astrophysical Journal*, 141:336.

Mahadevan, R., Narayan, R. and Yi, I. (1996). Harmony in Electrons: Cyclotron and Synchrotron Emission by Thermal Electrons in a Magnetic Field. *Astrophysical Journal*, 465:327.

Malkan, M.A., Gorjian, V. and Tam, R. (1998). A Hubble Space TelescopeImaging Survey of Nearby Active Galactic Nuclei. *The Astrophysical Journal Supplement Series*, 117(1):25–88.

Malkan, M.A. and Moore, R.L. (1986). The ultraviolet excess of quasars. III - The highly polarized quasars PKS 0736 + 017 and PKS 1510 - 089. *Astrophysical Journal*, 300:216.

Malzac, J. (2014). The spectral energy distribution of compact jets powered by internal shocks. *Monthly Notices of the Royal Astronomical Society*, 443(1):299–317.

Marcowith, A., Henri, G. and Pelletier, G. (1995). Gamma-ray emission of blazars by a relativistic electron-positron beam. *Monthly Notices of the Royal Astronomical Society*, 277(2):681–699.

Marscher, A.P. (1980). Relativistic jets and the continuum emission in QSOs. *The Astrophysical Journal*, 235:386–391.

Mertens, F. et al (2015). Velocity fields of parsec scale jets.

Meyer, E.T. and Georganopoulos, M. (2013). FERMIRULES OUT THE INVERSE COMPTON/CMB MODEL FOR THE LARGE-SCALE JET X-RAY EMISSION OF 3C 273. *The Astrophysical Journal*, 780(2):L27.

Meyer, E.T. et al (2015). Ruling out IC/CMB X-rays in PKS 0637-752 and the Implications for TeV Emission from Large-Scale Quasar Jets. *eprint arXiv:1504.00577*.

Nagai, H. et al (2014). LIMB-BRIGHTENED JET OF 3C 84 REVEALED BY THE 43 GHz VERY-LONG-BASELINE-ARRAY OBSERVATION. *Astrophysical Journal*, 785(1):53.

Nalewajko, K. et al (2012). HERSCHELPACS AND SPIRE OBSERVATIONS OF BLAZAR PKS 1510–089: A CASE FOR TWO BLAZAR ZONES. *Astrophysical Journal*, 760(1):69.

O'dell, S.L. (1981). Radiation force on a relativistic plasma and the Eddington limit. *Astrophysical Journal*, 243:L147–L149.

Onuchukwu, C.C. and Ubachukwu, A.A. (2013). On the Lorentz factor of superluminal sources. *Research in Astronomy and Astrophysics*, 13(5):509–516.

Paltani, S. and Turler, M. (2005). The mass of the black hole in 3C 273. *Astronomy and Astrophysics*, 435(3):811–820.

Pearson, T.J. et al (1981). Superluminal expansion of quasar 3C273. *Nature*, 290(5805):365–368.

Pelletier, G. (2004). Black Hole Induced Ejections. *eprint arXiv:astro-ph/0405113*.

Peterson, B.M. (2006). The Broad-Line Region in Active Galactic Nuclei. In *link.springer.com*, pages 77–100. Springer Berlin Heidelberg.

Peterson, B.M. et al (2004). Central Masses and Broad-Line Region Sizes of Active Galactic Nuclei. II. A Homogeneous Analysis of a Large Reverberation-Mapping Database. *Astrophysical Journal*, 613(2):682–699.

Phinney, E.S. (1982). Acceleration of a Relativistic Plasma by Radiation Pressure. *Monthly Notices of the Royal Astronomical Society*, 198:1109.

Pian, E., Falomo, R. and Treves, A. (2005). Hubble Space Telescope ultraviolet spectroscopy of blazars: emission-line properties and black hole masses. *mnras.oxfordjournals.org*.

Pian, E. and Treves, A. (1993). The Ultraviolet Continua of Blazars: A Reconsideration of IUE Archives. *Astrophysical Journal*, 416:130.

Piner, B.G. and Edwards, P.G. (2004). The Parsec-Scale Structure and Jet Motions of the TeV Blazars 1ES 1959+650, PKS 2155-304, and 1ES 2344+514. *Astrophysical Journal*, 600(1):115–126.

Piner, B.G. and Edwards, P.G. (2014). FIRST-EPOCH VLBA IMAGING OF 20 NEW TeV BLAZARS. *Astrophysical Journal*, 797(1):25.

Piner, B.G., Pant, N. and Edwards, P.G. (2010). THE JETS OF TeV BLAZARS AT HIGHER RESOLUTION: 43 GHz AND POLARIMETRIC VLBA OBSERVATIONS FROM 2005 TO 2009. *Astrophysical Journal*, 723(2):1150–1167.

Readhead, A.C.S. (1994). Equipartition brightness temperature and the inverse Compton catastrophe. *Astrophysical Journal*, 426:51–59.

Rees, M.J. (1966). Appearance of Relativistically Expanding Radio Sources. *Nature*, 211(5):468–470.

Renaud, N. (1999). Modélisation des jets relativistes et de l'émission haute énergie des blazars et des microquasars galactiques. *tel.archives-ouvertes.fr*.

Renaud, N. and Henri, G. (1998). The terminal bulk Lorentz factor of relativistic electron-positron jets. *Monthly Notices of the Royal Astronomical Society*, 300(4):1047–1056.

Reynolds, C.S. (2013). Measuring Black Hole Spin Using X-Ray Reflection Spectroscopy. *Space Science Reviews*, 183(1-4):277–294.

Rybicki, G.B. and Lightman, A.P. (1986). Radiative Processes in Astrophysics. *Radiative Processes in Astrophysics*.

Saito, S. et al (2013). VERY RAPID HIGH-AMPLITUDE GAMMA-RAY VARIABILITY IN LUMINOUS BLAZAR PKS 1510-089 STUDIED WITH FERMI-LAT. *The Astrophysical Journal*, 766(1):L11.

Salpeter, E.E. (1964). Accretion of Interstellar Matter by Massive Objects. *Astrophysical Journal*, 140:796.

Saugé, L. (2004). MODELISATIONS DE L'EMISSION NON-THERMIQUE DES BLAZARS DU TeV PAR UNE DISTRIBUTION RELATIVISTE QUASI-MAXWELLIENNE. *tel.archives-ouvertes.fr*.

Saugé, L. and Henri, G. (2004). TeV blazar gamma-ray emission produced by a cooling pile-up particle energy distribution function. *arXiv.org*.

Schlickeiser, R. (1984). An explanation of abrupt cutoffs in the optical-infrared spectra of non-thermal sources - A new pile-up mechanism for relativistic electron spectra. *Astronomy and Astrophysics*, 136:227–236.

Schmidt, M. (1963). 3C 273 : A Star-Like Object with Large Red-Shift. *Nature*, 197(4872):1040–1040.

Shakura, N.I. and Sunyaev, R.A. (1976). A theory of the instability of disk accretion on to black holes and the variability of binary X-ray sources, galactic nuclei and quasars. *Monthly Notices of the Royal Astronomical Society*, 175:613–632.

Shariati, A. and Khorrami, M. (1999). Equivalence Principle and Radiation by a Uniformly Accelerated Charge - Springer. *Foundations of Physics Letters*, 12(5):427–439.

Shields, G.A. (1999). A Brief History of Active Galactic Nuclei. *Publications of the Astronomical Society of the Pacific*, 111(760):661–678.

Sikora, M. and Madejski, G. (2000). On Pair Content and Variability of Subparsec Jets in Quasars. *Astrophysical Journal*, 534(1):109–113.

Sikora, M. et al (1996). Radiation drag in relativistic active galactic nucleus jets. *Monthly Notices of the Royal Astronomical Society*, 280(3):781–796.

Sol, H., Pelletier, G. and Asseo, E. (1989). Two-flow model for extragalactic radio jets. *Monthly Notices of the Royal Astronomical Society (ISSN 0035-8711)*, 237:411–429.

SWANENBURG, B.N. et al (1978). COS B observation of high-energy γ radiation from 3C273. *Nature*, 275(5678):298–298.

Tadhunter, C.N. et al (1993). Optical Spectroscopy of a Complete Sample of Southern 2-JY Radio Sources. *Monthly Notices of the Royal Astronomical Society*, 263:999.

Tanner, A.M. et al (1996). A Study of Quasar Absorption-Line Systems With IRAS. *The Astronomical Journal*, 112:62.

Tavecchio, F. and Ghisellini, G. (2008). The spectrum of the broad-line region and the high-energy emission of powerful blazars. *Monthly Notices of the Royal Astronomical Society*, 386(2):945–952.

Tavecchio, F. et al (2010). TeV BL Lac objects at the dawn of the Fermiera. *Monthly Notices of the Royal Astronomical Society*, 401(3):1570–1586.

Tombesi, F. and Cappi, M. (2014). On the presence of ultrafast outflows in the WAX sample of Seyfert galaxies. *Monthly Notices of the Royal Astronomical Society: Letters*, 443(1):L104–L108.

Tran, H.D., Osterbrock, D.E. and Martel, A. (1992). Extreme spectral variations of the Seyfert galaxy Markarian 993. *The Astronomical Journal*, 104:2072–2077.

Turland, B.D. (1975). 3C 219 - A double radio source with a jet. *Monthly Notices of the Royal Astronomical Society*, 172:181–189.

Turler, M. et al (1998). 30 years of multi-wavelength observations of 3C 273. *arXiv.org*, pages 89–101.

Urry, C.M. and Padovani, P. (1995). Unified Schemes for Radio-Loud Active Galactic Nuclei. *Publications of the Astronomical Society of the Pacific*, 107:803.

van BREUGEL, W.J.M. and MILEY, G.K. (1974). Radio /'jets/'. *Nature*, 265(5592):315–318.

Veron, P. (1974). *Les Quasars*. Presses Universitaires de France, 108 Boulevard Saint-Germain Paris, que sais-je? edition.

Vuillaume, T., Henri, G. and Petrucci, P.O. (2015). Variation of bulk Lorentz factor in AGN jets due to Compton rocket in a complex photon field. *Astronomy and Astrophysics*, 581:A18.

Wandel, A., Peterson, B.M. and Malkan, M.A. (1999). Central Masses and Broad-Line Region Sizes of Active Galactic Nuclei. I. Comparing the Photoionization and Reverberation Techniques. *Astrophysical Journal*, 526(2):579–591.

Whitney, A.R. et al (1971). Quasars Revisited: Rapid Time Variations Observed Via Very-Long-Baseline Interferometry. *Science*, 173(3993):225–230.

Woltjer, L. (1959). Emission Nuclei in Galaxies. *Astrophysical Journal*, 130:38.

Woo, J.H. and Urry, C.M. (2002). Active Galactic Nucleus Black Hole Masses and Bolometric Luminosities. *Astrophysical Journal*, 579(2):530–544.

Zdziarski, A.A. and Böttcher, M. (2015). Hadronic models of blazars require a change of the accretion paradigm. *Monthly Notices of the Royal Astronomical Society: Letters*, 450(1):L21–L25.

Zdziarski, A.A. and Pjanka, P. (2013). Compton scattering of blackbody photons by relativistic electrons. *Monthly Notices of the Royal Astronomical Society*, 436(4):2950–2955.

Zel'dovich, Y.B. (1964). The Fate of a Star and the Evolution of Gravitational Energy Upon Accretion. *Soviet Physics Doklady*, 9:195.

Modeling the emission of active galactic nuclei at Fermi's era

Abstract

Active galactic nuclei (AGN) are the most energetic objects known in the universe. Their fantastic luminosity is due to efficient conversion of gravitational energy of mass accreted on super-massive black-holes at the center of galaxy. About 10% of AGN are even more incredible as they display relativistic jets on galaxy scales. Those jets are observed at all energies, from far radio to the highest $\gamma - rays$. Despite intense study since their discovery in the 50's and more and more observations, encouraged by rapid progress in instrumentation, AGN are still widely misunderstood. The questions of formation, composition, and acceleration of jets are central but still a matter of debates. Models aiming at reproducing observed emission have been developed throughout the years. The most common one, the one-zone model, often relies on ad-hoc hypothesis and does not provide a satisfactory answer.

The two-flow paradigm developed at IPAG and based on an original idea from Sol et al. (1989) aims at giving a more coherent and physical representation of AGN jets. The principal assumption is that jets are actually composed of two coaxial flows: an inner spine made of a pure pair plasma, moving at relativistic speed and responsible for the non-thermal observed emission surrounded by an external sheath, made of a baryonic MHD plasma, mildly relativistic but carrying most of the power. The two-flow paradigm finds roots in observations as well as theoretical arguments and has been able to explain many AGN features.

During my PhD, I studied this paradigm and contributed to the development of a numerical model based on its concepts. I have been particularly interested in the inverse Compton scattering of thermal photons, fundamental process in the modeling of AGN emission, as well as the Compton rocket effect, key to the acceleration of the spine in the two-flow paradigm.
However, taking completely into account the inverse Compton emission can be very time consuming. To accomplish fast and efficient computation of the external Compton emission, I have had to formulate new analytical approximations of the scattering of a thermal distribution of photons.

I have also studied the Compton rocket effect, responsible for the acceleration of the inner spine in the two-flow paradigm. I showed that the resulting bulk Lorentz factor of the flow in the complex photon field of an AGN is subject to variations along the jet as a function of the distance to the central engine. These variations can have drastic effects on the observed emission and could induce variability, both spatially and temporally. I also showed that the terminal bulk Lorentz factor obtained are compatible with physical conditions expected in jets and with observations.

The complete model produce spectral energy distribution (SED) comparable to observed ones. However, the model is by nature erratic and it is difficult to make a direct link between the model parameters (input) and the SED (output). Unfortunately, standard data fitting procedures (e.g. based on gradient methods) are not adapted to the model due to its important number of parameters, its important computing time and its non-linearity. In order to circumvent this issue, I have developed a fitting tool based on genetic algorithms. The application of this algorithm allowed me to successfully fit several SED. In particular, I have also showed that the model, because based on a structured jet model, can reproduce observations with low bulk Lorentz factor, thus giving hope to match observations and theoretical requirements in this matter.